Aerospace Research Communications

January 2025

Flow Control

Issue Editors

Yao Zheng
Zhejiang University,
China

Song Fu
Tsinghua University,
China

Eusebio Valero
University of Madrid,
Spain

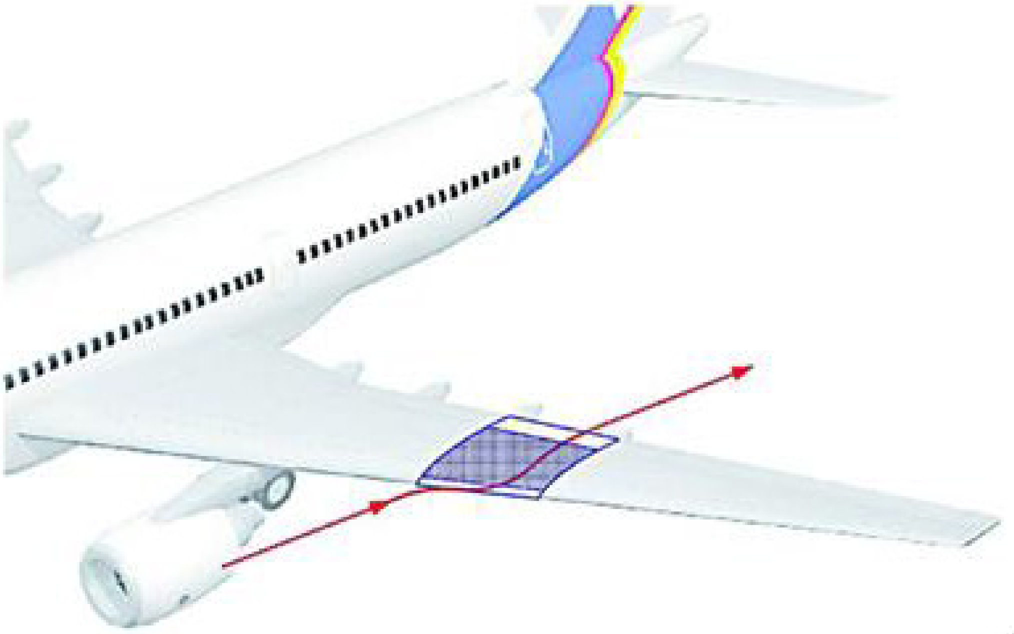

Special Issue cover photo taken from SSECOID project: “Stability and Sensitivity Methods for Flow Control and Industrial Design”, Grant agreement No 955923. MARIE SKŁODOWSKA-CURIE ACTIONS Innovative Training Networks (ITN).

frontiers | Publishing Partnerships

Flow Control

Flow control is a technical means of manipulating the behaviors and characteristics of fluid flows. The ultimate goal is to enhance or modify flow properties, such as velocity, pressure, and turbulence intensity, in order to achieve specific engineering objectives. Flow control can be broadly classified into two categories: passive and active. Passive flow control is generally simpler and more cost-effective than active control, but it may have limited effectiveness and may not be suitable for all types of flows. Active flow control, while more complex and often more expensive, can achieve higher levels of flow manipulation and may be applied to a wider range of flows.

The science behind Flow control is multidisciplinary and refers to aspects of fluid mechanics, materials science, control theory, and numerical modeling. The techniques of flow control have important applications in various fields, including aerospace, automotive, civil, and biomedical engineering, and can help to improve efficiency, to reduce energy consumption, to increase performance, and to improve safety and reliability.

This Special Issue from new open-access journal Aerospace Research Communications showcases recent advances and challenges in the fundamental understanding and practical implementation of flow control techniques.

ARC eBook
Copyright Statement

The copyright in the text of individual articles in this eBook is the property of their respective authors or their respective institutions or funders. The copyright in graphics and images within each article may be subject to copyright of other parties. In both cases this is subject to a license granted to Frontiers.
The compilation of articles constituting this eBook is the property of Frontiers.
Each article within this eBook, and the eBook itself, are published under the most recent version of the Creative Commons CC-BY licence. The version current at the date of publication of this eBook is CC-BY 4.0. If the CC-BY licence is updated, the licence granted by Frontiers is automatically updated to the new version.
When exercising any right under the CC-BY licence, Frontiers must be attributed as the original publisher of the article or eBook, as applicable.
Authors have the responsibility of ensuring that any graphics or other materials which are the property of others may be included in the CC-BY licence, but this should be checked before relying on the CC-BY licence to reproduce those materials. Any copyright notices relating to those materials must be complied with.
Copyright and source acknowledgement notices may not be removed and must be displayed in any copy, derivative work or partial copy which includes the elements in question.
All copyright, and all rights therein, are protected by national and international copyright laws. The above represents a summary only. For further information please read Frontiers' Conditions for Website Use and Copyright Statement, and the applicable CC-BY licence.

ISSN 2813-6209
ISBN 978-2-8325-5867-6
DOI 10.3389/978-2-8325-5867-6

Table of contents

AEROSPACE RESEARCH COMMUNICATIONS
SPECIAL ISSUE EDITORIAL
published: 06 January 2025
doi: 10.3389/arc.2024.14155

Editorial: Flow Control

Yao Zheng[1]*, *Song Fu*[2] *and Eusebio Valero*[3]

[1]*School of Aeronautics and Astronautics, Zhejiang University, Hangzhou, China,* [2]*School of Aerospace Engineering, Tsinghua University, Beijing, China,* [3]*School of Aeronautics, Polytechnic University of Madrid, Madrid, Spain*

Keywords: active flow control, passive flow control, drag reduction, multi-objective design, subsonic flow, supersonic flow, hypersonic flow

Editorial on the Special Issue

Flow Control

This Special Issue of Aerospace Research Communications showcases recent advances and challenges in the fundamental understanding and practical implementation of flow control techniques. Flow control is a technical means of manipulating the behaviors and characteristics of fluid flows. The ultimate goal is to enhance or modify flow properties, such as velocity, pressure, and turbulence intensity, in order to achieve specific engineering objectives. Flow control can be broadly classified into two categories: passive and active. Passive flow control is generally simpler and more cost-effective than active control, but it may have limited effectiveness and may not be suitable for all types of flows. Active flow control, while more complex and often more expensive, can achieve higher levels of flow manipulation and may be applied to a wider range of flows.

As an example of passive flow control, Yu et al. have carried out flow field analysis of a turbulent channel controlled by scalloped riblets. Riblets are small protruding surfaces along the direction of the flow, and are one of the most well-known passive turbulent drag reduction methods. The shape of a scalloped riblet is constructed by smoothly connecting two third-order polynomials and is not as sharp in the tip as corresponding triangular riblets with the same height-width ratio. Numerical simulations have been performed for turbulent channel flow with and without riblet control. It should be noted that the class of scalloped riblets discussed in this article is suitable for investigations on the influences of curvatures at the tip and the valley of the riblet in future.

As an example of active flow control, Huang et al. have investigated the Reynolds number effects on the drag reduction with a spanwise traveling wave of blowing and suction in turbulent channel flows. Turbulent channel flows with $Re\tau = 180$ and $Re\tau = 550$ are controlled to reduce the drag with a spanwise traveling wave of the blowing and suction method. An oscillatory spanwise motion above the wall is generated by a spanwise traveling wave with a periodically reversing propagation direction, similarly as the Stokes layer produced by the wall oscillation. Through an asymptotic expansion analysis, the authors found that the deterioration in drag reduction rates is due to the less effective lift-up effects from the actuation, less contribution from the inner layer region, and small-scale structures at a higher Reynolds number.

In general concept of enhancing wake vortex decay, Xu et al. have carried out numerical optimization on aircraft wake vortex decay enhancement. Blowing air at the end of the airport runway can accelerate the decay of the near-ground aircraft wake vortex, and thereby reducing the negative impact of the vortex on the following aircraft. However, the benefits of accelerating wake dissipation vary for different blowing parameters, so it is necessary to set appropriate parameters in order to obtain better acceleration results. Because of the high cost of traditional optimization

***Correspondence**
Yao Zheng,
✉ *yao.zheng@zju.edu.cn*

Received: *03 December 2024*
Accepted: *16 December 2024*
Published: *06 January 2025*

Citation:
Zheng Y, Fu S and Valero E (2025) Editorial: Flow Control. Aerosp. Res. Commun. 2:14155. doi: 10.3389/arc.2024.14155

methods, a Kriging surrogate model is used to obtain a better design of the blowing zone for enhancement of wake vortex decay. By overlapping and comparing the design spaces for different wake vortices, a multi-objective design is realized, which improves the engineering feasibility of the current blowing method.

As another example of active flow control, Li et al. have carried out numerical investigations of outer-layer turbulent boundary layer control for drag reduction through micro fluidic-jet actuators. The study aims to reduce turbulent drag by reshaping the flow structure within the turbulent boundary layer. To ensure the calculation accuracy of the core region and reduce the consumption of computing resources, a zonal LES/RANS strategy and WMLES method are proposed to simulate the effects of fluidic-actuators for outer-layer boundary control, in which high-performance computing has to be involved. The mechanism for drag reduction is analysed via a pre-multiplied spectral method and a parallel dynamic mode decomposition (DMD) method.

The above four articles are considered mainly for subsonic fluid dynamics. Finally, Lee et al. have provided a review article on flow control strategies for supersonic/hypersonic fluid dynamics. Supersonic and hypersonic flows have gained considerable attention in the aerospace industry in recent years. Flow control is crucial for refining the quality of these high-speed flows and improving the performance and safety of fast aircraft. The review addresses the distinctive characteristics of supersonic flows compared to low-speed flows, including phenomena such as boundary layer transition, shock waves, and sonic boom. These traits give rise to significant challenges related to drag, noise, and heat. Therefore, a review of several active and passive control strategies is provided, highlighting their significant advancements in flow transitions, reducing drag, minimizing noise, and managing heat. Furthermore, a comprehensive analysis is provided for various research methodologies used in the application of flow control engineering, including wind tunnel testing, flight testing, and fluid dynamics computation.

These five articles give an overview of the present state of flow control research, and offer insights into potential future advancements, including passive flow control and active flow control, and covering subsonic, supersonic, and hypersonic cases.

AUTHOR CONTRIBUTIONS

This editorial has been drafted by lead guest editor, YZ. He has shared it with the other guest editors. All authors contributed to the article and approved the submitted version.

CONFLICT OF INTEREST

The authors declare that the research was conducted in the absence of any commercial or financial relationships that could be construed as a potential conflict of interest.

GENERATIVE AI STATEMENT

The author(s) declare that no Generative AI was used in the creation of this manuscript.

AEROSPACE RESEARCH COMMUNICATIONS
REVIEW
published: 01 November 2024
doi: 10.3389/arc.2024.13149

A Review of Flow Control Strategies for Supersonic/Hypersonic Fluid Dynamics

Shibo Lee*[1], *Yunlong Zhao*[1], *Jiaqi Luo*[1], *Jianfeng Zou*[1], *Jifa Zhang*[1,2], *Yao Zheng*[1,2] and *Yang Zhang*[1,2]

[1]School of Aeronautics and Astronautics, Zhejiang University, Hangzhou, Zhejiang, China, [2]Zhejiang Institute of Turbomachinery and Propulsion Systems, Huzhou, Zhejiang, China

Supersonic and hypersonic flows have gained considerable attention in the aerospace industry in recent years. Flow control is crucial for refining the quality of these high-speed flows and improving the performance and safety of fast aircraft. This paper discusses the distinctive characteristics of supersonic flows compared to low-speed flows, including phenomena such as boundary layer transition, shock waves, and sonic boom. These traits give rise to significant challenges related to drag, noise, and heat. Therefore, a review of several active and passive control strategies is provided, highlighting their significant advancements in flow transitions, reducing drag, minimizing noise, and managing heat. Furthermore, we provide a comprehensive analysis of various research methodologies used in the application of flow control engineering, including wind tunnel testing, flight testing, and computational fluid dynamics (CFD). This work gives an overview of the present state of flow control research and offers insights into potential future advancements.

Keywords: supersonic, hypersonic, review, flow control, compressible flow

INTRODUCTION

Since Colonel Yeager piloted the X-1 aircraft to break the sound barrier in 1947 [1], humanity officially entered the supersonic era, as shown in **Figure 1**. Researchers and engineers have embarked on various scientific explorations and engineering practices in the field of high-speed manned or unmanned aircrafts [2]. The variable Mach number, Ma, is a non-dimensional parameter utilized to quantify compressibility in fluid dynamics, typically employed to differentiate between subsonic ($Ma < 1$) and supersonic ($Ma > 1$) flow. In contrast to subsonic flow, the supersonic flow exhibits distinctive physical phenomena, including shock waves, compressibility effects, and boundary layer transition dominated by the second mode, as illustrated in **Figure 2**. Hsue-Shen Tsien [7] first proposed that when $Ma \geq 5$, the flow might be classified as hypersonic flow. Over time, individuals gradually recognized the importance of hypersonic flow, and investigations uncovered several distinct attributes of hypersonic flow in comparison to supersonic flow, such as thin shock layers, entropy layers, viscous interactions, high-temperature flow, low-density flow, real gas effects, and chemical non-equilibrium effects.

Boundary layers and flow control are closely linked concepts. The idea of flow control has been there since Prandtl first introduced boundary layer theory in the early days. The study of laminar and turbulent flows has historically placed great emphasis on flow control, which has wide-ranging applications in aerospace engineering. The objective of flow control is to enhance the qualities of

***Correspondence**
Yang Zhang,
✉ yangzhang@zju.edu.cn

***Received:** 18 April 2024
***Accepted:** 21 October 2024
***Published:** 01 November 2024

***Citation:**
Lee S, Zhao Y, Luo J, Zou J, Zhang J, Zheng Y and Zhang Y (2024) A Review of Flow Control Strategies for Supersonic/Hypersonic Fluid Dynamics.
Aerosp. Res. Commun. 2:13149.
doi: 10.3389/arc.2024.13149*

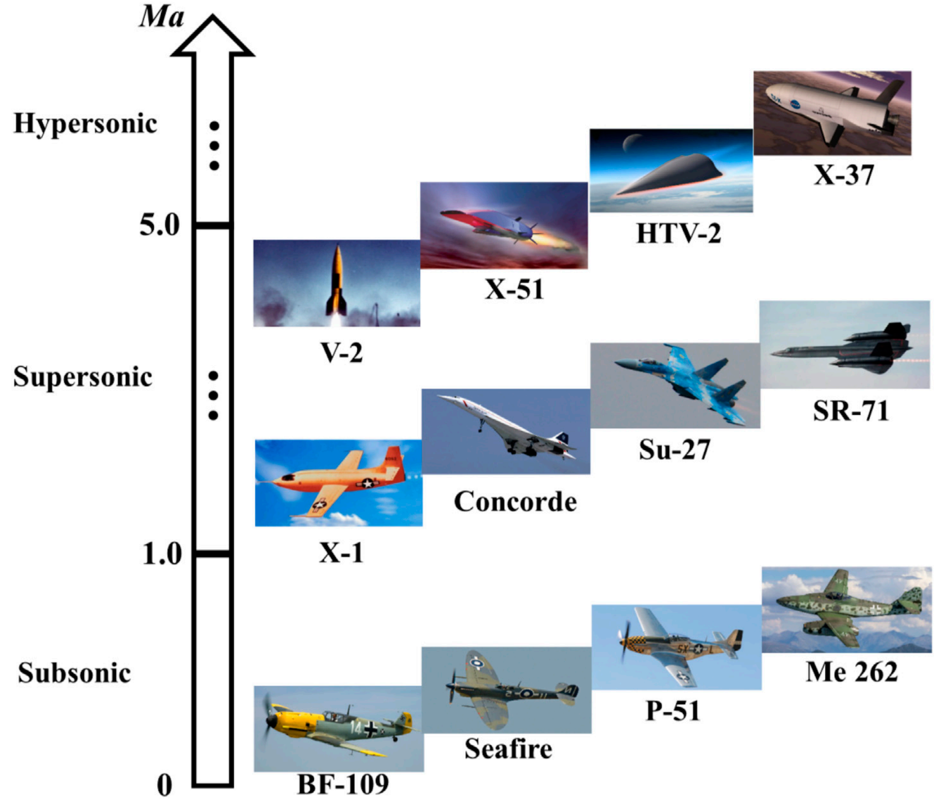

FIGURE 1 | Some famous aircraft and their flight Mach numbers.

fluids, such as lift-drag ratio, thermal protection, noise reduction, vibration attenuation, etc. [8–10], by using various methods to modify the flow patterns and evolutionary structures. These methods include altering flow separation, compressible mixing, turbulent transition, and more. In the 1970s, NASA Langley Research Center discovered that the tooth-like structure on the sharks' surface could decrease flow resistance while fast swimming. As a result, several groove control techniques were developed for aircraft surfaces, as shown in **Figure 3**. The blowing/suction technique involves adding or subtracting energy into the boundary layer to modify the properties of the average velocity profile. This can lead to a more active boundary layer or a thinner newly formed boundary layer, which aids in modifying the pressure gradient caused by flow separation and associated flow instability. The design of flow control systems is extremely intricate due to the complex interactions between shock waves and boundary layers, as well as the coupling effects of high-temperature, high-pressure, and strong discontinuities in high-speed flows. Despite their effectiveness and widespread use in engineering applications, these techniques also face significant challenges.

This paper presents a comprehensive analysis of flow control strategies and their advancements in the field of supersonic and hypersonic flows. The work focuses on the fundamental attributes of supersonic and hypersonic flows, and highlights the significance of investigating flow control within these regimes. The paper is organized as follows: The initial section introduces the attributes of supersonic and hypersonic flows and examines the significance of investigating flow control in these conditions. The second section presents the research progress in several typical phenomena: boundary layer transition, shock wave trains, shock wave/boundary layer interactions, and sonic boom. The third section shows common flow control strategies, examining them extensively within the frameworks of active control and passive control. The fourth section of the study concentrates on research methodologies for high-speed compressible flows, specifically examining research findings in the area of supersonic and hypersonic flow control. This analysis is conducted through the perspectives of CFD techniques, wind tunnel testing techniques, and flight testing techniques. The review of supersonic and hypersonic flow control techniques provides valuable insights into possible future research avenues.

TYPICAL PHENOMENA OF SUPERSONIC AND HYPERSONIC FLOWS

Boundary Layer and Flow Transition

A boundary layer transition from laminar to turbulent flow occurs when the Reynolds number exceeds the critical threshold [14], as shown in **Figure 4**. Accurately predicting

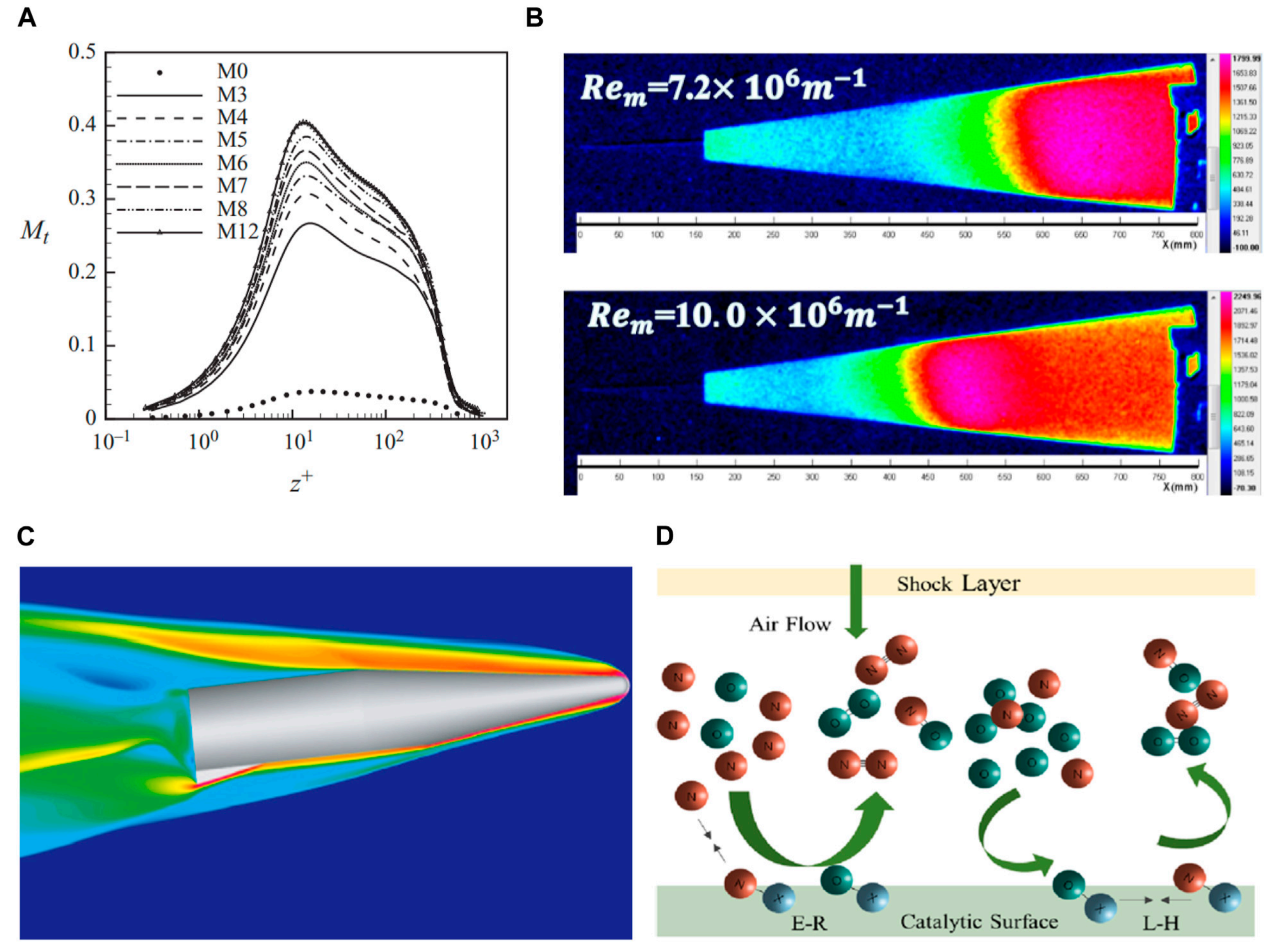

FIGURE 2 | Supersonic and hypersonic aircraft and complex flow phenomena [3–6]. **(A)** Compressibility effects **(B)** Boundary layer transition. **(C)** Shock waves **(D)** Chemical reaction.

flow transition and understanding the underlying flow mechanism are of utmost importance in engineering. Research discovered that the frictional resistance coefficient increases by a factor of 4 times [16] when the supersonic boundary layer with a freestream of *Ma* = 3 transitions. Following the transition of the hypersonic boundary layer, the turbulent region often experiences a significant increase in both friction resistance and heat flux, often reaching levels that are 3–5 times higher than before [17]. The literatures [18] review the progress of hypersonic boundary layer transition and highlights the limits of the current predominant approaches of predicting transition, which typically rely on transition data or empirical formulas. It also pointed out that flight tests can serve as a viable approach for conducting transition studies in authentic flight situations. Many countries have carried out many transition flight tests, such as the Hypersonic Boundary Layer Transition (HyBOLT) transition control flight test conducted by the United States, and the compression surface transition of the scramjet forebody (LEA) the flight test carried out by France. *Aircraft Flight Tests* section will introduce these flight tests in detail.

As a necessary experimental facility for simulating real flight, hypersonic wind tunnels play a pivotal role in the study of boundary layer transition. As shown in **Figure 5**, the quiet wind tunnel [19] built by the National Laboratory of Turbulence and Complex Systems of Peking University can cover supersonic and hypersonic flows in the range of Ma 3.0~6.5 with the diameter of nozzle exit being 300 mm. At present, the relatively powerful and easy-to-use near-wall measurement technologies mainly include temperature-sensitive paint (TSP), near-wall particle image velocimetry and Rayleigh-scattering visualization. They provide good experimental measurement methods for research transition. In addition, TSP is a non-contact optical temperature measurement technology that can achieve high spatial resolution temperature field measurement.

The hypersonic flow, being a type of high-enthalpy motion, must take into account some unique phenomena, including the failure of the calorically perfect gas assumption, thermochemical non-equilibrium effects, molecular vibration energy excitation, molecular ionization, material ablation, etc. Numerical modeling

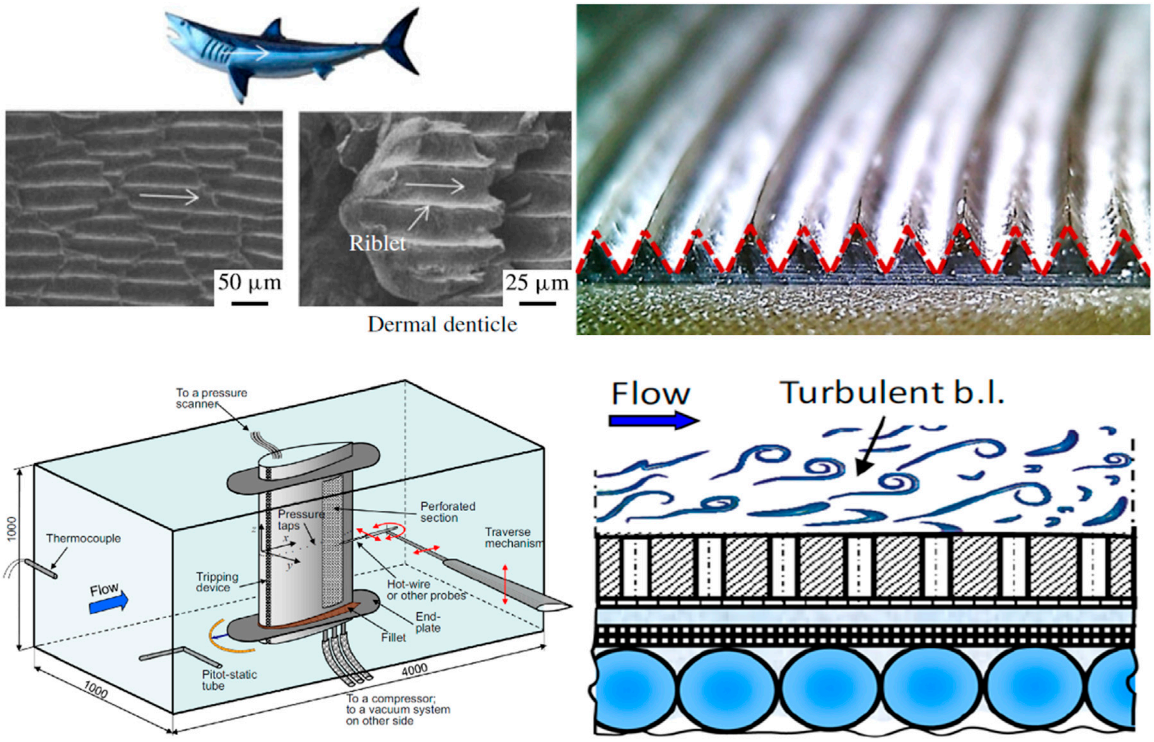

FIGURE 3 | Shark-skin grooves [11, 12] and blowing/suction control [13].

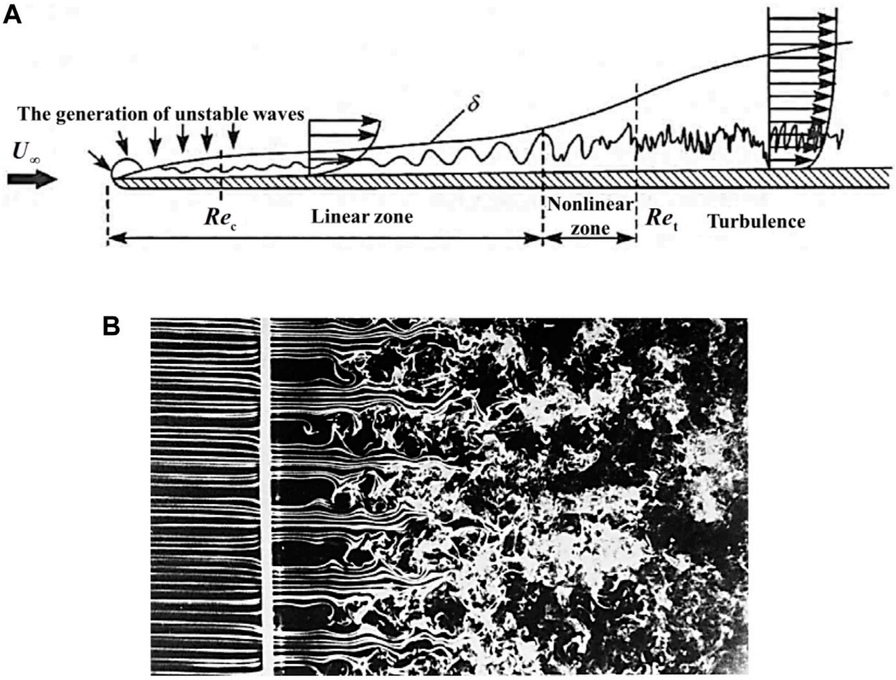

FIGURE 4 | Experimental and schematic diagram of the transition process. **(A)** Schematic diagram of the transition process [14]. **(B)** Experimental diagram of the transition process [15].

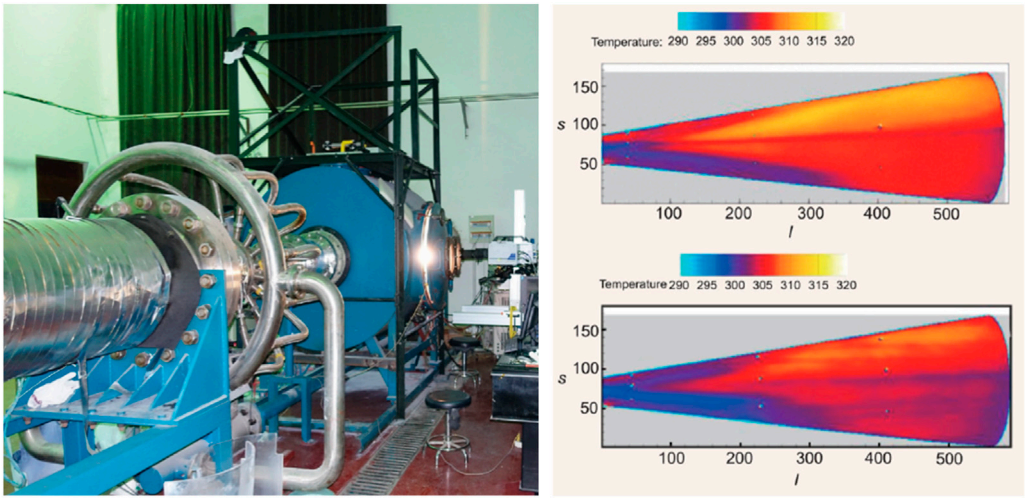

FIGURE 5 | Ma 6.0 low-noise wind tunnel of Peking University [19].

methods for high enthalpy flow transition and turbulence simulation [20] necessitate the development of many techniques, including real gas models and high-enthalpy boundary layer stability models. Several flow control strategies available for managing high enthalpy boundary layers were proposed, including but not limited to: 1) CO_2 injection, 2) wall blowing/suction, 3) wall porous coatings, and 4) roughness elements. The effectiveness of flow control in delaying the transition of hypersonic boundary layers in four forms of instability, namely, streamwise traveling waves instability, crossflow instability, Görtler instability, and attachment line instability, was highlighted by Liu et al. [21]. The employed techniques encompassed 1) roughness elements and finite amplitude band control, 2) wavy walls, 3) microporous surfaces, 4) localized heating/cooling of walls, 5) heavy gas injection, 6) synthetic jet, 7) blowing/suction, and so forth. The experimental progress in controlling hypersonic boundary layer transition was reviewed by Yang et al. [22]. The flow control techniques were thoroughly summarized and outlined, including roughness elements, cavities, porous walls, wavy walls, jets, wall cooling/heating, plasma, and more. Special emphasis was placed on the feasibility of plasma control to postpone the transition of hypersonic boundary layer.

To date, researchers have achieved proficiency in employing uncomplicated techniques to forecast the transition of boundary layers across fundamental geometries [23, 24]. Additionally, they have devised related algorithms or software [25], which offer valuable support for contemporary flow control analysis and engineering application [26]. However, the transition of hypersonic boundary layers remains a challenging task, and the underlying flow mechanisms are not yet completely comprehended. The aerodynamic and thermal protection design of the next-generation of hypersonic aircraft largely depends on the depth of understanding of transition mechanisms and the ability to control them.

Shock Wave Trains

A series of shock waves, which are frequently seen in supersonic inlets and at the heads of aircraft, define shock wave train, a complicated flow phenomenon [27]. Shock/shock interaction, which is intricately linked to shock wave trains, is a significant area of interest and obstacle. Understanding the mechanics of the subject matter and providing an accurate description and prognosis had substantial academic and practical significance. Schematic representations depicting six distinct shock/shock interactions on a blunt leading edge are illustrated in **Figure 6**.

A study was conducted to provide a comprehensive understanding of internal structures, oscillatory behaviors, and active/passive controls of shock wave trains [29]. The control methods in this study encompass three main approaches: 1) boundary layer suction, 2) bump control, 3) vortex generator. Via utilizing intelligent sensing technology, real-time information in the flow field is reconstructed. By employing adaptive adjustment of the suction air or vortex generator switch, the working efficiency is enhanced throughout a broad spectrum of inflow conditions. Luo et al. [30] provided detailed information on various techniques for controlling shock waves at the leading edge. These techniques include reverse jet flow, laser energy deposition, and plasma synthetic jets. For controlling oblique shock waves in the inlet and side wings, the main methods include plasma discharge, compression corner control, and magnetohydrodynamic methods. For controlling shock/shock interaction, the main methods include reverse supersonic jets, laser-based energy deposition methods, and plasma discharge.

As shown in **Figure 7**, in the SAV21 supersonic cascade [27], the shock wave train induced by high back pressure exhibits highly three-dimensional structure, facilitating the passage of the leading edge of the shock wave train down the throat. This phenomenon leads to a decrease in

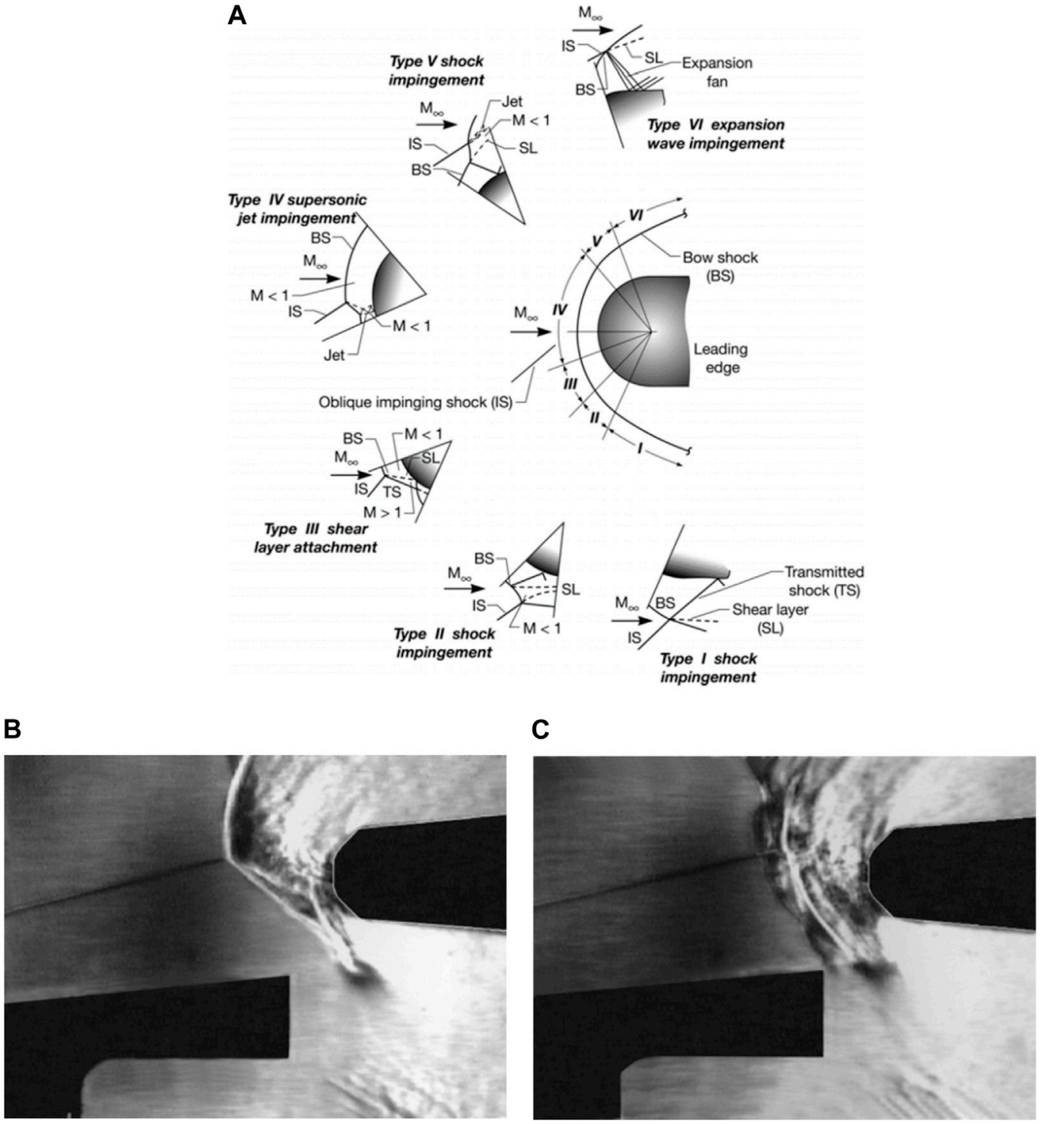

FIGURE 6 | Shock/shock interactions on a cowl leading edge [28]. **(A)** Six types of shock/shock interaction. **(B)** Type III before transition. **(C)** Type III after transition.

the mass-capturing coefficient and the occurrence of stall. When designed surface or end-wall suction slots were adopted, the maximum back pressure could be improved by 20%. Zhang et al. [31] investigated the asymmetry of oblique shock wave trains at $Ma = 2.7$. The experimental findings demonstrated that the oblique shock wave trains exhibited flow separation regions upon travelling ramps, characterized by a rapid increase in their motion velocity. Additionally, the direction of asymmetric separation deflection may undergo a change. Based on the interaction characteristics between the oblique shock wave train and upstream shocks, the slope control in the pipeline is employed to generate asymmetric upstream flow conditions by manipulating the deflection direction of the oblique shock wave trains.

Shock Waves/Boundary Layer Interactions (SWBLI)

The presence of shock waves/boundary layer interactions is prevalent in the flow patterns both within and outside transonic, supersonic, and hypersonic aircraft. Since first observed by Ferri [32] in 1939, it has quickly become a hot topic in the research of supersonic flow control. Simplified models are proposed to investigate the underlying physical mechanism of shock wave/boundary layer interactions, as

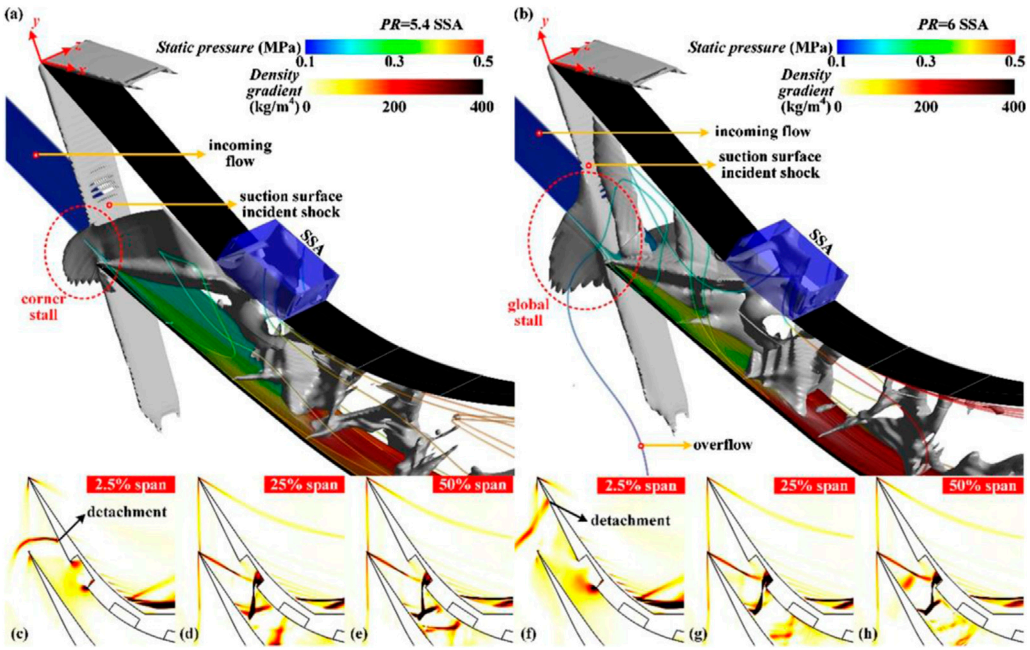

FIGURE 7 | Three-dimensional shock wave train in the SAV21 supersonic cascade [27]. **(A)** the isosurface of the streamwise density gradient at a contour value of $0.5 \times \partial\rho/\partial x - 0.87 \times \partial\rho/\partial y = 110$) and space streamlines rendered with static pressure contour when backpressure ratio $PR = 5.4$. **(B)** the isosurface of the streamwise density gradient at a contour value of $0.5 \times \partial\rho/\partial x - 0.87 \times \partial\rho/\partial y = 110$) and space streamlines rendered with static pressure contour when backpressure ratio $PR = 6$. **(C)** streamwise density gradient contour at 2.5% spans when $PR = 5.4$. **(D)** streamwise density gradient contour at 25% spans when $PR = 5.4$. **(E)** streamwise density gradient contour at 50% spans when $PR = 5.4$. **(F)** streamwise density gradient contour at 2.5% spans when $PR = 6$. **(G)** streamwise density gradient contour at 25% spans when $PR = 6$. **(H)** streamwise density gradient contour at 50% spans when $PR = 6$.

shown in **Figure 8**, owing to the intricate nature. Swept compression ramps are commonly found in the inlets or surfaces of supersonic/hypersonic aircraft. Similarly, the utilization of dual-fin design is frequently observed in the upper sections of sidewall compressions. Surface protrusions on aircraft surfaces are frequently fabricated using cylinders, half cones, and fins as their primary shapes.

What we need to regulate is the most important aspect of flow control. Dolling [34] considered that the flow control of shock wave/boundary layer interactions was to reduce peak heat flux, decrease the fluctuating pressure loads, diminish the scale of separated flow, and move the frequency of fluctuation outside of the critical range. There are three strategies for controlling shock wave/boundary layer interactions summarized [35]: 1) increasing energy in the bottom layer of the boundary layer to enhance its resistance to adverse pressure gradients; 2) reducing pressure differences before and after shock waves in the near-wall region; 3) injecting energy to increase wall temperature, which raises the speed of sound and lowers the intensity of the shock wave. Specifically, methods such as bleeding and transpiration, perforations and porous media, MART technology (Mesoflaps for Aeroelastic Recirculating Transpiration, MART), streamwise slots, secondary flow circulation, and wall bump were employed. Zhong et al. [36] provided an overview of the evolution of shock/boundary layer interactions and its impacts on the flow process. Furthermore, Shi et al. [37] elaborated on methods for controlling shock wave/turbulent boundary layer interactions, including micro-vortex generators, plasma control, electromagnetic coupling effects, and other techniques.

The interaction between shocks and boundary layers is an inherent physical phenomenon that is commonly observed in high-speed aircraft. This phenomenon can manifest in several areas, including inlets, flow corners, and wings. Nevertheless, the majority of existing flow control studies primarily concentrate on supersonic flow characterized by Mach numbers spanning from 1 to 4, and there is still little research on hypersonic flows. Consequently, there is a pressing requirement for further exploration of hypersonic flow in forthcoming research endeavors. Furthermore, it is crucial to consider the significance of low-frequency oscillations [38] in the flow control of shock/boundary layer interactions.

Sonic Boom

The phenomenon of sonic boom is exclusive to supersonic flight. As illustrated in **Figure 9**, when an aircraft operates at supersonic speeds, its components and the gas emitted will cause significant disruptions in the surrounding air, leading to the formation of shock/expansion wave systems. The interaction and propagation of these wave systems towards the ground result in the formation of two primary shock waves, known as leading and trailing. As these two shock waves sweep across the ground, an observer perceives two explosive-like sounds, which are referred to as a "sonic boom" [40].

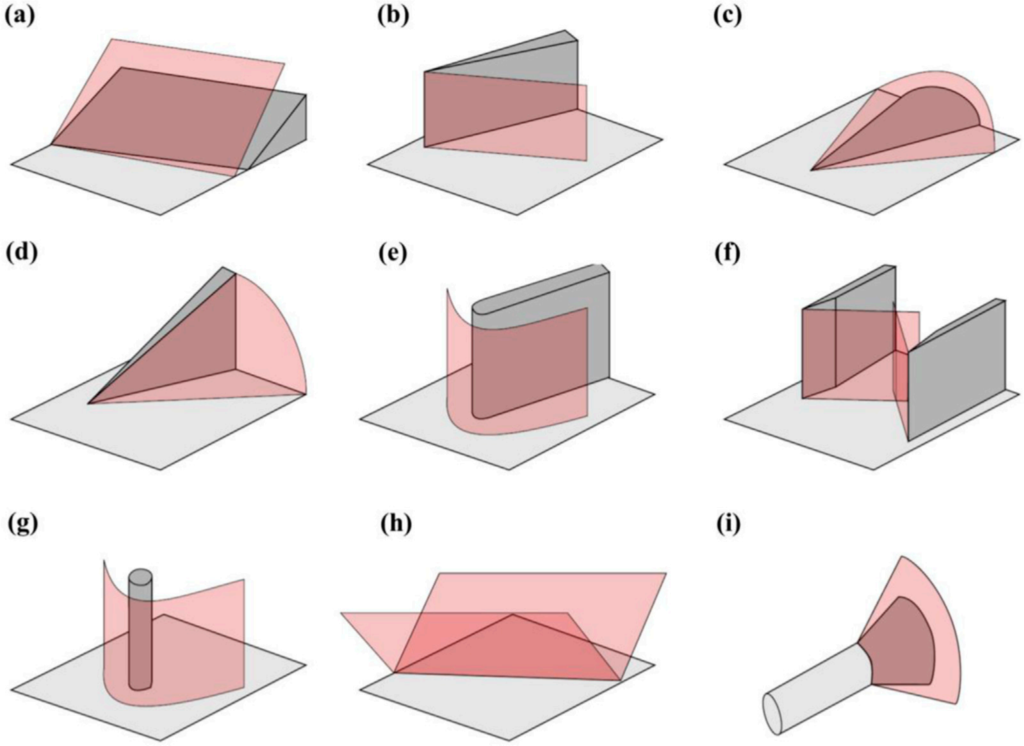

FIGURE 8 | Canonical three-dimensional SWBLI configurations in high-speed aircraft applications [33]. **(A)** swept compression conrner. **(B)** sharp unswept fin. **(C)** semi-cone. **(D)** swept fin. **(E)** blunt fin. **(F)** double fin. **(G)** vertical cylinder. **(H)** swept impinging shock. **(I)** flared cylinder.

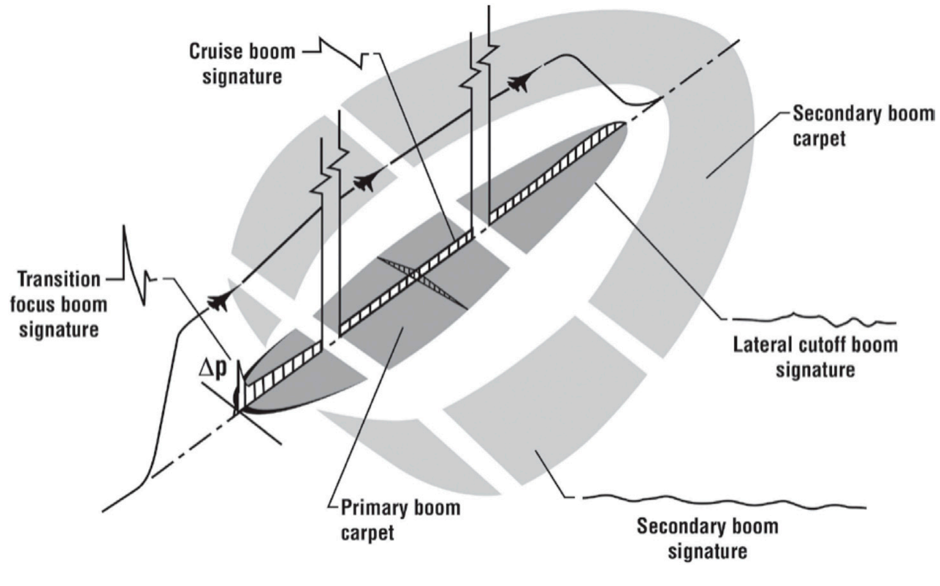

FIGURE 9 | Schematic diagram of sonic boom [39].

Zhang et al. [40] conducted a review on the sonic booms, covering the generation mechanisms, prediction methods and suppression techniques. The flow controls involved in mitigating sonic booms include: 1) quite spike, 2) staged aft body, 3) energy injection, 4) membrane vibration. Sonic boom refers to the acoustic phenomena that occurs when pressure waves originating from a supersonic source propagate through the atmosphere [41], and the flow control will be an important

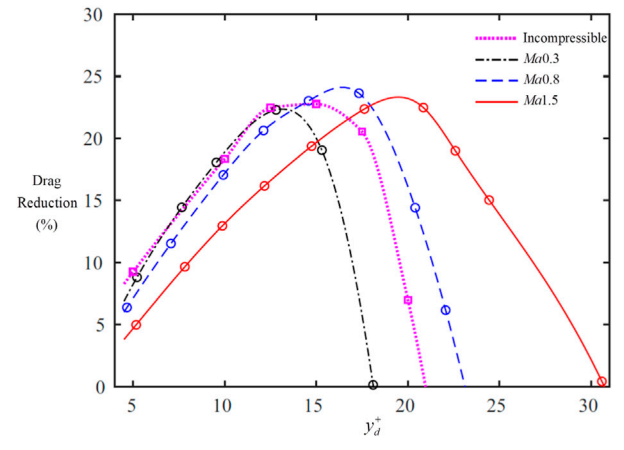

FIGURE 10 | Drag reduction at different Mach numbers [49].

means for suppressing sonic booms in future supersonic civil aircraft. There are several potential flow control systems that could be considered for future application. These tactics encompass thermal energy injection, electromagnetic focusing, acoustic impedance, and vectored thrust engine technology. It was found that the use of a noise-reducing nose cone on an aircraft [42] leads to a notable decrease in the magnitude of the sonic boom, but with a slight increase in the drag coefficient. The critical length of the quiet cone varies with the flying altitude and the Mach number. Therefore, the use of multi-stage quiet cones with each level reaching its critical length was suggested. Ye et al. [43, 44]proposed an active control method of suppressing sonic booms. The proposed technique entails the establishment of an aperture in close proximity to the leading edge of the lower surface of an airfoil to facilitate suction. Simultaneously, an ejecting flow is introduced at the trailing edge of the aforementioned surface, while ensuring an equitable distribution of suction and ejection. The proposed methodology has the potential to substantially reduce the sonic boom level and flow drag experienced by supersonic aircraft. When a mass flow rate of 7.5 kg/s was applied to a NACA0008 airfoil, the absolute value of the maximum negative overpressure decreased by 56.77% and the drag coefficient was reduced by 10.96%.

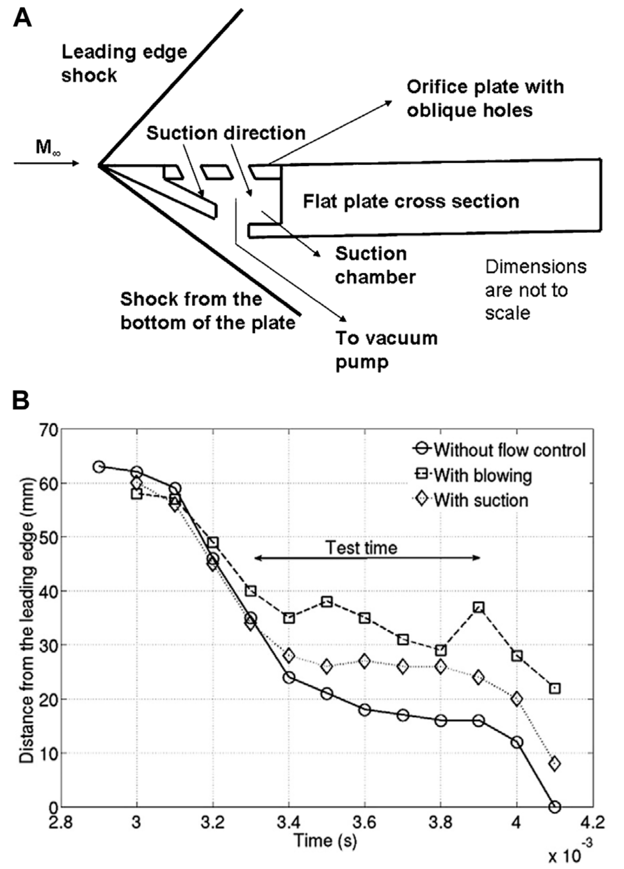

FIGURE 11 | Schematic diagram of suction experiment by Sriram and Jagadeesh and the control effect [52]. **(A)** Schematic diagram of suction control experiment. **(B)** The separation location from the leading edge with and without control.

FLOW CONTROL STRATEGIES

Flow control strategies refer to the manipulation of flow characteristics and properties through artificial interventions to meet certain requirements or accomplish specified goals. They can be categorized into two groups based on whether the energy input is active or passive. Passive controls encompass several strategies such as employing geometric shaping techniques to adjust the pressure gradient, utilizing fixed mechanical vortex generators for separation control, and strategically placing longitudinal grooves on a surface to reduce drag. For active control, design trade-offs must be thoroughly evaluated, and due to the energy supply devices, compromises are frequently required to achieve a particular design objective. In addition, machine learning, especially reinforcement learning, offers more flexibility and versatile iterative methods based on data-driven strategies for active control [45].

Active Control

Blowing Control

Blowing control is a method that employs a blowing apparatus positioned upstream of the site of impact to introduce a fluid with high kinetic energy into the boundary layer in proximity to the wall. Deng et al. [46] conducted experiments with four different blowing configurations positioned between the nozzle of the Ma = 6.5 hypersonic wind tunnel and the engine isolation portion. The investigation revealed that employing a blend of “top slot,” “side slot,” and “bottom hole” blowing techniques yielded blowing effects that closely resembled the outcomes derived from free jet calculations. The study conducted by Li et al. [47] examined the impact of active air-blowing control on the boundary layer of a hypersonic flat-plate. The Mach number is 7 and 8, and the unit

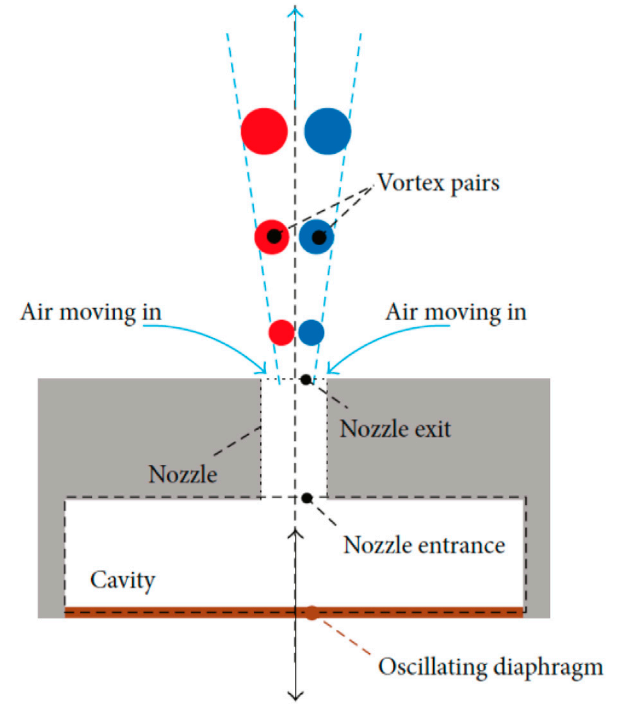

FIGURE 12 | Schematic diagram of a synthetic jet actuator [55].

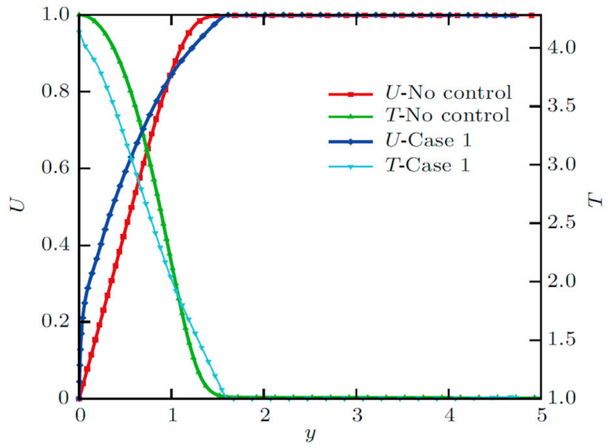

FIGURE 13 | The comparison of velocity and temperature profile with and without control [58].

Reynolds number is 1.25×10^6 m^{-1}. The investigation focused on different mass flow rates of blowing and the incoming Mach numbers. The findings indicate that the air blowing had a notable impact on the characteristics of the sonic line and boundary layer profile. This leaded to the generation of blowing oblique shock waves and caused changes in the instability mechanisms of the two transition states. Moreover, a higher Mach numbers enhanced the compressibility effects, stabilized the boundary layer and caused an increase in the thickness of the blowing boundary layer and air film. However, Kametani et al. [48] studied the effect of global blowing and suction with Re = 3,000 under Ma = 0.8 and Ma = 1.5 conditions, and found that the drag reduction rate and net energy saving rate of compressible turbulence were mainly affected by the blowing amplitude, but not related to the Mach number, and the control gain increased with the increase of Mach number. As depicted in **Figure 10**, Yao and Hussain [49] used opposition drag control to study the drag reduction at different Ma (Ma = 0.3, 0.8, 1.5, Re = 3,000) and discovered that maximum drag reduction does not vary significantly with Ma and the sensing-plane location y_d^+ for achieving maximum drag reduction increases with increasing Ma.

Blowing control only consumes a small amount of blowing energy, and can bring a certain amount of drag reduction. Currently, it has been verified that blowing can efficiently reduce drag, but the impact of flow characteristic parameters such as input Mach number, Reynolds number, etc. on the drag reduction is still a subject of debate. Furthermore, it is important to thoroughly comprehend the impact of blowing control strategies, such as blowing amplitude and frequencies, on the turbulent boundary layer.

Suction Control

The suction control in the boundary layer is a method of removing the low-kinetic-energy fluid near the wall to achieve the effect of suppressing boundary layer separation. Up to now, the suction control has been effectively applied in hypersonic intake ducts [50]. He et al. [51] employed suction slots to regulate the separation of the corner at a shock Mach number of Ma = 5.9. An observation was made that placing suction slots in the spanwise direction on the sidewall can effectively reduce the length of the shock wave train at the same back pressure. Additionally, removing low-momentum fluid near the corner can effectively ease the interaction between the shock wave and the boundary layer. As shown in **Figure 11A**, Sriram et al. [52] investigated the effect of wall suction on separation bubbles on a flat plate at free-stream Ma = 5.96, $Re_\infty = 4 \times 10^6$ m^{-1} in wind tunnel experiments. They found that the suction control reduced the length of the boundary layer separation by 13.33%, which was depicted in **Figure 11B**, but it could potentially lead to enhancement of flow field instability. Subramanian et al. [53] conducted an experiment on the effects of suction control on hypersonic intakes at Ma = 2, $Re_\infty = 4.3\times10^7$ m^{-1}. They found that the suction pressure at the bottom of the groove could eliminate the formation of separation bubbles in the boundary layer, thus restoring the pressure losses caused by the shock/boundary layer interaction.

Suction control within the boundary layer is both straightforward and reliable, emerging as one of the most effective methods in contemporary engineering. By removing low-kinetic-energy fluid from the boundary layer, suction reduces flow loss due to separation and is frequently combined with blowing to enhance flow control. However, it also results in increased wall friction drag, leading to additional flow loss. Thus, finding an optimal balance between the benefits and drawbacks of suction remains a critical consideration.

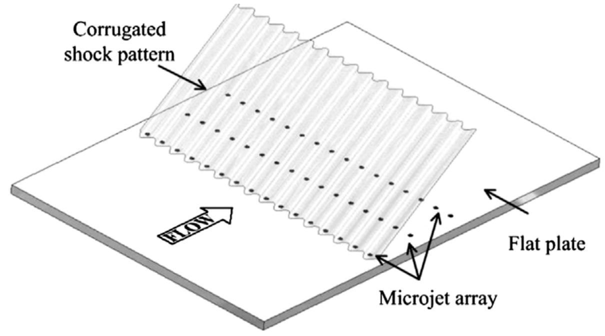

FIGURE 14 | Schematic diagram of a microjet array [61].

Synthetic Jet Control

One kind of jet flow produced by a diaphragm oscillating inside a cavity is called a synthetic jet. Without the need for an outside airflow source, this oscillatory motion creates a number of vortex formations [54] that both intake and expels fluid, producing an air jet, as depicted in **Figure 12**. This technology is utilized in various applications, including cooling and flow control, owing to its effective manipulation of fluid dynamics. Hong et al. [56] provided a review of the geometric parameters influencing synthetic jet performance, which they categorized as: the aspect ratio of the rectangular orifice, the orifice depth, the cavity height, and the cavity diameter. Luo et al. [57] provided a comprehensive review to introduce the fundamental characteristics of synthetic jet actuators and their basic design principles applied in flow control for separated flow, intake ducts, thermal management, anti-icing, and underwater propulsion. Liu et al. [58] proposed a velocity-temperature coupling control method based on synthetic cold/hot jets on a supersonic flat-plate flow with Ma = 4.5, Re = 5,000. It was found that the temperature of the jet significantly affected the size of the unstable region and the growth rate of disturbance modes. As shown in **Figure 13**, the jet control changes the velocity and temperature of the boundary layer, which will affect the first mode and the second mode. Temperature fluctuations accelerated the transition from laminar to turbulent flow when the jet temperature was different from the incoming flow temperature. This led to a fuller velocity profile in the boundary layer, strengthened resistance to disturbances, and enhanced flow stability. Li and Zhang [59] proposed a novel hybrid synthetic jet actuator, which, compared to plasma synthetic jet actuators, exhibited higher peak velocity, gas refilling rate, and gas ejection rate. This method enhanced the duration and reliability of supersonic active flow control.

Synthetic jet control has the capability to improve the efficiency of momentum and energy transfer in jets, allowing for precision control over complex flow patterns. Also, it does not necessitate the introduction of external fluids, hence preventing any impact on the mass and energy equilibrium of the system.

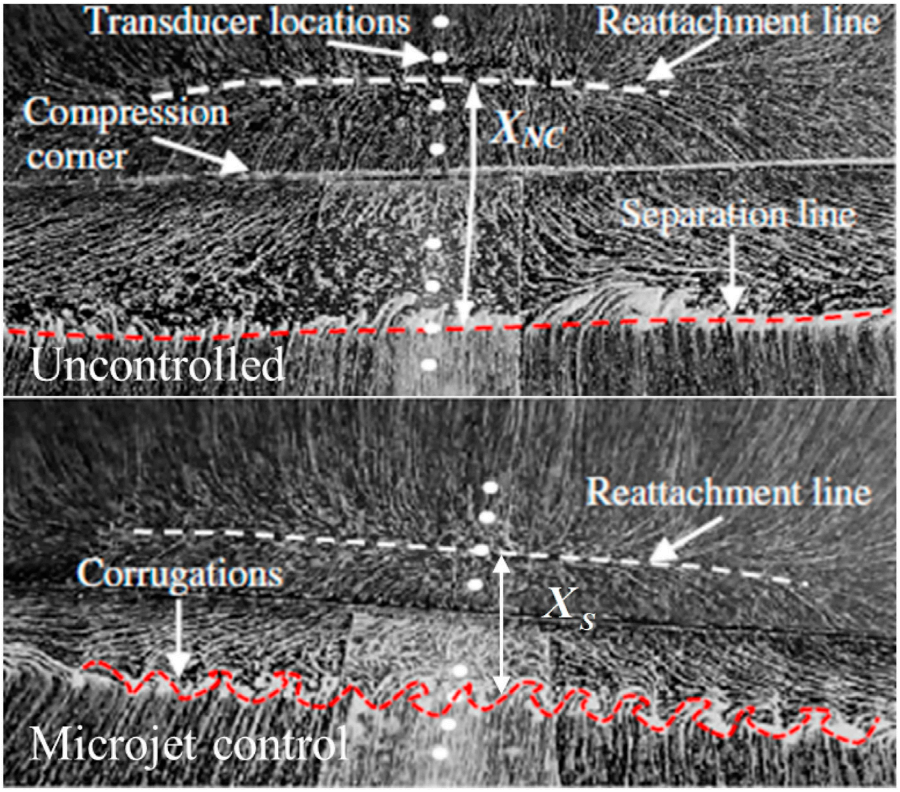

FIGURE 15 | The comparison of surface oil visualization with and without control [62].

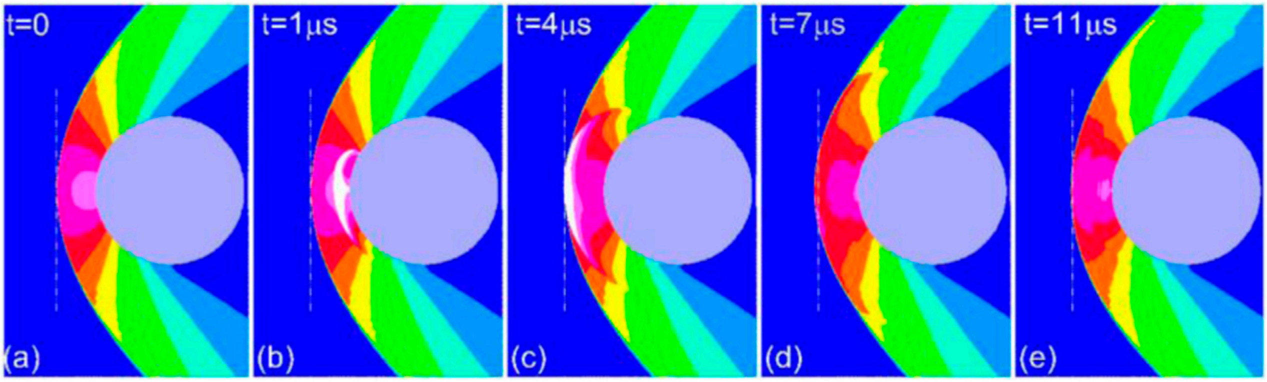

FIGURE 16 | The detached shock wave moves away from the cylinder caused by plasma discharge [67]. **(A)** $t = 0$. **(B)** $t = 1\mu s$. **(C)** $t = 4\mu s$. **(D)** $t = 7\mu s$. **(E)** $t = 11\mu s$.

Furthermore, they exhibit little energy consumption and robust integration, making them suitable for a wide range of flow control scenarios. Nevertheless, synthetic jets encounter obstacles such as the synchronization and interference of jets, as well as issues with jet stability. They prove challenging to successfully manage flow separation on a wider scale or apply under hypersonic settings.

Microjet Control

Microjet control is a method for controlling jet arrays typically with a small diameter of the jet hole [60], as shown in **Figure 14**. At the freestream $Ma = 2.0$ and $Re = 7.07 \times 10^6$ based on the plate length, Verma and Manisankar [62] conducted an experimental study to investigate the effects of the spacing, pitch, and skew angles on the separation and shock unsteadiness. It can be seen from **Figure 15** that the separation length X_S is significantly reduced after using microfluidic control. The actuator produces pulsed high-speed microjets under $Ma = 1.5$, $Re_D = 8.5 \times 10^5$ based on the cavity depth by exploiting the resonance of an impinging microjet source [63]. Additionally, the actuator's resonant frequency may be actively regulated through the integration of intelligent materials into its structure. The microjets under freestream $Ma = 2.9$ approach utilizes the counter-rotating vortex pair (CVP) as its control mechanism [64]. This CVP is created by the microjet and serves to mix the low-energy flow within the boundary layer with the high-energy flow near the boundary layer. The magnitude of the vortex core in this controlled vortex pair is crucial for managing the SWBLI. The larger and more proximal vortex nucleus facilitates superior regulation of SWBLI.

Microjet control effectively manages flow separation and stalling due to its high frequency and low mass flow rate, which enable rapid response to flow variations. However, it faces certain limitations. Managing large-scale flows is difficult because of the small action area of microjets. The effectiveness of the jet is highly sensitive to factors such as injection frequency, angle, and jet velocity, all of which must be meticulously adjusted to suit varying flow conditions. Despite these operational and technological constraints, microjet technology holds substantial potential for advancing flow control.

Plasma Control

Plasma control is a technology that involves using forms of discharge such as arcs to penetrate the gas within the boundary layer, to generate plasma and induce energy transport in the surrounding gas in order to suppress flow separation. Li and Wu [65] summarized the progress of the plasma excitation for flow control. They elaborated on the relevant principles, fundamental issues, flow control principles and methods. Additionally, they discussed applications in aircraft, engines, combustion, and made prospects for future development. The impacts of plasma synthetic jets on typical hypersonic flow in the consideration of the thermal perfect gas effect were studied by numerical simulations [66]. The results showed that during the first cycle after discharge, synthetic jets could reduce the average drag of the spherical head and increase the shock detachment distance, thus achieving flow control. Nanosecond dielectric barrier discharge (NS-DBD) was applied by Zheng et al. [67] to conduct experiments on a cylinder at $Ma = 4.76$. As shown in **Figure 16**, they discovered that the micro shock wave produced by plasma discharge interacted with the detached shock wave, causing the bow shock wave in front of the cylinder to move forward. At the same time, the plasma changed the pressure distribution near the cylinder, reducing the drag by 8.3%. Wang et al. [68] used NS-DBD plasma actuation for flow control ($Ma = 1.5$, $Re = 1.8 \times 10^5 \sim 2.7 \times 10^6$) and found that such actuation induces a distorted flow structure on the suction surface of the blade, thereby enhancing shock wave oscillations in the blade passage and suppressing flow separation on the pressure surface. By introducing the research history and specific applications of Pulsed Plasma Synthetic Jets (PPSJ), Russell et al. [69] concluded that the working conditions of high frequency and actuators may be areas for further research in the future, and that a standard needs to be established to determine the impact of the geometric shape of actuators on PPSJ performance.

The primary advantage of plasma control lies in its ability to achieve contactless fluid control, thereby circumventing the complexities associated with mechanical installation and potential interference. Additionally, plasma control offers

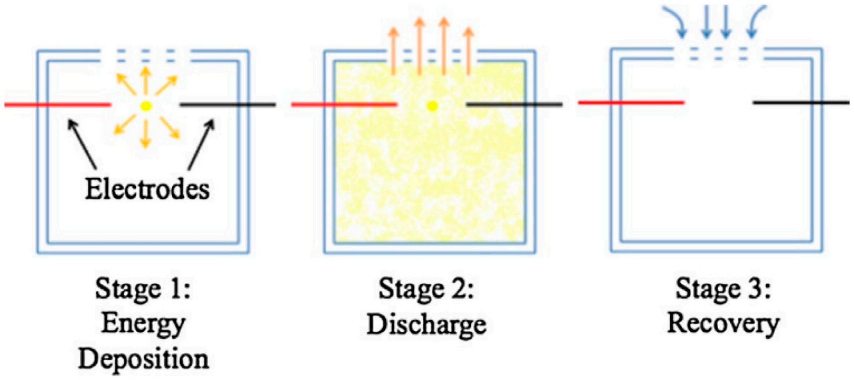

FIGURE 17 | Three stages of Sparkjet operating cycle [70].

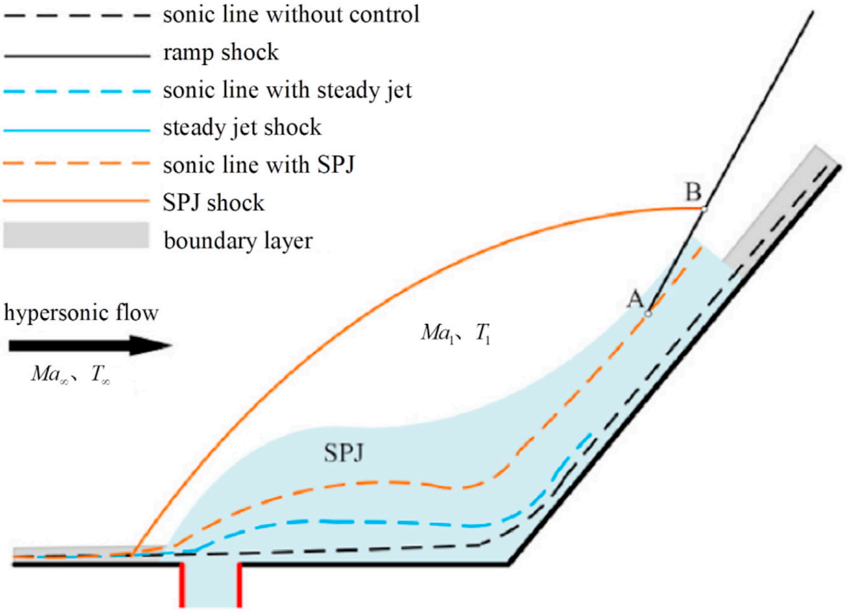

FIGURE 18 | Shock waves and sonic lines with and without control [73].

rapid response capabilities and the ability to adjust the flow field in real time. However, maintaining and controlling plasma over a large flow field demands substantial energy and sophisticated equipment, which limit the application of plasma in engineering. Despite these limitations, the plasma control technology possesses significant potential for future development.

Energy Deposition Control

Energy Deposition (ED) is a method of introducing energy into the front part of an aircraft by means of techniques like electrode discharge, laser excitation or sparkjet. **Figure 17** shows the three stages of sparkjet operating cycles. The purpose of this is to modify the configuration of shock waves and airflow properties at the aircraft's nose, resulting in a decrease in aerodynamic drag produced by shock waves [71]. The mechanism of energy deposition was consisted of three main steps [72]: the formation and deformation of high-temperature plasma, the interaction between high-temperature plasma and bow shock, and the recovery of pressure and heat flux at the nose of the aircraft. Among these steps, the interaction between plasma and shock waves is the key to drag reduction. Additionally, the main parameters affecting energy deposition can be categorized as deposition energy, deposition location, energy repetition frequency, and freestream Mach number. Xie et al. [73] used SparkJet (SPJ) to control the shock wave interaction of high-enthalpy flow at $Ma = 6.9$. The experimental results revealed that within a certain range, the control effect of SPJ on ramp shock waves continued to improve with the increase of pressurized cavity pressure, ramp distance and the decrease of ramp

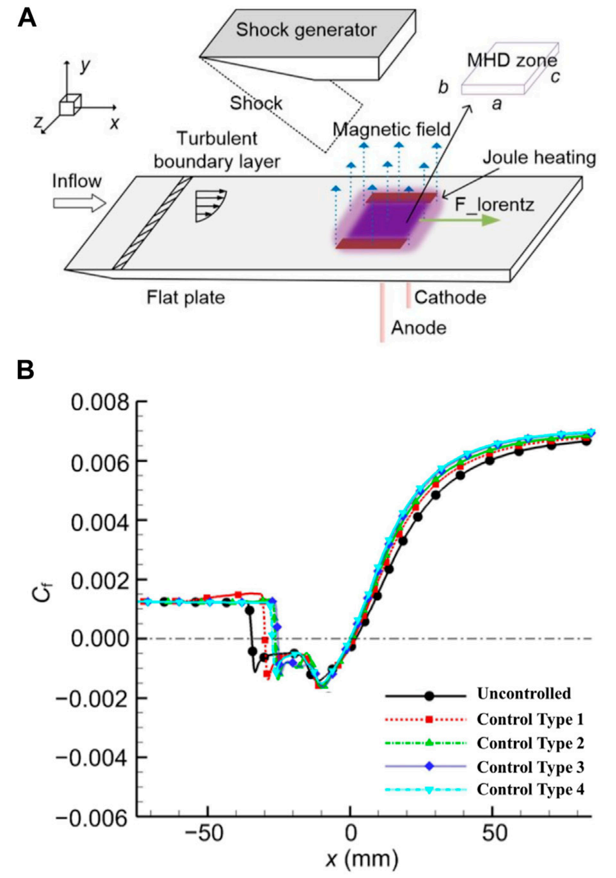

FIGURE 19 | Magnetohydrodynamic experiments in SWBLI [77]. **(A)** Schematic diagram of MHD experiment. **(B)** Wall skin friction coefficient distributions of uncontrolled and four control types. Control type 4 reached the largest drag reduction.

inclination angle. As pictured in **Figure 18**, SPJ shock decreased the Mach number, leading the sonic line move upward, which weakened the ramp shock wave. Azarova et al. [74] suggested implementing drag force control through the utilization of multiple energy sources within the supersonic shock layer (*Ma* = 1.89~3.45). The utilization of multiple energy sources led to a decrease in frontal drag force by 19% for a blunt cylinder and 52% for a hemisphere-cylinder.

Energy deposition has excellent instantaneous response capabilities and wide applicability, and can change flow characteristics by rapidly heating the fluid. Nevertheless, energy deposition flow control also faces significant challenges. Energy deposition technology has high energy requirements. In addition, it is prone to unstable phenomena in practical applications, such as local overheating or uncontrollable changes in the shock wave structure, which may lead to unstable flow control effects. Therefore, further research is needed due to the complicated nature of the system, expensive costs, and unique properties such as ionization and chemical reactions generated by high-energy fluid [75].

Magnetohydrodynamic Control

Magnetohydrodynamic (MHD) control is a method of controlling fluids by the interaction between magnetic field and conducting fluid. Zhang et al. [76] provided an overview of the application of MHD control in hypersonic flow. They focused on three major MHD techniques: 1) large-scale flow control to expand the flight envelope in terms of Mach number and angle of attack, 2) near-surface flow control to mitigate shock wave/boundary layer interactions, and 3) leading-edge heating-transfer control to manage enormous thermal loads on the leading edge of compression ramps. As shown in **Figure 19A**, Jiang et al. [77] employed the k-ω SST model to conduct a numerical investigation on the impact of various magnetic field and plasma combinations on SWBLI at *Ma* = 5.0, Re_∞ = 3.67 × 10^7 m^{-1}. The utilization of electromagnetic control enhances the energy of the boundary layer, and the pressure gradient within the separation bubble is of comparable magnitude to the exerted electromagnetic force. The largest separation reduction reached 0.296 as illustrated in **Figure 19B**. The effectiveness of MHD control in separated flow at *Ma* = 14.1, Re_∞ = 2.32 × 10^5 m^{-1} was found by Luo et al. [78] to be mostly dependent on the streamwise direction of the Lorentz force's flow acceleration. It is possible to accelerate the low-velocity fluid in the boundary layer by introducing an external electromagnetic field. Additionally, there was a perfect place to apply the MHD zone, which could totally remove flow separation from the surface.

MHD is a non-contact control technology that reduces mechanical friction loss and the resultant additional resistance, and can be used in some extreme environments with high temperature and high pressure. However, at the same time, MHD flow control consumes a lot of energy to generate and maintain a strong magnetic field. Therefore, how to save energy as much as possible while ensuring the effect of MHD flow control is an important issue in future research.

Passive Control

Micro Vortex Generator Control

Micro Vortex Generator (MVG) control is a method that utilizes streamwise vortices to attract high-momentum fluid into the boundary layer, hence improving its ability to resist flow separation [79]. Four types of micro vortex generators are shown in **Figure 20**. The impacts of MVG arrays at *Ma* = 7.0, *Re* = 5.03 × 10^6 were numerically calculated by employing the DES model [81]. The results showed that the MVG arrays have a significant impact on the boundary layer of hypersonic fluids. This leads to a decrease in the size of separation bubbles, a reduction in the intensity of separation shock waves, and an increase in the velocity gradient in both the separation bubbles and the downstream fluid. As a result, there is a potential reduction in total pressure losses of up to 1.9%. Zhu and Wang [82] discovered that at *Ma* = 2.0, placing the jet after the MVG can greatly improve the ability of the isolated segment to withstand backpressure, resulting in better flow control performance. Gnani et al. [83] mentioned that compared to traditional generators, MVGs, while increasing parasitic drag,

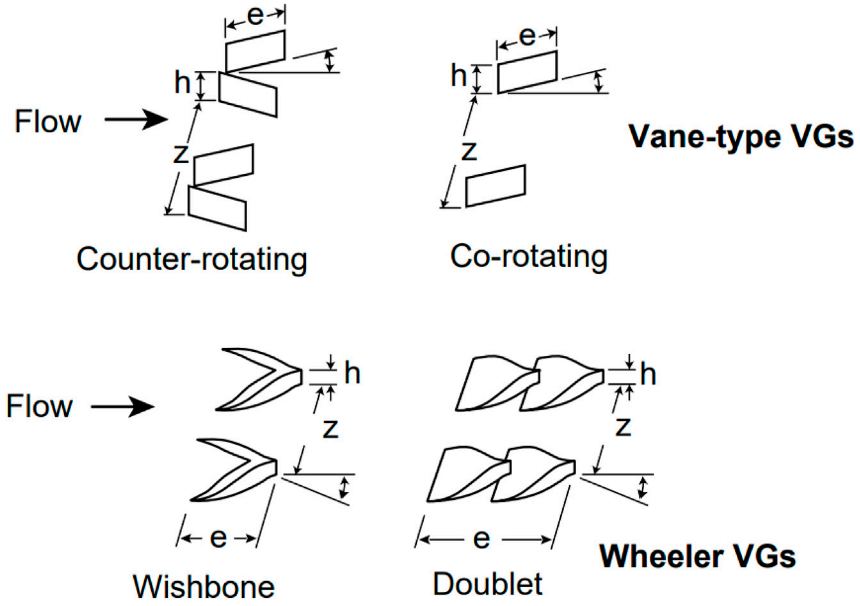

FIGURE 20 | Types of micro vortex generators [80].

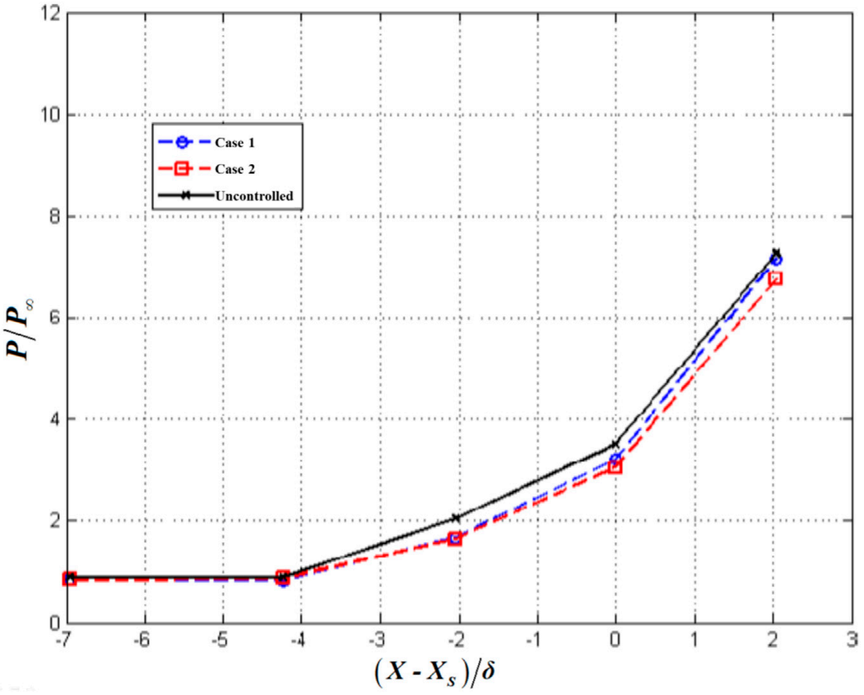

FIGURE 21 | Pressure distribution in the streamwise direction with and without control [84].

still offer advantages in generating a slightly thicker boundary layer and reducing drag. Experimental methods such as schlieren photography, surface flow visualization, and infrared thermography were used by Saad et al. [84] to study the effect of micro-ramps on the shock wave/boundary layer interaction at $Ma = 5$. As illustrated in **Figure 21**, the experiment confirmed

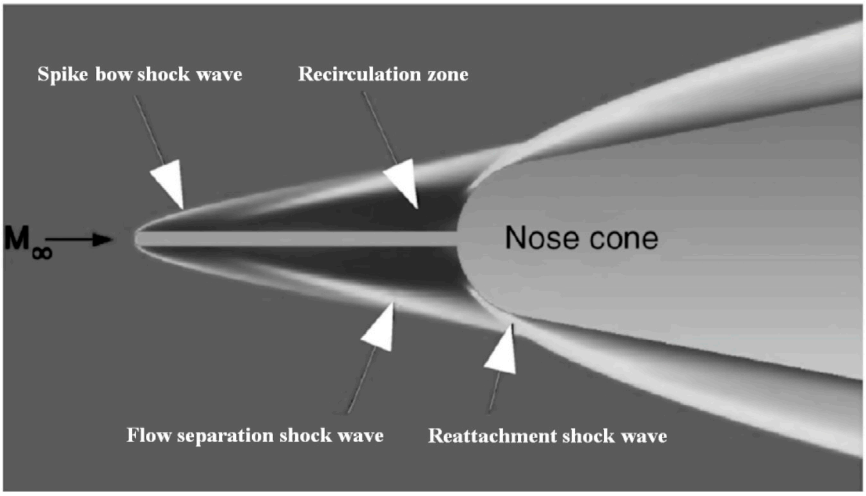

FIGURE 22 | Aerospike-induced flow field [85].

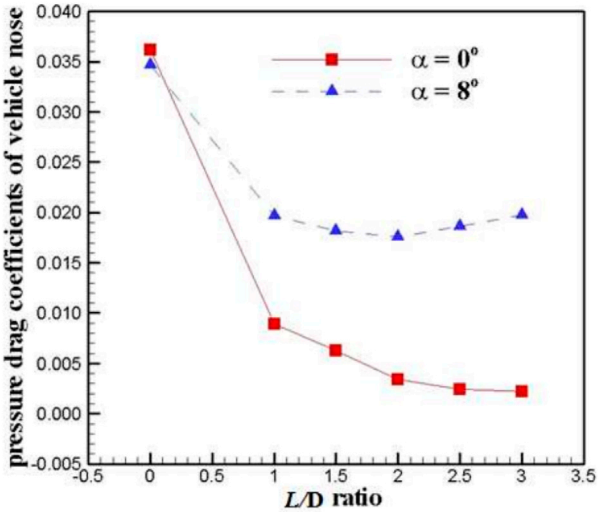

FIGURE 23 | Pressure drag coefficients of vehicle nose varies with L/D ratio of spike [87].

that the presence of micro-ramps delayed the pressure rise, reduced the upstream interaction length, and thus suppressed the shock wave/boundary layer interaction.

MVGs are used to manipulate airflow over surfaces to enhance aerodynamic performance. They are much smaller than conventional vortex generators, often only a few millimeters in size, and are strategically placed on the surface of an aircraft or other vehicles to control the boundary layer, reduce drag, delay flow separation and improve overall efficiency. Despite the benefits, MVGs must be carefully designed and placed to avoid adverse effects such as increased turbulence or noise. The design of MVGs requires precise aerodynamic analysis to ensure they provide the intended benefits without introducing new issues.

Aerospike Control

As shown in **Figure 22**, Aerospike control utilizes a pointed rod mounted on the nose of an aircraft to increase the standoff distance of the bow shock and to transform the strong bow shock into an oblique shock, with the aim of drag reduction [85]. Guan et al. [86] set up an incoming flow condition with $Ma = 2.2$ and $Re_D = 2.6 \times 10^5$ based on nose diameter to test four types of aerospikes under zero and non-zero angles of attack. The measurement results processed by three statistical methods indicated that the aerospikes effectively suppressed airflow fluctuations under any angle of attack tested in the experiment. As shown in **Figure 23**, Deng et al. [87] studied the aerodynamic performance of disk spikes in a hypersonic flow ($Ma = 8.0$). Their results indicated that using a hemispherical disk spike at the nose, with a spike length-to-nose diameter ratio (L/D) of 2, provided the optimal drag reduction effect. At an 8° angle of attack, the maximum drag on the nose and the entire vehicle was reduced by 49.3% and 4.39%, respectively. Another study [88] proved that an aerospike with the aspect ratio of 4 at a $Ma = 7.0$ flow has the capability to diminish the impact body's resistance by 52.57%. According to Xu et al. [89], the aerospike with a cone shape exhibited the least effective reduction in drag and heat. In contrast, the aerospike with a flat profile demonstrated the highest heat reduction and the hemispherical aerospike the highest drag reduction. Elevating the aspect ratio of the aerospike results in a substantial improvement in both its resistance to heat and drag.

Aerospike control is advanced aerodynamic devices used primarily for flow control in hypersonic application. In practical applications, aerospike control provides a straightforward configuration that obviates the necessity for an extra energy provision system, thereby efficiently

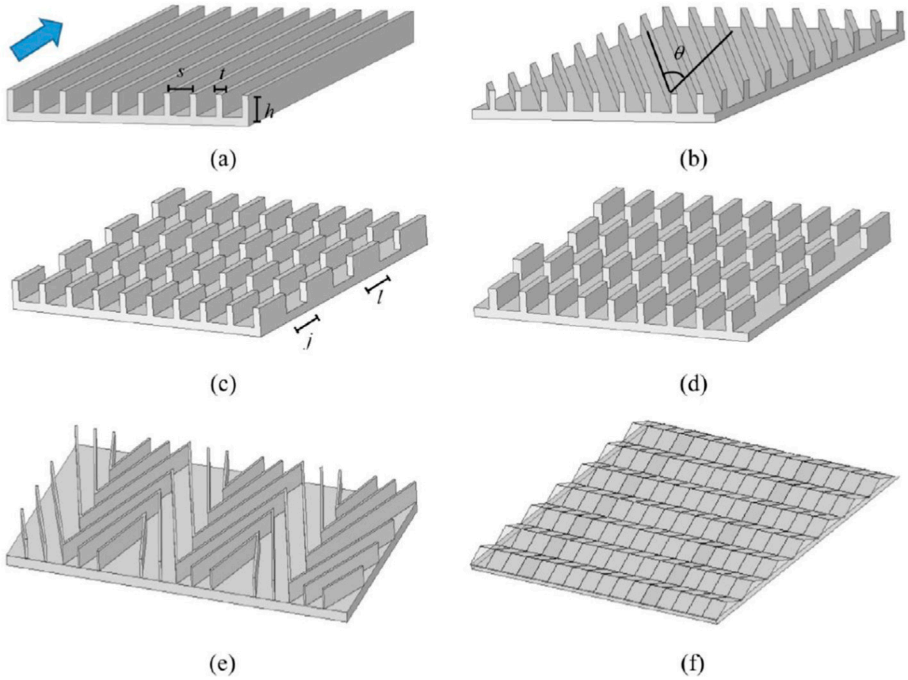

FIGURE 24 | Catalog of riblet configurations [90]. **(A)** continuous longitudinal. **(B)** continuous in yaw. **(C)** inline segmented. **(D)** staggered segmented. **(E)** herringbone. **(F)** zigzag.

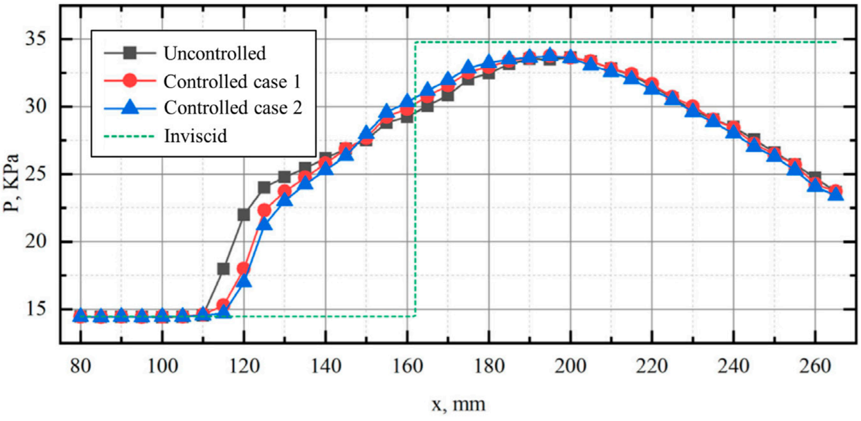

FIGURE 25 | Comparison of streamwise surface pressure distributions in the controlled and controlled cases [94].

diminishing drag. Unlike traditional control surfaces like fins or flaps, aerospikes are pointed structures that extend forward into the flow, manipulating the shock waves and boundary layers to enhance stability, reduce drag, or control flow separation at extremely high velocities. At the same time, at hypersonic speeds, aerospikes are subjected to extreme aerodynamic and thermal stresses, so consideration must be given to the thermal protection of aerospikes in high-temperature environments. Ensuring the structural integrity and thermal resistance of the aerospike is a significant design challenge.

Riblet Control

Riblet control is inspired by shark skin and utilizes micro-sized, serrated structures on the surface to achieve drag reduction and noise mitigation. Generally, there are six kinds of riblet configurations, as listed in **Figure 24**. Ran et al. [91] computed a steady-state covariance matrices that allow for examining the impact of riblets on the dominant turbulent structures. The study shows that at small scales, triangular riblets limit the wall-normal momentum transfer associated with near-wall cycle and the generation of secondary flow structures around

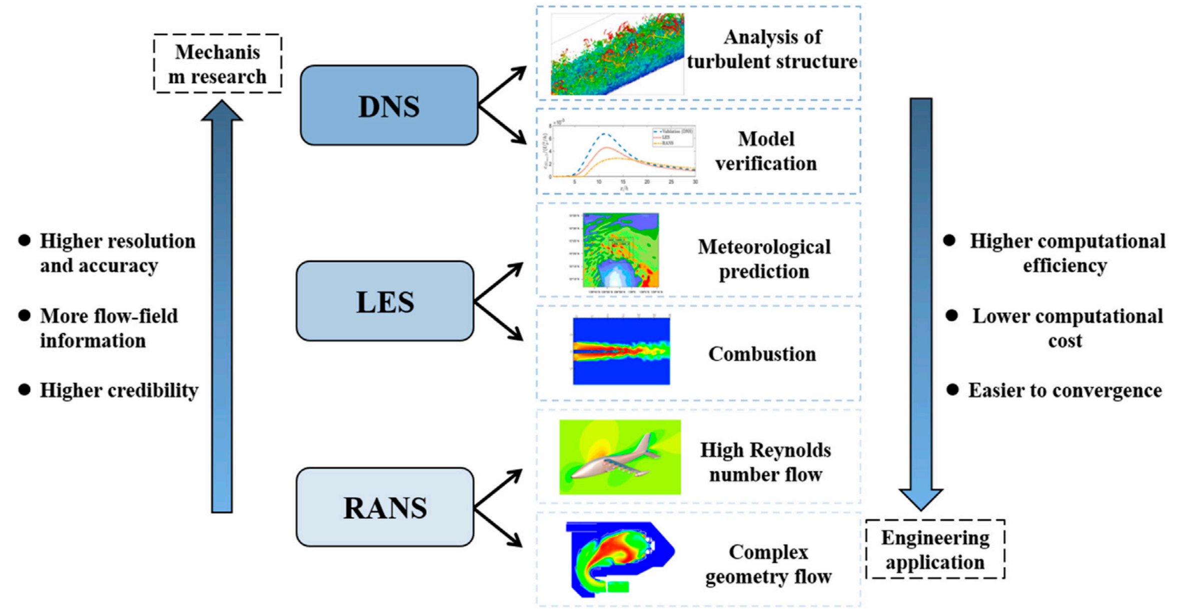

FIGURE 26 | Comparison of DNS [95, 96], LES [97, 98] and RANS [99].

the riblet tips. Riblet-equivalent boundary conditions on smooth computational walls were introduced by Li et al. [92] to simplify the difficulties associated with numerical simulations. The effectiveness of the association between non-dimensional geometric parameters and wall roughness has been established by experimental investigation at $Ma = 0.4$. Applying the riblet model to a particular missile resulted in a 2.4% decrease in the total drag coefficient and a 3.4% reduction in surface friction. Zhou et al. [93] conducted a study on the impact of riblets at $Ma = 6.0$ and $Re_\infty = 1\times10^7\ \mathrm{m}^{-1}$. They discovered that riblets have the ability to affect the turbulent surface friction by suppressing or disturbing large-scale vortex formations. The drag reduction rises as the groove height grows and the distance between grooves reduces, within a suitable range. Wen et al. [94] experimentally assessed the effects of chevron-shaped grooves on the interaction between shock waves and turbulent boundary layers at $Ma = 1.85$ and $Re_\infty = 1.26 \times 10^7\ \mathrm{m}^{-1}$. As shown in **Figure 25**, the pressure distribution curves indicate that the riblet control delays the rise of surface pressure compared with the uncontrolled case. This is because the boundary layer downstream of the riblet center is thinner, the extent of flow separation is extenuated, and it is closer to inviscid flow.

Riblet control is a highly effective drag reduction technique that leverages microscopic surface textures to manipulate turbulent flow near a surface. By reducing skin friction drag, riblets offer significant performance and efficiency gains in aerospace, marine, and various industrial applications. However, riblet surfaces can be prone to damage from abrasion, fouling, or environmental exposure, which can diminish their effectiveness. Maintaining the integrity of riblet structures is crucial for sustained performance.

RESEARCH METHODS OF FLOW CONTROL

High-Speed Computational Fluid Dynamics

As shown in **Figure 26**, the numerical methods employed for simulating high-speed flow primarily consist of direct numerical simulation (DNS), Reynolds-averaged Navier-Stokes simulation (RANS), and large eddy simulation (LES). The DNS directly solves the discretized Navier-Stokes equations, yielding very comprehensive information about the flow field. This includes time series data of three-dimensional flow fields, spatial structures of turbulence, as well as time-averaged values and fluctuations of specific flow variables. To address the upwind issue in the convective term of the Navier-Stokes equations, various approaches have been developed. These include flux vector splitting techniques such as Steger-Warming, Lax-Friedrich, Van Leer, as well as flux difference splitting schemes like Roe and HLLC. Shock-capturing techniques with high accuracy include the WENO, NND, GVC and WCNS. For high-enthalpy hypersonic flows, due to chemical non-equilibrium effects, there exists a weak coupling relationship between the vibrational energy of gas molecules and pressure. The shock sensors proposed by Jameson [100] or Ducro [101] are no longer applicable. Passiatore et al. [102] enhanced the shock sensor by replacing pressure variables with vibrational temperature, resulting in the effective detection of shock waves and contact discontinuities. Pirozzoli [103] identified several concerns about discontinuous regions. Overcoming Gibbs phenomena and integrating artificial dissipation continue to be difficult for DNS.

The advantage of the RANS method lies in its allowance for larger grid scales, which reduces computational costs significantly. However, it is necessary to develop models for

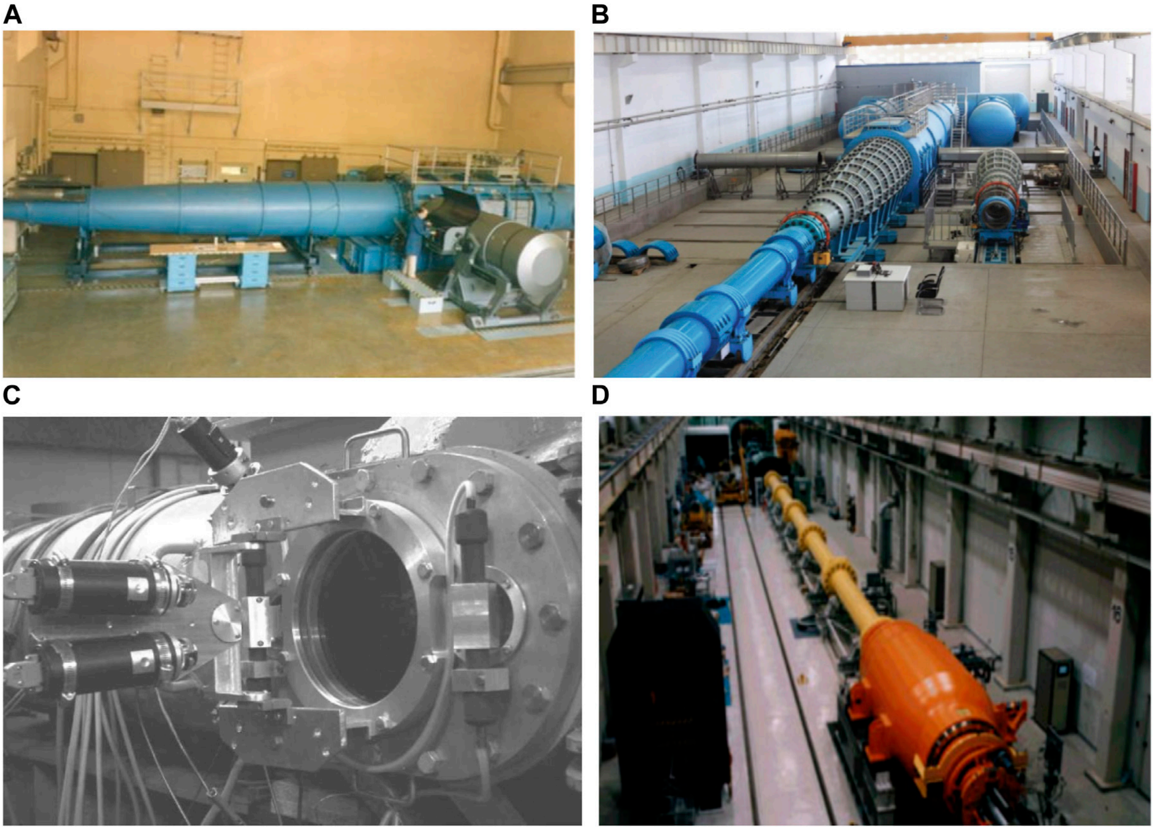

FIGURE 27 | Some hypersonic wind tunnels over the world. **(A)** AEDC T9 [115] **(B)** IMCAS JF-12 [116]. **(C)** TsAGI UT-1M [117] **(D)** JAXA HIEST [118].

the Reynolds stress terms. There are various prominent turbulence models, such as the k-ε model, the k-ω model, the SST model, and the S-A model. Knight and Degrez [104] performed a comprehensive evaluation of turbulence models for analyzing SWBLIs using RANS. The findings revealed that each turbulence model has a specific range in which it is suitable, and simulating flows with distinct characteristics could lead to substantial inaccuracies. Fu and Wang [105] summarized the RANS model for high-speed flows and proposed a RANS model with wider applicability and better robustness. The fundamental idea behind the LES approach is that small- and large-scale vortices are separated by the filter function, with the small-scale vortices being modelled and the large-scale vortices being solved directly [106–109]. This method's computing cost lies in between the other two numerical approaches since it may be thought of as a hybrid of the DNS and RANS methods.

Supersonic and hypersonic flow control often involves dealing with complex geometric boundaries, such as grooved surfaces, wavy walls and porous media. Studying such problems should not directly employ real geometric boundaries for computation. Instead, it's preferable to model and handle these boundary conditions equivalently. Wang et al. [110] utilized an aperture-type acoustic metasurface model for equivalent treatment, thereby avoiding the need to solve complex geometric boundaries and simplifying the computation process. Zeng et al. [111] employed a channel flow DNS program combined with the immersed boundary method to model and simulate flow over non-smooth blade surfaces in real-world scenarios, considering parameters such as arithmetic mean height, roughness, and effective slope. Ghosh et al. [112–114] employed the immersed boundary method (IBM) and a hybrid RANS/LES approach to solve for flow phenomena related to shock-boundary layer interactions.

With the rapid development of parallel computing technology, CFD methods have become increasingly imperative and gradually served as a mainstream approach in flow control research. Utilizing CFD methods for flow control in drag reduction and thermal protection applications enables the calculation of physical quantities that may be difficult or impossible to measure experimentally, and provides rapid access to flow information, which demonstrates strong flexibility. However, this method also has its limitations. For instance, the accuracy of CFD methods relies on the accuracy of the computational models and the applicability of the assumptions made, hence it is important to consider beforehand whether the selected model is suitable for the intended application.

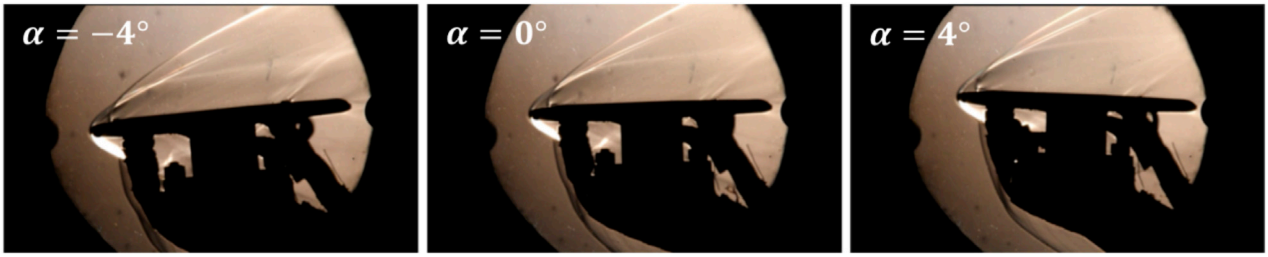

FIGURE 28 | Schlieren images at different angles of attack [124].

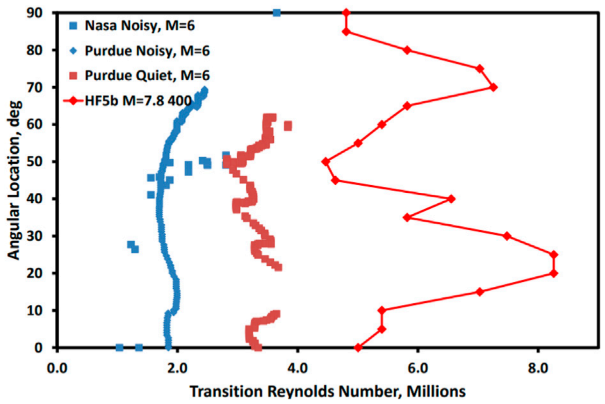

FIGURE 29 | Comparison of transition Reynolds number of HIFiRE-5b and wind tunnels [129].

Wind Tunnel Experiments

Wind tunnel experiments are a critical tool for investigating high-speed flow control. By placing scale or subscale models within a wind tunnel, equipped with various sensors and flow visualization instruments, these experiments can simulate the real flow situations. Here are some famous hypersonic wind tunnels illustrated in **Figure 27**. Liu et al. [119] conducted a review of experiments on the receptivity stage and the linear growth stage of hypersonic boundary layer transition. The Supersonic Nano-tracer Planar Laser Scattering (NPLS) approach was described by Yi et al. [120] Based on this principle, further techniques for detecting density fields, Reynolds stress, and aerodynamic optics were also developed. A survey of flow control techniques for reducing heat and drag in supersonic and hypersonic flows [121] was conducted, including forward-facing cavities, counter-flowing jets, aerospikes, and energy deposition, as well as the advancements in experimental studies pertaining to their combination. Berry et al. [122] carried out experiments on the effect of multiple porous models of the Hyper-X on boundary layer transition. The findings confirmed that the configurations with serrated grooves or a single row of large holes can effectively force a boundary layer transition. Borg and Schneider [123] placed a 20% scale model of the X-51A fore-body in a quiet wind tunnel and equipped it with a trip wire. They discovered reducing the noise level of freestream could increase the transition Reynolds number by 2.4 times, significantly affecting the transition caused by roughness. As demonstrated in **Figure 28**, Zhu et al. [124] investigated the impact of the jet on the aerodynamic performance of the airfoil at various angles of attack in a *Ma* = 5.0 hypersonic wind tunnel. The findings indicated that manipulating the jet has a positive impact on the lift and pitch torque coefficients, and this effect becomes more pronounced as the jet outlet flow rises at each angle of attack. Xia et al. [125] studied the effects of Ramp-VG array (ramp vortex generator array, RVGA) on the supersonic mixing layer. The results confirm that RVGA can improve the energy distribution in the supersonic mixing layer, achieving the performance of increasing flow velocity and delaying transition.

In the past few years, supersonic and hypersonic wind tunnels have achieved significant progress, with the advent of high-enthalpy wind tunnels, shock wind tunnels and gun wind tunnels, making a further enhancement in the modeling capabilities of wind tunnel experiments. Nevertheless, there is still potential for further progress in wind tunnel tests. There is a need to enhance the manufacturing capabilities and precision of models, as well as to systematically address the effects caused by scale factors. However, it is imperative to optimize the efficiency of wind tunnels in order to simulate a wide range of flow environments.

Aircraft Flight Tests

Although numerous studies have explored flow control in high-speed fields, practical engineering applications in aircraft is still limited. This discrepancy highlights a gap between theoretical advancements and their implementation in practical flying scenarios [126]. This gap can be attributed to several factors, including the complexity of integrating flow control technologies into existing aircraft designs, the high cost of development and testing, and the challenges associated with scaling laboratory results to full-scale applications.

Choosing suitable flow control techniques for an aircraft's transition in-flight is challenging because of the variations in flow conditions between flight and being on the ground. Without actual flight data as a reference, it becomes impossible to make accurate decisions. Consequently, numerous countries are currently engaged in active hypersonic boundary layer transition flight tests in order to get further flow data that corresponds to these tests. As shown in **Figures 30A, B**, the United States, in conjunction with Australia, launched the HIFiRE-1 [127] and HIFiRE-5b [128] vehicles in 2010 and

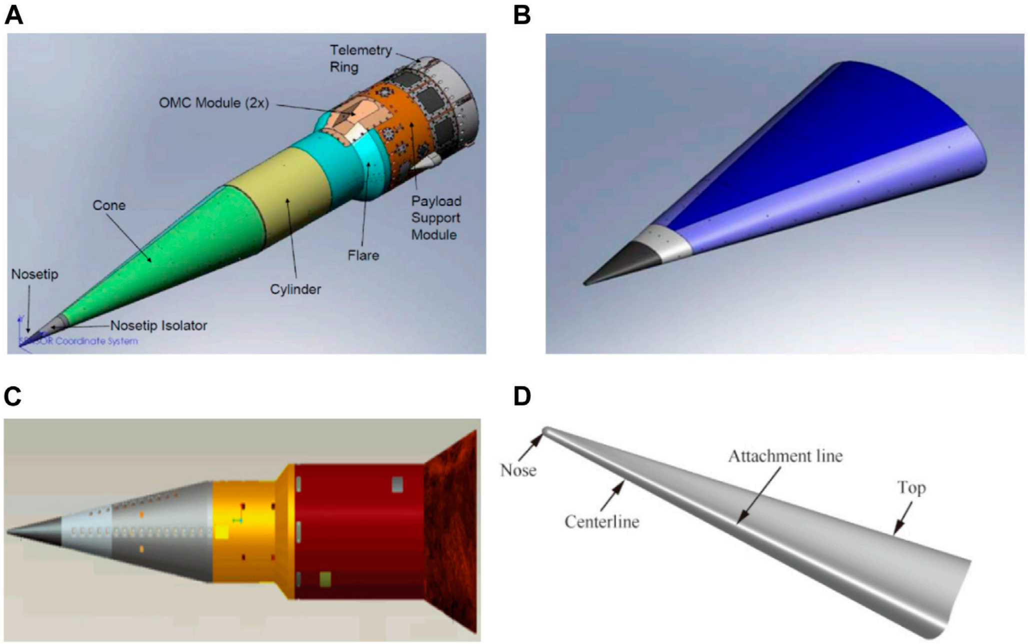

FIGURE 30 | Schematic diagrams of flight tests of hypersonic boundary layer transition. **(A)** Schematic diagram of HIFiRE-1 [127]. **(B)** Schematic diagram of HIFiRE-5b [128]. **(C)** Schematic diagram of MF-1 [130]. **(D)** Schematic diagram of HyTRV [131].

2016, respectively. HIFiRE-1 is a blunt cone with zero angle of attack, a half-cone angle of 7°, and a head radius of 2.5 mm, flying at Mach numbers ranging from approximately 3.04–5.79. HIFiRE-5b is an elliptical cone with a short axis half-angle of 7°, an aspect ratio of 2:1, and a head radius of 2.5 mm. It can be clearly seen from **Figure 29** that there is a significant discrepancy between the real transition Reynolds number of HIFiRE-5b and the wind tunnel experimental results. As shown in **Figures 30C, D**, two vehicles, the MF-1 [130] and HyTRV [131], were launched in China in 2015 and 2019, respectively, and are used to collect transition data for blunt cones with a small angle of attack and lifting bodies with a variable angle of attack at hypersonic speeds. These data provided information on pressure, heat flux, and unstable wave amplitudes under different flow situations.

In some flight tests, attempts have been made to employ active flow control designs. A collaborative effort involving the United States, France, and other countries was conducted in the HyShot program, aimed at exploring the basic performance of scramjet engines at high Mach numbers. In 2002, the HyShot II [132] experiment was conducted, utilizing a fixed-geometry two-dimensional inlet with suction devices in the inlet to ensure its initiation. Active flow control could also enhance rudder authority by reducing airflow separation during large rudder deflections and significant sideslip angles. In 2015, Boeing and NASA [133] tested a pneumatic sweeping-jet-based active flow control system on the modified Boeing 757 eco Demonstrator. The flight test data suggested that the flow control actuation might be able to provide an approximately 14% increase in side force at the maximum tested rudder deflection and at critical sideslip angles.

In addition, some flight experiments achieved passive control by altering the flow profile through the installation of aerospikes or quiet spikes. For example, aerospikes were utilized on the HIFiRE 7 aircraft [134]. Gulfstream and NASA [135] installed multi-stage quiet spikes in front of the F-15B nose, conducting multiple flight tests in the range of from Mach 0.8 to 1.8. It was found that the quiet spikes successfully attenuated the strong shock waves at the nose into a series of weaker shocks, effectively reducing the sonic boom. The X-43A aircraft used rough strips [136] at the front end of the air inlet to induce forced transition of the boundary layer and lessen the sensitivity to flow separation. Saric et al. [137] conducted a study on the infrared thermal imaging results of the swept wings of the F-15B aircraft at Ma = 1.85. They discovered that the inclusion of periodic discrete roughness elements can increase the laminar flow area to 70% ~80% and reduce drag by 20%~25%.

Flight experiments remain the most genuine and dependable step for pushing flow control to practice application. Given the exorbitant expenses associated with flight experiments, it is imperative to explore various methods to mitigate these expenditures. However, it is crucial to extract the maximum amount of relevant information from the minimal flight data that is accessible. Furthermore, it is imperative to enhance the sophistication and dependability of measurement instruments and sensors, while consistently investigating the potential for combining flying experiments with other research methodologies. As a result, while research continues to advance the theoretical understanding of flow control, translating these innovations into practical solutions for aircraft requires overcoming significant technical and economic hurdles. Addressing these challenges could potentially lead to enhanced performance, fuel efficiency, and overall safety in future aerospace vehicles.

CONCLUSION

Supersonic and hypersonic flows play a crucial role in the study of fluid dynamics at high speeds. This study provides an overview of the typical physical phenomena, flow control strategies, and research methodologies related to two specific flows. Several studies have been conducted on flow phenomena that are specific to supersonic flow, including the previously mentioned boundary layer transition, shock waves, and sonic explosions. Nonetheless, translating the present research discoveries into tangible implementations for flow control presents a formidable obstacle. It is also important to consider the potential interactions that may occur between these phenomena, such as boundary layer transition interference and shock waves.

Active flow control methods consist primarily of plasma control, jet control, energy deposition control, magnetohydrodynamic control, and others; these techniques are distinguished by their superior performance and high efficiency. These methodologies offer a means to dynamically adjust and enhance the metrics in response to real-time flow conditions, with the ultimate goal of achieving optimal flow efficiency. Notwithstanding its merits, active control continues to encounter challenges that require future resolution, including but not limited to relatively elevated expenses, technological intricacy, and the possibility of substantial energy downfall. Conversely, passive flow control systems, such as aerospike control, riblets control, micro vortex generator control, and others, are distinguished by their cost-effectiveness and dependability. Given that these techniques do not require the addition of additional energy, they offer the advantages of energy conservation and environmental protection. Nevertheless, due to the fact that regulation is accomplished by modifying flow shapes, the control efficacy might be susceptible to the fluctuations of fluid dynamics. In the future, endeavors ought to be concentrated on improving the geometry and properties of passive flow control in order to accommodate a more extensive flow scenario.

Common research methodologies for supersonic and hypersonic flow control include flight testing, numerical simulation, and wind tunnel experiments. Although numerical simulation is generally more cost-effective and can generate vast amounts of detailed data for a variety of flow conditions, capturing flows with a high Reynolds number precisely frequently necessitates substantial computational resources. Experiments in wind tunnels provide a means to directly observe the flow and acquire comprehensive results. On account of the scale effect and additional variables, discrepancies between these results and actual flow are possible. Flight testing has the potential to yield the most precise and dependable data for directly evaluating the efficacy of flow control. Large-scale implementation, however, is both impractical and prohibitively costly. As a result, each of the three approaches possesses distinct merits and demerits. Future research must incorporate careful consideration of the study's focus, while also evaluating the merits and drawbacks of each approach in order to determine the most appropriate one.

AUTHOR CONTRIBUTIONS

SL: Writing, Review, Editing, Original draft. YZo: Writing, Editing, Investigation, Original draft. JL: Review, Formal analysis. JZo: Review, Formal analysis. JZh: Resources, Investigation. YZe: Resources, Project administration; Supervision. YZa: Review, Editing, Investigation, Supervision. All authors contributed to the article and approved the submitted version.

FUNDING

The author(s) declare that no financial support was received for the research, authorship, and/or publication of this article.

CONFLICT OF INTEREST

The authors declare that the research was conducted in the absence of any commercial or financial relationships that could be construed as a potential conflict of interest.

REFERENCES

1. Tishkoff JM, Anderson JD. Breaking the Sound Barrier. In: AIAA Scitech 2019 Forum, January 7–11, 2019, San Diego, CA, (2019). p. 2194. doi:10.2514/6.2019-2194
2. Abdulrahman GA, Qasem NA, Imteyaz B, Abdallah AM, Habib MA. A Review of Aircraft Subsonic and Supersonic Combustors. *Aerosp Sci Technol* (2023) 132:108067. doi:10.1016/j.ast.2022.108067
3. Duan L, Beekman I, Martin M. Direct Numerical Simulation of Hypersonic Turbulent Boundary Layers. Part 3. Effect of Mach Number. *J Fluid Mech* (2011) 672:245–67. doi:10.1017/S0022112010005902
4. Chen JF, Xu Y, Xu XB, Zou QF, Ling G, Zhang YF. Pressure Fluctuation Experiments of Hypersonic Boundary-Layer on a 7-Degree Half-Angle Sharp Cone. *J Exp Fluid Mech* (2023) 37(6):51–60. doi:10.11729/syltlx20210054
5. Candler GV. Rate Effects in Hypersonic Flows. *Annu Rev Fluid Mech* (2019) 51:379–402. doi:10.1146/annurev-fluid-010518040258
6. Song XX, Zhang S, Zhang JF, Zheng Y. Study on the Variation of Gas Radiation Characteristics of Hypersonic Reentry Vehicles. *AIAA J* (2023) 61(12):5277–87. doi:10.2514/1.J063001
7. Tsien HS. Similarity Laws of Hypersonic Flows. *J Math Phys* (1946) 25:247–51. doi:10.1002/sapm1946251247
8. Zhang Y, Ye ZX, Li BH, Xie L, Zou J, Zheng Y. Numerical Analysis of Turbulence Characteristics in a Flat-Plate Flow With Riblets Control. *Adv Aerodyn* (2022) 4:29. doi:10.1186/s42774-022-00115-z
9. Zhang Y, Zhao YL. Novel Design of a Circulation Control Airfoil With Cylinder Rotation. *Phys Fluids* (2023) 35:085113. doi:10.1063/5.0158974
10. Xie L, Li BH, Zhang Y, Zheng Y, Zou J. Effects of Temperature on Drag Reduction in a Subsonic Turbulent Boundary Layer via Micro-Blowing Array. *Chin J Aeronaut* (2022) 35(9):174–93. doi:10.1016/j.cja.2022.01.003

11. Martin S, Bhushan B. Fluid Flow Analysis of Continuous and Segmented Riblet Structures. *Tsc Adv* (2016) 6:10962–78. doi:10.1039/c5ra20944g
12. Ye ZX, Zhang Y, Zou JF, Zheng Y. Tunnel Measurement of Riblet Drag Reduction. *Instr Mes Metrol* (2019) 18(4):361–7. doi:10.18280/i2m.180405
13. Kornilov V. Combined Blowing/Suction Flow Control on Low-Speed Airfoils. *Flow Turbul Combust* (2021) 106:81–108. doi:10.1007/s10494-020-00157-7
14. Tang DB. *Boundary Layer Transition*. Beijing: Science Press Inc. (2015).
15. Van Dyke M. *An Album of Fluid Motion*. California: Parabolic Press Stanford Inc. (1982).
16. Zhao YF, Liu W, Gang DD, Yi SH, Deng XG. Study of Surface Roughness Induced Supersonic Boundary Layer Transition. *J Astronaut* (2015) 36(6): 739–46. doi:10.3873/j.issn.1000-1328.2015.06.016
17. Li F, Xie SF, Bi ZX, Gong J, Chen X, Ji F, et al. Experimental Study of Several on Aerodynamic Problems on Hypersonic Vehicles. *Mod Defence Technol* (2014) 42(5):1–7. doi:10.3969/j.issn.1009-086x.2010.05.001
18. Chen JQ, Tu GH, Zhang FY, Xu GL, Yuan XX, Chen C. Hypersonic Boundary Layer Transition: What We Know, Where Shall We Go. *Acta Aerodyn Sin* (2017) 35(3):311–37. doi:10.7638/kqdlxxb-2017.0030
19. Lee CB, Chen SY. Recent Progress in the Study of Transition in the Hypersonic Boundary Layer. *Natl Sci Rev* (2019) 6(1):155–70. doi:10.1093/nsr/nwy052
20. Chen XL, Fu S. Progress in the Research of Hypersonic and High-Enthalpy Boundary Layer Instabilities and Transition. *Chin J Theor Appl Mech* (2022) 54(11):2937–57. doi:10.6052/0459-1879-22-184
21. Liu Q, Tu GH, Luo ZB, Chen JQ, Zhao R, Yuan XX. Progress in Hypersonic Boundary Layer Transition Delay Control. *Acta Aeronaut Astronaut Sin* (2022) 43(7):025357. doi:10.7527/S1000-6893.2021.25357
22. Yang HS, Liang H, Guo SG, Tang M, Zhang C, Wu Y, et al. Research Progress of Hypersonic Boundary Layer Transition Control Experiments. *Adv Aerodyn* (2022) 4:18. doi:10.1186/s42774-022-00105-1
23. Su CH, Zhou H. Transition Prediction of a Hypersonic Boundary Layer Over a Cone at a Small Angle of Attack With the Improvement of e^N Method. *Sci Sin Phys Mech Astron* (2009) 39(1):123–30.
24. Su CH, Zhou H. Transition Prediction for Supersonic and Hypersonic Boundary Layers on a Cone With an Angle of Attack. *Sci Sin Phys Mech Astron* (2009) 39(6):874–82.
25. Wan BB, Chen X, Chen JQ, Yuan XX, Duan MC, Huang ZF, et al. Applications of HyTEN Software for Predicting Three-Dimensional Boundary-Layer Transition in Typical Hypersonic Models. *Aerosp Technol* (2023) (1) 150–8. doi:10.16338/j.issn.2097-0714.20220206
26. Huang ZF, Wan BB, Duan MC. Progresses in engineering Application Research on Hypersonic Flow Stability and Transition. *Acta Aerodyn Sin* (2020) 38(2):368–78. doi:10.7638/kqdlxxb-2020.0047
27. Wang Z, Chang JT, Li YF, Kong C. Investigation of Shock Wave Control by Suction in a Supersonic Cascade. *Aerosp Sci Technol* (2021) 108:106382. doi:10.1016/j.ast.2020.106382
28. Albertson C, Venkat V. Shock Interaction Control for Scramjet Cowl Leading Edges. In: AIAA/CIRA 13th International Space Planes and Hypersonics Systems and Technologies Conference, May 16–20, 2005, Capua, Italy (2005). p. 3289.
29. Wang ZA, Chen RY, Li YM, Chang JT. Recent Research Progress on the Flow Field Characteristics and Control Methods of Shock Train in Supersonic Internal Flow. *J Eng Thermophys* (2022) 43(9):2275–91.
30. Luo ZB, Xie W, Xie XZ, Zhou Y, Liu Q. Research Progress of Active Flow Control of Shock Wave and its Interaction. *Acta Aeronaut Astronaut Sin* (2023) 44(15):529002.
31. Zhang ZG, Cheng C, Zhang LT, Li Y, Xue L, Wang C, et al. Asymmetry of Oblique Shock Train and Flow Control. *J Aerospace Eng* (2024) 238(4): 427–38. doi:10.1177/09544100241232160
32. Ferri A. *Experimental Results With Airfoils Tested in the High-Speed Tunnel at Guidonia*. Washington: National Advisory Committee for Aeronautics Inc (1940).
33. Sabnis K, Babinsky H. A Review of Three-Dimensional Shock Wave–Boundary-Layer Interactions. *Prog Aerosp Sci* (2023) 143:100953. doi:10.1016/j.paerosci.2023.100953
34. Dolling DS. Fifty Years of Shock-Wave/Boundary-Layer Interaction Research: What Next? *AIAA J* (2001) 39(8):1517–31. doi:10.2514/2.1476
35. Wang DQ, Xu CH, Jiang CW, Gao ZX. Research Progress of Control Technique for Hypersonic Flow. *Aerodyn Missile J* (2015)(09) 24–30. doi:10.16338/j.issn.1009-1319.2015.09.04
36. Zhong XY, Huang W, Niu YB, Li J. A Review of Shock/Boundary Layer Interference Control Methods for Hypersonic Vehicles. *Aerodynamic Missile J* (2021)(6) 42–8. doi:10.16338/j.issn.1009-1319.20210827
37. Shi XT, Lyu M, Zhao Y, Tao SC, Hao L, Yuan XJ. Flow Control Technique for Shock Wave/Turbulent Boundary Layer Interactions. *Acta Aeronaut Astronaut Sin* (2022) 43(1):625929. doi:10.7527/S1000-6893.2021.25929
38. Fan XH, Tang ZG, Wang G, Yang YG. Review of Low-Frequency Unsteadiness in Shock-Wave/turbulent Boundary-Layer Interaction. *Acta Aeronaut Astronaut Sin* (2022) 43:9–29. doi:10.7527/S1000-6893.2021.25917
39. Maglieri DJ, Bobbitt PJ, Plotkin KJ, Shepherd KP, Coen PG, Richwine DM. Sonic Boom: Six Decades of Research. *NASA Sp-2014-622 Langley* (2014).
40. Zhang LW, Song WP, Han ZH, Qian ZS, Song BF. Recent Progress of Sonic Boom Generation, Propagation, and Mitigation Mechanism. *Acta Aeronaut Astronaut Sin* (2022) 43(12):025649. doi:10.7527/S1000-6893.2021.25649
41. Qian ZS, Han ZH. Progress and Challenges of Sonic Boom Research. *Acta Aerodyn Sin* (2019) 37(4):601–19. doi:10.7638/kqdlxxb-2019.0054
42. Feng XQ, Song BF, Li ZK. Research of Low Sonic Boom Quiet Spike Design Method. *Acta Aeronaut Astronaut Sin* (2013) 34(5):1009–17. doi:10.7527/S1000-6893.2013.0190
43. Ye LQ, Ye ZY, Ma BP. An Active Control Method for Reducing Sonic Boom of Supersonic Aircraft. *J Northwest Polytech Univ* (2021) 39(3):566–75. doi:10.1051/jnwpu/20213930566
44. Ye LQ, Ye ZY, Ye K, Wu J, Miao S. A Low-Boom and Low-Drag Design Method for Supersonic Aircraft and Its Applications on Airfoils. *Adv Aerodyn* (2021) 3:25. doi:10.1186/s42774-021-00079-6
45. He YB, Chang JT, Bao W, Huang H, Yu D. Numerical Investigation of Local Resistance to Backpressure in Hypersonic Inlet With Suction. *J Propul Power* (2016) 32(6):1531–43. doi:10.2514/1.B36043
46. Deng WX, Yang SH, Zhang WZ, Wang XY, Tian Y, Le JL. Study on Air Blowing Control Method for Hypersonic Flow. *J Propul Technol* (2017) 38(4): 759–63. doi:10.13675/j.cnki.tjjs.2017.04.005
47. Li ZX, Liu MK, Han GL, Wang D, Jiang Z. Numerical Simulation of Hypersonic Flat-Plate Boundary-Layer Blowing Control. *Phys Fluids* (2023) 35:126111. doi:10.1063/5.0174498
48. Kametani Y, Kotake A, Fukagata K, Tokugawa N. Drag Reduction Capability of Uniform Blowing in Supersonic Wall-Bounded Turbulent Flows. *Phys Rev Fluids* (2017) 2(12):123904. doi:10.1103/physrevfluids.2.123904
49. Yao J, Hussain F. Drag Reduction via Opposition Control in a Compressible Turbulent Channel. *Phys Rev Fluids* (2021) 6(11):114602. doi:10.1103/physrevfluids.6.114602
50. Sepahi-Younsi J, Feshalami BF, Maadi SR, Soltani MR. Boundary Layer Suction for High-Speed Air Intakes: A Review. *J Aerospace Eng* (2018) 233(9): 3459–81. doi:10.1177/0954410018793262
51. He Y, Huang HY, Yu DR. Investigation of Corner Separation and Suction Control in Constant Area Duct. *Aerosp Sci Technol* (2017) 66:70–82. doi:10.1016/j.ast.2017.01.029
52. Sriram R, Jagadeesh G. Shock Tunnel Experiments on Control of Shock Induced Large Separation Bubble Using Boundary Layer Bleed. *Aerosp Sci Technol* (2014) 36:87–93. doi:10.1016/j.ast.2014.04.003
53. Subramanian S, Kontis K. Flow Control of SBLI Using Grooves With Suction. *Solid State Technol* (2020) 63(1):860–71.
54. Glezer A, Amitay M. Synthetic Jets. *Annu Rev Fluid Mech* (2002) 34:503–29. doi:10.1146/annurev.fluid.34.090501.094913
55. Butler MG, Ekmekci A, Sullivan PE. Multiphysics Modeling of a Synthetic Jet Actuator in Operation. *Actuators* (2024) 13:60. doi:10.3390/act13020060
56. Hong MH, Cheng SY, Zhong S. Effect of Geometric Parameters on Synthetic Jet: A Review. *Phys Fluids* (2020) 32:031301. doi:10.1063/1.5142408
57. Luo ZB, Xia ZX, Deng X, Wang L, Li YJ, Ma Y, et al. Research Progress of Dual Synthetic Jets and Its Flow Control Technology. *Acta Phys Sin* (2017) 35(2):252–64. doi:10.7638/kqdlxxb-2017.0053
58. Liu Q, Luo ZB, Deng X, Yang SK, Jiang H. Linear Stability of Supersonic Boundary Layer With Synthetic Cold/Hot Jet Control. *Acta Phys Sin* (2017) 66(23):234701. doi:10.7498/aps.66.234701

59. Li JF, Zhang XB. Active Flow Control for Supersonic Aircraft: A Novel Hybrid Synthetic Jet Actuator. *Sensors Actuat A-Phys* (2020) 302:111770. doi:10.1016/j.sna.2019.111770
60. Szwaba R. Shock Wave Induced Separation Control by Streamwise Vortices. *J Therm Sci* (2005) 14(3):249–53. doi:10.1007/s11630-005-0009-z
61. Kumar R, Ali MY, Alvi FS, Venkatakrishnan L. Generation and Control of Oblique Shocks Using Microjets. *AIAA J* (2011) 49(12):2751–9. doi:10.2514/1.J051148
62. Verma S, Manisankar C. Control of Compression-Ramp-Induced Interaction With Steady Microjets. *AIAA J* (2019) 57(7):2892–904. doi:10.2514/1.J057509
63. Kreth PA, Alvi FS. Using High-Frequency Pulsed Supersonic Microjets to Control Resonant High-Speed Cavity Flows. *AIAA J* (2020) 58(8):3378–92. doi:10.2514/1.J058912
64. Xu H, Huang W, Du ZB, Meng Y, Liu C, Yan L. Influences of Microjet Pressure and Number of Microjets on the Control of Shock Wave/Boundary Layer Interaction. *Aerosp Sci Technol* (2023) 138:108345. doi:10.1016/j.ast.2023.108345
65. Li YH, Wu Y. Research Progress and Outlook of Flow Control and Combustion Control Using Plasma Actuation. *Sci Sin Technol* (2020) 50:1252–73. doi:10.1360/SST-2020-0111
66. Chen JZ, Hu GT, Fan GC, Chen WF. Bow Shock Wave Control and Drag Reduction by Plasma Synthetic Jet. *Acta Aeronaut Astronaut Sin* (2021) 42(7):124773. doi:10.7527/S1000-6893.2020.24773
67. Zheng JG, Cui YD, Li J, Khoo BC. A Note on Supersonic Flow Control With Nanosecond Plasma Actuator. *Phys Fluids* (2018) 30(4). doi:10.1063/1.5012054
68. Wang YZ, Zhang HD, Wu Y, Li Y, Zhu Y. Supersonic Compressor Cascade Flow Control Using Plasma Actuation at Low Reynolds Number. *Phys Fluids* (2022) 34(2). doi:10.1063/5.0081685
69. Russell A, Zare-Behtash H, Kontis K. Joule Heating Flow Control Methods for High-Speed Flows. *J Electrostat* (2016) 80:34–68. doi:10.1016/j.elstat.2016.01.004
70. Emerick T, Ali M, Foster C, Alvi FS, Popkin S. SparkJet Characterizations in Quiescent and Supersonic Flowfields. *Exp Fluids* (2014) 55:1858. doi:10.1007/s00348-014-1858-6
71. Zhu GS, Yao SY, Duan Y. Research Progress and Engineering Application of Flow Control Technology for Drag and Heat Reduction of High-Speed Vehicles. *Acta Aeronaut Astronaut Sin* (2023) 44(15):529049. doi:10.7527/S1000-6893.2023.29049
72. Han LY, Wang B, Pu L, Chen Q, Zheng HB. Research Progress on Mechanism and Related Problems of Energy Deposition Drag Reduction Technology. *Acta Aeronaut Astronaut Sin* (2022) 43(9):026032. doi:10.7527/S1000-6893.2021.26032
73. Xie W, Luo ZB, Zhou Y, Gao T, Wu Y, Wang Q. Experimental Study on Shock Wave Control in High-Enthalpy Hypersonic Flow by Using SparkJet Actuator. *Acta Astronaut* (2021) 188:416–25. doi:10.1016/j.actaastro.2021.07.032
74. Azarova O. Supersonic Flow Control Using Combined Energy Deposition. *Aerospace* (2015) 2:118–34. doi:10.3390/aerospace2010118
75. Knight D, Kianvashrad N. Review of Energy Deposition for High-Speed Flow Control. *Energies* (2022) 15:9645. doi:10.3390/en15249645
76. Zhang S, Hong G, Zhang DY, Cheng FQ. Progress in Hypersonic Inlet Flow Controls by Magnetohydrodynamic. *Appl Mech Mater* (2015) 730:311–5. doi:10.4028/www.scientific.net/AMM.730.311
77. Jiang H, Liu J, Luo SC, Wang J, Huang W. Hypersonic Flow Control of Shock Wave/Turbulent Boundary Layer Interactions Using Magnetohydrodynamic Plasma Actuators. *J Zhejiang Univ-sc A* (2020) 21(9):745–60. doi:10.1631/jzus.A2000025
78. Luo SC, Liu J, Jiang H, Wang J. Magnetohydrodynamic Control of Hypersonic Separation Flows. *Int J Aerospace Eng* (2021) 2021:1–13. doi:10.1155/2021/6652795
79. Wu H, Wang JH, Huang W, Du ZB, Yan L. Research Progress on Shock Wave/Boundary Layer Interactions and Flow Controls Induced by Micro Vortex Generators. *Acta Aeronaut Astronaut Sin* (2021) 42(6):025371. doi:10.7527/S1000-6893.2021.25371
80. Lin JC. Review of Research on Low-Profile Vortex Generators to Control Boundary-Layer Separation. *Prog Aerosp Sci* (2002) 38:389–420. doi:10.1016/s0376-0421(02)00010-6
81. Dong XR, Chen YH, Dong G, Liu YX. Studies on Hypersonic Shock Wave/boundary Layer Interactions and Flow Control Based on MVG Array. *Eng Mech* (2016) 33(7):23–30. doi:10.6052/j.issn.1000-4750.2014.12.1029
82. Zhu YY, Wang XD. Investigation on Flow Control Using Combination of Micro Vortex Generator and Vortex Generator Jet. *J Ordn Eq Eng* (2018) 39(7):175–9. doi:10.11809/bqzbgcxb2018.07.038
83. Gnani F, Zare-Behtash H, Kontis K. Pseudo-Shock Waves and Their Interactions in High-Speed Intakes. *Prog Aero Sci* (2016) 82:36–56. doi:10.1016/j.paerosci.2016.02.001
84. Saad MR, Zare-Behtash H, Che-Idris A, Kontis K. Micro-Ramps for Hypersonic Flow Control. *Micromachines* (2012) 3(2):364–78. doi:10.3390/mi3020364
85. Huang W, Chen Z, Yan L, Yan B, Du Z. Drag and Heat Flux Reduction Mechanism Induced by the Spike and Its Combinations in Supersonic Flows: A Review. *Prog Aerosp Sci* (2019) 105:31–9. doi:10.1016/j.paerosci.2018.12.001
86. Guan RQ, Qin QH, Wang YF, Xu J. Experimental Investigation of the Pulsing Flow Field Around Four Types of Spiked-Blunt Body at Mach 2.2. *Aerosp Sci Technol* (2023) 133:108129. doi:10.1016/j.ast.2023.108129
87. Deng F, Jiao ZH, Liang BB, Xie F, Qin N. Spike Effects on Drag Reduction for Hypersonic Lifting-Body. *J Spacecraft Rockets* (2017) 54:1185–95. doi:10.2514/1.A33865
88. Gauer M, Paull A. Numerical Investigation of a Spiked Blunt Nose Cone at Hypersonic Speeds. *J Spacecraft Rockets* (2008) 45(3):459–71. doi:10.2514/1.30590
89. Xu Y, Fang S. Numerical Investigation of Drag and Heat Flux Reduction in Hypersonic Vehicle with Aerospike. In: Proceedings of the 14th International Conference on Computer Modeling and Simulation, June 24-26, 2022, Chongqing, China (2022). p. 94–102. doi:10.1145/3547578.3547593
90. Soleimani S, Eckels S. A Review of Drag Reduction and Heat Transfer Enhancement by Riblet Surfaces in Closed and Open Channel Flow. *Intl J Thermofluids* (2021) 9:100053. doi:10.1016/j.ijft.2020.100053
91. Ran W, Zare A, Jovanovic MR. Model-Based Design of Riblets for Turbulent Drag Reduction. *J Fluids Mech* (2021) 906:A7. doi:10.1017/jfm.2020.722
92. Li JH, Liu YM, Wang J. Evaluation Method of Riblets Effects and Application on a Missile Surface. *Aerosp Sci Technol* (2019) 95:105418. doi:10.1016/j.ast.2019.105418
93. Zhou H, Li Xl Yu Cp . Study on Turbulence Drag Reduction of Riblet Plate in Hypersonic Turbulent Flows. *Int J Mod Phys C* (2020) 31(3):2050046. doi:10.1142/S0129183120500461
94. Wen B, Zhong S, Wang G, Li L. Effects of Herringbone Riblets on Shock-Wave/turbulent Boundary-Layer Interactions. *Aerosp Sci Technol* (2024) 146:108914. doi:10.1016/j.ast.2024.108914
95. Olad P, Esposito MC, Brandt L, Innings F, Hakansson A. Towards Best Practice Recommendations for Turbulence Modelling of High-Pressure Homogenizer Outlet Chambers–Numerical Validation Using DNS Data. *Chem Eng Sci* (2022) 258:117748. doi:10.1016/j.ces.2022.117748
96. Institute of Aerodynamics and Gas Dynamics. Working Group Boundary Layers. Available from: https://www.iag.uni-stuttgart.de/en/working-groups/boundary-layers (Accessed April 10, 2024).
97. Jing Y, Wang H, Zhu P, Li Y, Ye L, Jiang L, et al. The Sensitivity of Large Eddy Simulations to Grid Resolution in Tropical Cyclone High Wind Area Applications. *Remote Sens* (2023) 15:3785. doi:10.3390/rs15153785
98. Stanford University. Large Eddy Simulation of Premixed and Non-premixed Gas Combustion. Available from: https://web.stanford.edu/group/pitsch/Research/LES.htm (Accessed April 10, 2024).
99. NASA. Using CFD to Develop NASA's X-57 Maxwell Flight Simulator. Available from: https://www.nas.nasa.gov/SC19/demos/demo13.html (Accessed April 10, 2024).
100. Jameson A, Schmidt W, Turkel E. Numerical Solution of the Euler Equations by Finite Volume Methods Using Runge Kutta Time Stepping Schemes. In: 14th Fluid and Plasma Dynamics Conference, June 23–25, 1981, Palo Alto, CA (1981). p. 1259.
101. Ducros F, Ferrand V, Nicoud F, Weber C, Darracq D, Gacherieu C, et al. Large-Eddy Simulation of the Shock/Turbulence Interaction. *J Comput Phys* (1999) 152:517–49. doi:10.1006/jcph.1999.6238

102. Passiatore D, Sciacovelli L, Cinnella P, Pascazio G. Evaluation of a High-Order Central-Difference Solver for Highly Compressible Flows Out of Thermochemical Equilibrium. *Comput Fluids* (2024) 269:106137. doi:10.1016/j.compfluid.2023.106137
103. Pirozzoli S. Numerical Methods for High-Speed Flows. *Annu Rev Fluid Mech* (2011) 43:163–94. doi:10.1146/annurev-fluid-122109-160718
104. Knight DD, Degrez G. Shock Wave Boundary Layer Interactions in High Mach Number Flows a Critical Survey of Current Numerical Prediction Capabilities. *AGARD Advisory Rep Agard Ar* (1998) 2:1–35.
105. Fu S, Wang L. RANS Modeling of High-Speed Aerodynamic Flow Transition With Consideration of Stability Theory. *Prog Aerosp Sci* (2013) 58:36–59. doi:10.1016/j.paerosci.2012.08.004
106. Kametani Y, Fukagata K, Örlü R, Schlatter P. Drag Reduction in Spatially Developing Turbulent Boundary Layers by Spatially Intermittent Blowing at Constant Mass-Flux. *J Turbul* (2016) 17(10):913–29. doi:10.1080/14685248.2016.1192285
107. Rizzetta DP, Visbal MR. Large-Eddy Simulation of Supersonic Cavity Flowfields Including Flow Control. *AIAA J* (2003) 41(8):1452–62. doi:10.2514/2.2128
108. Yang G, Yao YF, Fang J, Gan T, Li Q, Lu L. Large-Eddy Simulation of Shock-Wave/Turbulent Boundary Layer Interaction With and Without SparkJet Control. *Chin J Aeronaut* (2016) 29(3):617–29. doi:10.1016/j.cja.2016.04.001
109. Bisek N, Poggie J. Large-Eddy Simulations of Separated Supersonic Flow With Plasma Control. In: 51st AIAA Aerospace Sciences Meeting including the New Horizons Forum and Aerospace Exposition, January 7–10, 2013, Dallas/Ft. Worth Region, Texas (2013). p. 528. doi:10.2514/6.2013-528
110. Wang WZ, Kong WX, Yan H, Zao R. Acoustic Metasurfaces for Stabilization of Broadband Unstable Modes in High Speed Boundary Layer. *J Beijing Univ Aero Astro* (2021) 49(2):388–96. doi:10.13700/j.bh.1001-5965.2021.0235
111. Zeng X, Zhang Y, Cui JH, Xiao Z, Luo J. Direct Numerical Simulation of Channel Flow With Real Surface Roughness Using a Ghost Cell Immersed Boundary Method. *Phys Fluids* (2024) 36:036618. doi:10.1063/5.0195275
112. Ghosh S. *An Immersed Boundary Method for Simulating the Effects of Control Devices Used in Mitigating Shock/Boundary-Layer Interactions*. Raleigh, North Carolina: North Carolina State University (2010).
113. Ghosh S, Choi JI, Edwards JR. Simulation of Shock/Boundary-Layer Interactions With Bleed Using Immersed-Boundary Methods. *J Propul Power* (2010) 26(2):203–14. doi:10.2514/1.45297
114. Ghosh S, Edwards JR, Choi JI. Numerical Simulation of the Effects of Mesoflaps in Controlling Shock/Boundary-Layer Interactions. *J Propul Power* (2012) 28(5):955–70. doi:10.2514/1.B34297
115. Marineau EC, Moraru GC, Lewis DR, Norris JD, Lafferty JF, Wagnild RM, et al. Mach 10 Boundary Layer Transition Experiments on Sharp and Blunted Cones. In: 19th AIAA International Space Planes and Hypersonic Systems and Technologies Conference, June 16–20, 2014, Atlanta, GA (2014). p. 3108.
116. Jiang Z, Hu Z, Wang Y, Han G. Advances in Critical Technologies for Hypersonic and High-Enthalpy Wind Tunnel. *Chin J Aeronaut* (2020) 33(12):3027–38. doi:10.1016/j.cja.2020.04.003
117. Borovoy V, Mosharov V, Noev A, Radchenko V. Temperature Sensitive Paint Application for Investigation of Boundary Layer Transition in Short-Duration Wind Tunnels. *Prog Flight Phys* (2012) 3:15–24. doi:10.1051/eucass/201203015
118. Igra O, Seiler F. *Experimental Methods of Shock Wave Research*. Springer Inc. (2016).
119. Liu XH, Lai GW, Wu J. Boundary-Layer Transition Experiments in Hypersonic Flow. *Acta Aerodyn Sin* (2018) 36(2):196–211. doi:10.7638/kqdlxxb—2018.0017
120. Yi SH, Chen Z, Zhu YZ, He L, Wu Y, et al. Progress on Experimental Techniques and Studies of Hypersonic/Supersonic Flows. *Acta Aeronaut Astronaut Sin* (2015) 36(1):98–119. doi:10.7527/S1000-6893.2014.0230
121. Wang ZG, Sun XW, Huang W, Li S, Yan L. Experimental Investigation on Drag and Heat Flux Reduction in Supersonic/hypersonic Flows: A Survey. *Acta Astronaut* (2016) 129:95–110. doi:10.1016/j.actaastro.2016.09.004
122. Berry S, Nowak R, Horvath T. Boundary Layer Control for Hypersonic Airbreathing Vehicles. In: 34th AIAA Fluid Dynamics Conference and Exhibit, June 28–July 1, 2004, Portland, Oregon (2004). p. 2246.
123. Borg MP, Schneider SP. Effect of Freestream Noise on Roughness-Induced Transition for the X-51A Forebody. *J Spacecraft Rockets* (2008) 45(6):1106–16. doi:10.2514/1.38005
124. Zhu JC, Shi ZW, Fu JQ, Chen J. Aerodynamic Characteristics of Hypersonic Airfoils Based on Jet Flow Control Technology. *AIP Adv* (2021) 11:035036. doi:10.1063/5.0033779
125. Xia ZH, Ding HL, Yi SH, Sun MB, et al. Experimental Research on Supersonic Mixing Layer Flow Control Based on Ramp-VG Array. *Phys Gases* (2022) 7(2):49–56. doi:10.19527/j.cnki.2096-1642.0952
126. Berger KT, Anderson BP, Campbell C, Garske M, Saucedo L, Kinder G, et al. Boundary Layer Transition Flight Experiment Overview. In: 42nd AIAA Thermophysics Conference, June 27–30, 2011, Honolulu, Hawaii (2011). p. 3323.
127. Li F, Choudhari M, Chang CL, Kimmel R, Adamczak D, Smith M. Transition Analysis for the Ascent Phase of HIFiRE-1 Flight Experiment. *J Spacecraft Rockets* (2015) 52(5):1283–93. doi:10.2514/1.A33258
128. Kimmel RL, Adamczak D, Berger K, Choudhari M. HIFiRE-5 Flight Vehicle Design. In: 40th Fluid Dynamics Conference and Exhibit, June 28–July 1, 2010, Chicago, Illinois (2010).
129. Kimmel RL, Adamczak D, Hartley D, Alesi H, Frost MA, Pietsch R, et al. HIFiRE-5b Flight Overview. In: 47th AIAA Fluid Dynamics Conference, June 5–9, 2017, Denver, Colorado (2017). p. 3131.
130. Yuan XX, He K, Chen JQ, Zhang YF, Wang AL, Guo YJ, et al. Preliminary Transition Research Analysis of MF-1. *Acta Aerodyn Sin* (2018) 36(2):286–93. doi:10.7638/kqdlxxb-2018.0050
131. Chen JQ, Tu GH, Wan BB, Yuan XX, Yang Q, Zhuang Y, et al. Characteristics of Flow Field and Boundary-Layer Stability of HyTRV. *Acta Aeronaut Astronaut Sin* (2021) 42(6):124317. doi:10.7527/S1000-6893.2020.24317
132. Burrows S, Rana ZA, Prince S. Hypersonic Boundary Layer Reduction With Optimisation of the Hyshot II Intake Using Numerical Methods. In: AIAA SCITECH 2024 Forum, January 8–12, 2024, Orlando, FL (2024). p. 2861. doi:10.2514/6.2024-2861
133. Whalen EA, Shmilovich A, Spoor M, Tran J, Vijgen P, Lin JC, et al. Flight Test of an Active Flow Control Enhanced Vertical Tail. *AIAA J* (2018) 56(9):3393–8. doi:10.2514/1.J056959
134. Razzaqi SA, Silvester TB, Smart MK, Paull R, et al. The HIFiRE 7 Flight Experiment. In: 22nd AIAA International Space Planes and Hypersonics Systems and Technologies Conference, September 17–19, 2018, Orlando, FL (2018). p. 5256. doi:10.2514/6.2018-5256
135. Cowart R, Grindle T. An Overview of the Gulfstream/NASA Quiet SpikeTM Flight Test Program. In: 46th AIAA Aerospace Sciences Meeting and Exhibit, January 07–10, 2008, Reno, Nevada (2008). p. 123.
136. Berry S, Daryabeigi K, Wurster K, Bittner R. Boundary-layer Transition on X-43A. *J Spacecraft Rockets* (2010) 47(6):922–34. doi:10.2514/1.45889
137. Saric WS, Reed HL, Banks DW. Flight Testing of Laminar Flow Control in High-Speed Boundary Layers. In: RTO AVT Specialists' Meeting on 'Enhancement of NATO Military Flight Vehicle Performance by Managemenet of Interacting Boundary Layer Transition and Separation, October 4–7, 2004, Prague, Czechia (2004). p. 4–7.

AEROSPACE RESEARCH COMMUNICATIONS
ORIGINAL RESEARCH
published: 20 February 2024
doi: 10.3389/arc.2024.12506

Numerical Investigations of Outer-Layer Turbulent Boundary Layer Control for Drag Reduction Through Micro Fluidic-Jet Actuators

Li Li[1,2]*, *Junsheng Wu*[1]*, *Yihua Liang*[2] and *Zengdong Tian*[2]

[1]Department of Computer Science, Northwestern Polytechnical University, Xi'an, China, [2]AVIC Xi'an Aeronautics Computing Technique Research Institute, Xi'an, China

Drag reduction through turbulent boundary layer control (TBLC) is an essential way to develop green aviation technologies. Compared with traditional approaches for drag reduction, turbulence drag reduction is a relatively new technology, particularly for skin friction drag reduction, and it is becoming a hotspot problem worldwide. This paper focuses on the research of micro fluidic-jet actuators used for outer-layer boundary layer control with high-performance computing (HPC). This study aims to reduce turbulent drag by reshaping the flow structure within the turbulent boundary layer. To ensure the calculation accuracy of the core region and reduce the consumption of computing resources, a zonal LES/RANS strategy and WMLES method are proposed to simulate the effects of fluidic-actuators for outer-layer boundary control, in which high-performance computing has to be involved. The studies are performed on the classical zero-gradient turbulent flat plate cases, in which three different control strategies named "W-control," "V-control," and "VW-control" are used and compared to study the effects of drag reduction under a low Reynolds number at $Re_\tau = 470$ and a higher Reynolds number at $Re_\tau = 4700$. The mechanism for drag reduction is analysed via a pre-multiplied spectral method and a parallel dynamic mode decomposition (DMD) method. The results show that the present approach can effectively simulate the outer-layer turbulent boundary control where the "V-control" with the fluidic-jet actuator array behaves well to achieve an average drag reduction (DR) rate of more than 5% for the high Reynolds number case of the flat plate boundary layer. The high Reynolds shear stress and turbulent kinetic energy distribution in the boundary layer region show an obvious uplift under the effects of actuators, which is the main mechanism for drag reduction.

Keywords: flow control, drag reduction, turbulent boundary layer control, micro fluidic-jet actuators, computational fluid dynamics

***Correspondence**
Li Li,
westlili@163.com
Junsheng Wu,
wujunsheng@nwpu.edu.cn

Received: *01 December 2023*
Accepted: *24 January 2024*
Published: *20 February 2024*

Citation:
Li L, Wu J, Liang Y and Tian Z (2024) Numerical Investigations of Outer-Layer Turbulent Boundary Layer Control for Drag Reduction Through Micro Fluidic-Jet Actuators. Aerosp. Res. Commun. 2:12506. doi: 10.3389/arc.2024.12506

INTRODUCTION

In view of the requirement for civil aircraft, to face the more competitive civil aircraft market and the more rigorous runs environment (e.g., an increase of fuel cost, enhancement of noise, and emission limit), developing a safer, more economical, more environmental, and more comfortable aircraft is a permanent topic or target. Among them, drag reduction is a necessary means to

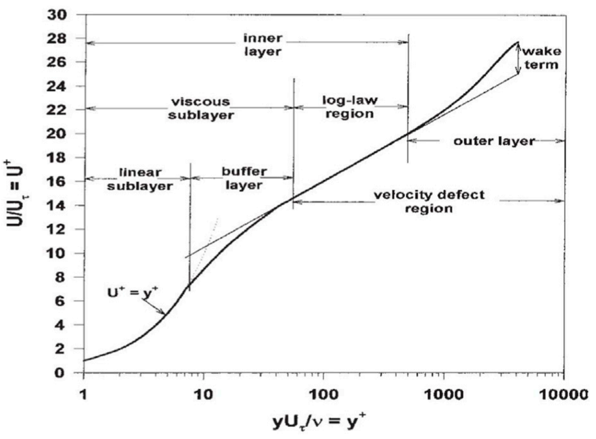

FIGURE 1 | An illustration of the characteristics of the turbulent boundary layer.

TABLE 1 | Control strategies with fluidic-jet arrays.

Notation	Meaning	Injection angle θ
W-control	Span-wise (w)	90°
V-control	Normal (v)	0°
VW-control	Normal plus span-wise (vw)	45°

TABLE 2 | Computational conditions for the model problem.

	Case 1	Case 2
Re_τ	470	4,700
$\delta\ [m]$	0.058	0.058
$\mu\ [Pa \cdot S]$	4.4483×10^{-6}	4.4483×10^{-7}
$\rho\ [kg \cdot m^{-3}]$	1.0	1.0

increase the economy of aircraft and keep global competitiveness. The statistical data from the actual flights of civil aircraft indicate that there is a close correlation between drag and fuel economy.

Drag reduction is a fundamental science problem. Since people learned how to utilize aerodynamic forces, drag has been a main issue for aircraft design. In view of mechanics, when the aircraft flies on a cruise, the gravitation of the aircraft is balanced by the lift, and the drag is balanced by the propulsion from engines so that the energy cost of engines is mainly used to overcome drag. Followed Breguet's approximate range equation for voyage [1], the flying range is farther with a smaller drag and larger ratio of lift to drag, and for a typical large commercial aircraft, when keeping a constant voyage, at least eight passengers (250 pounds per passenger) would be reduced if one drag unit ($\Delta C_D = 0.0001$) is increased. The fact is that the drag coefficient for most large civil aircraft is between 0.03 and 0.04, which indicates that, even when one drag unit is reduced, the resulting benefit is considerable.

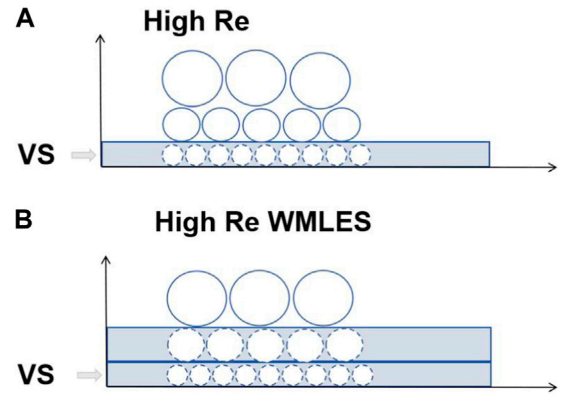

FIGURE 2 | An illustration of the principle of the WMLES approach; **(A)** original LES; **(B)** WMLES.

In view of fluid dynamics, there are only two types of drag. One is the contribution from the difference in pressure, and the other is from the viscosity of the fluid. However, for convenience in drag reduction design, people usually use an alternative viewpoint to classify the contributions to drag according to the sources of drag, in which the main contributions to drag include the skin friction, the induced drag, the interference drag, the wave drag, the drag from roughness, and the others [2, 3]. In order to reduce these different drags, different pertinent means have to be used [4–6]. Among them, turbulence boundary layer control (TBLC) is becoming a promising way for skin friction drag reduction [7, 8].

In this paper, numerical investigations of outer-layer turbulent boundary layer control for drag reduction through micro fluidic-jet actuators are performed. The primary objective is to establish an effective numerical method to model the turbulent boundary layer and to investigate the effect of TBLC with micro fluidic-jet actuators. To do that, a zonal LES/RANS strategy and WMLES method are proposed for the numerical simulation purpose. Then, numerical studies are performed on the classical zero-gradient turbulent flat plate case with and without micro fluidic-jet actuators. Three different control strategies with the fluidic-jet actuators array named "W-control," "V-control," and "VW-control" are used and compared to study the effects of drag reduction, particularly with the outer layer TBLC concept [7, 8], under a low Reynolds number at $Re_\tau = 470$ and a higher Reynolds number at $Re_\tau = 4700$. The idea can be illustrated by understanding the characteristics of the turbulent boundary layer as shown in **Figure 1**. It can be seen that a typical turbulent boundary layer consists of four layers: the linear sublayer, the buffer layer, the log-law region, and the wake term. The basic idea of outer layer TBCL here is to directly target existent streamwise vortices to suppress or mitigate the effect of these vortices in the buffer layer, which provides a new sight for turbulence drag reduction other than the traditional ways, e.g., using small riblets to reshape the structure of the boundary layer. For further details, refer to [7].

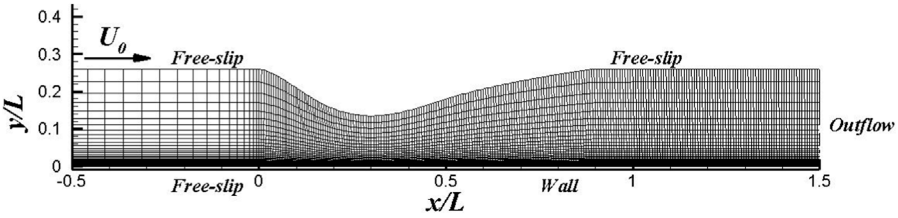

FIGURE 3 | The sketch of the computational grid for the adverse gradient flat plate case.

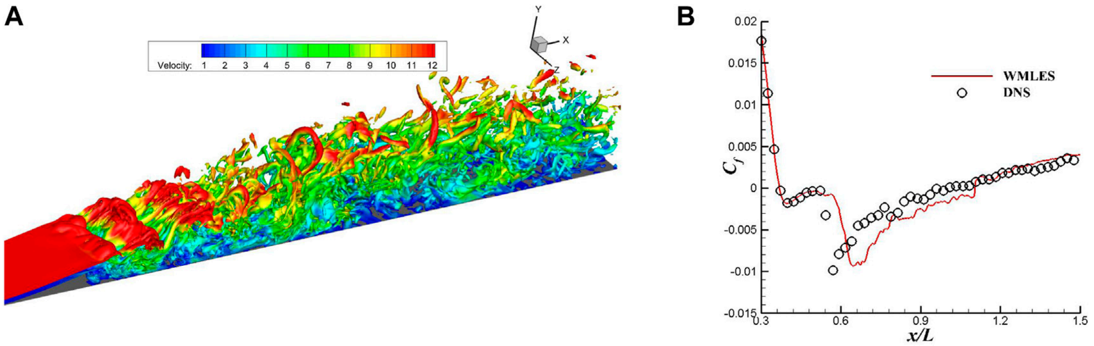

FIGURE 4 | Numerical results for the adverse gradient flat plate case from the WMLES approach: **(A)** typical transient flow field; **(B)** comparison of the skin friction distribution with DNS.

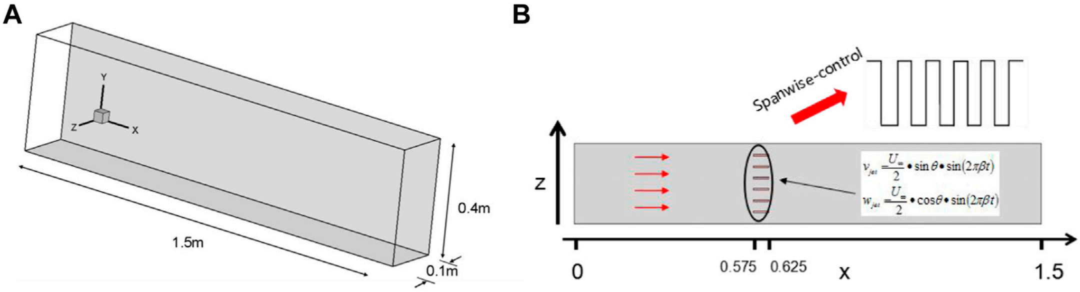

FIGURE 5 | The model problem of TBCL: **(A)** set-up for the base flow and **(B)** set-up for the flow control.

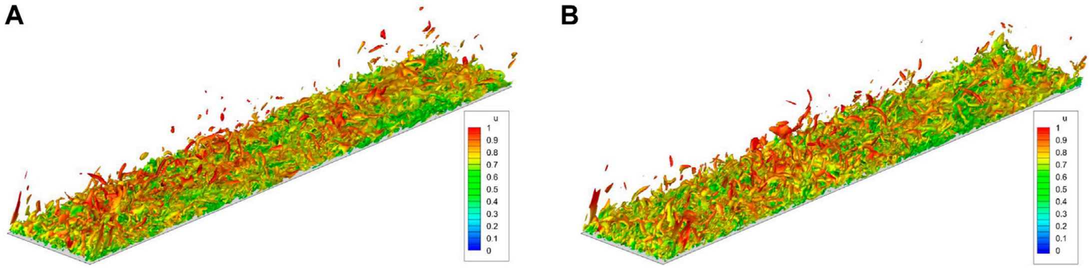

FIGURE 6 | Transient flow field of **(A)** base flow and **(B)** controlled flow with VW-control at Re_τ = 470.

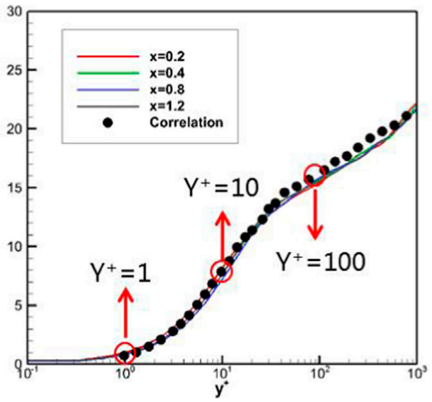

FIGURE 7 | Velocity profiles at different locations for the base flow at $Re_\tau = 470$.

The full paper is organized as follows. In the first section, the WMLES approach is outlined, followed by some typical validation results. In the second section, the model problems and results for TBLC on the turbulent flat plate boundary layer are presented. Finally, some conclusions with several findings are drawn.

THE WMLES APPROACH AND VALIDATION

The present work mainly uses a wall-modelled large eddy simulation (WMLES) approach under a hybrid RANS-LES framework. The formulation starts from the governing Navier-stokes equation with the Favre average, which can be written in tensor form as in **Eq. 1**:

$$\begin{gathered}\frac{\partial\bar{\rho}}{\partial t}+\frac{\partial\bar{\rho}\tilde{u}_j}{\partial x_j}=0\\ \text{e}\ \frac{\partial\bar{\rho}\tilde{u}_i}{\partial t}+\frac{\partial\bar{\rho}\tilde{u}_i\tilde{u}_j}{\partial x_j}+\frac{\partial\bar{p}}{\partial x_i}=\frac{\partial\bar{\tau}_{ij}}{\partial x_j}-\frac{\partial\tau_{ij}^{sgs}}{\partial x_j}\\ \frac{\partial\bar{\rho}\tilde{E}}{\partial t}+\frac{\partial\left(\bar{\rho}\tilde{E}+\bar{p}\right)\tilde{u}_j}{\partial x_j}=\frac{\partial\tilde{u}_i\tilde{\tau}_{ij}}{\partial x_j}-\frac{\partial\tilde{q}_j}{\partial x_j}-\frac{\partial\tilde{u}_i\tau_{ij}^{sgs}}{\partial x_j}-\frac{\partial q_j^{sgs}}{\partial x_j}\end{gathered}\tag{1}$$

where $(\bar{\bullet})$ terms as a filter operation and $(\tilde{\bullet})$ terms as the Favre filter, and the subgrid-scale (SGS) stress tensor and the viscous tensor can be written as in **Eq. 2**:

$$\begin{aligned}\tau_{ij}^{sgs}&=\bar{\rho}\left(u_iu_j-\tilde{u}_i\tilde{u}_j\right)\\ q_j^{sgs}&=\bar{\rho}\left(u_iT-\tilde{u}_i\tilde{T}\right)\end{aligned}\tag{2}$$

For the traditional LES approach, the SGS stress tensor is often computed via a so-called LES SGS model. Alternatively, for the present WMLES simulation, the traditional Smagorinsky subgrid-scale (SGS) model in LES is replaced with a hybrid one, which can be read as in **Eq. 3**:

$$\nu_t = f_D \min\left\{(Ky)^2, (C_{SMAG}\Delta)^2\right\}\sqrt{2S_{ij}S_{ij}}\tag{3}$$

where $K = 0.41$ is the von Karman's constant and $C_{SMAG} = 0.18$ is the SGS model constant, while the damping function is written as in **Eq. 4**:

$$f_D = 1 - \exp\left(-y^+/A^+\right), y^+ = \frac{yu_\tau}{\nu}, A^+ = 26\tag{4}$$

and the length scale is defined as in **Eq. 5**:

$$\Delta = \min\left(\Delta_x, \Delta_y, \Delta_z\right)\tag{5}$$

The idea of the above WMLES approach can be regarded as using the Prandtl mixing length model near the wall; whereas, away from the wall, it switches over to the Smagorinsky SGS model. Actually, from the model equation (**Eq. 1**), one can see that when $Ky \ll C_{SMAG}\Delta$, the model turns out the Prandtl mixing length assumption, while when $Ky > C_{SMAG}\Delta$, the model turns out the Smagorinsky SGS model. The above model can also be regarded as an alternative to the classical LES with the advantage of reducing the stringent and Reynolds number-dependent grid resolution requirements of the classical wall-resolved LES.

From the formulation, in the WMLES approach, the RANS portion of the model is only activated in the inner part of the logarithmic layer (at $y^+ < 15$–20) and the outer part of the boundary layer is covered by a modified LES formulation. Since the inner portion of the boundary layer is responsible for the Reynolds number dependency of the LES model, the WMLES approach can be applied at the same grid resolution to an ever-increasing Reynolds number, which can be seen as illustrated in **Figure 2**. As shown in the figure, with the increasing Reynolds number, small-scale eddies confined within the viscous sublayer (VS) would get smaller and smaller such that it is necessary to avoid resolving them by using the WMLES approach. However, even at that, it is worth pointing out that the WMLES is still time-consuming as one kind of time-accurate computation method, and it is necessary to involve high-performance computing during the whole computation procedure [9].

The numerical considerations here include a central difference scheme (which has low numerical dissipation and dispersion), second-order time accuracy, and explicit time integration with dual time stepping. Besides, the two-dimensional VM method is introduced during the procedure for the inflow turbulence generation [10], which seems quite important for an LES or WMLES calculation for practical use.

In order to validate the efficiency of the present WMLES approach, numerical computation for an adverse-gradient flat plate case taken from [11] is performed, and the results are compared with those from the direct numerical simulation (DNS).

The flow condition is at $U_\infty = 9m/s$ and $Re_L = 60000$. In **Figure 3**, the sketch of the computational grid for the case is shown, where a grid density 500 × 200 × 160 is used to ensure enough dense grid density for the case. In **Figure 4**, typical results from the WMLES approach are given. From **Figure 4A**, one can see that the WMLES approach can predict the unsteady flow features very well and can give a very comprehensive detail of

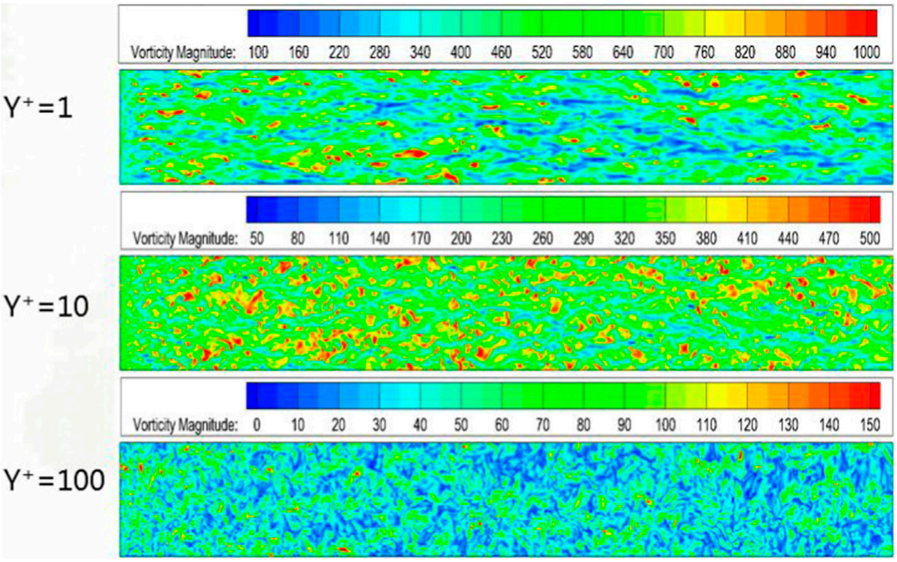

FIGURE 8 | Contours of vorticity magnitude at three typical $y^+ = 1$ locations for the base flow at $Re_\tau = 470$.

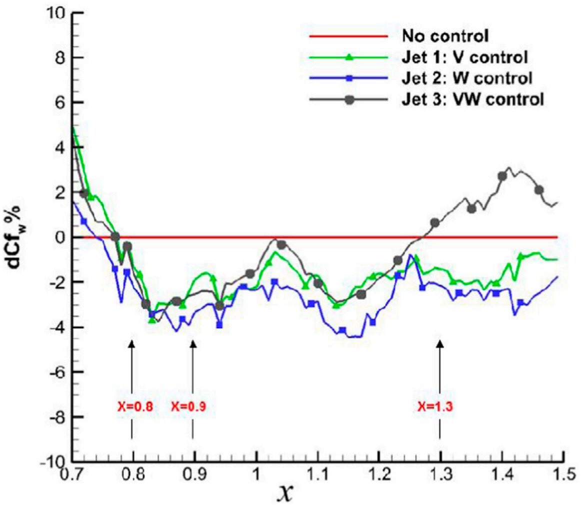

FIGURE 9 | The effect of different controls for drag reduction for the lower Reynolds number case at $Re_\tau = 470$.

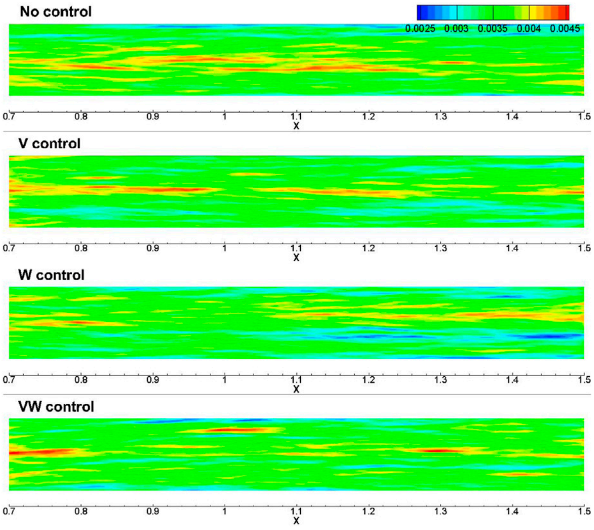

FIGURE 10 | Comparison of average skin friction for the lower Reynolds number case between base flow and controlled flow at $Re_\tau = 470$.

transient flow structures, which are coloured by velocity. **Figure 4B** shows that the present WMLES can give comparable results from DNS, which indicates that the WMLES can predict turbulence boundary layer very well, even with transition flow.

NUMERICAL RESULTS OF TBCL WITH FLUIDIC-JET ACTUATOR

Model Problems

In **Figure 5**, an illustration of the model problem of TBCL is shown. In the cases, a zero-gradient flat plate boundary layer with a length of 1.5 m is simulated as base flow, and six small span-wise rectangle slot holes are used to install fluidic-jet actuator arrays, which can take effect both for flow control in stream-wise and in span-wise. In the present study, all the fluidic-jet actuator arrays centre at $x = 0.6m$, which have a slot width of $h = 0.002m$, a slot length of $L = 0.05m$, and a slot spacing of $d = 0.012m$.

In the simulation, three different control strategies are investigated (as shown in **Table 1**), which are named "W-control," "V-control," and "VW-control." With such strategies, the fluidic-jet actuator can be modelled numerically by

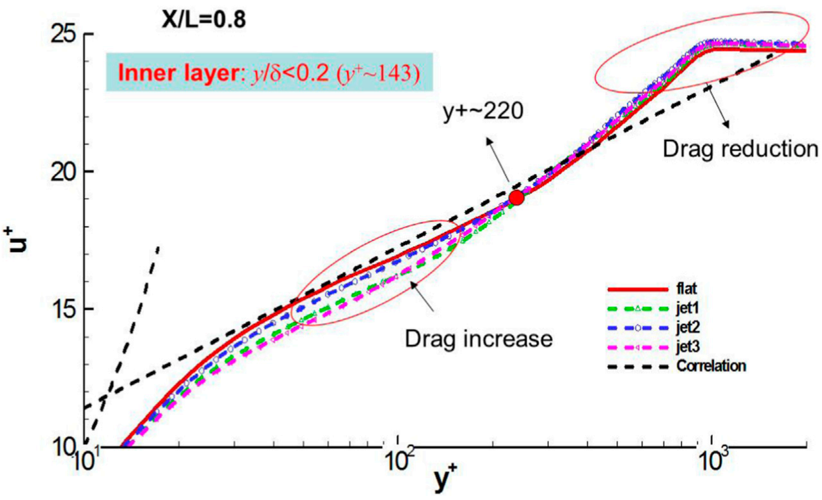

FIGURE 11 | Comparison of the velocity profile at a typical location, *x*= 0.8, between controlled flows and the base flow at $Re_\tau = 470$.

considering its specific application for the outer boundary layer control as in **Eq. 6**:

$$\begin{cases} v_{jet} = \dfrac{U_\infty}{2}\bullet \sin\theta\bullet \sin(2\pi\beta t) \\ w_{jet} = \dfrac{U_\infty}{2}\bullet \cos\theta\bullet \sin(2\pi\beta t) \end{cases} \tag{6}$$

where θ is the injection angle, and β is the actuating frequency. In the simulation, $\beta = 20Hz$ is used for all simulations of TBLC of the turbulent flat plane.

The computational condition for the model problem can be found in **Table 2**, where both a low Reynolds number at $Re_\tau = 470$ and a higher Reynolds number at $Re_\tau = 4700$ are considered with the same free stream condition at $U_\infty = 1.047m/s$ and the same inlet boundary layer thickness at $\delta = 0.058m$.

For the simulation, for the lower Reynolds number case, the grid with a total cell of around 13.9 million and grid density of $857 \times 117 \times 139$ is used to ensure enough dense grid density for the case, while for the higher Reynolds number case, the grid with a total cell of around 53.2 million and grid density of $1495 \times 177 \times 201$ is used.

Results for Low Reynolds Number Case at $Re_\tau = 470$

In **Figure 6**, a typical transient flow field coloured by streamwise velocity, *u*, both for the base flow and the

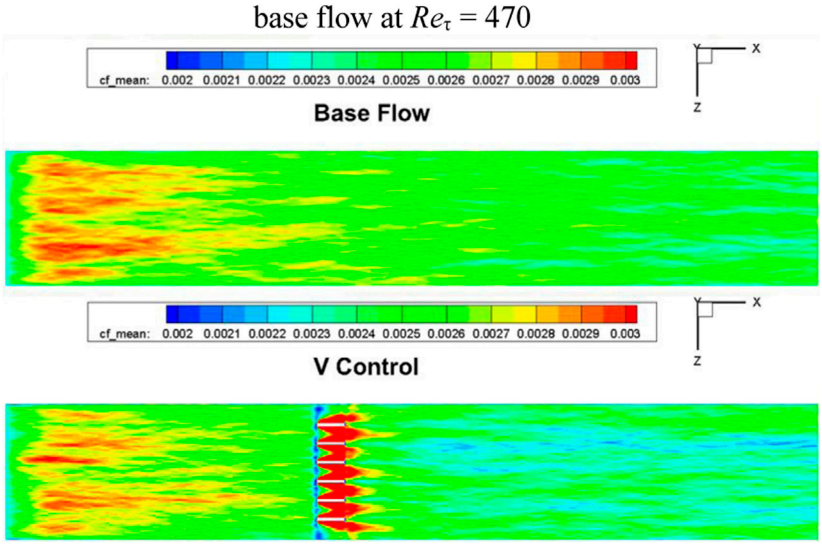

FIGURE 12 | Comparison of average skin friction for the higher Reynolds number case between base flow and controlled flow at $Re_\tau = 4700$.

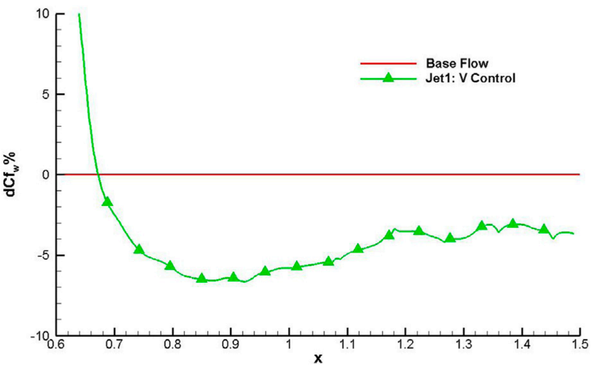

FIGURE 13 | Effect of "V-control" for drag reduction for the higher Reynolds number case at $Re_\tau = 4700$.

controlled flow (with "VW-control" strategy) at the same physical time is shown, where the Q-criterion = 200 is used to capture the large and small vortices structure of the turbulent boundary layer. From the results, one can conclude that a very clear and reasonable flow structure of the boundary layer of the present model problem can be obtained with the novel WMLES simulation.

In **Figure 7**, mean velocity profiles taken at four different locations, $x = 0.2$, $x = 0.4$, $x = 0.8$, and $x = 1.2$, from the base flow are further shown and compared with the classical empirical correlation formulation. From the figure, one can also see that all the numerical profiles given by WMLES agree with the theoretical formulation very well, which validates the present numerical approach. Besides, from the figure, since all the numerical profiles are almost identical, it partly shows that a fully developed turbulent boundary layer is achieved in the case. In **Figure 8**, contours of vorticity magnitude at three typical locations, $y^+ = 1$, $y^+ = 10$, and $y^+ = 100$, are further shown. The streaks and streamwise vortices within the boundary layer are evident.

In **Figure 9**, the effect of the three different control strategies for drag reduction for the lower Reynolds number case is investigated, where the local drag reduction (DR) rate is defined in **Eq. 7**:

$$dCf_w(\%) = \frac{C_f - C_{f,base}}{C_{f,base}} \times 100\% \tag{7}$$

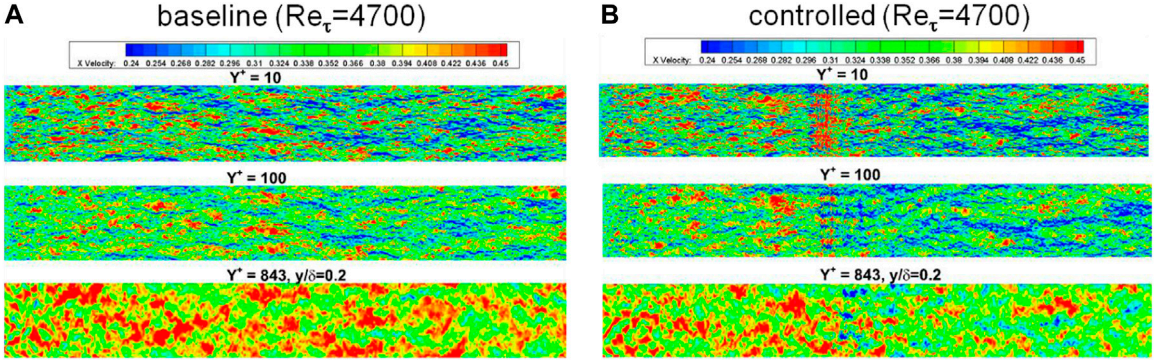

FIGURE 14 | Typical footprints with and without "V-control" at $Re_\tau = 4700$: **(A)** base flow; **(B)** controlled flow.

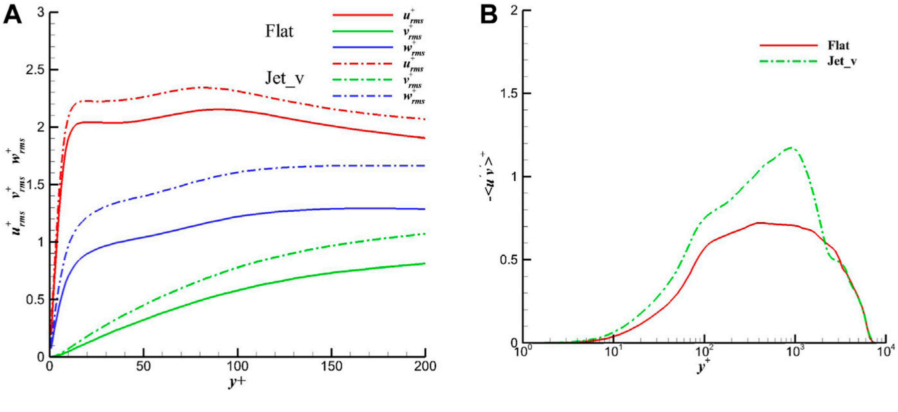

FIGURE 15 | u'_{rms}, v'_{rms}, w'_{rms}, and $< u'v' >$ plots with and without "V-control" at $Re_\tau = 4700$.

From the result, an averaged local DR rate at 2%–3% for all types of flow control behind the actuator array can be achieved, and comparably, the "V-control" strategy can achieve a robust drag reduction downstream. In **Figure 10**, the contour of the average skin friction behind the jet actuator array is further shown. From the figure, one can see that different levels of drag reduction can be achieved through present control strategies via micro jet-actuators array.

In order to analyse the origin targeting drag reduction with TBLC for these cases, in **Figure 11** gives comparisons of the velocity profile at a typical location, $x = 0.8$, between controlled flows and the base flow. From the figure, since the inner layer can be estimated to be around within $y^+ = 143$, one can find that for all these controlled cases, the inner layer would contribute to drag increase, while the outer layer would contribute to drag reduction. By contrast, the "V-control" strategy (marked as jet2) would achieve the smallest drag increase contribution from the inner layer. One can also conclude that since total drag reduction is achieved as shown in **Figure 9**, drag reduction is mainly contributed from the outer layer as we wanted.

Results for Higher Reynolds Number Case at Re_τ = 4700

Based on previous findings with different control strategies at the low Reynolds number case at $Re_\tau = 470$, the "V-control" strategy is further investigated for TBLC of the higher Reynolds number case at $Re_\tau = 4700$ in this section. In **Figure 12**, the comparison of the skin friction distribution between the base flow and the controlled flow is shown. It is found that, again, similar to the low Reynolds number case at $Re_\tau = 470$, an obvious drag reduction will be achieved for the present higher Reynolds number case at $Re_\tau = 4700$.

In **Figure 13**, the local DR rate through the present "V-control" strategy is compared. It is found that compared with the low Reynolds number case at $Re_\tau = 470$, a larger DR rate will be achieved at $Re_\tau = 4700$. The maximum DR rate is more than 6%, and the average DR rate is approximately 5%.

Mechanism Analysis for TBLC

As shown in **Figure 14**, a consequence of the control is a significant increase in the spanwise inter-streak distance, as determined from the spanwise two-point correlation, suggesting an increase in the scale of the near-wall streaks. Also, the control had a significant effect on the outer structures, in which the control weakened the streaky structure in the outer region.

Figure 15 shows u'_{rms}, v'_{rms}, w'_{rms}, and $< u'v' >$ plots with and without control. It can be seen that for all types of RMS, results from the controlled case are higher than those from the base flow. Therefore, it can be noticed that the control increases the RMS of velocities as well as the shear Reynolds stress. Besides, from the plot of u'_{rms} without control, one can clearly find two peaks.

Figure 16 further shows the plots of pre-multiple energy spectra for streamwise velocity at $x/c = 0.8$ with and without control. Again, two peaks, where one is the inner peak and another is the outer peak, which generally occurs only for high Reynolds number flow, can be found for both cases. For the base flow case, the inner peak, associated with the streaks, is at around $y^+ \sim 15$ with $\lambda^+ \sim 100$, which corresponds to the small-scale motion; meanwhile, the outer peak is at around $y^+ \sim 100$ with $\lambda^+ \sim 398$. With control, the inner maximum in the spectra moves to $y^+ \sim 39$ with $\lambda^+ \sim 170$, and the outer maximum to $y^+ \sim 794$ with $\lambda^+ \sim 630$. As such, one can conclude that present TBLC using a "V-control" strategy with jet-actuators array can result in the outer peak moving forward and result in the intensity of energy spectral increasing as well.

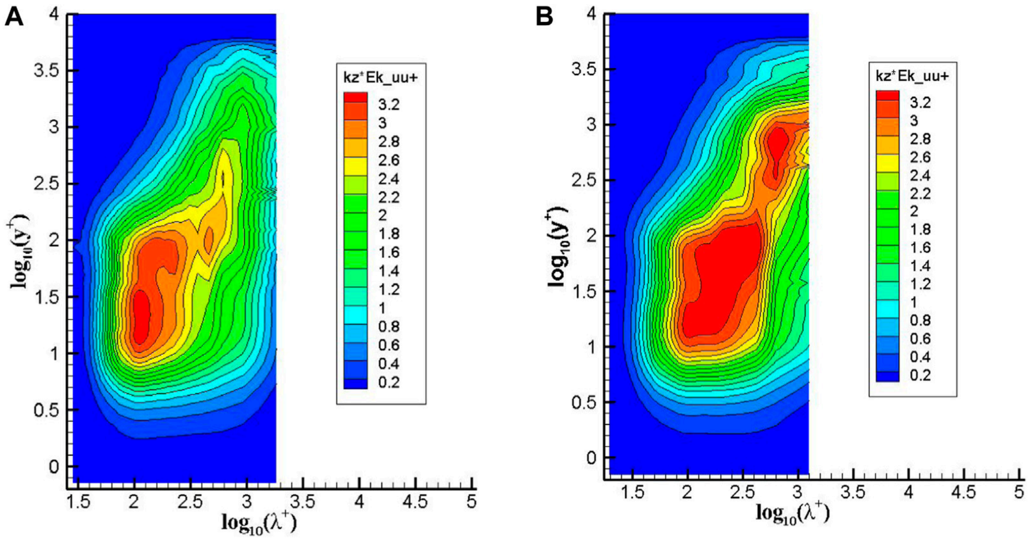

FIGURE 16 | Pre-multiple energy spectral for the streamwise velocity at x/c = 0.8 with and without "V-control" at Re_τ = 4700.

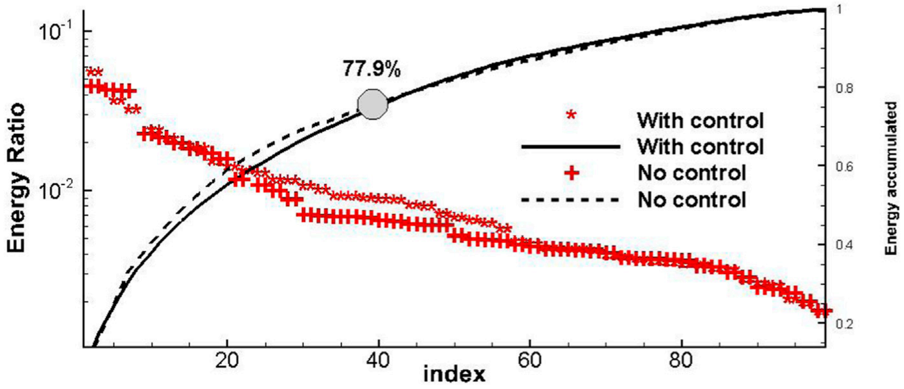

FIGURE 17 | DMD mode distribution at $y^+ = 15$ with and without "V-control" at $Re_\tau = 4700$.

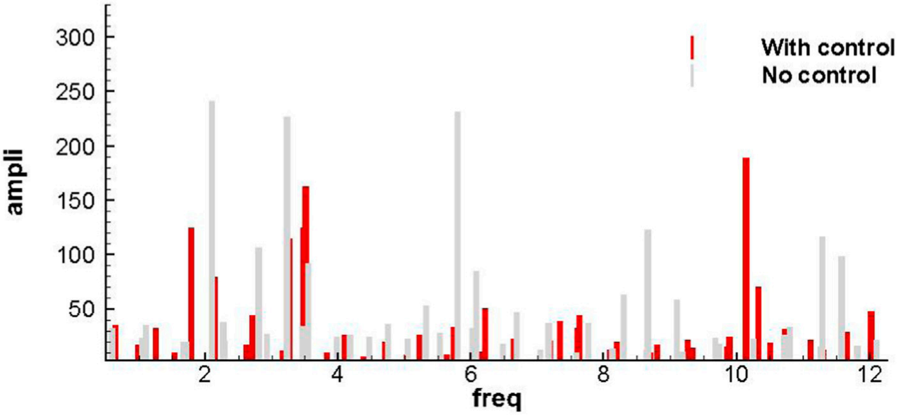

FIGURE 18 | Frequency-amplitude plot at $y^+ = 15$ with and without "V-control" at $Re_\tau = 4700$.

In order to further investigate the mechanics for drag reduction of the outer layer TBLC for the flat plate boundary layer, a parallel dynamic mode decomposition (DMD) approach is introduced to implement the analysis for the whole flow field [12], where the DMD modes can be ordered according to their contribution to the energy and then examine which frequencies are most influential in terms of the energy contribution. **Figure 17** shows energetically ordered distributions of DMD modes for both the canonical and controlled flows at the wall-normal plane $y^+ = 15$. As shown in the figure, approximately 40 modes are needed to recover around 78% of the energy. According to the plot of energy versus mode number, the difference between base flow and controlled flow is quite small. However, if we look at the plot of frequency versus amplitude for $y^+ = 15$ as shown in **Figure 18**, with jet injection, a reduction in the frequency of most energetically relevant modes is found. It seems to suggest that the injection increases the importance of large-scale structures, possibly by the injection creating such structures in the inner layer.

CONCLUSION

A wall-modelled LES (WMLES) approach combined with high-performance computing is presented for the numerical investigation of outer-layer turbulent boundary layer control for drag reduction through micro fluidic-jet actuators. The studies are performed on the classical zero-gradient turbulent flat plate cases, in which three different control strategies named "W-control," "V-control," and "VW-control" are used and compared to study the effects of drag reduction under a low Reynolds number at $Re_\tau = 470$ and a higher Reynolds number at $Re_\tau = 4700$. Both the pre-multiplied spectral method and a parallel dynamic mode decomposition (DMD) method are introduced for analysis of the mechanism of the outer-layer boundary layer control for drag reduction. From the results, several conclusions can be drawn as follows.

First, it can be marked that the WMLES approach presented in this paper combined with high-performance computing is an efficient way for an accurate prediction of the turbulent flat plate boundary layer.

Second, for the model problem of TBLC based on the zero-gradient flat plate boundary layer, the Reynolds number is an important factor. For the lower Reynolds number at $Re_\tau = 470$, an averaged local DR rate of around 2%–3% for all types of flow control behind the actuator array can be achieved, while for the higher Reynolds number at $Re_\tau = 4700$, an average local DR rate of around 5%–6% can be achieved.

Finally, both the pre-multiplied spectral method and the DMD analysis indicate that the outer-layer TBLC with fluidic-jet actuator can increase the importance of large-scale structures of the boundary layer such that the structures in the inner layer would be affected. The obvious uplift of Reynolds shear stress and turbulent kinetic energy distribution may be the main mechanism for drag reduction.

DATA AVAILABILITY STATEMENT

The original contributions presented in the study are included in the article/supplementary material, further inquiries can be directed to the corresponding authors.

AUTHOR CONTRIBUTIONS

The first author, LL, conceptualization, methodology, numerical computation, and draft writing. The second author, JW, conceptualization, data analysis, and draft reviewer. The third author, YL, conceptualization, data analysis, and draft reviewer. The fourth author, ZT, conceptualization, numerical computation. All authors contributed to the article and approved the submitted version.

FUNDING

This work is partially supported by the China-EU Cooperation project, DRAGY (grant number: 690623), and the Shaanxi Key Research and Development Program (grant number: 2022ZDLGY02-07).

CONFLICT OF INTEREST

The authors declare that the research was conducted in the absence of any commercial or financial relationships that could be construed as a potential conflict of interest.

REFERENCES

1. Ma HD. Drag Prediction and Reduction for Civil Transportation Aircraft. *Mech Eng* (2007) 29(2):1–8.
2. Valero E, Abbas A, Ferrer E. Drag Reduction Technology Review. In: *2nd GRAIN2 Open Workshop on "Greening Aviation – A Global Challenge"*. Xi'an, China: Chinese Aeronautical Establishment (2005).
3. Reneaux J. Overview on Drag Reduction Technologies for Civil Transport Aircraft. In: *European Congress on Computational Methods in Applied Sciences and Engineering*. Jyvaskyla, Finland: ECCOMAS (2004).
4. Obert E. *Aerodynamic Design of Transport Aircraft*. Delft, Netherlands: Delft University Press (2009).
5. Zhang JH, Li BH, Wang YF, Jiang N. Effects of Single Synthetic Jet on Turbulent Boundary Layer. *Chin Phys B* (2022) 31:074702. doi:10.1088/1674-1056/ac4bd0
6. Schueller M, Lipowski M, Schirmer E, Walther M, Otto T, Geßner T, et al. Integration of Fluidic Jet Actuators in Composite Structures. In: *Proc. SPIE 9431, Active and Passive Smart Structures and Integrated Systems*. San Diego, California, United States: SPIE (2015).943113
7. Abbas A, Bugeda G, Ferrer E, Fu S, Periaux J, Pons-Prats J, et al. Drag Reduction via Turbulent Boundary Layer Flow Control. *Sci China Technol Sci* (2017) 60(9):1281–90. doi:10.1007/s11431-016-9013-6
8. Pierre R, Martin S, Michael AL. A Review of Turbulent Skin-Friction Drag Reduction by Near-Wall Transverse Forcing. *Prog Aerospace Sci* (2021) 123: 100731.
9. Li L, Wu JS, Liang YH, Tian ZD. A Wall-Modeled Large Eddy Simulation Approach Based on Large Scale Parallel Computing for Post Stall Flow Over an Iced Airfoil. *J Northwest poly-technical Univ* (2023) 41(5):1–10.
10. Zhou L, Yang QS, Yan BW, Wang J, Van Phuc P. Review of Inflow Turbulence Generation Methods With Large Eddy Simulation for Atmospheric Boundary Layer. *Eng Mech* (2020) 37(5):15–25. doi:10.6052/j.issn.1000-4750.2019.06.0340
11. Wissink J, Rodi W. Direct Numerical Simulations of Transitional Flow in Turbomachinery. *J Turbomach* (2006) 128:668–78. doi:10.1115/1.2218517
12. Tan WW, Bai JQ, Tian ZD. Parallel Dynamon for Rayleigh-Taylor Instability Flows. In: *Asia-Pacific International Symposium on Aerospace Technology*. Chendu, China: Springer (2019).

AEROSPACE RESEARCH COMMUNICATIONS
ORIGINAL RESEARCH
published: 24 January 2024
doi: 10.3389/arc.2024.12444

Numerical Optimization on Aircraft Wake Vortex Decay Enhancement

*Ziming Xu and Dong Li**

School of Aeronautics, Northwestern Polytechnical University, Xi'an, China

Blowing air at the end of the airport runway can accelerate the decay of the near-ground aircraft wake vortex, thereby reducing the negative impact of the vortex on the following aircraft. However, the benefits of accelerating wake dissipation vary for different blowing parameters, so it is necessary to set appropriate parameters in order to obtain better acceleration results. Because of the high cost of traditional optimization methods, this research uses a Kriging surrogate model to optimize the blowing parameters. The results show that the current optimization algorithm can deal with the global optimization problem well. After obtaining 205 sample points, the response surface model of the blowing parameters and blowing yield was accurately established. A relatively optimal parameter setting range was given, and numerical simulation shows that the current parameter setting can obtain improved benefits from accelerated vortex dissipation. In addition, since the optimization process is partially dimensionless, the above optimization results can be used to achieve multi-objective design, that is, the same set of blowing devices can efficiently accelerate the dissipative process of the tail vortices of different aircraft types, thus improving the engineering feasibility of the current blowing method.

Keywords: active flow control, aircraft wake vortex, multi-objective design, Kriging, CFD

INTRODUCTION

Wake Vortex Hazards

The lift of an aircraft originates from the interaction between the aircraft and the air. While the aircraft gains lift, the air will flow along the wing spanwise and form high-intensity aircraft wake vortices at the wingtips, which may lead to sudden lift loss or uncontrollable rolling for the trailing aircraft, with fatal effects. Due to the presence of the ground, the primary vortex induces secondary vortices, which have the opposite sign of vorticity and may drive the primary vortex rebound to the flight altitude [1]. Although the near-ground aircraft wake vortex pair will gradually move away from the flight path due to the induction of the mirror vortex, a crosswind with specific strength (e.g., when the height of the wake vortex is 1 b_0 and the crosswind speed is 0.5 ω_0) compensates for this speed, resulting in the upwind vortex staying in the flight path for an extended period of time [2, 3].

In order to ensure the flight safety of civil aircraft, the existing measure is to control the flight distance between two adjacent approaching aircrafts. For instance, the International Civil Aviation Organization (ICAO) regulations ensure that when the preceding and following aircraft are heavy or medium types, the wake separation of the aircrafts should be 9.3 km [4], which corresponds to a time interval of more than 2 min. This method is certainly effective, but it also greatly restricts the growth of airport traffic, and when there are extremely unfavourable meteorological conditions for wake vortex dissipation, the current regulations still cannot guarantee the safety of the following aircraft.

***Correspondence**
Dong Li,
ldgh@nwpu.edu.cn

Received: *19 November 2023*
Accepted: *05 January 2024*
Published: *24 January 2024*

Citation:
Xu Z and Li D (2024) Numerical Optimization on Aircraft Wake Vortex Decay Enhancement. Aerosp. Res. Commun. 2:12444. doi: 10.3389/arc.2024.12444

Methods on Wake Alleviation

Researchers have proposed three methods for wake vortex control. The first method, Low-Vorticity-Vortex (LVV), reduces the induced roll moment on the following aircraft by redistributing the load of the preceding aircraft [5, 6]. The second method, the Quickly-Decaying-Vortex (QDV), seeks to trigger stronger instability for the vortex pair by exerting perturbations [7, 8] or by constructing a multi-vortex system [9–11]. Numerical simulations and wind tunnel experiments have proved such improvements effective, at least within ten times the wingspan of the aft fuselage [6]. However, both of these methods require modifications on aircrafts themselves, which might negatively affect the flight performance.

The third method hopes to accelerate vortex pair dissipation by applying perturbations to the wake vortices after their roll-up process. Cho et al. proposed to configure the relative positions of the preceding and following aircraft so that their wake vortices would interact and dissipate into harmless turbulence more quickly [12]. Nevertheless, this method is only suitable for vortices at a relatively high altitude and requires a precise prediction of the position of the preceding wake vortex. The acceleration of aircraft wake dissipation by ground-based equipment was first proposed by Kohl. His wind-tunnel experiments confirmed the effectiveness of these methods [13]. Stephan et al. quantitatively investigated the ground obstacles effects on in-ground-effect (IGE) wake vortex, with Large Eddy Simulation (LES) and towing tank experiments. They found that the hairpin vortices generated by ground obstacles entangle the primary and secondary vortices together, which ultimately advance the rapid decay to a large extent [14]. In addition, numerical simulations and field measurements have demonstrated that impressive acceleration results can still be obtained after simplifying the columnar obstacle into a flat plate array [15, 16]. In 2020, field experiments at Vienna International Airport further confirmed the effectiveness of this approach: the use of flat plate arrays reduced the wake vortex lifespan by 21%–35% [17]. But as the obstacles placed near the runway are large in size ($0.2b_0 \times 0.2b_0$), navigation equipment might be influenced.

Present Study

To overcome the limitations of above methods, we investigated the effect of ground blowing on wake vortex dissipation. As an active flow control method, this strategy is able to reduce the lifespan of the IGE wake vortex without affecting flight safety. Numerical simulations indicated that although the direct effect of the blowing airflow on the vortices is limited, the starting vortex produced by the blowing air can develop into a hairpin vortex, inducing the interference between the primary and secondary vortices, and thus accelerating the wake dissipation [18]. Further, we have also investigated the blowing effect in crosswind conditions and screened for optimal blowing parameters [19].

Although increasing the blowing zone area and blowing velocity improves the blowing effect, maintaining a large flow rate consumes a huge amount of energy. With restrictions to the blowing flux and blowing zone area, a better choice—and the aim of this study—is to find a set of blowing zone parameters that can best enhance the wake decay through the blowing process. Since there is no analytical function between the blowing parameters and blowing effect, it is difficult to find an explicit optimal solution. On this basis, a surrogate model was adopted to approximate the relationship between blowing parameters and blowing effect. Different blowing aspect ratios and positions were tested. A rich number of sample points were used to establish the response surface, so that the optimal design of the blowing parameters could be estimated.

The structure of this paper is as follows: the first section introduces the research background; the second section introduces the numerical method adopted, the third section introduces and validates the surrogate optimization method; the fourth section demonstrates the optimization results; the fifth section presents the optimization settings for different aircraft types, and the final section is the summary.

NUMERICAL BACKGROUNDS

Turbulence Modelling

The numerical simulation in this paper was conducted by solving the incompressible Navier-Stokes equation. The finite volume method was used for spatial discretization. In order to capture the eddies in the flow, the Large Eddy Simulation (LES) method was used for turbulence modelling. The filtered incompressible Navier-Stokes equation can be written as **Equations 1, 2**:

$$\frac{\partial \bar{u}_i}{\partial x_i} = 0 \tag{1}$$

$$\frac{\partial \bar{u}_i}{\partial t} + u_j \frac{\partial \bar{u}_i \bar{u}_j}{\partial x_j} = -\frac{1}{\rho}\frac{\partial \bar{p}}{\partial x_i} + \nu \frac{\partial^2 \bar{u}_i}{\partial x_j \partial x_j} + \frac{\partial \bar{\tau}_{ij}}{\partial x_j} \tag{2}$$

where x_i and u_i represent the coordinates and the corresponding velocity components in the Cartesian coordinate system, respectively; p, ρ, t, and ν represent the pressure, density, time, and kinematic viscosity (molecular kinematic viscosity), respectively. $\bar{\tau}_{ij} = \bar{u}_i \bar{u}_j - \overline{u_i u_j}$ is the sub-grid stress. It could be modelled as $\bar{\tau}_{ij} = 2\nu_t \bar{S}_{ij} - \frac{1}{3}\bar{\tau}_{kk}\delta_{ij}$, where ν_t is the sub-grid viscosity and $\bar{S}_{ij} = \frac{1}{2}\left(\frac{\partial \bar{u}_i}{\partial x_j} + \frac{\partial \bar{u}_j}{\partial x_i}\right)$. Note that $\nu = 0.023\mathrm{m}^2/\mathrm{s}$ ($Re_{\Gamma,\mathrm{A340}} = \Gamma_0/\nu = 23144$) was adopted in this study to allow a wall-resolved LES simulation. An existing study has proven that no significant distinction exists between wake decay mechanism at $Re_\Gamma = 23144$ and in real flight [15]. The sub-grid viscosity mentioned in $\bar{\tau}_{ij}$ was solved using the dynamic Smagorinsky-Lilly sub-grid model [20]. Specifically, the local Smagorinsky coefficients were obtained by spatially averaging over the considered cell and its neighboring cells during the computation.

The SIMPLE algorithm was used in the calculations to handle the pressure-velocity coupling, with both convective and diffusive terms discretized using the second-order central difference scheme. The unsteady term was advanced using the second-order implicit scheme.

Boundary and Initial Conditions

In this study, the wake vortices of two types aircraft were considered, and the parameters are listed in **Table 1**. The characteristic time and time were obtained by $\omega_0 = \Gamma_0/2\pi b_0$ and $t_0 = b_0/\omega_0$. The length,

TABLE 1 | Wake vortex parameters of A340 and A380.

Aircraft type	Initial circulation (Γ_0, m^2/s)	Initial vortex spacing (b_0, m)	Characteristic velocity (ω_0, m/s)	Characteristic time (t_0, s)
A340	530	47.4	1.7796	26.63
A380	825	62.6	2.0975	29.85

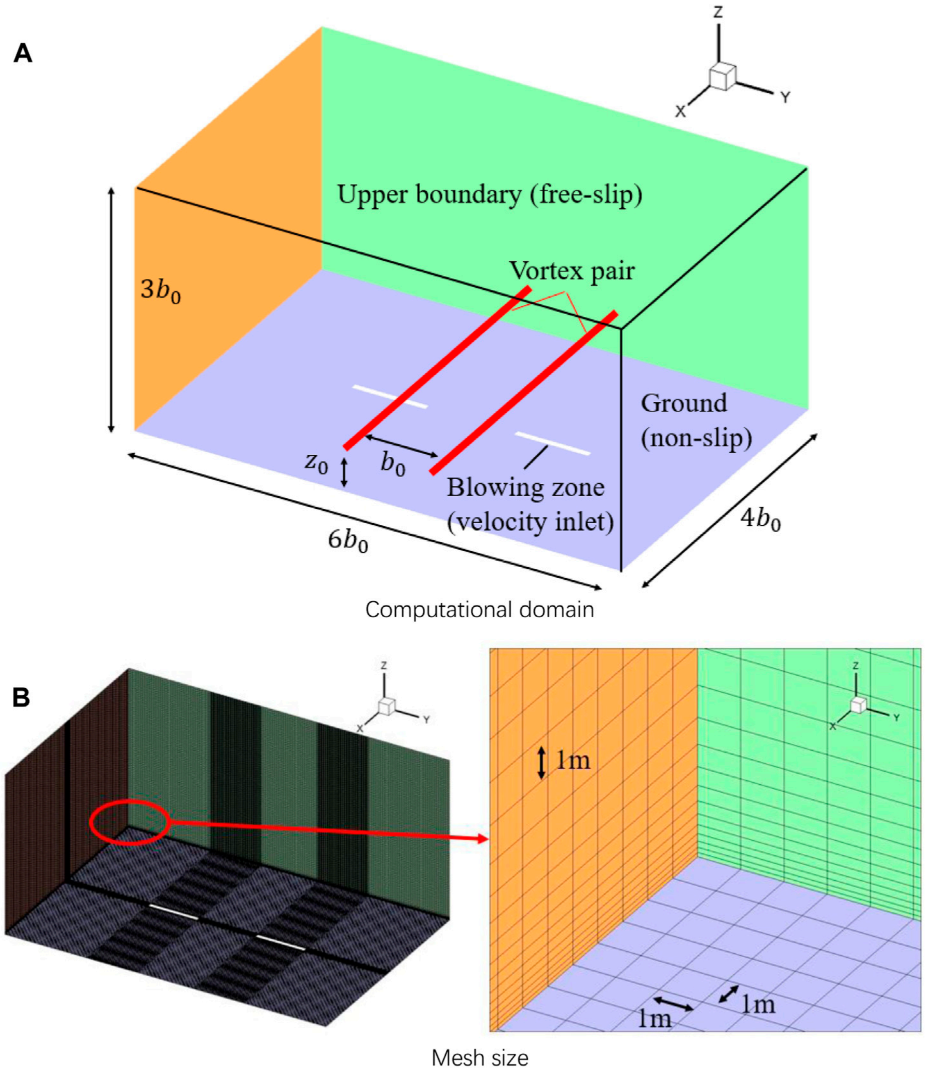

FIGURE 1 | Schematic of the computational domain. **(A)** Computational domain, **(B)** Mesh size.

velocity, time, and vortex circulation were non-dimensionalized using the initial values as $x^* = x/b_0$, $y^* = y/b_0$, $z^* = z/b_0$, $u^* = u/\omega_0$, $v^* = v/\omega_0$, $w^* = w/\omega_0$, $t^* = t/t_0$, and $\Gamma^* = \Gamma/\Gamma_0$.

Figure 1 shows the computational domain of the LES simulations ($L_x \times L_y \times L_z = 4b_0 \times 6b_0 \times 3b_0$). Periodic conditions were applied to x and y boundaries. The bottom of the domain is a non-slip boundary while the top is a free-slip wall. To model the blowing flow, velocity inlet conditions were applied to the blowing zone.

The height of the first layer of the mesh near the ground is 0.1 m ($z^+ \approx 1$) with a growth rate of 1.2, and the mesh size along all three directions are 1 m. Consequently, the total cell numbers for A340 and A380 wake simulations are 12 million and 24 million, respectively. A timestep of $dt = 0.01$ s was employed in all the simulations, corresponding to a non-dimensional timestep of $3.76 \times 10^{-4} t_0$ and $3.35 \times 10^{-4} t_0$ for A340 wake and A380 wake, respectively. Besides, 3.4 t_0 of wake evolution was simulated in this study, corresponding to 90 s and 102 s for A340 wake and A380 wake, respectively.

The wake vortex pairs were initialised using the Lamb-Oseen model, which describes the velocity field as **Equation 3**:

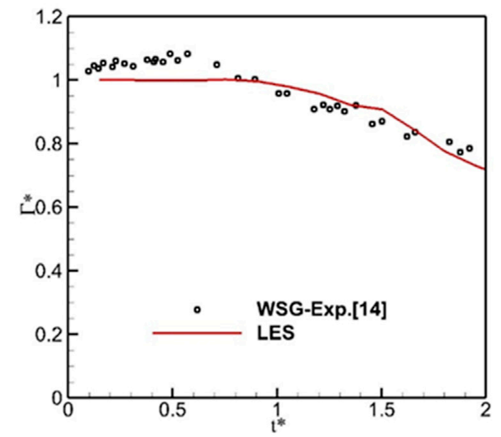

FIGURE 2 | Vortex circulation evolution, CFD vs. Exp.

$$V_\theta(r) = \frac{\Gamma_0}{2\pi r}\left(1 - \exp\left(\frac{-r^2}{r_c^2}\right)\right) \tag{3}$$

r and r_c represent the distance to the vortex center and the vortex core radius, respectively. According to the Class II airport operating standard, the topographic relief height should be less than 1 m within 300 m of the end of the runway. Therefore, the blowing zone is placed 300 m away from the end of the runway. This corresponds to $z_0 = 31\text{m}$ of the initial wake vortex height [19]. It is highlighted that the non-dimensional initial vortex altitudes for A340 and A380 are different, resulting in a partial non-dimensional optimization in *Optimization for Enhanced Wake Vortex Decay* section.

Methods Validation

To validate the numerical methods, a numerical simulation was performed and the result was compared with the water-tank experiment data [14]. In the validation, the wake vortex of A340 was employed and the initial vortex height was reduced to $z_0 = 0.5\ b_0$ to match the experiment setup. Other parameters such as timestep and mesh size remain the same as *Boundary and Initial Conditions* section.

To evaluate the vortex strength decay history, the vortex centre was tracked by considering the local minimum pressure and the extreme vorticity values first. After that, the vortex circulation on a specify axial plane was obtained by **Equation 4**:

$$\Gamma_{5-15} = \frac{1}{11}\sum_{d=5m}^{15m}\int_0^d \omega\, dA \tag{4}$$

where $\int_0^d \omega dA$ represents the integration of axial vorticity over the circular region with a radius of d [14]. Finally, the circulation values were averaged along several axial planes.

Figure 2 shows the comparison between the CFD result and the experimental data. Before $t^* < 0.5$, the circulation in the simulation remains constant while the circulation in the experiment exhibits a slow growth. This is due to the roll-up process of the vorticity sheet generated by the wing model, even though the circulation curve of CFD shows similar trend after $t^* = 1$ and agrees with the experiment data well. Thus, current numerical methods will be adopted in following studies.

OPTIMIZATION METHOD

Kriging Surrogate Model

Surrogate models, also known as response surface models, are approximate mathematical tools used as an alternative to complex numerical analysis, which reduce the difficulty of the optimization process. By learning from the sample data, the computer trains and fits a function mapping the relationship between the design parameters and the corresponding objective values that satisfy a certain accuracy range [21, 22]. The upper and lower bounds of the design variables X determine the design space, and the initial data set is $X = X_1, X_2, \ldots, X_{np}$, where np is the amount of the design variables, letting the unknown function between the response value Y and the design variables X be **Equation 5**

$$Y = f(X) \tag{5}$$

In the Kriging surrogate model, the actual function Y is expressed as **Equation 6**:

$$Y = f(X) + Z(X) \tag{6}$$

$f(X)$, also written as β, is acquired with the sample points, it represents the global approximation to the design space; $Z(X)$ is a random function with a mean of 0 and a variance of σ^2, representing the deviation from the global approximation, its covariance matrix is expressed as **Equation 7**:

$$Cov\left[Z(x^i), Z(x^j)\right] = \sigma^2 \boldsymbol{R}R(x^i) \tag{7}$$

$\boldsymbol{R}$ is the correlation matrix. $i = 1, 2, 3 \ldots n_s$ represents the number of the samples. The Gauss function was chosen as the correlation function, R. The estimation of response value $Y(X)$ at an arbitrary point X is given by **Equation 8**:

$$\hat{Y} = \hat{\beta} + r^T(X)\boldsymbol{R}^{-1}\left(Y - f\hat{\beta}\right) \tag{8}$$

The superscript T means the transposition of a matrix. r^T is the correlation vector between X and the sample points, $\hat{\beta}$ and $\hat{\sigma}$ are expressed as **Equations 9**, **10**:

$$\hat{\beta} = \left(f^T\boldsymbol{R}^{-1}f\right)^{-1} f^T\boldsymbol{R}^{-1}Y \tag{9}$$

and

$$\hat{\sigma}^2 = \frac{\left(Y - f\hat{\beta}\right)^T\boldsymbol{R}^{-1}\left(Y - f\hat{\beta}\right)}{n_s} \tag{10}$$

Infill-Sampling Criteria

A parallel infill-sampling criteria combing two criteria was used to better approximate the real function. The first criterion, minimizing surrogate prediction (MSP), selects the minimum of the objective function obtained by the current surrogate model

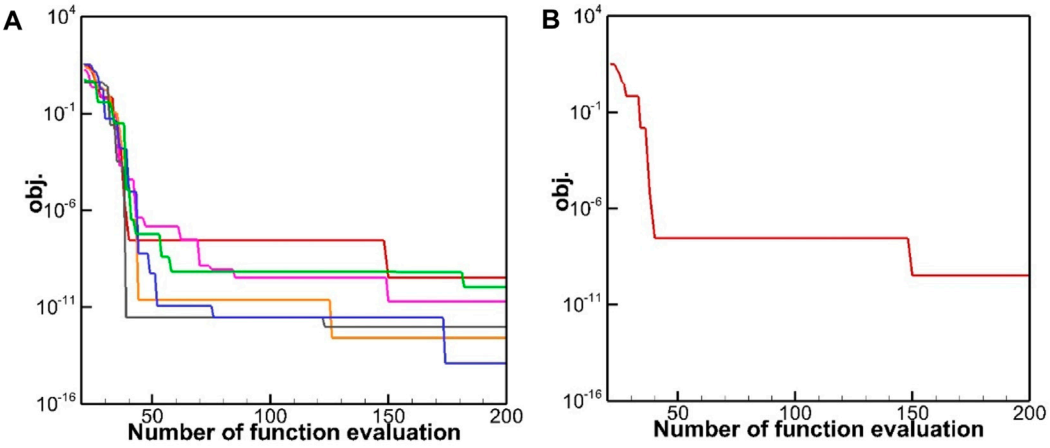

Convergence histories of 6 optimizations

Average convergence histories of 30 optimizations

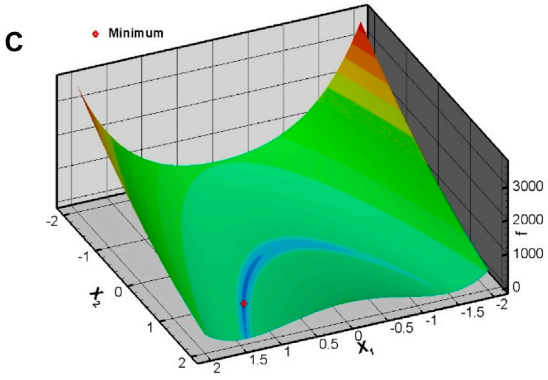

Schematic of Rosenbrock function

FIGURE 3 | Rosenbrock function and the convergence history. **(A)** Convergence histories of 6 optimizations, **(B)** Average convergence histories of 30 optimizations, **(C)** Schematic of Rosenbrock function.

as the new sample point [23, 24]. The MSP sub-optimization problem with constraints can be written as **Equation 11**

$$\begin{gathered}\operatorname{Min} \hat{Y}(X) \\ \text{s.t.} \begin{cases} \hat{g}_i(X) \le 0 \; i = 1, 2, \ldots, n_c \\ X_l \le X \le X_u \end{cases}\end{gathered} \tag{11}$$

$\hat{g}_i$ is the constraint function, and n_c is the number of constraints. The subscripts, l and u, represent the lower bound and upper bound, respectively.

The second infill-sampling criteria, expected improvement (EI), is also known as the efficient global optimization algorithm [25]. The standard EI function can be written as **Equation 12**:

$$\mathrm{E}[\mathrm{I}(X)] = \begin{cases} \left(Y_{min} - \hat{Y}\right)\Phi\left(\dfrac{Y_{min} - \hat{Y}}{s}\right) + s\phi\left(\dfrac{Y_{min} - \hat{Y}}{s}\right) & s > 0 \\ 0 \; s = 0 \end{cases} \tag{12}$$

Y_{min} is the current minimum of the objective function. Suppose the function values predicted by the model at the measured points follow a normal distribution, then $\hat{Y}$ is the predicted mean value, and $s(X)$ is the standard deviation. Φ and ϕ are standard normal distribution function and standard normal distribution probability density function, respectively.

In this study, the gradient optimization is combined with the Kriging surrogate model to conduct the optimization process. To be specific, the optimization process consists of the following steps:

1) initial sample points are chosen with the Latin hypercube sampling method and the functional responses are evaluated by CFD solver;
2) initial surrogate models for the objective and constraint functions are constructed based on the current samples;
3) parallel infill-sampling criteria combing the EI and MSP criterion is conducted to obtain new sample points, and the corresponding response values are obtained using CFD;
4) the surrogate model is updated, and the sub-optimization process is performed based on it;
5) steps 3 and 4 are repeated until the termination condition is satisfied.

Benchmark Analytical Test Cases

To validate the above-mentioned optimization framework, three analytical test cases were used.

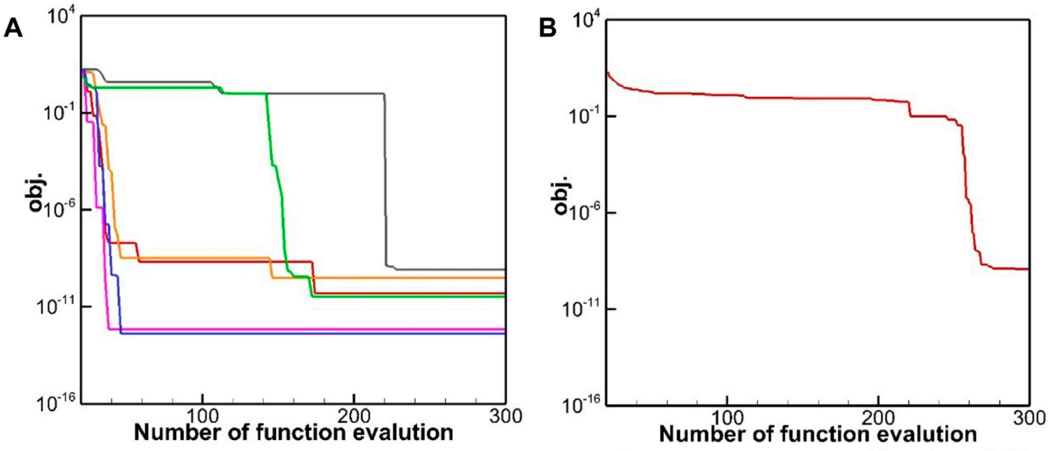

Convergence histories of 6 optimizations

Average convergence histories of 30 optimizations

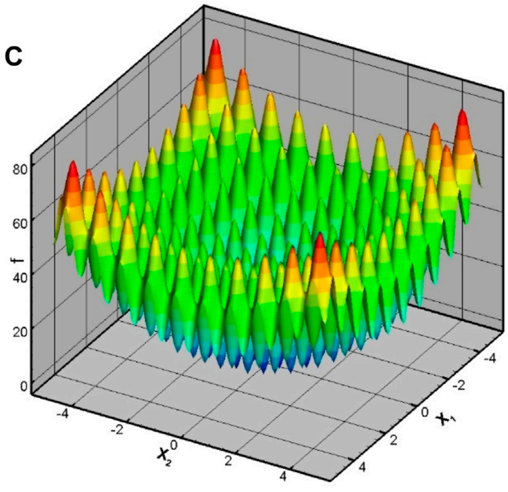

Schematic of Rastrigin function

FIGURE 4 | Rastrigin function and the convergence history. **(A)** Convergence histories of 6 optimizations, **(B)** Average convergence histories of 30 optimizations, **(C)** Schematic of Rastrigin function.

Rosenbrock Test Case

The Rosenbrock function has a minimum that lies in a "flat valley" (**Figure 3C**), around which the gradient value is small [24]. Thus, this case assessed the local optimization capability of the algorithm. The Rosenbrock function is expressed as **Equation 13**:

$$\begin{gathered}\text{Min } f(X_1, X_2) = (1.0 - X_1)^2 + 100.0\left(x_2 - {X_2}^2\right)^2 \\ \text{s.t. } X_1, X_2 \in [-2.0, 2.0]\end{gathered} \tag{13}$$

The optimization was performed 30 times and **Figure 3** shows the convergence histories. In all calculations, when the number of the function evaluations (NFE) reaches 100, the predicted minimum of the function drops to the order of 10^{-8}, and when NFE is 200, the predicted minimum of the function drops below 10^{-10}. In particular, the best predicted value is close to 10^{-14}, which proves that the algorithm performs well in local optimization problems.

Rastrigin Test Case

Rastrigin function is written as [22] **Equation 14**:

$$\begin{gathered}\text{Min } f(X_1, X_2) = 20 + {X_1}^2 + {X_2}^2 - 10(\cos 2\pi X_1 + \cos 2\pi X_2) \\ \text{s.t. } X_1, X_2 \in [-5.0, 5.0]\end{gathered} \tag{14}$$

The optimal solution of the Rastrigin function is $f(0, 0) = 0$, while there exist multiple minima in the feasible region (**Figure 4C**). For instance, in other positions such as $(1, 0)$, $(1, 1)$, and $(2, 0)$, the minimum values obtained by the function are 1, 2, and 4, respectively. **Figure 4A** shows the convergence histories of six rounds of optimization. Note the sudden drops in the convergence curves, these imply that the local minimum region of $f(0, 0)$ is found, and only local optimization is needed. However, it must be highlighted that the probing of the global minimum is a random process which might take hundreds of function evaluations. As the average convergence curve in **Figure 4B** drops to the order of

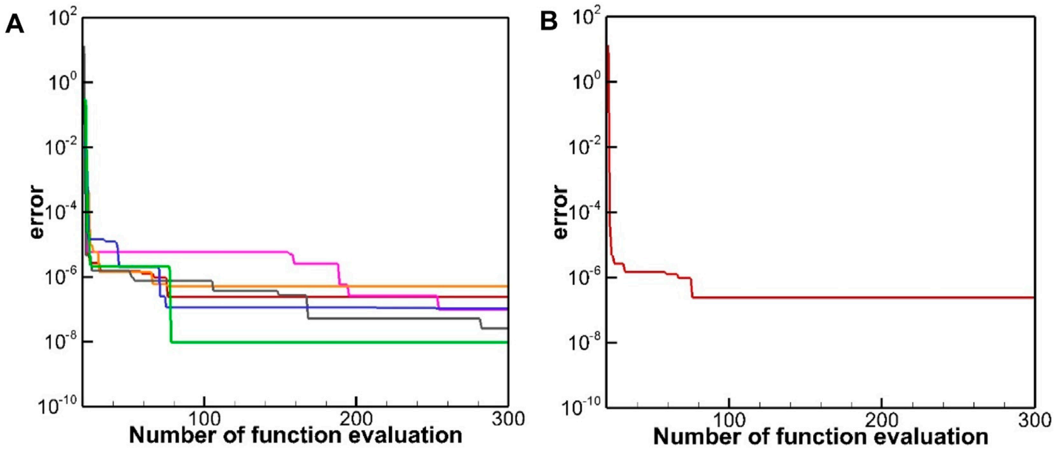

Convergence histories of 6 optimizations

Average convergence histories of 30 optimizations

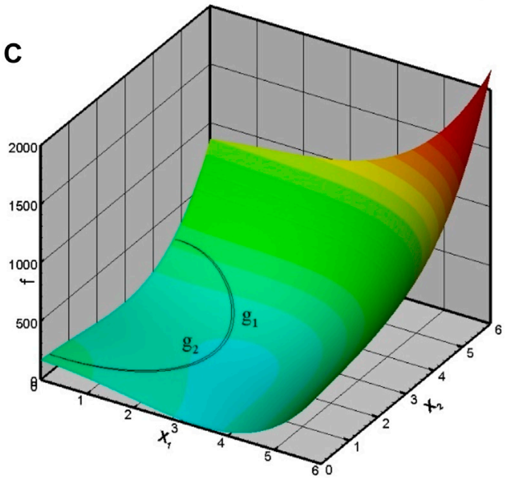

Schematic of the objective function

FIGURE 5 | Function of test case 3 and the convergence history. **(A)** Convergence histories of 6 optimizations, **(B)** Average convergence histories of 30 optimizations, **(C)** Schematic of the objective function.

10^{-8}, all the 30 rounds of optimization end when the global minimum is found, implying that the current algorithm has powerful global optimization capability.

Constraint Handling Test Case

In this case, two constraints are applied. As shown in **Figure 5C**, the feasible region is a narrow interval between the constraints, and the minimum of the objective function lies approximately in the middle of the feasible region. The optimization problem is described as [25] **Equation 15**:

$$\begin{aligned} \text{Min}\,.\, f(X_1, X_2) &= \left(X_1^{\,2} + X_2 - 11\right)^2 + \left(X_1 + X_2^{\,2} - 7\right)^2 \\ \text{s.t. } g_1(X_1, X_2) &= 4.84 - (X_1 - 0.05)^2 - (X_2 - 2.5)^2 \geq 0 \\ g_2(X_1, X_2) &= X_1^{\,2} + (X_2 - 2.5)^2 - 4.84 \geq 0 X_1, X_2 \in [0, 6] \end{aligned} \tag{15}$$

Before optimizing, it was checked to ensure that all the initial sample points lie within the feasible region. When using the logarithmic barrier method, the optimization problem can be rewritten as **Equation 16**:

$$\begin{aligned} \text{Min}\,.\, F(X_1, X_2) &= f(X_1, X_2) \\ &\quad - \mu\left[\ln\left(g_1(X_1, X_2)\right) + \ln\left(g_2(X_1, X_2)\right)\right] \end{aligned} \tag{16}$$

where $\mu = c\mu_0$ is the dynamic penalty factor with $c = 0.1$. During the optimization progress, μ approaches zero gradually, and the unconstrained optimization problem converges to the original constrained optimization problem. **Figure 5B** shows that before the number of the function evaluations reaches 50, the optimization error has decreased to an order of 10^{-5}. The best result exhibits an error of an order of 10^{-8} in **Figure 5A**.

In summary, the current algorithm combing the Kriging surrogate model and the gradient optimization method is able to deal with both constrained and unconstrainted problems, and will be used for the subsequent study.

OPTIMIZATION FOR ENHANCED WAKE VORTEX DECAY

Before the optimization, the enhancement of wake vortex decay by active flow control method will be introduced briefly. Two rectangular blowing zones were equipped symmetrically about the runway central line, at the end of the runway. When air flows (blowing) vertically from the blowing zones, starting vortices are generated at the edges of the rectangular zones. At the same time, secondary vortices are induced and roll up inhomogeneously, due to the presence of the blowing air. Naturally, these vortical structures interact and develop into a hairpin like vortex (Ω vortex) and loop around the primary vortex fast. Under the self-induction effect, the vortex loop extends along the flight direction, interacting with the primary vortex intensely and leading to rapid dissipation of the aircraft wake vortex [18]. It is highlighted that the blowing process was modelled by applying velocity boundary conditions at the blowing zones to simplify the simulation. Therefore, the depth of the blowing zone was not considered. The definition of a blowing zone could be found in **Figure 7**, the aspect ratio is defined as $AR = length/width$, where $width = area/length$. It was found that the blowing effect is improved by an increasing blowing velocity and blowing zone area [18]. Therefore, it is believed that the optimization on blowing velocity and zone area is not necessary. In this study, the blowing zone area was fixed at $0.04b_0^2$, and blowing velocity of ω_0 was adopted [18].

The wake vortex of A340 is considered in this section, the detailed vortex parameters are listed in **Table 1**, and the initial vortex altitude is $z_0^* = 0.654$ ($z_0 = 31$ m). The time step of the simulation is 0.01s ($3.76 \times 10^{-4} t_0$) and 90s ($3.4\ t_0$) of wake evolution is simulated. The blowing zone area is $0.04b_0^2 = 89.87\text{m}^2$, and the blowing velocity is $\omega_0 = 1.7796$ m/s. With a fixed blowing area, the parameters that affect the enhancement are blowing zone aspect ratio (AR, determined by the blowing zone length) and blowing zone position (P). Thus, our aim in this section is to find the optimum selection of AR and P and obtain the best enhancement effect.

Vortex circulation at an axial position is generally used to evaluate the vortex strength. However, instantaneous circulation is affected by many random factors and is unrepresentative for the entire wake decay process. Therefore, the vortex strengths at $x^* = 0$, $x^* = 1$, and $x^* = 2$ (defined in **Figure 7**) are considered comprehensively.

Taking the case 1 in reference [19] as an example, as shown in **Figure 6**, the shadow area Γ_s reflects the mean circulation in the entire simulation process. For the $x^* = 0$ section, smaller Γ_s indicates lower local vortex strength after the rapid decay. For $x^* = 1$ and $x^* = 2$ sections, smaller Γ_s corresponds to an earlier beginning of the rapid decay, which reflects the higher extension velocity and stronger intensity of the helical vortices. Therefore, the objective function of the optimization can be expressed as **Equation 17**:

$$\text{Min}: obj = \frac{\int_{t_0}^{t_{end}} \left(\Gamma^*_{x^*=0} + \Gamma^*_{x^*=1} + \Gamma^*_{x^*=2}\right) \mathrm{d}t}{3} \tag{17}$$

During the simulation, the flow field data is logged at 4s interval, and thus, the objective function can be simplified as **Equation 18**:

$$\text{Min}: obj = \frac{\sum_{i=1}^{N} \left(\Gamma^*_{x^*=0,i} + \Gamma^*_{x^*=1,i} + \Gamma^*_{x^*=2,i}\right)}{3} \tag{18}$$

where i is the i th instant and N is the total number of recorded instants. Since both circulation and time are non-dimensionalized, the objective function is also a non-dimensional value. **Figure 7** demonstrates the two parameters considered in the optimization. The blowing zone length X_1 restricts the aspect ratio, and the distance between the centre of the blowing zone and the central axis, X_2, defines the blowing position. If the boundaries of the blowing zone could not exceed the computational domain boundaries, the constraints for the optimization can be expressed as **Equation 19**:

$$\begin{aligned} \text{s.t. } X_2 - \frac{X_1}{2} &> 0 \\ 3b_0 - \frac{X_1}{2} - X_2 &> 0 \\ 2b_0 - \frac{0.02b_0^2}{X_1} &> 0 \end{aligned} \tag{19}$$

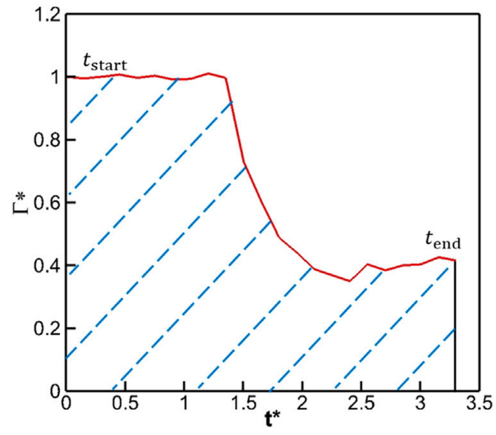

FIGURE 6 | Circulation history of case 1 in reference [19].

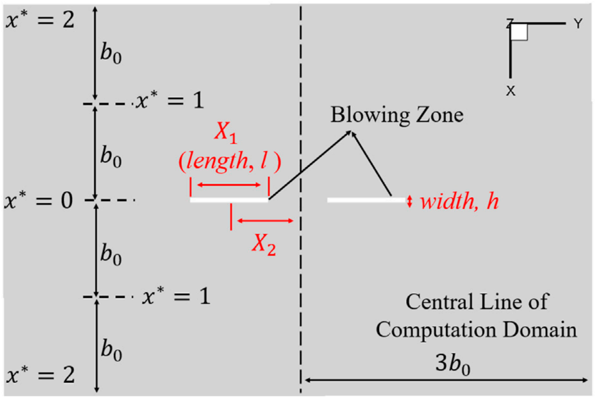

FIGURE 7 | Definition of the optimization parameters (bottom of the computational domain).

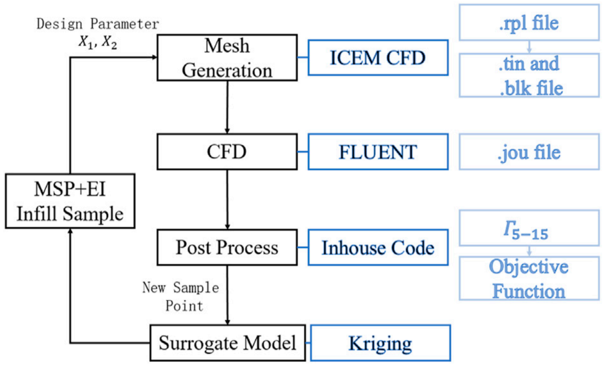

FIGURE 8 | Processes for new sample evaluation.

It must be noted that the response value for every new sample point is evaluated by CFD, which may consume more than 20 h when using a 64 cores server. The automated process is as follows (**Figure 8**):

1) for a new sample point, the batch file is generated according to the input design parameters; then, the structured mesh is generated using the batch files in ICEM CFD;
2) the CFD simulation is conducted using ANSYS FLUENT, in which the *.jou* file controls the CFD simulation details such as timestep and turbulence modelling etc.;
3) the flow field information is extracted and post-processed using an in-house code to get the objective function value;
4) the new sample point parameter and corresponding objective function value is transferred to update the surrogate model;
5) another round of sample infilling is conducted if necessary.

Considering the high cost of the CFD, two termination conditions are employed:

1) the total number of samples exceeds 210 ($n_{\text{sample}} \geq 210$)
2) the error of the adjacent two iterations is smaller than 10^{-5}

As shown in **Figure 9A**, the optimal design of the current problem is found at the 20th sample point, while none of the subsequent sample points show a significant decrease in the objective function value. The better designs are concentrated around *obj.* = 11. Nevertheless, as the number of sample points increases, the surrogate model gradually stabilizes, and the adjacent error of the optimal value found by the surrogate model exhibits an overall decreasing trend. At the end of the optimization, the adjacent decreases to the order of 10^{-5} (**Figure 9B**).

Figure 10 illustrates the modelling when the error of the optimal value decreases to the order of 10^{-3}, 10^{-4}, and 10^{-5} for two adjacent iterations. **Figures 10A, C, E** are coloured using the objective function values, obj., while **Figures 10B, D, F** are coloured using the EI values. Above the black dashed line in the figures is the feasible domain. When $n_{\text{sample}} = 36$, the max of the EI values in the feasible domain is less than 0.1, indicating that the surrogate model already has high credibility. The response surface of $n_{\text{sample}} = 36$ is close to that of $n_{\text{sample}} = 181$, lower *obj.* value is observed in the middle of the design space. It is observed that in most of the region of $x_1 \in [0.1b_0, 1b_0]$ and $x_2 \in [0.5b_0, 1.1b_0]$, obj. is smaller than 12, and in the neighbouring region of $x_1 = 0.3\ b_0$ and $x_2 = 0.8\ b_0$, *obj.* is smaller than 11. When n_{sample} is increased to 205, EI values decrease further throughout the region while there is only limited change to the response surface, implying that the current surrogate model has converged and is reliable.

Figures 11–17 exhibit the vortex structures of two initial sample cases, four infilled sample cases, and the best performing sample case during the optimization. All the relative positions in the design space are shown in **Figure 18**,

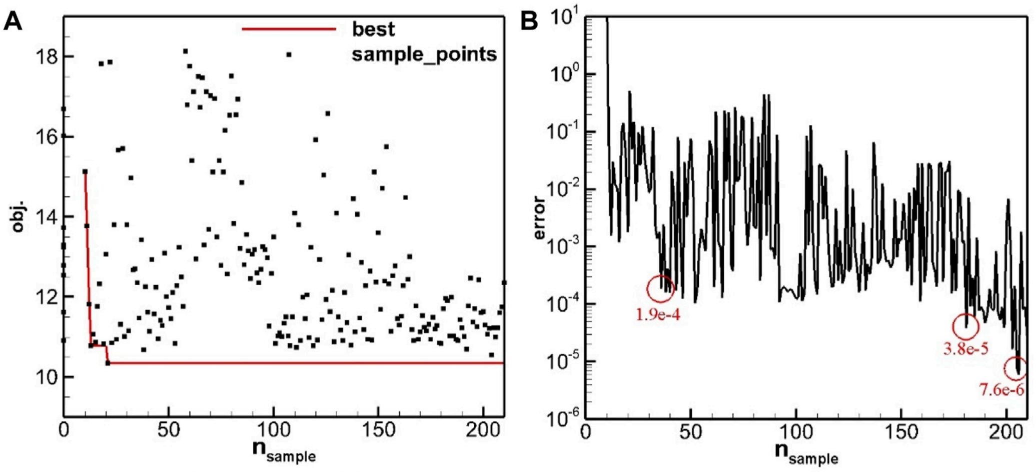

Convergence history

Adjacent error

FIGURE 9 | Convergence history of blowing zone optimization. **(A)** Convergence history, **(B)** Adjacent error.

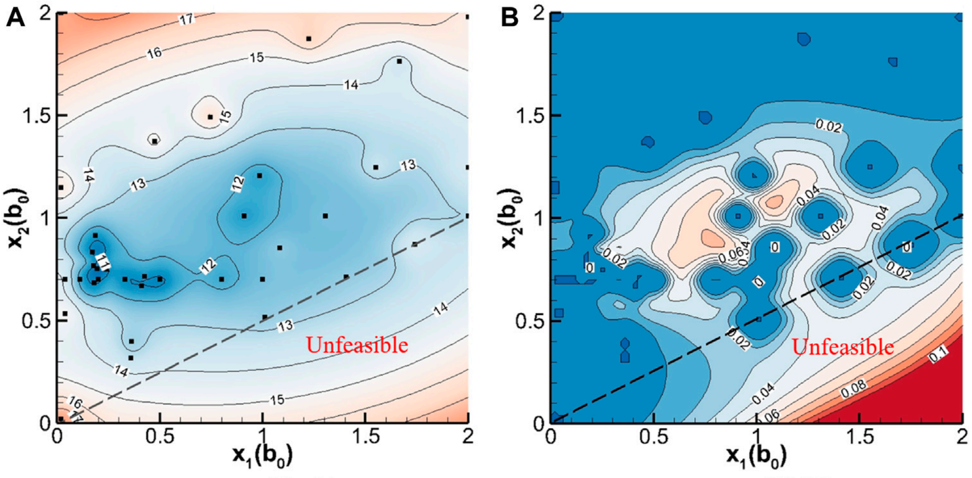

n_{sample}=36, obj.

n_{sample}=36, EI

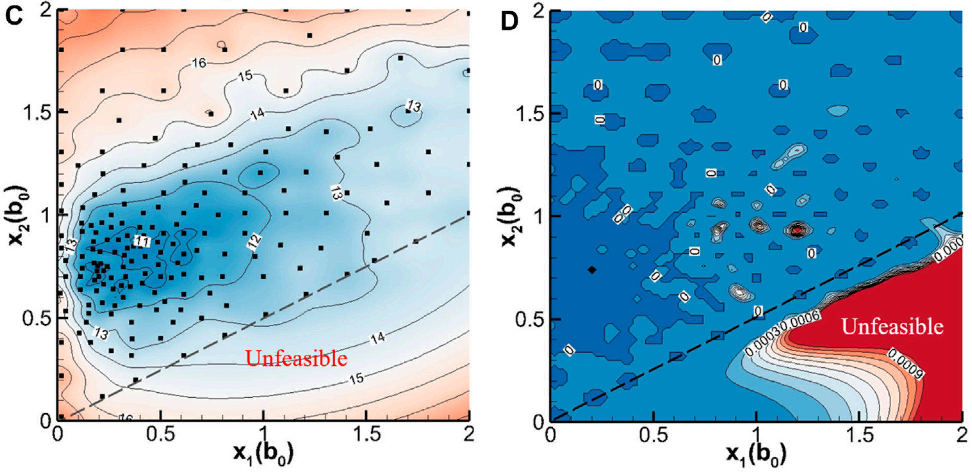

n_{sample}=181, obj.

n_{sample}=181, EI

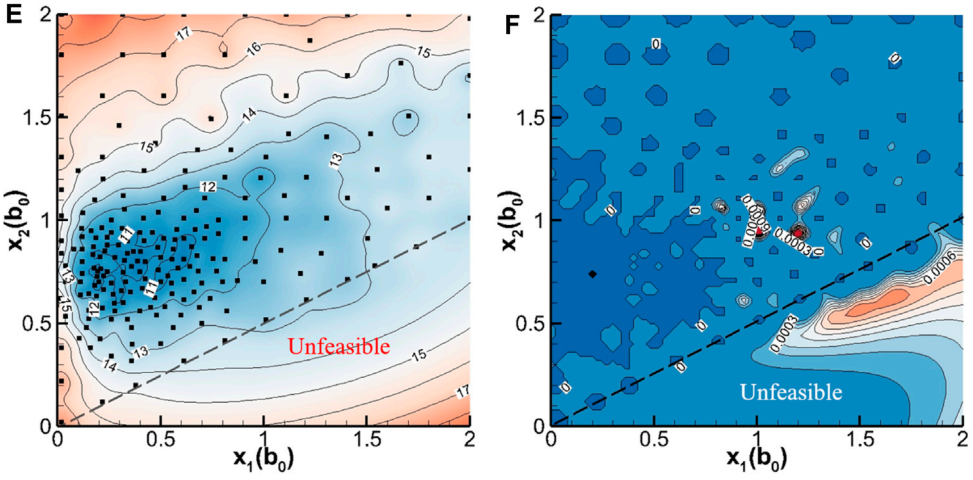

n_{sample}=205, obj.

n_{sample}=205, EI

FIGURE 10 | Response surface and EI contour. **(A)** n_{sample} = 36 obj, **(B)** n_{sample} = 36 EI, **(C)** n_{sample} = 181 obj, **(D)** n_{sample} = 181 EI, **(E)** n_{sample} = 205 obj, **(F)** n_{sample} = 205 EI.

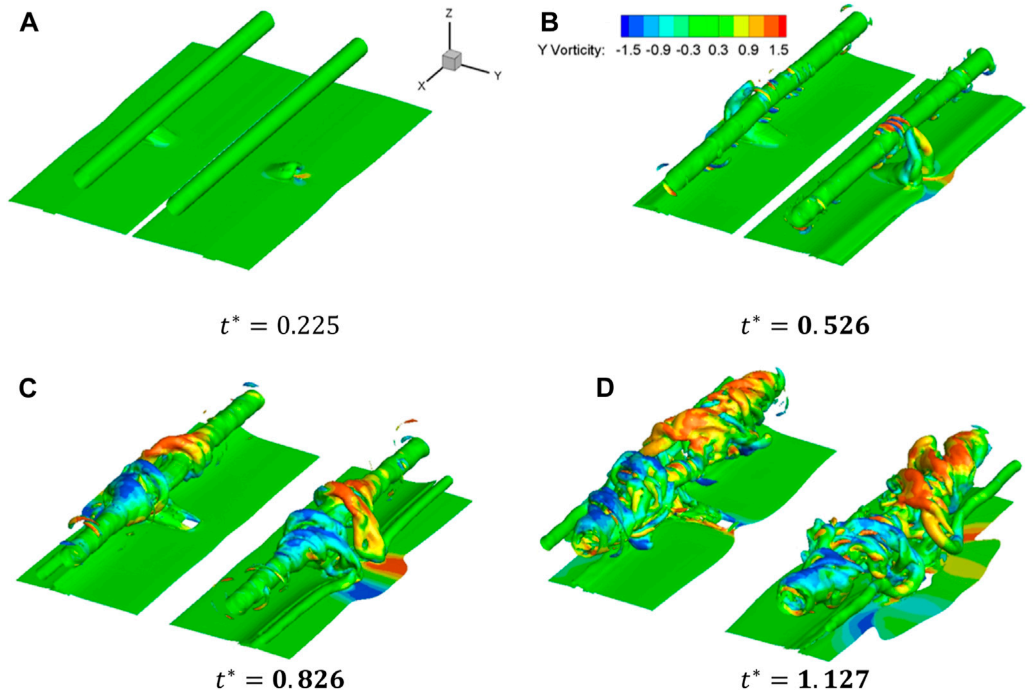

FIGURE 11 | Structures of initial sample 1. **(A)** t^* = 0.225, **(B)** t^* = 0.526, **(C)** t^* = 0.826, **(D)** t^* = 1.127.

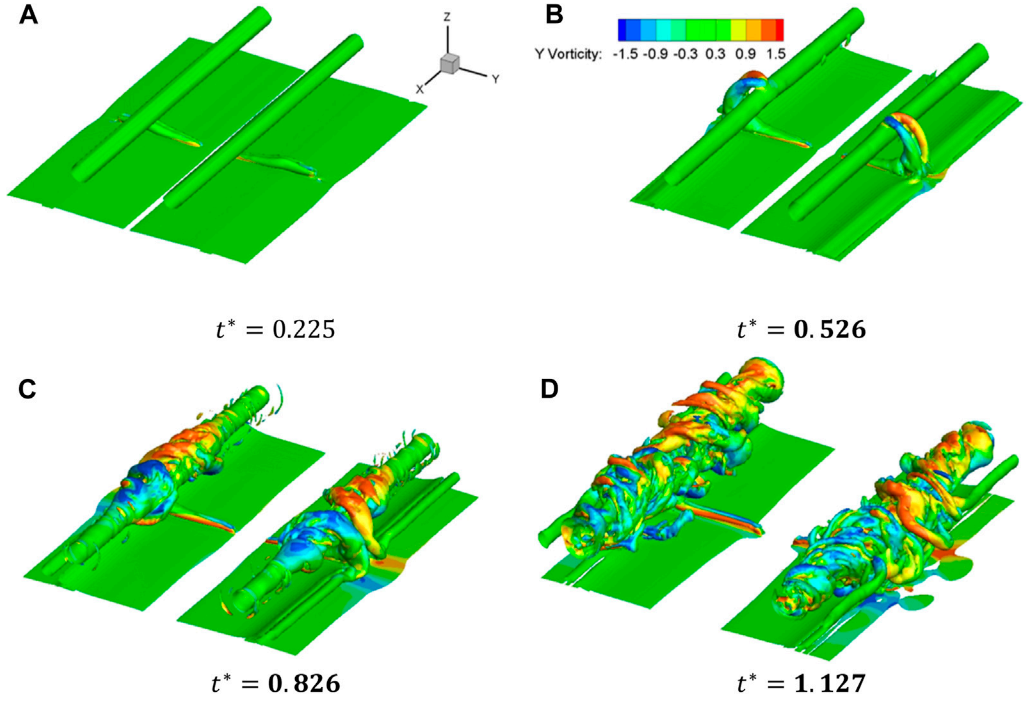

FIGURE 12 | Structures of initial sample 2. **(A)** t^* = 0.225, **(B)** t^* = 0.526, **(C)** t^* = 0.826, **(D)** t^* = 1.127.

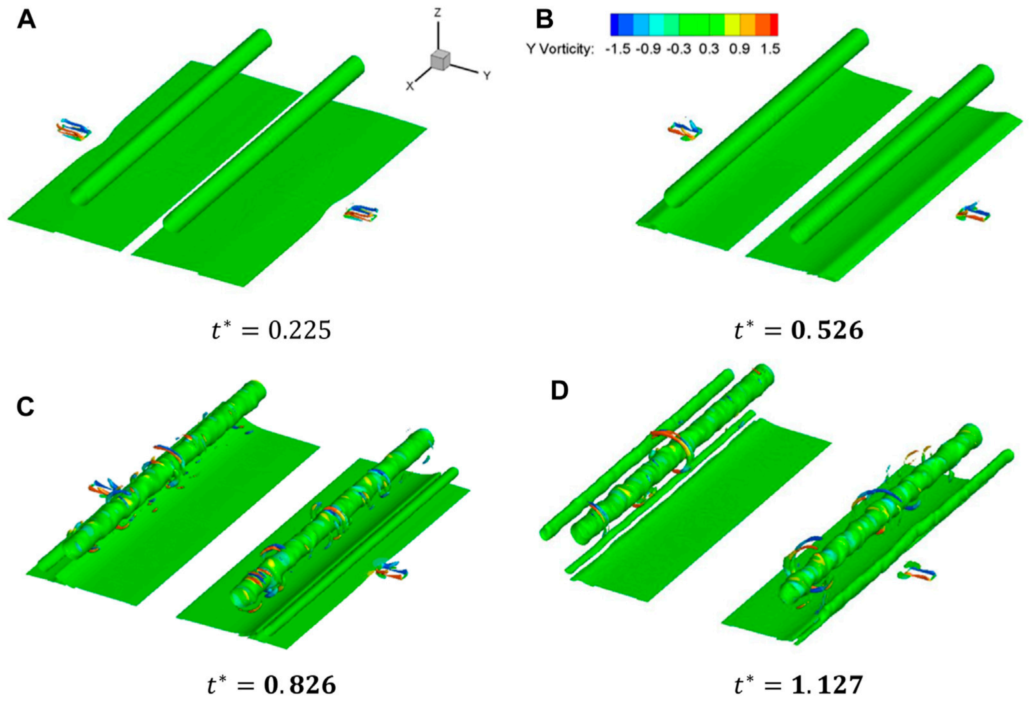

$t^* = 0.225$ $t^* = \mathbf{0.526}$

$t^* = \mathbf{0.826}$ $t^* = \mathbf{1.127}$

FIGURE 13 | Structures of sample 70. **(A)** t^* = 0.225, **(B)** t^* = 0.526, **(C)** t^* = 0.826, **(D)** t^* = 1.127.

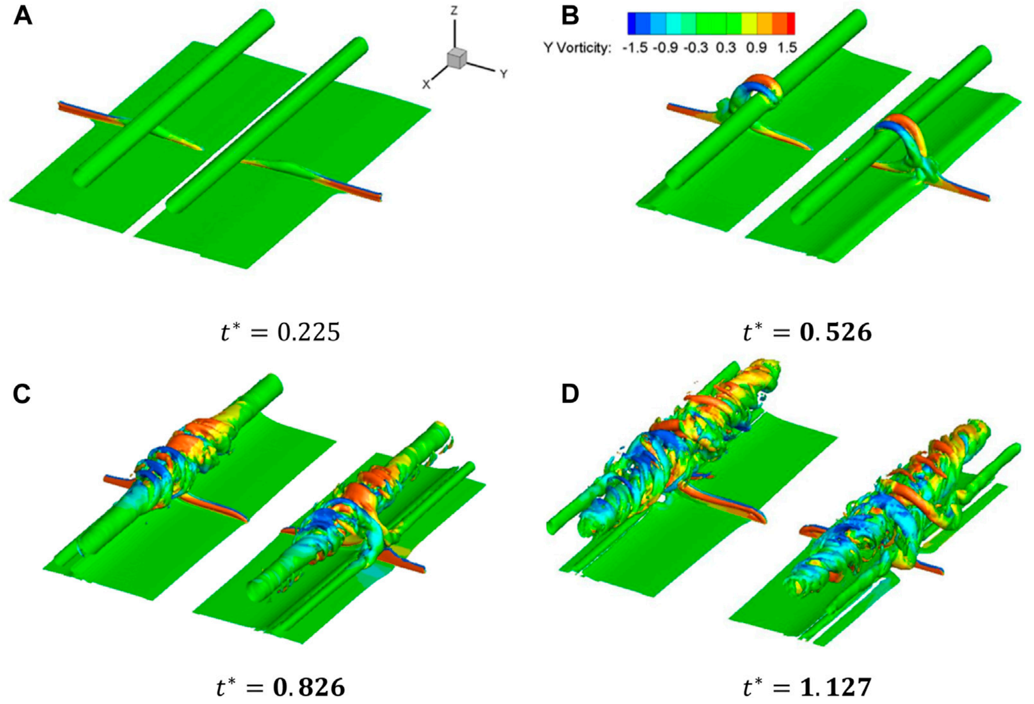

$t^* = 0.225$ $t^* = \mathbf{0.526}$

$t^* = \mathbf{0.826}$ $t^* = \mathbf{1.127}$

FIGURE 14 | Structures of sample 73. **(A)** t^* = 0.225, **(B)** t^* = 0.526, **(C)** t^* = 0.826, **(D)** t^* = 1.127.

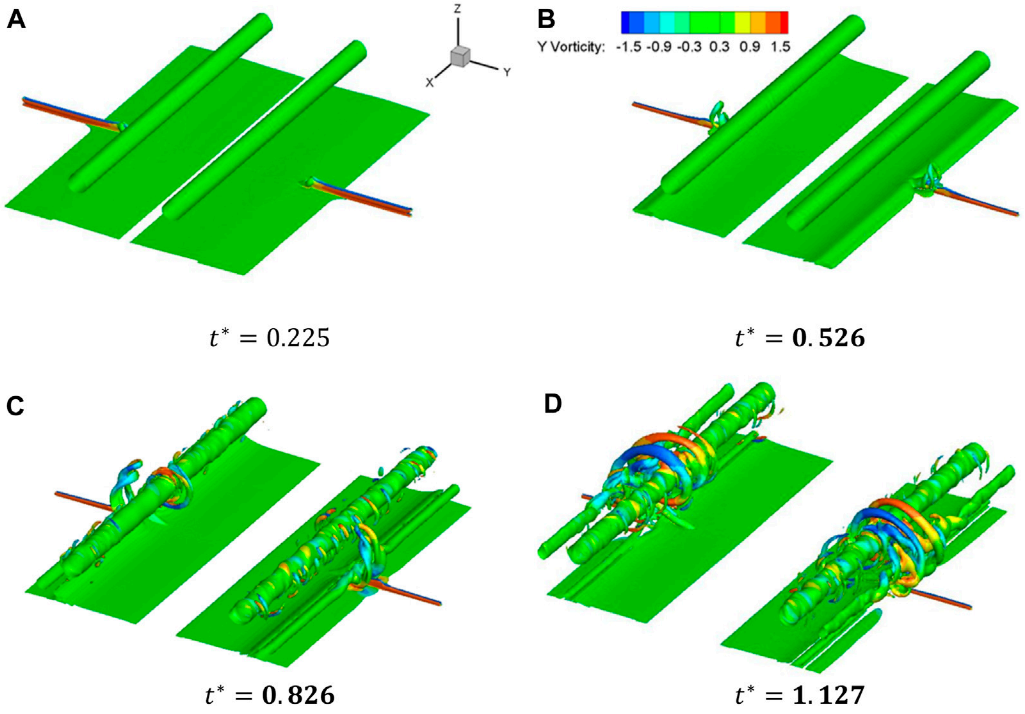

$t^* = 0.225$ $t^* = \mathbf{0.526}$

$t^* = \mathbf{0.826}$ $t^* = \mathbf{1.127}$

FIGURE 15 | Structures of sample 76. **(A)** t^* = 0.225, **(B)** t^* = 0.526, **(C)** t^* = 0.826, **(D)** t^* = 1.127.

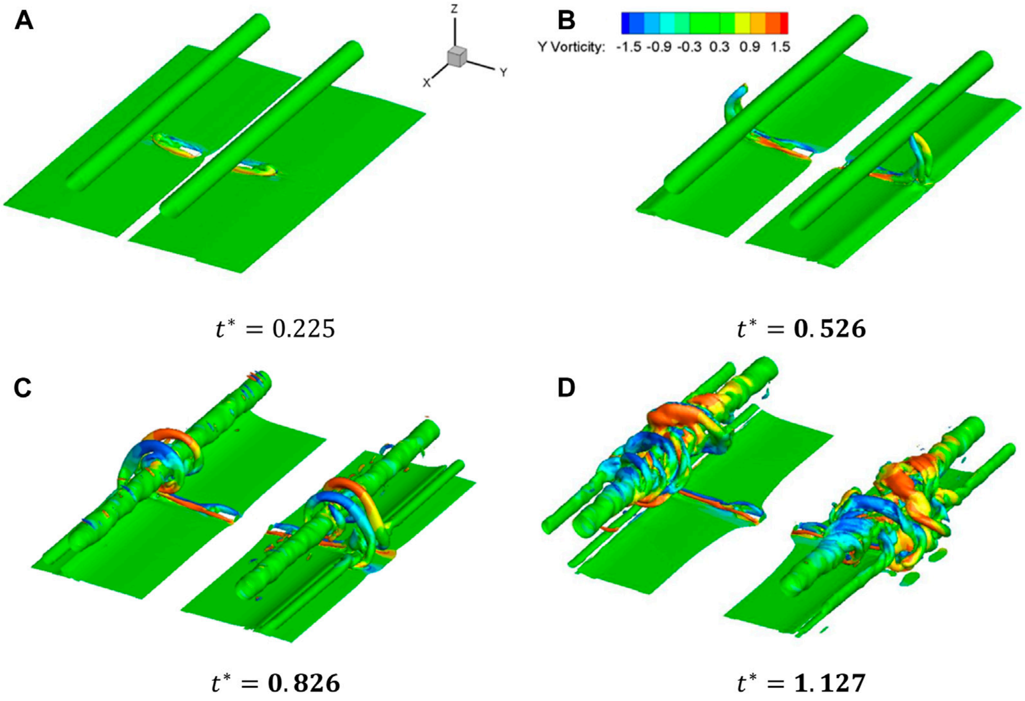

$t^* = 0.225$ $t^* = \mathbf{0.526}$

$t^* = \mathbf{0.826}$ $t^* = \mathbf{1.127}$

FIGURE 16 | Structures of sample 150. **(A)** t^* = 0.225, **(B)** t^* = 0.526, **(C)** t^* = 0.826, **(D)** t^* = 1.127.

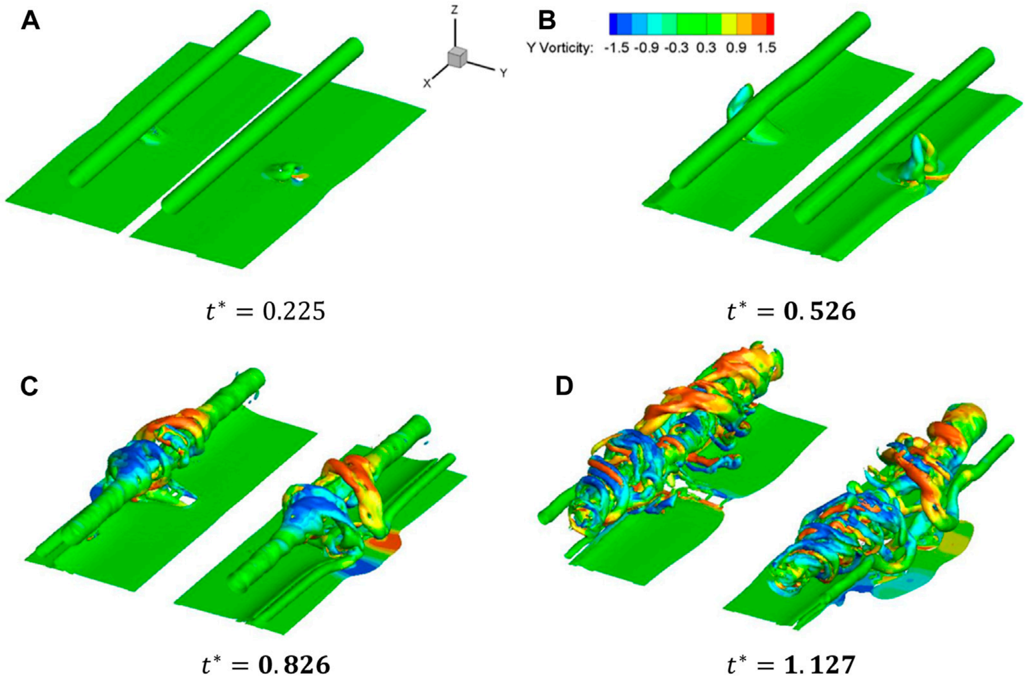

FIGURE 17 | Structures of the optimal sample. **(A)** t^* = 0.225, **(B)** t^* = 0.526, **(C)** t^* = 0.826, **(D)** t^* = 1.127.

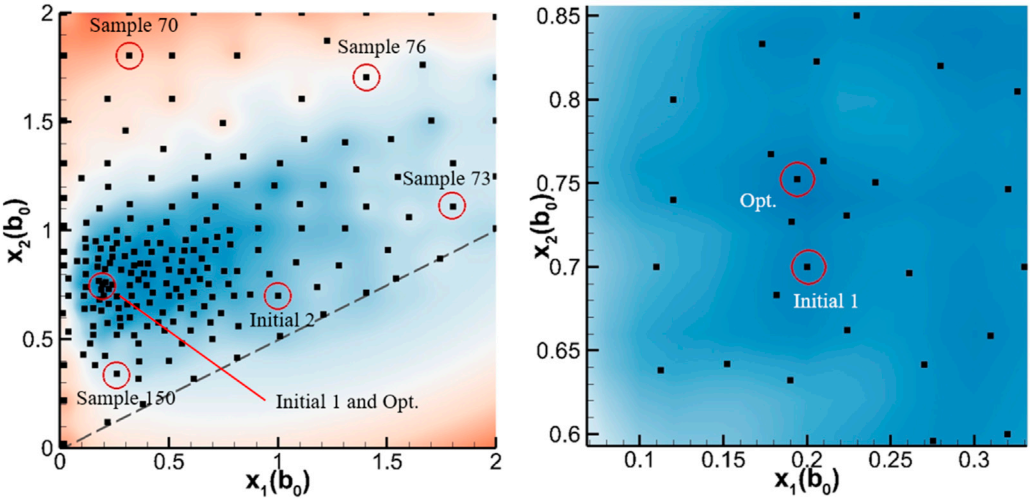

FIGURE 18 | Samples to be demonstrated.

the design parameters are shown in **Table 2**, and the circulation decay histories are exhibited in **Figure 19**.

Take sample cases *76* and *150* as examples. The Ω vortex in *Sample 73* has already had contact with the primary vortex at $0.526t_0$; and at $1.127t_0$, the helical vortex has already reached the boundaries of the computational domain. By comparison, the helical vortex just reached x^* = 1 at $1.127t_0$. **Figure 19** also shows that at different positions, the rapid decay in *Sample 150* sets off later than that in *Sample 73*. It is noted that the slope of the circulation curves at x^* = 1 and x^* = 2 of *Sample 150* are steeper than those in *Sample 73*. This is because the blowing zone in *Sample 150* has a smaller length (X_1) and larger width, which produces a stronger starting vortex and more intense interaction on the aircraft wake vortex [16]. *Sample 70* is an exception of the above cases. Since the blowing zone is far from the centre line (X_2 = $1.802b_0$) and the length of the blowing zone is small (X_1 = $0.317b_0$), the blowing airflow never effectively interferes with the secondary vortex, and eventually the primary vortex

TABLE 2 | Design parameters of initial samples and the best performing sample.

Case	X_1	X_2	Aspect ratio	Obj.
Initial 1	0.2 b_0	0.7 b_0	1	10.77
Initial 2	1.0 b_0	0.7 b_0	25	12.32
Sample 70	0.317 b_0	1.802 b_0	2.512	17.02
Sample 73	1.802 b_0	1.109 b_0	81.181	13.49
Sample 76	1.406 b_0	1.703 b_0	49.421	15.11
Sample 150	0.260 b_0	0.340 b_0	1.69	13.59
Opt.	0.194 b_0	0.752 b_0	0.941	10.35

simply undergoes a natural dissipation process. At $t^* = 1.127$, the primary vortex structure still remains intact (**Figure 13**), and the rapid decay in *Sample 76* sets off late. **Figure 15B** shows that the Ω vortex forms at $0.526t_0$. As a result, the wake decay enhancement of *Sample 76* is only better than that of *Sample 70*.

The vortex structures in the two initial sample cases and the best performing case are similar. Considering the induced lateral movement of the IGE vortex, a large value of $X_2 = 0.7b_0$ is selected for the two initial sample cases [19]. Since the starting vortex interacts with the wake vortex at $x^* = 0$ directly, the local circulation in these three cases drops fast at 0.45 t_0. At least until 0.9 t_0, the blowing zone aspect ratio does not obviously affect accelerated wake dissipation. However, due to the weak starting vortex, the circulation in case *Initial 2* experienced a rebound between $1 < t^* < 2.5$. At $x^* = 1$ and $x^* = 2$, the local rapid decay in *Initial 2* sets off later than those in other two cases, which is also the consequence of the weak starting vortex. The helical vortex in *Initial 2*, developed from the starting vortex, extends slower and affects the wake vortex to a limited extension. Compared with *Initial 1*, the design parameters and vortex decay history in *Opt.* is similar. It is noticed that, although the starting vortex in *Opt.* is relatively weak, due to the influence of the blowing zone position, the circulation in *Opt.* is lower after the rapid decay phase.

Overall, the vortex evolutions in most cases are similar: a) the starting vortex generated by blowing air is raised by the blowing air and primary vortex induction b) the starting vortex evolves into a hairpin vortex (Ω vortex) and interacts with the

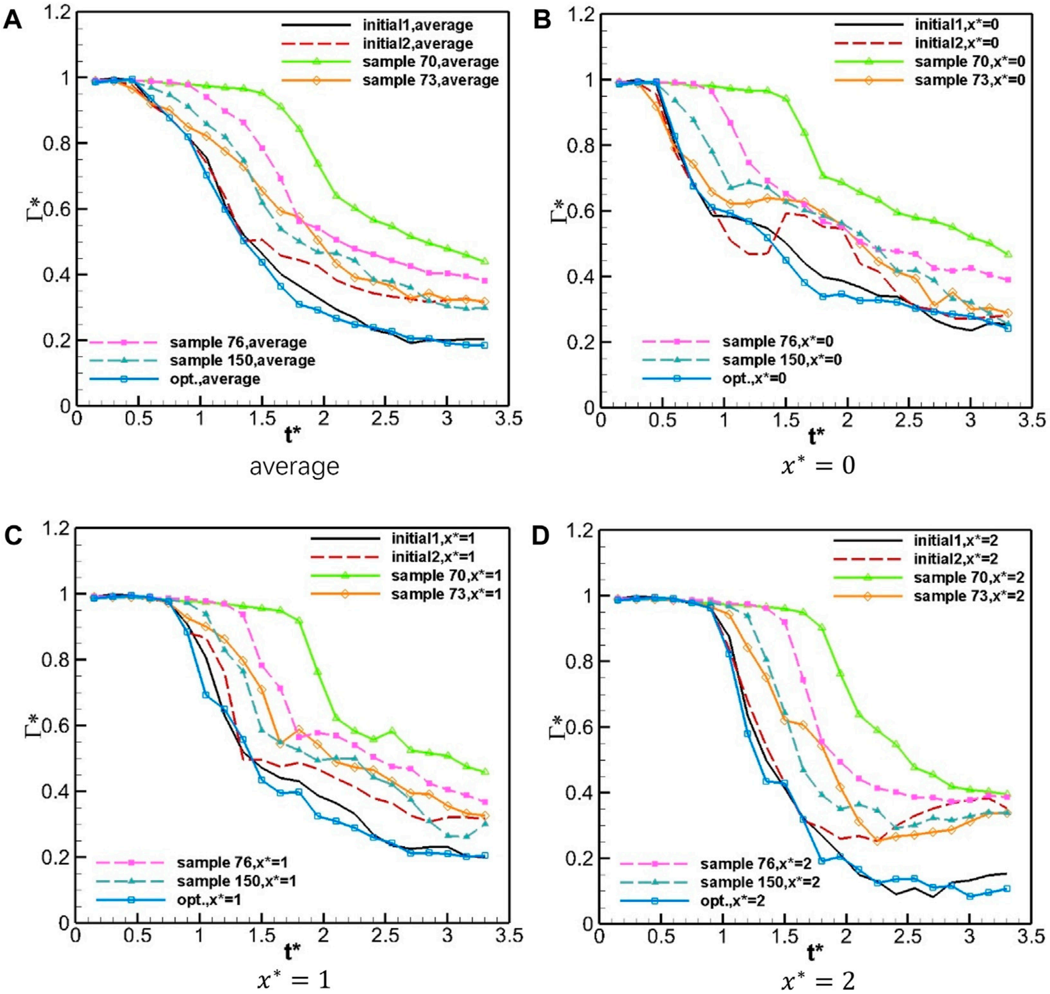

FIGURE 19 | Circulation history at different axial positions (seven cases). **(A)** average, **(B)** x* = 0, **(C)** x* = 1, **(D)** x* = 2.

TABLE 3 | Parameters for different wake simulations.

Aircraft type	Initial circulation (m^2/s)	Initial vortex spacing (m)	Initial vortex altitude (m)	Dimensionless initial altitude
A340	530	47.4	31	0.654
A380	825	62.6	31	0.495

primary vortex c) Ω vortex loops around the primary vortex and extends along the x direction. The main difference between different cases is the timing and intensity of the above processes. From **Figure 10E**, the surrogate model shows that the best performing setting for A340 wake decay enhancement is $X_1 = 0.194b_0, X_2 = 0.752b_0$. Since the blowing zone area is fixed to $0.04b_0^2$, it is obtained that the blowing zone aspect ratio is close to 1. Besides, in the range of $X_1 \in [0.1b_0, 1b_0]$ and $X_2 \in [0.5b_0, 1.1b_0]$, the objective function is smaller than 12, which is still a considerable enhancement for wake vortex decay.

MULTI-OBJECTIVE DESIGN

The optimum blowing zone for an A340 wake vortex pair may not be enough to destroy the wake of a heavier aircraft, such as an A380, within a short period. Therefore, a better design could be obtained by overlapping the design space of two blowing zone types, which are for different aircraft wake decay enhancements, respectively. Taking the above optimization result as an example, **Figure 10E** can be dimensionalized using A340 and A380 parameters (**Table 3**). It is highlighted that the optimization process in the previous section is partially dimensionless. Since the initial vortex altitude of $z_0 = 31$m during the landing phase applies for all types of aircrafts, the dimensionless altitude for aircrafts with different wingspans varies in a certain range. Therefore, the final selection of design parameters should be based on the characteristic parameters of the aircraft with the largest wingspan, which is taken as the characteristic parameters of A380 in the present study. The basis for this selection is:

1) for A380 (aircraft with larger span), the dimensionless initial altitude is less than that used in the optimization;
2) for A340 (aircraft with shorter span), the dimensionless blowing area is larger than that used in the optimization.

These two facts ensure that the simulated blowing effect is not worse than that predicted by the surrogate model.

The design space is divided by the contour lines of the response surface (objective function), the value of the objective function inside the contour lines is smaller than that of the objective function on the contour lines. **Figure 20** shows the contour lines on which the objective function equals 11.5. When the design parameters inside the blue contour line (D_{340}) are used, the objective function of A340 wake vortex is smaller than 11.5. The critical value of 11.5 is chosen because it already corresponds to an impressive enhancement on wake vortex decay. The intersection region of D_{380} and D_{340} (shadow zone) represents the optimum design space (D_{opt}), with which the blowing process is most effective for both A340 wake and A380 wake. Considering that a longer blowing zone improves the blowing effect [19], the final selection of the design, $X_1 = 43$m and $X_2 = 47.5$m, is close to the right boundary of D_{opt}. According to the parameters of the A380 wake, the width of the blowing zone is $h = (0.2 \times 62.6)^2/43\text{m} = 3.65\text{m}$.

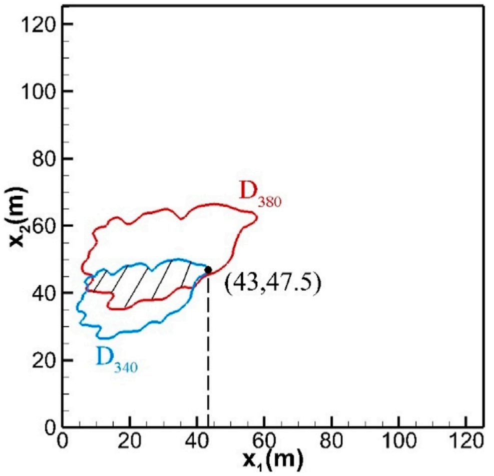

FIGURE 20 | Design space of blowing zone for different aircraft wake vortex (Opt. < 11.5).

Two simulations are performed to validate the optimization results. For A340 and A380 wake vortex simulations, the same non-dimensional computation domain ($4b_0 \times 6b_0 \times 3b_0$) and non-dimensional blowing velocity (ω_0) are employed, meaning that the absolute computational domain and blowing velocity are different. But the blowing areas are exactly the same as the above optimized result ($x_1 = 43$m, $x_2 = 47.5$m and $h = 3.65$m). It is noted that for A380 wake simulation, the timestep is 0.01s ($3.35 \times 10^{-4} t_0$) and 102s (3.4 t_0) of wake evolution is simulated. The blowing zone area is $0.04b_0^2 = 156.75\text{m}^2$, and the blowing velocity is $\omega_0 = 2.0975$ m/s.

Figure 21 and **Figure 22** show the wake vortex structures of A340 and A380 under the blowing effect. Due to the large initial circulation of the A380 wake vortex, the starting vortex experiences high induced velocity and is raised quickly. **Figure 22B** shows that a vortex loop is evolved from the Ω vortex at $t = 14$s in the case of A380 case, while in the case of A340, the Ω vortex has just formed and approached the primary vortex. After that, under the self-induction, the vortex loop extends along the x direction and forms helical vortices, which destruct the wake vortex structures rapidly. It is noted that at $t = 22$s, the helical vortices in the case of A380 develop faster than

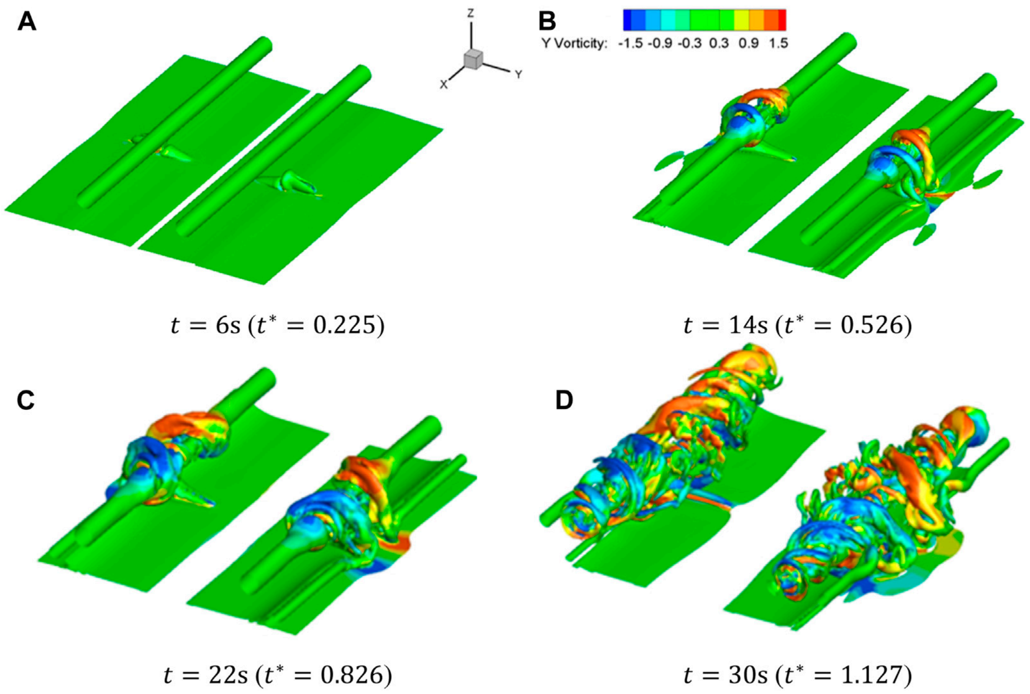

$t = 6\text{s}\ (t^* = 0.225)$

$t = 14\text{s}\ (t^* = 0.526)$

$t = 22\text{s}\ (t^* = 0.826)$

$t = 30\text{s}\ (t^* = 1.127)$

FIGURE 21 | Structures of A340 wake vortex (coloured by *y* vorticity 1/s). **(A)** t = 6s (t* = 0.225), **(B)** t = 14s (t* = 0.526), **(C)** t = 22s (t* = 0.826), **(D)** t = 30s (t* = 1.127).

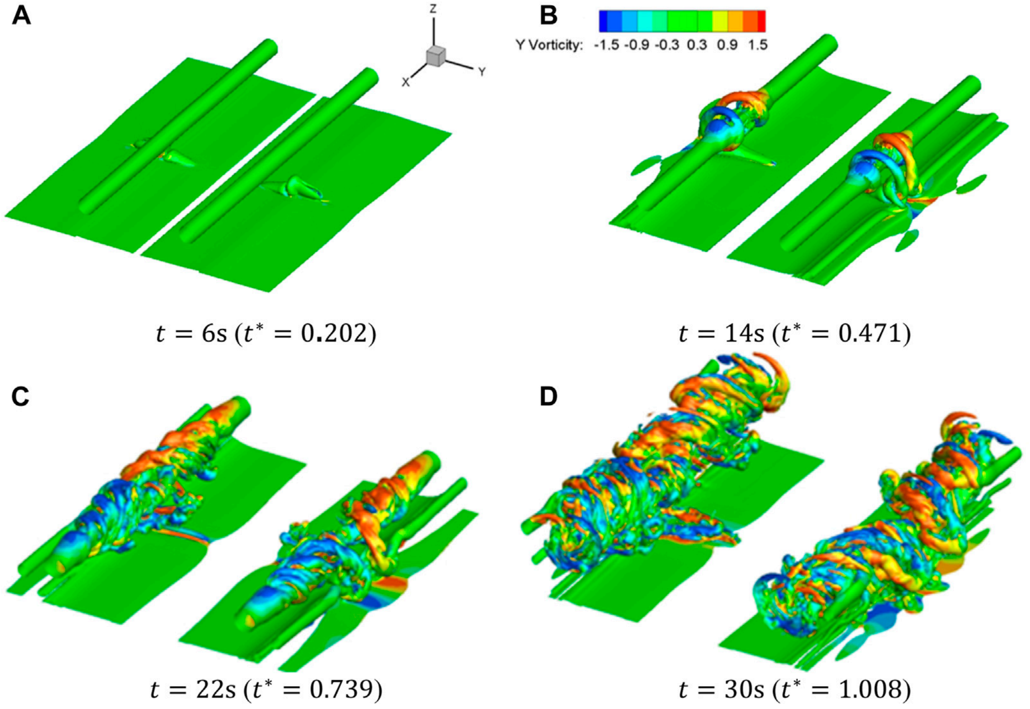

$t = 6\text{s}\ (t^* = 0.202)$

$t = 14\text{s}\ (t^* = 0.471)$

$t = 22\text{s}\ (t^* = 0.739)$

$t = 30\text{s}\ (t^* = 1.008)$

FIGURE 22 | Structures of A380 wake vortex (coloured by *y* vorticity 1/s). **(A)** *t* = 6s (*t** = 0.202), **(B)** *t* = 14s (*t** = 0.471), **(C)** *t* = 22s (*t** = 0.739), **(D)** *t* = 30s (*t** = 1.008).

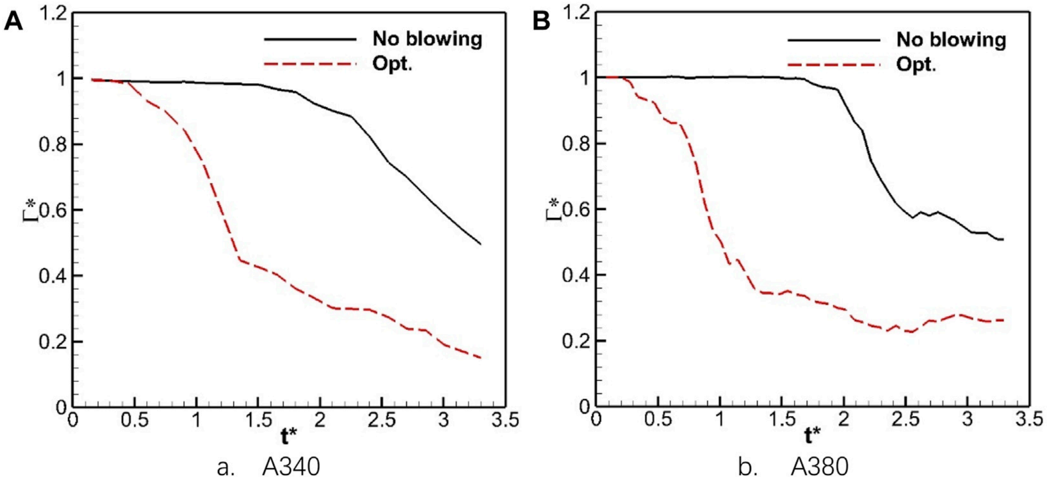

FIGURE 23 | Averaged circulation histories for different aircraft wakes with optimized blowing zones. **(A)** A340, **(B)** A380.

that in the case of A340, implying that the interference between the primary vortex and the blowing induced structures is more intense in the case of A380.

Figure 23 shows the decay history of the A340 and A380 wake vortex with optimized blowing zones. Due to the interference of the starting vortex, the rapid decay of the A340 wake vortex is brought approximately 1.5 t_0 ahead by blowing. At $t^* = 3.3$, the average circulation of the A340 wake with blowing decreases to 0.15, which is much lower than that of the baseline case. The initial dimensionless altitude of the A380 wake vortex is smaller than 0.5, resulting in a better blowing effect. Consequently, the rapid decay sets off at 0.2 t_0 in the blowing case. The objective function values for the A340 and A380 cases are 11.12 and 10.19, respectively. With the current blowing zone settings, the wake vortex decay for both aircraft types is enhanced and reaches the design objective (objective function < 11.5).

CONCLUSION

In this paper, the Kriging surrogate model is used to help obtain a better design of the blowing zone for enhancement of wake vortex decay. By overlapping and comparing the design spaces for different wake vortices, a multi-objective design is realized, which improves the engineering feasibility of the current blowing method. The main findings are as follows:

1. The current optimization algorithm combing Kriging surrogate model and gradient optimization algorithm deal with the global optimization problems and constrained problems well;
2. The blowing effect is non-linearly related to the blowing zone aspect ratio and position. The blowing zone should not be too close to the centre of the computational domain and the blowing zone aspect ratio should be close to 1;
3. For the A340 wake vortex with an initial altitude of $z = 31\text{m}$ ($z^* = 0.654$), the objective function is smaller than 12 in the range of $X_1 \in [0.1b_0, 1b_0]$ and $X_2 \in [0.5b_0, 1.1b_0]$, and the best performing setting is $X_1 = 0.194\text{b}_0$, $X_2 = 0.752\text{b}_0$;
4. By overlapping the design spaces, an optimized blowing zone, which enhances the decay of A340 and A380 wake vortex, is founded. Numerical simulation proves this blowing zone effective and reduces the objective function to 11.12 and 10.19 for the different wake vortices, respectively.

DATA AVAILABILITY STATEMENT

The original contributions presented in the study are included in the article/Supplementary Material, further inquiries can be directed to the corresponding author.

AUTHOR CONTRIBUTIONS

ZX (the first author) was responsible for numerical simulations, data processing and manuscript writing. DL (the second author) was responsible for the conceptual design of the study, funding support and the manuscript review. All authors contributed to the article and approved the submitted version.

CONFLICT OF INTEREST

The authors declare that the research was conducted in the absence of any commercial or financial relationships that could be construed as a potential conflict of interest.

REFERENCES

1. Gerz T, Holzäpfel F, Darracq D. Commercial Aircraft Wake Vortices. *Prog Aerospace Sci* (2002) 38(3):181–208. doi:10.1016/s0376-0421(02)00004-0
2. Holzäpfel F, Tchipev N, Stephan A. Wind Impact on Single Vortices and Counterrotating Vortex Pairs in Ground Proximity. *Flow Turbulence and Combustion* (2016) 97(3):829–48. doi:10.1007/s10494-016-9729-2
3. Xu Z, Li D, Cai J. Long-Wave Deformation of In-Ground-Effect Wake Vortex Under Crosswind Condition. *Aerospace Sci Tech* (2023) 142:108697. doi:10.1016/j.ast.2023.108697
4. ICAO. *ICAO DOC 4444 Air Traffic Management - Procedures for Air Navigation Services (PANS-ATM)*. 16. Montréal, Quebec, Canada: ICAO (2016).
5. Holbrook GT, Dunham DM, Greene GC. *Vortex Wake Alleviation Studies With a Variable Twist Wing*. Technical Paper 2442. Hampton, Virginia, United States: NASA (1985).
6. Breitsamter C. Wake Vortex Characteristics of Transport Aircraft. *Prog Aerospace Sci* (2011) 47(2):89–134. doi:10.1016/j.paerosci.2010.09.002
7. Ruhland J, Heckmeier FM, Breitsamter C. Experimental and Numerical Analysis of Wake Vortex Evolution Behind Transport Aircraft With Oscillating Flaps. *Aerospace Sci Tech* (2021) 119:107163. doi:10.1016/j.ast.2021.107163
8. Breitsamter C, Allen A. Transport Aircraft Wake Influenced by Oscillating Winglet Flaps. *J Aircraft* (2009) 46(1):175–88. doi:10.2514/1.37307
9. Cheng Z, Wu Y, Xiang Y, Liu H, Wang FX. Benefits Comparison of Vortex Instability and Aerodynamic Performance From Different Split Winglet Configurations. *Aerospace Sci Tech* (2021) 119:107219. doi:10.1016/j.ast.2021.107219
10. Rennich SC, Lele SK. Method for Accelerating the Destruction of Aircraft Wake Vortices. *J Aircraft* (1999) 36(2):398–404. doi:10.2514/2.2444
11. Stumpf E. Study of Four-Vortex Aircraft Wakes and Layout of Corresponding Aircraft Configurations. *J Aircraft* (2005) 42(3):722–30. doi:10.2514/1.7806
12. Cho J, Lee BJ, Misaka T, Yee K. Study on Decay Characteristics of Vertical Four-Vortex System for Increasing Airport Capacity. *Aerospace Sci Tech* (2020) 105:106017. doi:10.1016/j.ast.2020.106017
13. Kohl RE. *Model Experiments to Evaluate Vortex Dissipation Devices Proposed for Installation on or Near Aircraft Runways*. Hampton, Virginia, United States: NASA (1973).
14. Stephan A, Holzäpfel F, Misaka T, Geisler R, Konrath R. Enhancement of Aircraft Wake Vortex Decay in Ground Proximity: Experiment Versus Simulation. *CEAS Aeronaut J* (2013) 5(2):109–25. doi:10.1007/s13272-013-0094-8
15. Holzäpfel F, Stephan A, Rotshteyn G, Körner S, Wildmann N, Oswald L, et al. Mitigating Wake Turbulence Risk During Final Approach Via Plate Lines. *AIAA J* (2021) 2021:59. doi:10.2514/6.2020-2835
16. Xu Z, Li D, An B, Pan W. Enhancement of Wake Vortex Decay by Air Blowing From the Ground. *Aerospace Sci Tech* (2021) 118:107029. doi:10.1016/j.ast.2021.107029
17. Xu Z, Li D. Enhanced Aircraft Wake Decay Under Crosswind Conditions. *J Aircraft* (2023) 60(5):1687–99. doi:10.2514/1.C037127
18. Misaka T, Holzäpfel F, Hennemann I, Gerz T, Manhart M, Schwertfirm F. Vortex Bursting and Tracer Transport of a Counter-Rotating Vortex Pair. *Phys Fluids* (2012) 24(2):25104. doi:10.1063/1.3684990
19. Han Z, Chen J, Zhang K, Xu ZM, Zhu Z, Song WP. Aerodynamic Shape Optimization of Natural-Laminar-Flow Wing Using Surrogate-Based Approach. *AIAA J* (2018) 56(7):2579–93. doi:10.2514/1.j056661
20. Han Z. SURROOPT: A Generic Surrogate-Based Optimization Code for Aerodynamic and Multidisciplinary Design. In: 30th Congress of the International Council of the Aeronautic Sciences (2016).
21. Sasena MJ, Papalambros P, Goovaerts P. Exploration of Metamodeling Sampling Criteria for Constrained Global Optimization. *Eng optimization* (2002) 34(3):263–78. doi:10.1080/03052150211751
22. Parr JM, Keane AJ, Forrester AIJ, Holden CM. Infill Sampling Criteria for Surrogate-Based Optimization With Constraint Handling. *Eng optimization* (2012) 44(10):1147–66. doi:10.1080/0305215x.2011.637556
23. Jones DR, Schonlau M, Welch WJ. Efficient Global Optimization of Expensive Black-Box Functions. *J Glob optimization* (1998) 13(4):455–92. doi:10.1023/a:1008306431147
24. Rosenbrock HRH. An Automatic Method for Finding the Greatest or Least Value of a Function. *Comp J* (1960) 3(3):175–84. doi:10.1093/comjnl/3.3.175
25. Deb K. An Efficient Constraint Handling Method for Genetic Algorithms. *Comp Methods Appl Mech Eng* (2000) 186(2):311–38. doi:10.1016/s0045-7825(99)00389-8

AEROSPACE RESEARCH COMMUNICATIONS
ORIGINAL RESEARCH
published: 09 January 2024
doi: 10.3389/arc.2023.12272

Reynolds Number Effects on the Drag Reduction With a Spanwise Traveling Wave of Blowing and Suction in Turbulent Channel Flows

Yi Huang and Song Fu*

School of Aerospace Engineering, Tsinghua University, Beijing, China

Turbulent channel flows with $Re_\tau = 180$ and $Re_\tau = 550$ are controlled to reduce the drag with a spanwise traveling wave of the blowing and suction method. An oscillatory spanwise motion is generated with a periodically reversing propagation direction of the traveling wave, similarly as the wall oscillation. Direct numerical simulation (DNS) results show that this kind of blowing and suction control can achieve a drag reduction rate of 24.5% with $Re_\tau = 180$, and 7.5% with $Re_\tau = 550$. The reasons for the deterioration in drag reduction rates are thought to be the lift-up mechanism by the actuation through an asymptotic expansion method, and the controlled inner regions and small-scale structures having less significance when the Reynolds number is high.

Keywords: drag reduction, turbulent channel flows, spanwise traveling wave, blowing and suction, Reynolds number dependence

***Correspondence**
Song Fu,
fs-dem@tsinghua.edu.cn

Received: 22 October 2023
Accepted: 24 November 2023
Published: 09 January 2024

Citation:
Huang Y and Fu S (2024) Reynolds Number Effects on the Drag Reduction With a Spanwise Traveling Wave of Blowing and Suction in Turbulent Channel Flows.
Aerosp. Res. Commun. 1:12272.
doi: 10.3389/arc.2023.12272

INTRODUCTION

Nearly 55% of total drag is a viscous drag for a civil aircraft [1]. A 0.75% reduction in fuel consumption can be achieved with a 1% reduction in skin friction [2]. Thus, it has been an important goal to reduce the viscous drag in the area of flow control in turbulent boundary layer flows. There are two conventional routes for flow control near the wall, passive control and active control. For the former extra energy input is not needed and a drag reduction of about 10% can be achieved. The most popular passive control strategy is building streamwise riblets at the wall, which can reduce the viscous drag by about 7%–10%, with a restriction on the spanwise crossflow in the near wall region. However, the requirements of an effective riblet shape are strict [3–5]. In active control strategies, energy outside the flow was imposed and the turbulent skin friction is reduced more effectively compared with the passive control. The wall oscillation (noted as WOS hereinafter) was thought to be a simple and effective way to reduce the drag to an extent of about 40% with a total energy saving of 7%. [6–10] The flow generated by WOS, $w = W_m \cos(\omega t)$, is called the second Stokes problem or the Stokes layer [11], with a velocity distribution as (Eq. **1**):

$$w(y,t) = W_m \cos(\omega t - ky)e^{-ky}, k = \sqrt{\frac{\omega}{2\nu}} \tag{1}$$

Plenty of studies have tried to figure out how the Stokes layer reduces the drag and weakens the near-wall turbulence after Jung et al. first performed the numerical experiment of WOS control in a turbulent channel flow [6].

Since the spanwise velocity becomes non-negligible in the transport equations of Reynolds stresses after control, some studies analyzed the differences in the energy budget of turbulence. A reduced pressure-strain correlation term is believed to be closely related to the suppression of the wall-normal stress, which led to a reduction in the level of shear stress and streamwise stress. Hence, the near-wall turbulence is weakened, leading to a reduction of skin friction at the wall [12–15]. Also, the pressure-strain terms play a significant role during the transient response after control [16]. However, the mechanism of the Stokes layer suppressing the pressure-strain correlation is still unclear. The quasi-streamwise vortex and streaks are significant structures in the self-sustaining cycle of near-wall turbulence, and were found to be inclined periodically with the wall motion [17–19]. Some models based on linearized Navier–Stokes equations were proposed to described the relation between the Stokes layer and the inclination [17, 20]. It is also thought that the inclined streaks and vortex weaken the generation of turbulence, and thus led to a reduction in the drag [14, 15, 21]. The Reynolds number dependence of the WOS control is of vital significance, since the Reynolds number around a real aircraft, $Re_\tau \sim O(10^5)$, is much higher than that accessible with DNS. The drag reduction rates were found decrease with an increasing Reynolds number, and the trend is approximated as $DR \sim Re_\tau^{-(0.2\sim0.3)}$ [22, 23]. Hurst et al. thought the control effects in the viscous sublayer region are weakened at high Reynolds number, thus leading to lower drag reduction rates [23]. Further, they thought the drag reduction could remain at a level of 30% when the Re_τ went to infinity since the turbulence in the log-law region is always weakened [23]. It was also found the control effects on large-scale structures are weakened at high Reynolds number [24]. Agostini and Leschziner found the asymmetric modulation of $u' > 0$ and $u' < 0$ large-scale structures on the small-scale structures in a $Re_\tau = 1000$ channel flow with the WOS control [14, 25]. There is still not a generally accepted mechanism of the drag reduction deterioration in high Reynolds number flows, and reviews on the WOS control in drag reduction are referred to [2, 10, 26].

The Stokes layer is simple and proven effective in reducing drag by many experimental and numerical results, but the periodic wall motion might not be easily attainable in practical applications. Using other methods to generate an oscillatory spanwise motion to mimic the Stokes layer has also gained much research interest. A streamwise traveling wave of wall motion [27–30], rotating discs [31–33], wavy riblets [27], spanwise forcing [34–36], and spanwise jet [37] have been investigated and found effective in reducing drag. A spanwise traveling wave of the blowing and suction method is studied in the present work to reduce skin friction in a fully developed turbulent channel flow. Different from a streamwise traveling wave [38–40], which can reduce the drag even to a laminar level by increasing the flow rate, the spanwise traveling wave investigated here has a periodically reversing propagation direction, noted as WBS. The Reynolds number dependence of the drag reduction and its mechanism are mainly discussed in this study.

This manuscript is arranged as follows. *Control Strategy* section introduces the motion induced by the spanwise traveling wave and the uncontrolled base-flow. *Results and Discussion* section shows the performances of this control strategy and analyze the mechanism in the channel flows with $Re_\tau = 180$ and $Re_\tau = 550$. *Conclusion* section reports the conclusions.

CONTROL STRATEGY

The Motion Induced by the Traveling Wave

Min et al. found that an upstream traveling wave of blowing and suction can achieve a sustained sub-laminar drag in a turbulent channel flow [38]. However, some studies have proved that this kind of traveling wave can generate a flux opposed to the wave propagation direction [40], and it is more like a pumping than drag reduction effect [39]. Inspired by the streamwise traveling wave, we make the wave reverse in the spanwise direction periodically to mimic the oscillatory wall motion in WOS, shown in Eq. **2**.

$$\hat{v}_w = \begin{cases} \hat{V}_0 \cos\left(\hat{k}_z \hat{z} - \hat{\omega}\hat{t}\right) & , \quad 0 < \hat{t} < \hat{T}_a \\ \hat{V}_0 \cos\left(\hat{k}_z \hat{z} + \hat{\omega}\hat{t} + \hat{\phi}_0\right) & , \quad \hat{T}_a < \hat{t} < 2\hat{T}_a \end{cases} \tag{2}$$

where $\hat{\phi}_0 = -2\hat{\omega}\hat{T}_a$ is a constant phase as a result of the continuity at $\hat{t} = \hat{T}_a$ In the first half period $0 < \hat{t} < \hat{T}_a$, the wave travels in $+z$ direction and generates a$-z$ direction spanwise motion, while in the second half period $\hat{T}_a < \hat{t} < 2\hat{T}_a$, it travels in $-z$ direction and generates a$+z$ direction spanwise motion, as shown in **Figure 1**. With a non-dimensionalization in length scale by $z = \hat{k}_z \hat{z}$, time scale by $t = \hat{\omega}\hat{t}$, and velocity by $v = \hat{v}/\hat{V}_0$, respectively, the actuation is rewritten as:

$$v_w = \begin{cases} \cos(z - t) & , \quad 0 < t < \hat{\omega}\hat{T}_a \\ \cos(z + t + \phi_0) & , \quad \hat{\omega}\hat{T}_a < t < 2\hat{\omega}\hat{T}_a \end{cases} \tag{3}$$

To resolve the WBS induced flow in a quiescent background, an asymptotic expansion method is applied as shown in Eq. **4a–c**:

$$w = w_0 + \alpha w_1 + \alpha^2 w_2 + O\left(\alpha^3\right) \tag{4a}$$

$$v = v_0 + \alpha v_1 + \alpha^2 v_2 + O\left(\alpha^3\right) \tag{4b}$$

$$p = p_0 + \alpha p_1 + \alpha^2 p_2 + O\left(\alpha^3\right) \tag{4c}$$

where $\alpha = \hat{V}_0/\hat{c}$, the ratio of the blowing and suction amplitude over the wave speed, is assumed as a small parameter, (w_0, v_0, p_0) are the zero-order terms, (w_1, v_1, p_1) are the first order terms, and (w_2, v_2, p_2) and higher order terms are not considered here. Without losing generality, the zero order terms are solved in the first half period $t < \hat{\omega}\hat{T}_a$ as:

$$w_0(y,z,t) = \frac{iH}{2(1-H)}\left(e^{-y} - e^{-Hy}\right)e^{i(z-t)} + c.c. \tag{5a}$$

$$v_0(y,z,t) = \frac{1}{2(1-H)}\left(-He^{-y} + e^{-Hy}\right)e^{i(z-t)} + c.c. \tag{5b}$$

$$H = \sqrt{1 - i\beta} = a - bi \tag{5c}$$

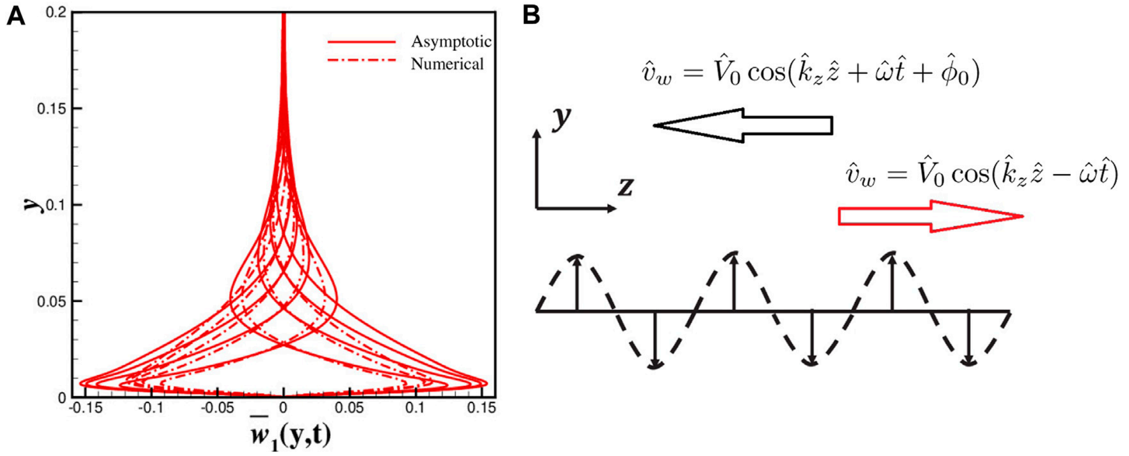

FIGURE 1 | (A) Spanwise velocity $\bar{w}_1(y,t) = 0$ from the numerical simulation (dash-dot line) and asymptotic solution (solid line, Eqs **8a-e**) and **(B)** the sketch of the actuation.

$$a = \sqrt{\frac{1}{2}\left(\sqrt{\beta^2+1}+1\right)} \tag{5d}$$

$$b = \sqrt{\frac{1}{2}\left(\sqrt{\beta^2+1}-1\right)} \tag{5e}$$

where $i = \sqrt{-1}$ is the imaginary unit, and *c.c.* represents the complex conjugate. The Reynolds number β is based on the frequency $\hat{\omega}$ and wave number $\hat{k}_z$ as:

$$\beta = \frac{\hat{\rho}\hat{\omega}}{\hat{\mu}\hat{k}_z^2} \tag{6}$$

The zero-order terms are a traveling wave in the same direction as actuation, which is also called the harmonic part in the manuscript. The harmonic part decays as the distance to the wall y increases, and the protrusion height is defined as $\hat{\delta} = 0.73\hat{\lambda}_z$, where the amplitude of the velocity is only 1% of that at the wall.

The average of the first order terms is of much significance in this study:

$$\bar{w}_1(y,t) = \lim_{L\to\infty}\int_{-L}^{L} w_1(y,z,t)dz \tag{7}$$

And it can be solved with known zero order terms (Eq. **5a, b**):

$$\bar{w}_1(y,t) = \sum_{n=1}^{\infty} f_n(y)\exp(in\omega_0 t) + c.c.$$

$$f_n(y) = C_n \exp\left(-\sqrt{in\beta\omega_0 y}\right) + f_{n,1}(y) + f_{n,2}(y) + f_{n,3}(y) \tag{8a}$$

$$f_{n,1}(y) = \frac{[2(1+a)-in\gamma]\cos(by) - 2(1+a)b\sin(by)}{[2(1+a)-in\gamma]^2 + 4(1+a)^2 b^2}$$

$$\times \frac{b^2(a-a^2+1)\beta}{2a(a-1)in\pi}[(-1)^n - 1]e^{-(1+a)y} \tag{8b}$$

$$f_{n,2}(y) = \frac{[2(1+a)-in\gamma]\sin(by) + 2(1+a)b\cos(by)}{[2(1+a)-in\gamma]^2 + 4(1+a)^2 b^2}$$

$$\times \frac{b^2(a+1)\beta}{2a(a-1)in\pi}[(-1)^n - 1]e^{-(1+a)y} \tag{8c}$$

$$f_{n,3}(y) = \frac{b}{2(a-1)(4a^2 - in\gamma)in\pi}\beta[(-1)^n - 1]e^{-2ay} \tag{8d}$$

$$\gamma = \beta\omega_0, \omega_0 = \frac{\pi}{\omega T_a} \tag{8e}$$

where the constant $C_n = -[f_{n,1}(0) + f_{n,2}(0) + f_{n,3}(0)]$ determined by the $\bar{w}_1(y,t) = 0$ boundary condition at $y = 0$. This asymptotic solution matches the numerical results well with a slightly smaller amplitude, as shown in **Figure 1A**. The expression $\exp(-\sqrt{in\beta\omega_0 y})\exp(in\omega_0 t)$ in Eqs **8a-e** is the same as the Stokes layer with frequency $n\omega_0$.In other words, the induced oscillatory spanwise motion $\bar{w}_1(y,t)$ comprises a series of the Stokes layers with a frequency $n\pi/\hat{\omega}\hat{T}_a$. Obviously, a large divergence exists between $\bar{w}_1(y,t)$ and the Stokes layers within a very thin region above the wall as a result of different boundary conditions. The thickness of the first Stokes layer in the series (Eqs **8a-e**), $\delta_s = 4.6\sqrt{2/(\omega_0\beta)}$ or $\hat{\delta}_s \propto \sqrt{\hat{T}_a}$ with dimensions, is also regarded as the penetration height of the spanwise motion. The higher order terms in Eqs **8a-e**, or the Stokes layers with multiple frequency $n\omega_0$, are always neglected for analysis as their thickness is $1/\sqrt{n}$ less and the amplitude is $1/n$ less. In the limit of $\hat{\omega}\to\infty$, the amplitude of $\bar{w}_1(y,t)$ can be approximated by $\hat{W}_m \approx \hat{V}_0^2/\sqrt{8\hat{\nu}\hat{\omega}}$. When the frequency is zero, $\hat{\omega} = 0$, there is no average spanwise motion since the traveling wave degenerates to a constant blowing and suction. It is noticed that the relative error of asymptotic solutions is approximately less than 10% when the parameter $\alpha = \hat{V}_0\hat{k}_z/\hat{\omega}$ satisfies $\alpha < 0.5$. As a result, the oscillatory spanwise motion in Eqs **8a-e** is called the Stokes part in the rest of the manuscript.

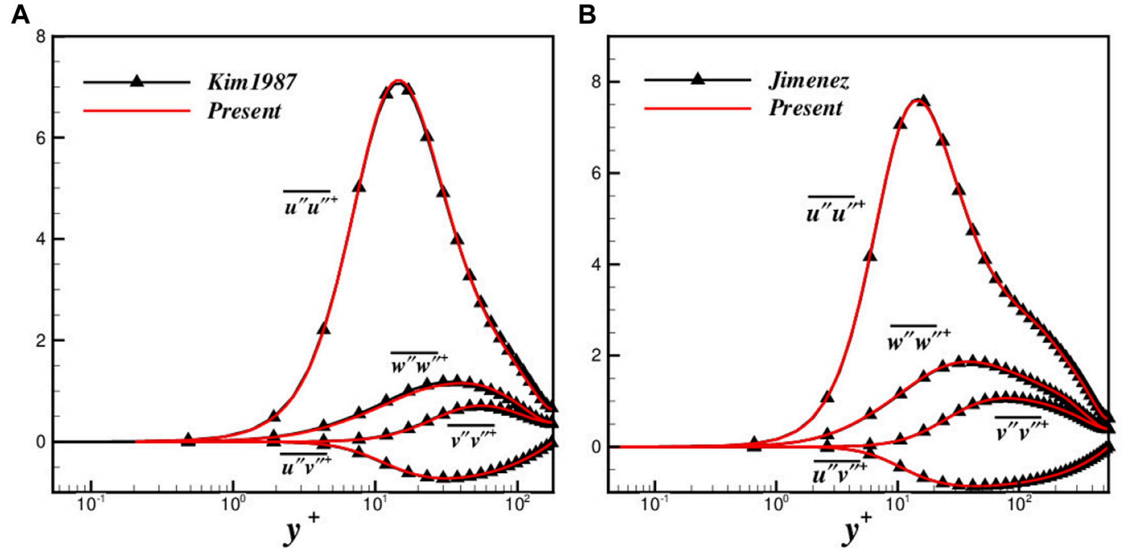

FIGURE 2 | Comparison of Reynolds stress **(A)** between the present study and Kim et al. [45] with $Re_\tau = 180$, and **(B)** between the present study and Jiménez et al. [46] with $Re_\tau = 550$.

In summary, the motion induced by the spanwise traveling wave can be approximately decomposed into a harmonic part (Eq. **5a, b**) and a Stokes part (Eqs **8a-e**) with the asymptotic solution.

The Numerical Method and Base Flow

Incompressible fully developed turbulent channel flows with $Re_\tau = u_\tau h/\nu \approx 180$ ($Re_b = \rho U_b h/\mu = 2800$) and $Re_\tau = u_\tau h/\nu \approx 550$ ($Re_b = \rho U_b h/\mu = 10000$) are chosen as the base flow for control, where $u_\tau = \tau_w/\rho$ is the friction velocity and U_b is the bulk velocity of the channel. For the $Re_\tau = 180$ channel flow, the computation domain is set as $[0, 2\pi h]$ in streamwise (x) direction, $[-1, 1]$ in wall-normal (y) direction, and $[0, \pi h]$ in spanwise (z) direction, with h the half channel height. In this study, (u, v, w) represents the velocities in (x, y, z) direction, respectively. The grid points are $N_x \times N_y \times N_y = 113 \times 169 \times 113$ with a corresponding resolution $\Delta x^+ \approx 10.1$, $\Delta z^+ \approx 5.0$. Here, the "+" superscript represents inner-scale variables normalized by u_τ and $\delta_\nu = \nu/u_\tau$. A hyperbolic tangent function $y = \tanh[r(2y_i - 1)]/\tanh(r)$, $y_i = (i-1)/(N_y - 1)$ decides the grid distribution in wall-normal direction. The resolution $0.2 < \Delta y^+ < 5.2$ is achieved with a stretch ratio $r = 2.4$. And for the channel flow with $Re_\tau = 550$, the computation domain is $[0, 3\pi h] \times [-1, 1] \times [0, 2\pi h]$ to resolve the large-scale structures [41, 42], with the resolution $\Delta x^+ \approx 7.6$, $\Delta z^+ \approx 7.7$, and $0.04 < \Delta y^+ < 2.9$.

High order methods based on CPR(correction procedure via reconstruction) [43] are used here and seventh order polynomials are used for space discretization. For the viscous term, it is discretized with BR2 (the second approach of Bassi and Rebay) [44] and interior penalty method. The time advancement strategy is a third order explicity Euler scheme with a time step $dt = 1 \times 10^{-4}$ ($dt^+ = dt \cdot u_\tau/\delta_\nu \approx 0.00116$). A constant flow rate (CFR) method is chosen in the computations of the channel flows. All the computations in this study are conducted with this type of direct numerical simulations (DNS).

The length and velocity scales are normalized by h and U_b in the turbulent channel flows without particular specification, respectively. Comparisons of our numerical results with those from Kim et al. [45]($Re_\tau = 180$, and with those from Jiménez et al. [46]($Re_\tau = 550$) in Reynolds stress of the uncontrolled channel flows is done firstly for verification of our computation code, which show a satisfying match in **Figure 2**. The vortex structures detected by Q-value also show a good match with previous work, see **Figures 3A, B**.

RESULTS AND DISCUSSION

The spanwise traveling wave of blowing and suction control is imposed only at the bottom wall ($y = -1$) of the channel flow with an uncontrolled upper wall ($y = 1$), as shown in **Figure 3C**. In this section, the drag reduction performance of the WBS control is studied, and the drag reduction rate, noted as DR, is defined as:

$$\begin{aligned} DR &= \frac{\tau_{w0} - \tau_w}{\tau_{w0}} \times 100\%, \\ \tau_w &= \frac{1}{N_x N_y N_t} \sum_{n=1}^{N_t} \sum_{i=1}^{N_x} \sum_{k=1}^{N_z} \mu \left. \frac{\partial u(i,k,n)}{\partial y} \right|_{y=-1} \end{aligned} \tag{9}$$

where τ_w is the averaged skin friction of the bottom wall, and the subscript with '0' means the results in uncontrolled flow. The test cases in this manuscript are show in **Table 1**. In our previous work [15], it has been shown that the WBS control leads to a close drag reduction rate to the WOS control with the same parameter (W, T_a). The drag reduction rates are much smaller with $Re_\tau =$

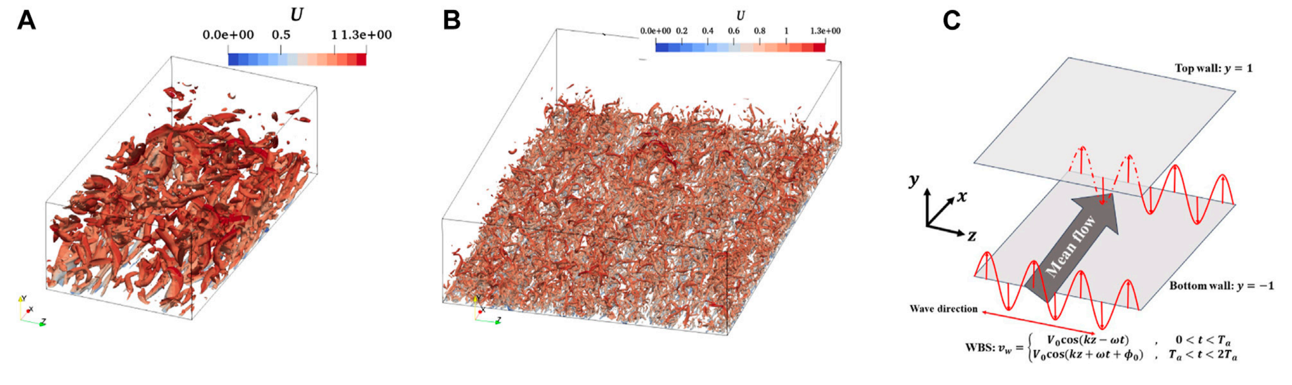

FIGURE 3 | (A) Q iso-surface in Re_τ = 180, and **(B)** Re_τ = 550. **(C)** The sketch of WBS control strategy.

TABLE 1 | The parameters and drag reduction rates of the test cases with $W = V_0^2/\sqrt{8\nu\omega}$.

Re_τ	Cases	(V_0, k_z, ω)	W^+	T_a^+	DR
55	WBS-1	$(0.37, 16, 32\pi)$	10.2	60	5.8%
	WBS-2	$(0.37, 32, 32\pi)$	10.2	60	7.5%
	WBS-3	$(0.37, 32, 16\pi)$	10.2	60	−2.4%
180	WBS-4	$(0.5, 16, 16\pi)$	10.2	116	21.3%
	WBS-5	$(0.5, 16, 16\pi)$	10.2	57.9	24.5%
	WBS-6	$(0.5, 8, 16\pi)$	10.2	57.9	20.7%

TABLE 2 | Drag reduction decomposition of the cases.

Cases	DR^I	DR^O	DR^P	DR
WBS-1	2.2%	11.0%	−1.5%	5.8%
WBS-2	2.2%	13.1%	−0.2%	7.5%
WBS-3	1.0%	−2.3%	−3.4%	−2.4%
WBS-4	10.2%	32.8%	−1.3%	21.3%
WBS-5	12.0%	38.9%	−0.7%	24.5%
WBS-6	11.3%	30.2%	−0.1%	20.7%

550 than those with $Re_\tau = 180$, while they have nearly the same optimal period $T_a^+ \approx 60$. Gatti et al. [22, 47] has shown the drag reduction rate dependence on Reynolds number $DR \sim Re_\tau^{-(0.2\sim0.3)}$, in WOS control. Obviously, the decrease in DR with increasing Re_τ in WBS control is much larger.

FIK Identity Analysis

The variables in WBS control are decomposed into three parts:

$$\begin{aligned} a(x,y,z,t) &= \bar{a}(y) + \tilde{a}(y,\phi) + a''(x,y,z,t) \\ &= \langle a\rangle(y,\phi) + a''(x,y,z,t) \end{aligned} \tag{10}$$

where $\bar{a}$ is the ensemble average, $\langle a\rangle(y,\phi)$ the phase average with ϕ representing the phase, and $a''(x,y,z,t)$ the turbulent fluctuations $\tilde{a} = \bar{a} - \langle a\rangle$ is the difference between the phase average and ensemble average, which is also called the periodic part. Fukagata, Iwamoto and Kasagi proposed an identity (known as FIK identity) relating the skin friction at the wall and the turbulent shear stress in the interior field. While in WBS control, it is rewritten as:

$$\begin{aligned} 2C_f^b - C_f^u = \underbrace{\frac{6}{Re_b}}_{C_f^L} + \underbrace{3\int_{-1}^{1}(1-y)\left(-\overline{u''v''}\right)dy}_{C_f^T} \\ + \underbrace{3\int_{-1}^{1}(1-y)\left(-\overline{\tilde{u}\tilde{v}}\right)dy}_{C_f^P} \end{aligned} \tag{11}$$

where C_f^L is the skin friction in uncontrolled flow, C_f^T the contribution from turbulent shear stress, and C_f^P the contribution from the shear stress formed by the periodic parts, respectively.

The turbulent skin friction part can be further decomposed into two parts [23, 24], one from the inner region ($y^+ < y_P^+ \approx 30$) and the other from the outer region ($y^+ > 30$), as shown in Eq. **12**.

$$\begin{aligned} 3\int_{-1}^{1}(1-y)\left(-\overline{u''v''}\right)dy = \int_{-1}^{y_P}(1-y)\left(-\overline{u''v''}\right)dy \\ + \int_{y_P}^{1}(1-y)\left(-\overline{u''v''}\right)dy \end{aligned} \tag{12}$$

Therefore the drag reduction rate can be decomposed as shown in Eqs **13a-d**:

$$2\cdot DR = DR^I + DR^O + DR^P \tag{13a}$$

$$DR^I = \frac{1}{C_{f0}}\left[3\int_{-1}^{y_P}(1-y)\left(\overline{u''v''}_0 - \overline{u''v''}\right)dy\right] \tag{13b}$$

$$DR^O = \frac{1}{C_{f0}}\left[3\int_{y_P}^{1}(1-y)\left(\overline{u''v''}_0 - \overline{u''v''}\right)dy\right] \tag{13c}$$

$$DR^P = \frac{1}{C_{f0}}\left[3\int_{-1}^{1}(1-y)\left(-\overline{u''v''}\right)dy\right] \tag{13d}$$

where DR^I, DR^O, and DR^P represents the drag reduction rate from the inner region, outer region, and periodic part, respectively. The factor "2" on the left-hand side of Eqs **13a-d** comes from the one-side control in the channel flows. The drag reduction decomposition of the cases is shown in **Table 2**. The DR is mainly from DR^I and DR^O. DR^P is always negative, which means the periodic blowing and suction has a negative effects to the drag reduction. On the other hand, compared to DR^I and

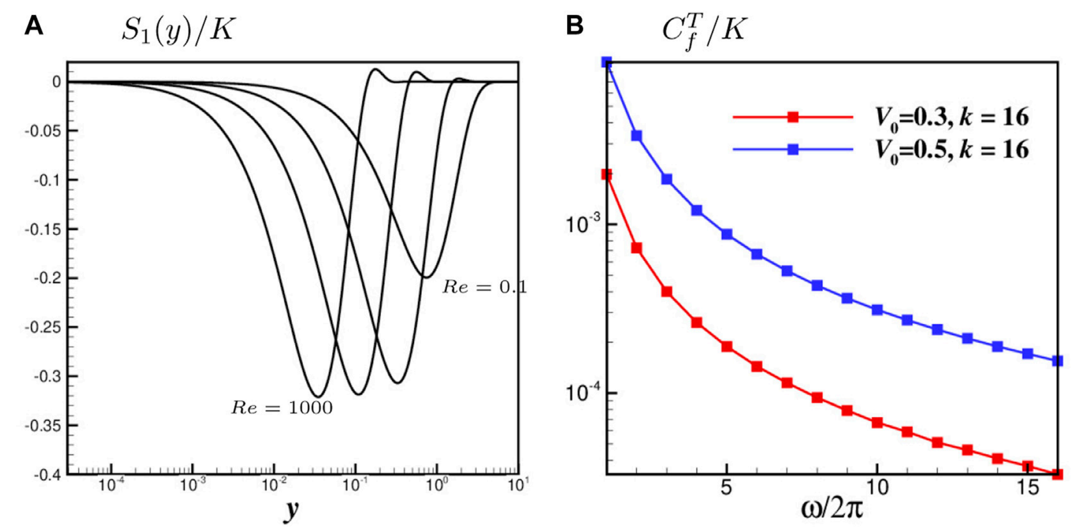

FIGURE 4 | (A) $S_1(y)/K$ with different Reynolds number and **(B)** C_f^P/K variation with different frequency ω.

DR^O, DR^P is much smaller and even can be neglected when $Re_\tau = 180$. While $Re_\tau = 550$, the DR^P becomes larger and even dominates in Case WBS-3. The strength of the oscillatory spanwise motion W^+ is larger in Case WBS-3 compared to other cases with Re_τ, but DR decreases a lot to a negative value. This means the negative effects of the periodic part on DR in this case become significant. The wavenumber increases from $k_z = 8$ (Case WBS-6) to $k_z = 16$ (Case WBS-5), the increases in DR are mainly from DR^O, as a result of a smaller protrusion height $\delta = 0.73\lambda_z$. In addition, the DR gets smaller mainly from the decreases of DR^O when Re_τ increases, similar to the results in WOS control [23, 24].

The effects of DR^P can be described by the lift-up mechanism from the harmonic parts of blowing and suction. Based on the asymptotic expansion (Eq. **4a–c**), the streamwise velocity can be written as $u = u_0 + \alpha u_1 + \alpha^2 u_2 + O(\alpha^3)$, and its equation is:

$$\frac{\partial u}{\partial x}+\alpha\left(v\frac{\partial u}{\partial y}+w\frac{\partial w}{\partial z}\right)=-\frac{\partial p}{\partial x}+\frac{1}{Re}\left(\frac{\partial^2 u}{\partial y^2}+\frac{\partial^2 u}{\partial z^2}\right) \tag{14}$$

Since it is uniform in streamwise direction, there is no $\partial/\partial x$ terms in the equation, and u can be solved with a known (v, w). In addition, u_0 is the prescribed baseflow and not dependent on (v, w). Here, it is assumed that $u_0 = Ky$ without losing generality, since the linear relation is always true in the linear law region [48]. Thus, the first order term u_1 can be solved with (v_0, w_0):

$$u_1 = K\left[\frac{iH}{2(1-H)}\left(e^{-y}-e^{-Hy}\right)-\frac{Re}{4H(1-H)ye^{-Hy}}\right]\exp[i(z-t)] + c.c. \tag{15}$$

It is obvious that $u_1 < 0$ above the blowing regions and $u_1 > 0$ above the suction region, which is thought as a lift-up mechanism. Thus, there forms a negative shear stress uv, which is closely related to the C_f^P. Further, the spanwise average of the shear stress, noted as $S(y)$, can be deduced:

$$S(y) = \lim_{L_z\to\infty}\frac{1}{L_z}\int_0^{L_z} uv dz = S_0(y) + \alpha S_1(y) + O(\alpha^2) \tag{16a}$$

$$S_0(y) = 0 \tag{16b}$$

$$S_1(y) = \lim_{L_z\to\infty}\frac{1}{L_z}\int_0^{L_z} u_1 v_0 dz = \frac{K}{(1-a)^2+b^2}\left(Sy_1 + Sy_2\right) \tag{16c}$$

$$Sy_1 = \left[-(a^2+b^2)\sin by + \frac{Re(\cos by - 2ab\sin by)}{2(a^2+b^2)}y + (b\cos by + a\sin by)\right]e^{-(1+a)y} \tag{16d}$$

$$Sy_2 = -\left[b + \frac{aRe}{2(a^2+b^2)}y\right]e^{-2ay} \tag{16e}$$

In addition, the skin friction from the periodic part, C_f^P, can be evaluated as:

$$C_f^P \approx 3\int_{-1}^{1}(1-y)[-S(y)]dy \approx 3K\int_{-1}^{1}(1-y)\left(-\alpha\frac{S(y)}{K}\right)V_0^2 dy \tag{17}$$

As shown in **Figure 4**, the $S(y)/K$ is always negative, leading to a positive C_f^P. As a result, the periodic parts always increase the skin friction, just as shown in **Table 2**. C_f^P decreases with an increasing frequency ω, which is also compliant with the results of Case WBS-2 and WBS-3. It is also found that $C_f^P \propto K$, which means that the larger the shear $K = \partial U/\partial y$ is in the background flow, the larger C_f^P is. When Re_τ changes from 180 to 550, K increases and leads to a larger C_f^P, just as the results in **Table 2**.

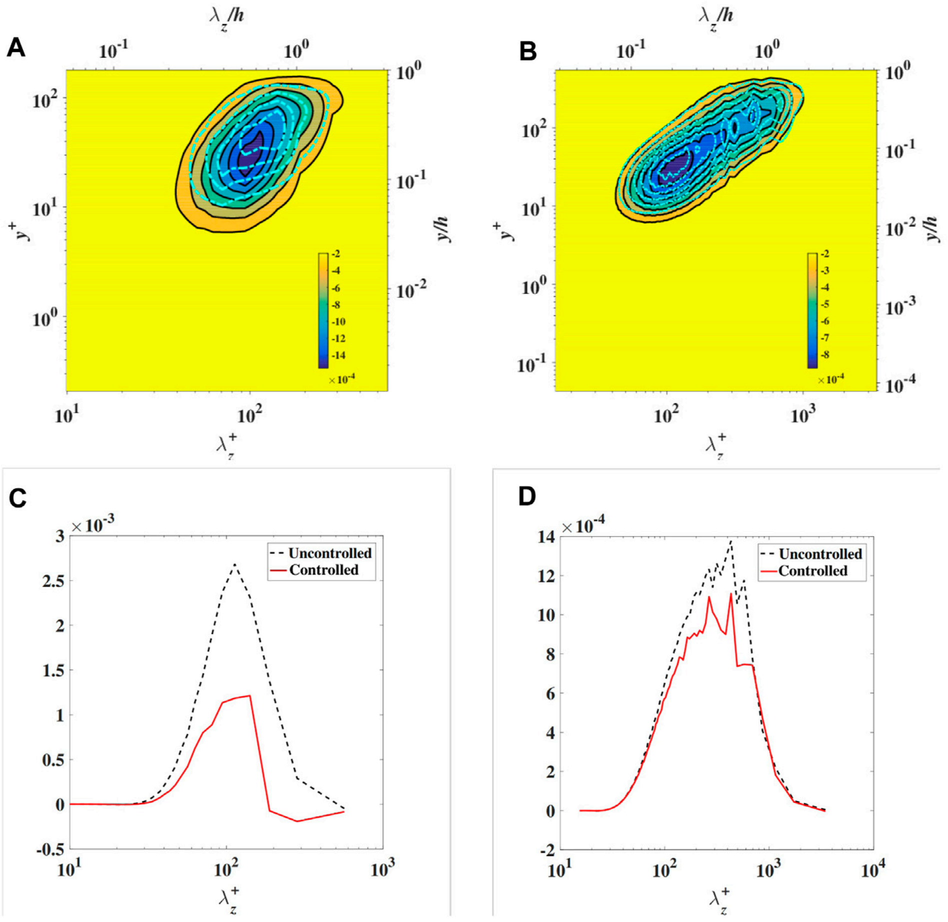

FIGURE 5 | The pre-multiplied shear stress $\kappa\overline{u''v''}(\kappa)$ in **(A)** Case WBS-5, and **(B)** Case WBS-2, and skin friction coefficients $\kappa C_f^T(\kappa)$ in **(C)** Case WBS-5, and **(D)** Case WBS-2. The dash-line represent the results in the uncontrolled case.

As discussed in *Control Strategy* section, the induced flow by the traveling wave of blowing and suction with a periodically reversed wave speed can be decomposed into two parts, one is the harmonic part (zero order terms) and the other is the Stokes part (first order terms). The harmonic part will induce a negative shear stress, as shown in Eq. **16c**, and lead to a positive contribution the skin friction through C_f^P. An effective way to reduce C_f^P is increasing ω, while an increased ω will lead to a smaller strength $W = V_0^2/\sqrt{8\nu\omega}$ of the Stokes part. Therefore, there should be an optimal frequency in the WBS control, which is not discussed in details in this manuscript. In addition, C_f^P becomes larger with an increasing mean flow shear $\partial u/\partial y$ in the viscous sublayer when Re_τ changes from 180 to 550. This is thought to be the first reason that the drag reduction rate is smaller in $Re_\tau = 550$ cases.

Scale Separation Analysis

In this section, a Fourier expansion based on spanwise direction is imposed to the fluctuation field variables, $u'' = \sum_{\kappa=1}^{\infty}\hat{u}(\kappa)\exp(i\kappa z) + c.c.$ Thus the stress can be decomposed into different scales as:

$$\overline{u_i''u_j''} = \overline{\left(\sum_{\kappa=1}^{\infty}\hat{u}_i(\kappa)\exp(i\kappa z) + c.c.\right)\left(\sum_{\kappa=1}^{\infty}\hat{u}_j(\kappa)\exp(i\kappa z) + c.c.\right)} = \sum_{\kappa=1}^{\infty}\overline{\hat{u}_i(\kappa)\hat{u}_j(\kappa)^*} \tag{18}$$

where the superscript "*" represents the complex conjugate. As a result, the skin friction coefficient from the turbulent shear stress, C_f^T can be also decomposed:

$$C_f^T = 3\int_{-1}^{1}(1-y)\left(-\overline{u''v''}\right)dy = \sum_{\kappa=1}^{\infty}\underbrace{\left[3\int_{-1}^{1}(1-y)\left(-\overline{u''v''}(\kappa)\right)dy\right]}_{C_f^T(\kappa)} \tag{19}$$

Thus, the contribution from the scale $\lambda = 2\pi/\kappa$ to the turbulent skin friction is $C_f^T(\kappa)$. The pre-multiplied spectrum of turbulent shear stress, $\kappa\overline{u''v''}(\kappa)$, and the skin friction coefficients, $\kappa C_f^T(\kappa)$,

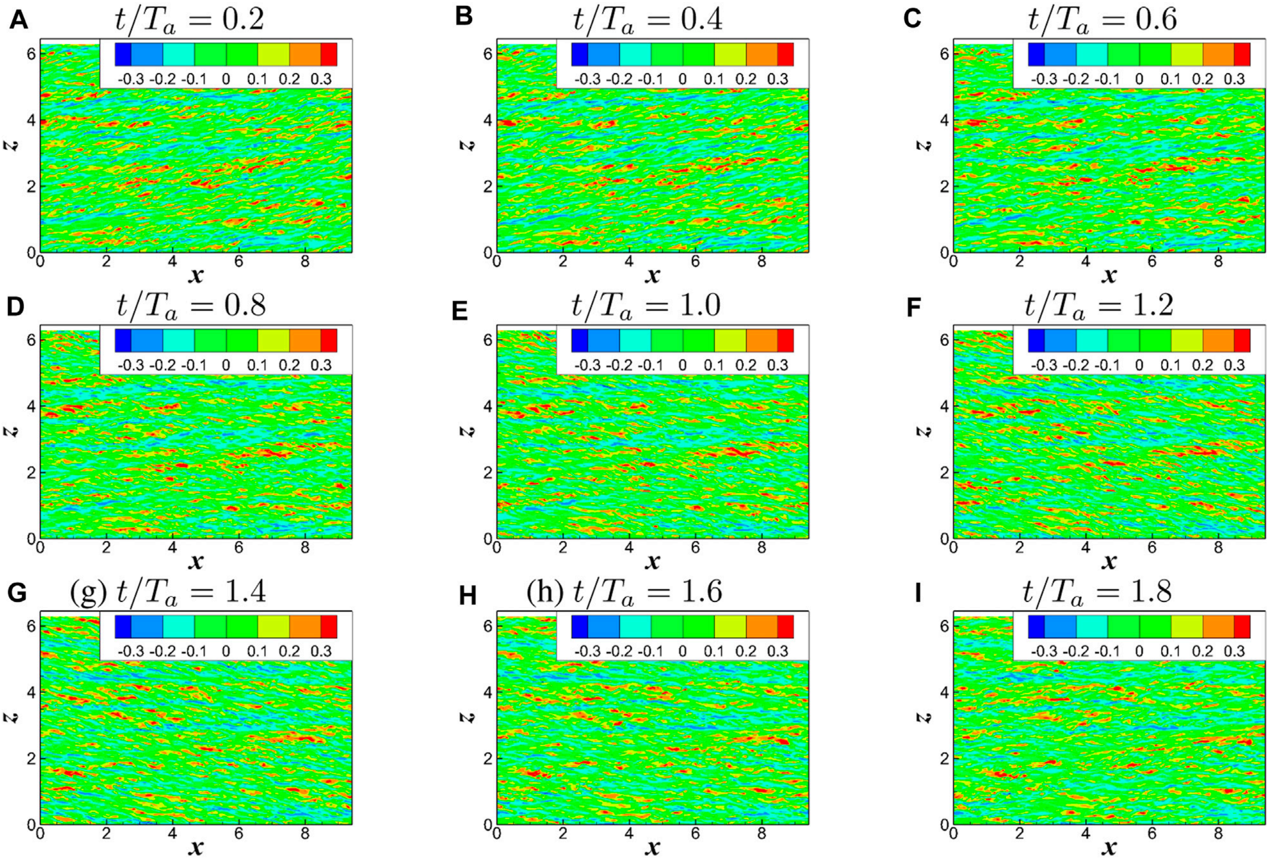

FIGURE 6 | The streaks (u'' contour) at $y^+ \approx 11$ in Case WBS-2 with $Re_\tau = 550$ at $t/T_a = 0.2$–1.8 in **(A–I)**.

of Case WBS-5 with $Re_\tau = 180$ and Case WBS-2 with $Re_\tau = 550$ are shown in **Figure 5**. The skin friction of all scale structure decreases after control in $Re_\tau = 180$ case, while that of the medium scale, $100 < \lambda^+ < 700$, decreases in $Re_\tau = 550$ case. In addition, the spectrum $\kappa\overline{u''v''}(\kappa)$ gets reduced nearly in the whole region, $y/h < 1$, while the spectrum gets reduced in the region $y^+ < 30$. As the Re_τ increases, the contribution to the skin friction in the outer region increases, while the spanwise motion mainly affects the inner region, so the drag reduction rate is smaller in $Re_\tau = 550$ than that in $Re_\tau = 180$, as shown in **Figure 5**. To further analyze the control effects on the structures with different scales, we use a cut-off wavelength to divide the whole scale into large-scale (noted as LS) and small-scale (noted as SS) structures. The cut-off wave length is chosen as $\lambda^+_{zc} = 300$, which separates the two local maximum in the pre-multiplied spectrum, that is:

$$u'' = \sum_{\kappa=1}^{\infty} u''(\kappa) = \underbrace{\sum_{\kappa<2\pi/\lambda_{zc}} u''(\kappa)}_{LS} + \underbrace{\sum_{\kappa>2\pi/\lambda_{zc}} u''(\kappa)}_{SS} \tag{20}$$

It was found that the vortex structures are inclined by the Stokes layers in WOS, which has a close relation to the drag reduction mechanism [14, 15, 17–19]. In our previous analysis based on the $Re_\tau = 180$ channel flow, the inclination is thought to be a representation of the stretch of the streamwise vortex, $\partial u''/\partial x$. $\partial u''/\partial x$ gets reduced after control, leading to a weakened pressure-strain term $\phi_{11} = \overline{p''\partial u''/\partial x}$. Thus, the energy transported into the wall-normal stress $\overline{v''v''}$ from the streamwise stress $\overline{u''u''}$ is reduced as a result of the incompressibility, $\phi_{11} + \phi_{22} + \phi_{33} = 0$ [15]. Here we revisited the inclination of vortex structures in the controlled flow with $Re_\tau = 550$. **Figure 6** shows the streaks at $y^+ \approx 11$ in Case WBS-2 in one period. The inclination of the streaks is similar as that in $Re_\tau = 180$ case. Also, the inclinations of streaks can be described by the inclinations of the two-point correlation, $C(\Delta x, \Delta z)$, which is defined as:

$$C(\Delta x, \Delta z) = \frac{\overline{u''(x, y, z, t)u''(x + \Delta x, y, z + \Delta z, t)}}{\overline{u''(x, y, z, t)u''(x, y, z, t)}} \tag{21}$$

The contours of the streaks and $C(\Delta x, \Delta z)$ of SS and LS structures are shown in **Figure 7**. Thus, an inclination angle, noted as θ in radians, is defined as the angle between the axis of the iso-value line of $C(\Delta x, \Delta z)$ and the streamwise direction to give a quantitative description of the inclination of streaks. The

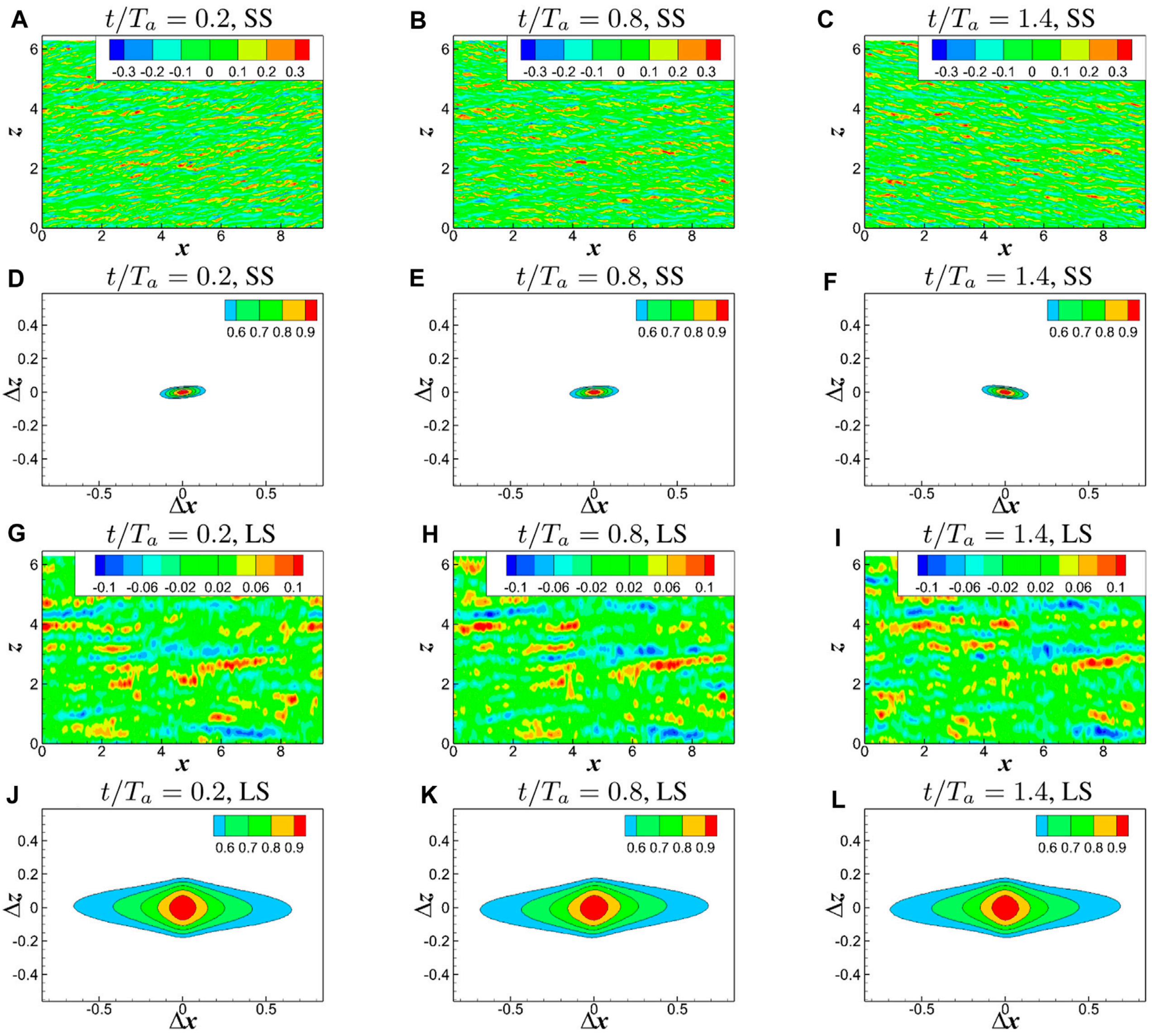

FIGURE 7 | The streaks at $y^+ = 11$ of SS structures **(A–C)** and LS structures **(G–I)**, and two-point correlation $C(\Delta x, \Delta z)$ of SS structures **(D–F)** and LS structures **(J–L)**.

angle $\theta(y,t)$ of whole scales and separated scales (SS and LS) in Case WBS-2 are shown in **Figure 8**. It is shown that the angle $\theta(y,t)$ has a phase difference at different wall distance y, which is induced by the spanwise motion [12, 14, 15]. The angle is largest at $y^+ \approx 11$, recalling that the spanwise motion affects the structures at this region most. Further for SS and LS structures, the angle of SS is nearly the same as all scale (AS) and much larger than that of LS. This tells us that the spanwise motion affects the SS structure more than the LS. In addition, the inclination of SS and LS structures has a phase delay.

In physical space, the oscillatory spanwise motion or the Stokes part mainly weakens the inner region ($y^+ < 30$), as shown in **Figure 5**. When the Re_τ gets larger with an increasing dominance of the outer region, the contribution from the inner region gets reduced, leading to a smaller drag reduction rate. In spectrum space, the Stokes part mainly affects the small-scale structures ($\lambda^+ < 300$). While the Re_τ gets larger, the large-scale structures become more significant, and the drag reduction is thus reduced.

CONCLUSION

In this study, the drag reduction performance of the spanwise traveling wave of blow and suction with a periodically

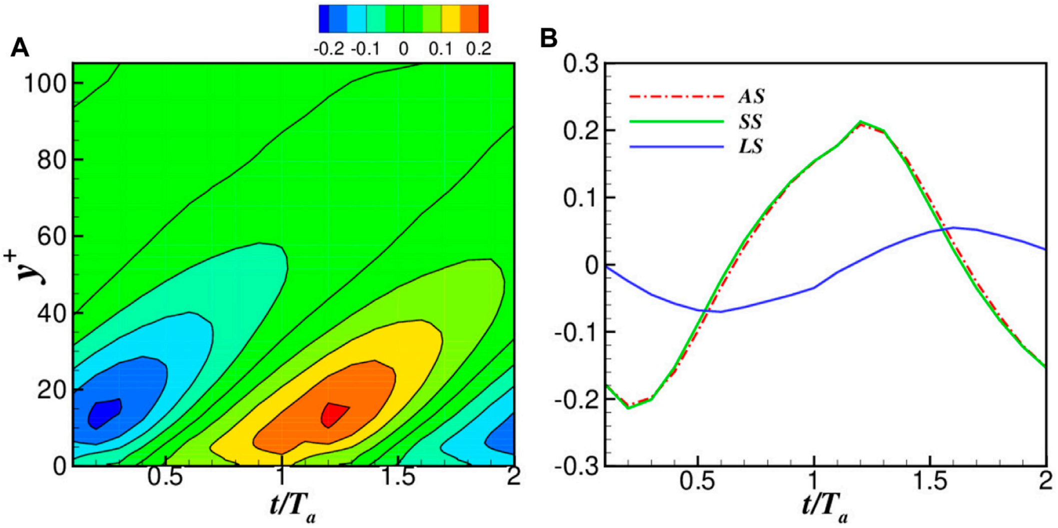

FIGURE 8 | The angles **(A)** $\theta(y, t)$ of whole scales and **(B)** $\theta(y^+ = 11, t)$ of LS, SS, and all-scale (AS).

reversing propagation direction in $Re_\tau = 180$ and $Re_\tau = 550$ turbulent channel flows is studied. An asymptotic expansion method is used to resolve the flow induced by this kind of actuation. The induced flow can be decomposed into the harmonic part ($O(\alpha^0)$ terms) and the Stokes part ($O(\alpha^1)$ terms), where the parameter $\alpha = V_0/c$ is the ratio of amplitude of blowing and suction over the wavespeed of the traveling wave. The harmonic part will induce a negative shear stress, and thus increase the skin friction of the channel. However, it is always at a negligible level compared to the turbulent shear stress with a proper set of parameters, such as a large ω and low Reynolds number Re_τ. The Stokes part, or oscillatory spanwise motion, can weaken the turbulence just as the wall oscillation control.

The drag reduction rates are much smaller in $Re_\tau = 550$ cases that those in $Re_\tau = 180$ cases. There are thought to be three reasons in this study. Firstly, the negative effects on the drag reduction rate from the harmonic part get larger in $Re_\tau = 550$ cases. Secondly, the Stokes part can weaken the turbulence in the inner region, while the inner region becomes less dominant in high Reynolds number cases. Thirdly, the Stokes part mainly affect the small-scale structure, and similarly the small-scale structures are less dominant in high Reynolds number cases.

DATA AVAILABILITY STATEMENT

The original contributions presented in the study are included in the article/supplementary material, further inquiries can be directed to the corresponding author.

AUTHOR CONTRIBUTIONS

All authors listed have made a substantial, direct, and intellectual contribution to the work and approved it for publication.

FUNDING

China-EU Program: Drag Reduction via Turbulent Boundary Layer Flow Control (DRAGY), Grant agreement ID: 690623.

CONFLICT OF INTEREST

The authors declare that the research was conducted in the absence of any commercial or financial relationships that could be construed as a potential conflict of interest.

REFERENCES

1. Schrauf G. Status and Perspectives of Laminar Flow. *Aeronaut J* (2005) 109(1102):639–44. doi:10.1017/s000192400000097x
2. Ricco P, Lesshziner MA. A Review of Turbulent Skin Friction Drag Reduction by Near Wall Transverse Forcing (2021). arXiv:2013.04719v1.
3. Choi H, Moin P, Moser R. Direct Numerical Simulation of Turbulent Flow Over Riblets. *J Fluid Mech* (1993) 255:503–39. doi:10.1017/s0022112093002575
4. Luchini P, Manzo F, Pozzi A. Resistance of a Grooved Surface to Parallel Flow and Cross-Flow. *J Fluid Mech* (1991) 228(228):87–109. doi:10.1017/s0022112091002641
5. Bechert DW, Bruse M, Hage JGT, Van Der Hoeven W, Hoppe G. Experiments on Drag-Reducing Surfaces and Their Optimization With an Adjustable Geometry. *J Fluid Mech* (1997) 338:59–87. doi:10.1017/s0022112096004673
6. Jung WJ, Mangiavacchi N, Akhavan R. Suppression of Turbulence in Wall-Bounded Flows by High-Frequency Spanwise Oscillations. *Phys Fluids A: Fluid Dyn* (1992) 4(8):1605–7. doi:10.1063/1.858381

7. Quadrio M, Ricco P. Initial Response of a Turbulent Channel Flow to Spanwise Oscillation of the Walls. *J Turbulence* (2003) 4(7):1–23. doi:10.1088/1468-5248/4/1/007
8. Ricco P, Quadrio M. Wall-Oscillation Conditions for Drag Reduction in Turbulent Channel Flow. *Int J Heat Fluid Flow* (2008) 29:891–902. doi:10.1016/j.ijheatfluidflow.2007.12.005
9. Quadrio M, Ricco P. Critical Assessment of Turbulent Drag Reduction Through Spanwise Wall Oscillations. *J Fluid Mech* (2004) 521:251–71. doi:10.1017/s0022112004001855
10. Quadrio M, Ricco P, Claudio V. Streamwise-Traveling Waves of Spanwise Wall Velocity for Turbulent Drag Reduction. *J Fluid Mech* (2009) 627:161–78.
11. Schlichting H, Gersten K. *Boundary Layer Theory*. 9 edition. Springer (2016).
12. Touber E, Leschziner MA. Near-Wall Streak Modification by Spanwise Oscillatory Wall Motion and Drag-Reduction Mechanisms. *J Fluid Mech* (2012) 693(2):150–200. doi:10.1017/jfm.2011.507
13. Ricco P, Ottonelli C, Hasegawa Y, Quadrio M. Changes in Turbulent Dissipation in a Channel Flow With Oscillating Walls (2012). *arXiv preprint arXiv:1202.3534*.
14. Agostini L, Touber E, Leschziner M. The Turbulence Vorticity as a Window to the Physics of Friction Drag Reduction by Oscillatory Wall Motion. *Int J Heat Fluid Flow* (2015) 51(3–15):3–15. doi:10.1016/j.ijheatfluidflow.2014.08.002
15. Huang Y, Wang L, Fu S. Drag Reduction in Turbulent Channel Flows by a Spanwise Traveling Wave of Wall Blowing and Suction. *Phys Fluids* (2021) 33: 095111. doi:10.1063/5.0061279
16. Xu C-X, Huang W-X. Transient Response of Reynolds Stress Transport to Spanwise Wall Oscillation in a Turbulent Channel Flow. *Phys Fluids* (2005) 17(1):018101. doi:10.1063/1.1827274
17. Blesbois O, Chernyshenko SI, Touber E, Leschziner MA. Pattern Prediction by Linear Analysis of Turbulent Flow With Drag Reduction by Wall Oscillation. *J Fluid Mech* (2013) 724:607–41. doi:10.1017/jfm.2013.165
18. Choi K-S. Near-Wall Structure of Turbulent Boundary Layer With Spanwise-Wall Oscillation. *Phys Fluids* (2002) 14(7):2530–42. doi:10.1063/1.1477922
19. Chernyshenko SI, Baig MF. The Mechanism of Streak Formation in Near-Wall Turbulence. *J Fluid Mech* (2005) 544:99–113. doi:10.1017/s0022112005006506
20. Moarref R, Jovanovic MR. Model-Based Design of Transverse Wall Oscillations for Turbulent Drag Reduction. *J Fluid Mech* (2012) 707: 205–40. doi:10.1017/jfm.2012.272
21. Yakeno A, Hasegawa Y, Kasagi N. Modification of Quasi-Streamwise Vortical Structure in a Drag-Reduced Turbulent Channel Flow With Spanwise Wall Oscillation. *Phys Fluids* (2014) 26(8):085109. doi:10.1063/1.4893903
22. Gatti D, Quadrio M. Performance Losses of Drag-Reducing Spanwise Forcing at Moderate Values of the Reynolds Number. *Phys Fluids* (2013) 25:125109. doi:10.1063/1.4849537
23. Hurst E, Yang Q, Chung YM. The Effect of Reynolds Number on Turbulent Drag Reduction by Streamwise Travelling Waves. *J Fluid Mech* (2014) 759: 28–55. doi:10.1017/jfm.2014.524
24. Yao J, Chen X, Hussain F. Reynolds Number Effect on Drag Control via Spanwise Wall Oscillation in Turbulent Channel Flows. *Phys Fluids* (2019) 31: 085108. doi:10.1063/1.5111651
25. Agostini L, Leschziner M. The Impact of Footprints of Large-Scale Outer Structures on the Near-Wall Layer in the Presence of Drag-Reducing Spanwise Wall Motion. *Flow, Turbulence and Combustion* (2018) 100:1037–61. doi:10.1007/s10494-018-9917-3
26. Leschziner MA. Friction-Drag Reduction by Transverse Wall Motion-A Review. *J Mech* (2020) 36:649–63.
27. Ghebali S, Chernyshenko SI, Leschziner MA. Turbulent Skin-Friction Reduction by Wavy Surfaces (2017). arXiv preprint arXiv:1705.01989.
28. Skote M. Turbulent Boundary Layer Flow Subject to Streamwise Oscillation of Spanwise Wall-Velocity. *Phys Fluids* (2011) 23(8):081703. doi:10.1063/1.3626028
29. Skote M. Temporal and Spatial Transients in Turbulent Boundary Layer Flow Over an Oscillating Wall. *Int J Heat Fluid Flow* (2012) 38(1–12):1–12. doi:10.1016/j.ijheatfluidflow.2012.08.004
30. Skote M. Comparison Between Spatial and Temporal Wall Oscillations in Turbulent Boundary Layer Flows. *J Fluid Mech* (2013) 730:273–94. doi:10.1017/jfm.2013.344
31. Wise DJ, Ricco P. Turbulent Drag Reduction Through Oscillating Discs. *J Fluid Mech* (2014) 746(10):536–64. doi:10.1017/jfm.2014.122
32. Wise DJ, Alvarenga C, Ricco P. Spinning Out of Control: Wall Turbulence Over Rotating Discs. *Phys Fluids* (2014) 26:125107. doi:10.1063/1.4903973
33. Wise DJ, Paolo O, Ricco P. Turbulent Drag Reduction Through Oscillating Discs-Corrigendum. *J Fluid Mech* (2018) 856:1064–6.
34. Jukes T, Choi K-S, Johnson G, Scott S. *Turbulent Drag Reduction by Surface Plasma Through Spanwise Flow Oscillation* (2006).
35. Jukes T. Turbulent Drag Reduction Using Surface Plasma. PhD thesis. Nottingham: University of Nottingham (2007).
36. Wilkinson S. Oscillating Plasma for Turbulent Boundary Layer Drag Reduction. *Int J Heat Fluid Flow* (2012) 38(1–12).
37. Xie F, Pérez-Muñoz JD, Ning Q, Pierre R. Drag Reduction in Wall-Bounded Turbulence by Synthetic Jet Sheets. *J Fluid Mech* (2022) 941:A63. doi:10.1017/jfm.2022.347
38. Min T, Kang SM, Speryer JL, Kim J. Sustained Sub-Laminar Drag in a Fully Developed Channel Flow. *J Fluid Mech* (2006) 558:309. doi:10.1017/s0022112006000206
39. Hœffner J, Fukagata K. Pumping or Drag Reducion. *J Fluid Mech* (2009) 635: 171–87. doi:10.1017/s0022112009007629
40. Woodcock JD, Sader JE, Marusic I. Induced Flow Due to Blowing and Suction Flow Control: An Analysis of Transpiration. *J Fluid Mech* (2011) 690:366–98. doi:10.1017/jfm.2011.441
41. Mathis R, Hutchins N, Marusic I. Large-Scale Amplitude Modulation of the Small-Scale Structures in Turbulent Boundary Layers. *J Fluid Mech* (2009) 628: 311–37. doi:10.1017/s0022112009006946
42. Mathis R, Monty JP, Hutchins N, Marusic I. Comparison of Large-Scale Amplitude Modulation in Turbulent Boundary Layers, Pipes, and Channel Flows. *Phys Fluids* (2009) 21(11). doi:10.1063/1.3267726
43. Shi L, Wang Z, Fu S, Zhang L. *A PnPm-CPR Method for Navier-Stokes Equations* (2012).
44. Bassi F, Rebay S. Discontinuous Galerkin Solution of the Reynolds Averaged Navier-Stokes and $K\,\omega$ Turbulence Model Equations. *J Comput Phys* (2005) 34: 507–40. doi:10.1016/j.compfluid.2003.08.004
45. Kim J, Moin P, Moser R. Turbulence Statistics in Fully Developed Channel Flow at Low Reynolds Number. *J Fluid Mech* (1987) 177:133–66. doi:10.1017/s0022112087000892
46. Jiménez J. *DNS Turbulent Channel Data* (2016).
47. Gatti D, Quadrio M. Reynolds-Number Dependence of Turbulent Skin-Friction Drag Reduction Induced by Spanwise Forcing. *J Fluid Mech* (2016) 802:553–82. doi:10.1017/jfm.2016.485
48. Pope SB. *Turbulent Flows*. Cambridge University Press (2000).

AEROSPACE RESEARCH COMMUNICATIONS
ORIGINAL RESEARCH
published: 18 December 2023
doi: 10.3389/arc.2023.12300

Flow Field Analysis of a Turbulent Channel Controlled by Scalloped Riblets

Haidong Yu[1], Yi Huang[1], Yiqian Wang[2]*, Yuehong Qian[2] and Song Fu[3]

[1]Beijing Institute of Astronautical System Engineering, Beijing, China, [2]School of Mathematical Sciences, Soochow University, Suzhou, China, [3]School of Aerospace Engineering, Tsinghua University, Beijing, China

Riblets are small protruding surfaces along the direction of the flow, and are one of the most well-known passive turbulent drag reduction methods. We investigated a scalloped riblet, the shape of which was constructed by smoothly connecting two third-order polynomials and was not as sharp in the tip as corresponding triangular riblets with the same height-width ratio. Numerical simulations were performed for turbulent channel flow with and without riblet control at an estimated optimum width of $W^+ = 20$ and a height-width ratio of 0.5. A drag reduction rate of 5.77% was obtained, which is generally larger than the reported drag reduction rates of corresponding triangular riblets from the literature. Mean flow fields and second-order statistics of velocity, vorticity, and Liutex, a quantity introduced to represent vortices, were reported. It was found that streamwise vortices just above the riblet tips, which have a length scale of 200 – 300 in wall units, have an important influence on those statistics and thus the turbulence generation cycle and the drag reduction mechanism. Pre-multiplied energy spectra of streamwise velocity and the Liutex component were reported to reveal the length scales in the flow field. Instantaneous vortical flow fields visualized by the Liutex method were provided with emphases on the streamwise vortices just above riblet tips. It should be noted that the class of scalloped riblets is suitable for investigations on the influences of curvatures at the tip and the valley of the riblet in future.

Keywords: riblet, drag reduction, turbulent channel, tip sharpness, scalloped

***Correspondence:**
Yiqian Wang
yiqian@suda.edu.cn

Received: *25 October 2023*
Accepted: *24 November 2023*
Published: *18 December 2023*

Citation:
Yu H, Huang Y, Wang Y, Qian Y and Fu S (2023) Flow Field Analysis of a Turbulent Channel Controlled by Scalloped Riblets. Aerosp. Res. Commun. 1:12300. doi: 10.3389/arc.2023.12300

INTRODUCTION

Drag reduction is of great importance because of the environmental and economic benefits from the reduced fuel consumption [1]. As one of the oldest and most investigated drag reduction methods, riblets, small protruding surfaces along the direction of the flow, had been known to be capable of reducing friction drag up to 8% with appropriate height and spacing in spite of the extra surface area. Early experiments conducted by Walsh et al. [2, 3], Bacher et al. [4], and Bechert et al. [5] tested different shapes including triangular, rectangular (or blade), trapezoidal, semi-circular, and other shape grooves with various sizes to get an optimal drag reduction rate. Experiments on concave and convex riblet shapes showed that drag reduction increases as the peak curvature increases, or as the radius of valley curvature increases, which means that an optimum riblet shape should have sharp peaks and curved valleys [2]. However, later investigations put more emphasis on the riblet tip rather than the valley, arguing that the tip sharpness plays an important role in damping the spanwise velocity fluctuations and thus limiting the momentum transport and turbulence intensity.

Two drag reduction regimes of riblets had been recognized [5], i.e., the "viscous regime," $W^+ < 10 - 15$, where the drag reduction rate increases almost linearly with the riblet width; and the "breakdown regime," $W^+ > 15 - 20$, where the drag reduction rate reaches a maximum and then decreases even to the point of drag increase. Here, W^+ represent the riblet width in wall units and the protruding surfaces would be referred to as roughness when entering the drag increase state. The physical mechanisms for drag reduction by riblets have been extensively studied, for example Walsh [6], Choi et al. [7], Choi [8], and Rstegari et al. [9]. Researchers often owe the credit to the interaction between the riblet surfaces and the longitudinal vortices of the turbulent boundary layer. One widely accepted explanation for riblets of the viscous regime, or for infinitesimal riblets, relies heavily on the concept of protrusion height [10, 11]. Intuitively, the protrusion height is understood as the distance between the riblet tip plane and the origin of the velocity profile, which lies between the riblet tip and riblet valley. The idea behind the emphasis of the protrusion height concept is that the influence of riblets is mainly constrained to within the inner layer and is thus viewed as an inner layer control strategy, and what the outer layer can "feel" is just the shear between the inner and outer layer. Therefore, the protrusion height denotes the location of a hypothetical flat plane that the outer layer perceives. The true protrusion height definition was given by Luchini et al. [11] From the intuitive definition above, we can easily define a longitudinal protrusion height $h_\parallel$ and a perpendicular protrusion height $h_\perp$ based on average streamwise and spanwise velocity respectively. Then the difference $\Delta h = h_\parallel - h_\perp$ is referred to as the protrusion height. The basic idea is that compared with streamwise flow, Δh represents the extent at which the cross-flow fluctuations are hampered, which had been viewed as critical for the turbulence generation cycle. In the viscous regime, the drag reduction rate is linearly dependent on this protrusion height Δh, a fact that has been verified by experiments and numerical simulations for various riblet shapes. However, the mechanism for the deterioration of drag reduction, or the "breakdown regime" remains controversial. The generation of secondary streamwise vortices by unsteady crossflow separation, which brings high speed flow towards the riblet surfaces, was suggested by Goldstein and Tuan [12], but secondary streamwise vortices do not necessarily lead to drag increase. For example, spanwise oscillation of the wall can also decrease drag [13, 14]. The second group of theories emphasized the scale interaction between riblet surfaces and turbulent coherent structures, i.e., near-wall streaks and streamwise vortices [7, 15]. Generally, the optimal lateral scale of riblets is an order of magnitude smaller than the spacing between low-speed streaks (about 100 in wall units). It was argued that for riblets larger than $W^+ \approx 20 - 30$, the near wall streamwise vortices could move freely and lodge inside the riblet valleys, which leads to an increase of wall surface area exposed to the sweep motion induced by those vortices. On the other hand, for smaller riblets, the streamwise vortices would stay above the riblet tips, and only the tip region could be subjected to the induced sweeps. Alternatively, Garcia-Mayoral and Jimenez [16] attributed the breakdown to the appearance of large-scale spanwise rollers. The mechanisms suggest plausible reasons based on experimental and numerical observations, but lack substantial support of improved design of riblets based on these theories.

As a bio-inspired technique mimicking the denticles of fast swim sharks, riblets are possibly the only turbulent drag reduction strategy that have been tested in application. Szodruch [17] reported that covering of riblets on 70% of the surface on an Airbus 320 commercial airplane leads to a 2% reduction in oil consumption. Instances of using riblets in sports, for example, on the hulls of boats and the surfaces of racing swimsuits, have been successful [18]. In contrast to the canonical arrangement, novel riblet concepts have been introduced. Nugroho et al. [19] explored the possibility of using ordered and directional surfaces to redirect the near wall flow. Benhamza et al. numerically investigated variable spacing riblets of rectangular shape in turbulent channel flows. Riblets with a sinusoidal variation along the streamwise direction [20, 21] had also been devised to mimic the spanwise oscillation strategy to reduce drag, however, these gained very little further drag reduction. Boomsma [22] numerically studied denticles resembles sharkskin in turbulent boundary layer, however, obtained drag increase instead of drag reduction. These expeditions generally failed to surpass the optimum drag reduction rate of conventional riblets, indicating a lack of full understanding of the drag reduction mechanism.

The plausible mechanisms of breakdown imply a requirement of tip sharpness of riblet for high drag reduction performance. However, sharp tips pose challenges for manufacturing and maintenance. Actually, Walsh [2] experimentally found that the optimum riblet appears to have sharp peaks and significant valley curvature. Launder and Li [23] also reported that the U-form (or scalloped) riblets can achieve a superior performance to the corresponding V-shaped riblets with the same height and width. Based on the protrusion height concept and numerical simulation of riblet controlled boundary layer transition, Wang et al. [24] showed that scalloped riblets could have better performance than corresponding triangular riblets with sharper tips. The scalloped riblet shape we considered is constructed by smoothly connecting two third-order polynomials.

$$\frac{y}{\gamma W} = \begin{cases} 2a\left(\frac{z}{W}\right)^3 - 2A\left(\frac{z}{W}\right)^2 + 1, 0 \le z \le z^\star \\ 2b\left(\frac{z}{W} - \frac{1}{2}\right)^3 + 2B\left(\frac{z}{W} - \frac{1}{2}\right)^2, z^\star < z \le \frac{W}{2} \end{cases} \quad (1)$$

where W is the width of the riblet, and the shape of the other half riblet ($W/2 < z \le W$) can be obtained by symmetry about $z = W/2$. Note, we have selected a coordinate system consistent with the following three-dimensional simulations. x, y, and z directions are streamwise, wall-normal, and spanwise directions respectively. Being aligned in the streamwise direction, x is not present in the riblet shape definition. γ is the height-width ratio while A and B are chosen parameters to determine the curvature at the tip and valley of the riblets. Note that an extra factor of 2 is introduced to make A and B the coefficients of second order terms when the width of the riblet is $S = 1$ and height-width ratio is $\gamma = 0.5$. a, b, and $z^{\star}$ are obtained by requiring the two polynomials smoothly connected, i.e., the functions value, first and second derivatives are continuous at $z^{\star}$. Despite the non-linearity in $z^{\star}$, the equations can be solved analytically

$$\frac{z^{\star}}{W} = \frac{6-B}{2(A-B)}, a = \frac{2(A+B)z^{\star}/W + A - B}{3z^{\star}/W}, \quad b = \frac{2(A+B)z^{\star}/W - 2B}{3(z^{\star}/W - 1/2)} \tag{2}$$

To guarantee that $z^{\star}/W$ is in the range of $(0, 0.5)$, we have to ensure that the given A and B satisfies

$$0 \le B < 6 < A, \text{or } 0 \le A < 6 < B \tag{3}$$

An extreme exists with $A = B = 6$, when the two polynomials are identical and the curvatures at the tip and valley are perfectly balanced. Thus, Eq. **1** represents a system of scalloped riblets, the tip and valley curvatures of which can be easily defined. Wang et al. [24] calculated the protrusion heights for scalloped riblets with various A, B, and γ values with a boundary element algorithm proposed by Luchini et al. [11], and found that for a larger height-width ratio γ, the protrusion height is mainly determined by A, i.e., the curvature at riblet tip, while for a smaller height-width ratio γ, the protrusion height is mostly dependent on B, i.e., the curvature at the riblet valley. However, for riblets in practical applications, the height-width ratio is generally in the range of $0.5 \le \gamma \le 1.2$, the protrusion height is influenced equally by A and B. Therefore, the shape of the riblet valley cannot be overlooked, and should be designed more carefully. It is also illustrated by direct numerical simulations of a boundary layer transition that a scalloped riblet, which is not as sharp in the tip as a corresponding triangular riblet with the same height-width ratio, nevertheless has a larger drag reduction rate, which is in accordance with protrusion height results. Another advantage of the scalloped riblet over the triangular riblet is its stronger resilience to riblet tip erosion, which means better manufacturing and maintenance performances. For the current study, we will focus on the same scalloped riblet as in Wang et al. [24] with $A = 25$, $B = 1.6$ and $\gamma = 0.5$. It was obtained, to four decimal digits, that $a = 100.6970$, $b = -1.4793$ and $z^{\star}/W = 0.0940$. Note that similar groove shapes had been studied by Klumpp et al. [25] for boundary layer transition but without detailed information of the groove shape. In addition, there are two methodologies to resolve the riblet shapes in numerical simulations, which involve the utilization of either body-fitted meshes or an immersed boundary method. With body-fitted meshes, the riblet shapes are better represented, but lack the versability of representing different shapes and sharp corners, especially when high-order numerical methods are adopted. On the other hand, the immerse boundary method can easily be used to simulate different riblet shapes even with the same mesh, which, however, has been criticized for low accuracy near the wall surfaces. For the current study, we choose the immersed boundary method for its versability and adopt Lagrange interpolation [26] to improve the accuracy near the wall surface.

One important aspect in understanding the flow dynamics is the identification of vortices. Noted by Küchemann [27], vortices are the "sinews and muscles of the flow." However, no consensus on the definition of vortices has been reached. Popular methods including Q, Δ, λ_2, λ_{ci}, Ω [28–32] and other criteria have been introduced to visualize vortices in various flows. However, these methods mainly suffer from two issues: 1) These methods are different with different physical reasoning and dimension units among each other; 2) as scalar-valued methods, no directional information about the rotational motion is provided. To overcome these issues, a new vortex vector, Liutex vector [33, 34], was introduced with its magnitude as twice the angular velocity of the rigid rotation part of the fluid motion and its direction as the local rotational axis. An explicit expression for the Liutex vector $\boldsymbol{R}$ in terms of vorticity $\boldsymbol{\omega}$, eigenvalues and eigenvectors of the velocity gradient tensor is proposed by Wang et al. [35] which leads to efficiency improvement and physical intuitive comprehension as

$$\boldsymbol{R} = R\boldsymbol{r} = \left[\boldsymbol{\omega} \cdot \boldsymbol{r} - \sqrt{(\boldsymbol{\omega} \cdot \boldsymbol{r})^2 - \lambda_{ci}^2}\right]\boldsymbol{r} \tag{4}$$

where λ_{ci} is the imaginary part of the complex conjugate eigenvalues and $\boldsymbol{r}$ is the real eigenvector of velocity gradient tensor. Thereafter, multiple vortex identification methodologies have been developed including the Liutex iso-surfaces, Liutex-Ω method [36, 37], Liutex core line method [38, 39], objective Liutex method [40], etc. In addition, a particular feature of the Liutex vector is that it is free from shear contamination. Kolář and Šístek [41] found that only the Liutex vector is not contaminated by stretching and shear in that an arbitrary adding or subtracting of stretching and shear would not alter the resulting vortex identification. This distinctive feature has been utilized by Ding et al. [42] to develop a new Liutex-based sub-grid model for large eddy simulation, which has been proved to outperform the famous Smagorinsky model in homogeneous isotropic turbulence and turbulent channel flows. In the current study, the Liutex vortex identification method will be adopted to analyze the flow field of riblet controlled turbulent channels.

The paper is organized as follows. Section *Numerical Methods and Case Setup* introduced the numerical methods adopted, especially the customized immersed boundary method that we use to model riblet surfaces. Section *Numerical Results* presents the numerical results, discussing the drag reduction rate, mean flow and turbulent statistics, premultiplied power spectrum density, and instantaneous flow field, with particular attention paid to the Liutex field. Finally, conclusions are drawn in Section *Conclusion*.

NUMERICAL METHODS AND CASE SETUP

The canonical case of a turbulent channel flow at Reynolds number $Re_{\tau} = 180$ was considered and used to study the drag reduction capacity of the scalloped riblets. The open-source finite difference software "Incompact3d" [43, 44] was adopted to simulate the flat plate and riblet channels, with which the incompressible Navier-Stokes equations were numerically solved. Periodic conditions were

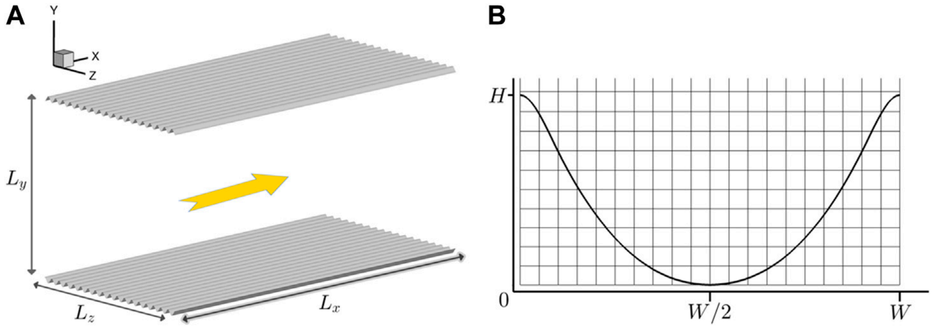

FIGURE 1 | (A) Sketch of the computational domain; **(B)** The mesh around the riblet surface.

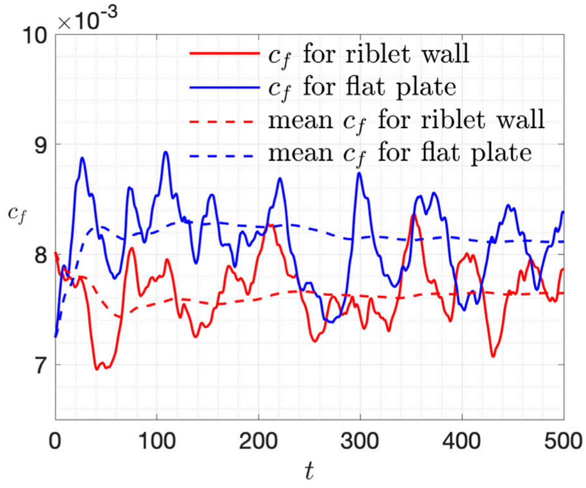

FIGURE 2 | Time history and cumulative mean of skin friction coefficients at both riblet and flat walls.

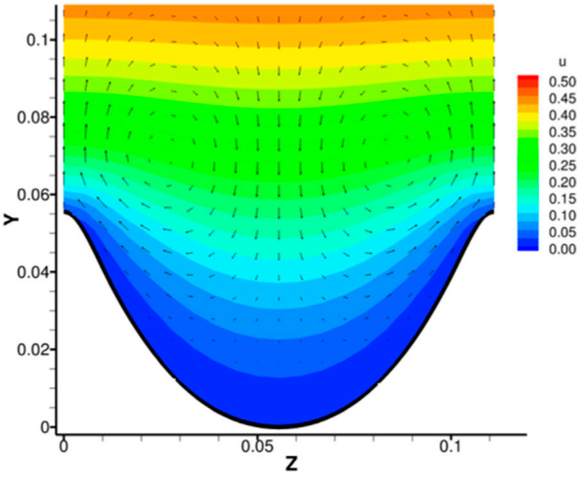

FIGURE 3 | Contours of mean streamwise velocity in the $y-z$ plane with in-plane velocity vectors.

naturally employed in the streamwise (x) and spanwise (z) direction, whilst no-slip conditions were applied in the upper and lower walls in the wall normal direction (y). For the riblet case, the no-slip condition was implemented with the immersed boundary method (IBM) which will be elaborated in the following. Sixth order compact schemes were adopted for spatial derivatives and a low-storage third-order Runge-Kutta scheme was used for time advancement. The pressure Poisson equation was solved with a pseudo-spectral method to ensure divergence-free condition up to machinery accuracy. The lengths for the computational domain were selected to be $L_x = 4h$, $L_y = 2h$ and $L_z = 2h$ with h as the half channel height. The domain is generally smaller compared to other direct numerical simulations of turbulent channel at $Re_\tau = 180$, but still sufficient to capture all the length scales and meanwhile limits the overall mesh point number to accelerate the simulations. A schematic of the flow with riblets is shown in **Figure 1A**. Both meshes for the two cases were identical and include 256 × 129 × 360 grid points in the streamwise, wall normal, and spanwise directions respectively. Uniform grids were used in the streamwise and spanwise directions, whilst a stretching grid was used in the normal direction with points clustered towards the wall surfaces. In wall units, the intervals in the streamwise and spanwise directions were $\Delta x^+ \approx 2.81$ and $\Delta z^+ \approx 1.00$ while the first interval adjacent to the wall was $\Delta y^+ \approx 0.98$. Normally, this resolution is more than sufficient to resolve all the scales in channel flow, especially in the spanwise direction. With 18 riblets arranged spanwise, 20 mesh points were used to resolve one riblet, and the riblet width in wall units was $W^+ = 20$, which was around the optimum width. The distribution of mesh points near one riblet surface is shown in **Figure 1B**. The flow rate was kept constant every time step and the bulk velocity u_b was thus kept as 2/3 with a bulk Reynolds number of 2800. Note that the bulk Reynolds number was exact while the friction Reynolds number was only approximately 180 and the wall unit lengths in the current study were all obtained based on $Re_\tau = 180$ unless otherwise stated.

The riblet surfaces were modeled with a customized immersed boundary method in "Incompact3d" based on an alternating direction forcing to ensure a no-slip boundary condition at the wall of the solid body [26]. A particular treatment was that no-zero velocities were set inside the solid body when computing derivatives to avoid

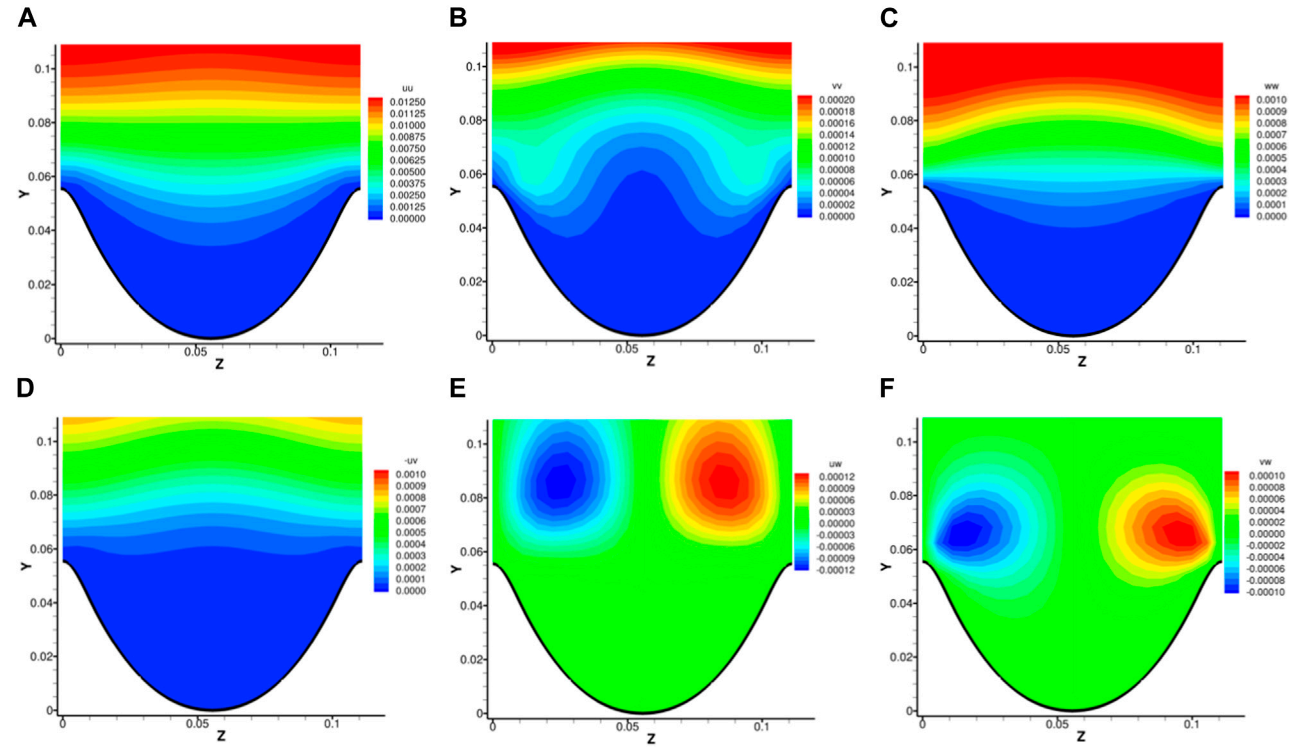

FIGURE 4 | Distributions of Reynolds stresses near riblet surfaces. **(A)** $\overline{u'u'}$, **(B)** $\overline{v'v'}$, **(C)** $\overline{w'w'}$, **(D)** $-\overline{u'v'}$, **(E)** $\overline{u'w'}$, **(F)** $\overline{v'w'}$.

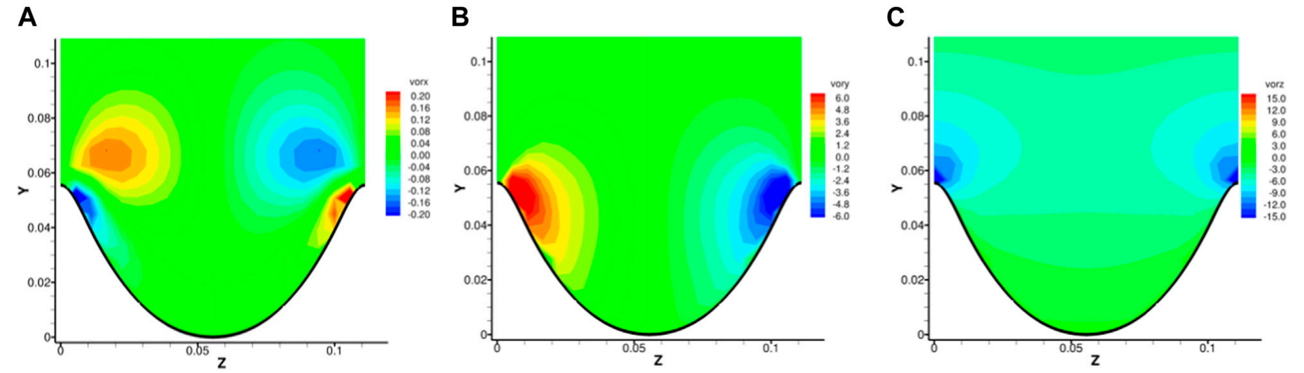

FIGURE 5 | Distribution of mean vorticity near riblet surfaces. **(A)** $\overline{\omega_x}$, **(B)** $\overline{\omega_y}$, **(C)** $\overline{\omega_z}$.

discontinuities of the velocity field, which, of course, would not be used when outputting numerical results. Because the technique is important for both correctly resolving the riblet wall surfaces and precisely calculating the friction drag, which is certainly critical especially when aiming for about 5~10 percent drag reduction, the procedure is described in more detail in the following.

For the adopted compact finite difference scheme, the derivatives along a directional line, which could cover both fluid and solid regions, were calculated simultaneously in a so-called implicit manner by solving systems of linear algebraic equations. If the condition of velocity component $u_i = 0$ was to be set everywhere inside the solid domain, then the spatial derivative at the interfaces between fluid and solid would not be ensured to be continuous, which leads to deterioration of the solution. The problem only has a minor impact for low-order numerical scheme. When combined with high-order schemes, however, spurious oscillations would be generated at the interfaces. To deal with this issue, non-zero values inside the solid domain were set based on Lagrange or cubic spline interpolation from points on and adjacent to the interfaces. This described 1D procedure was dealt with sequentially for the

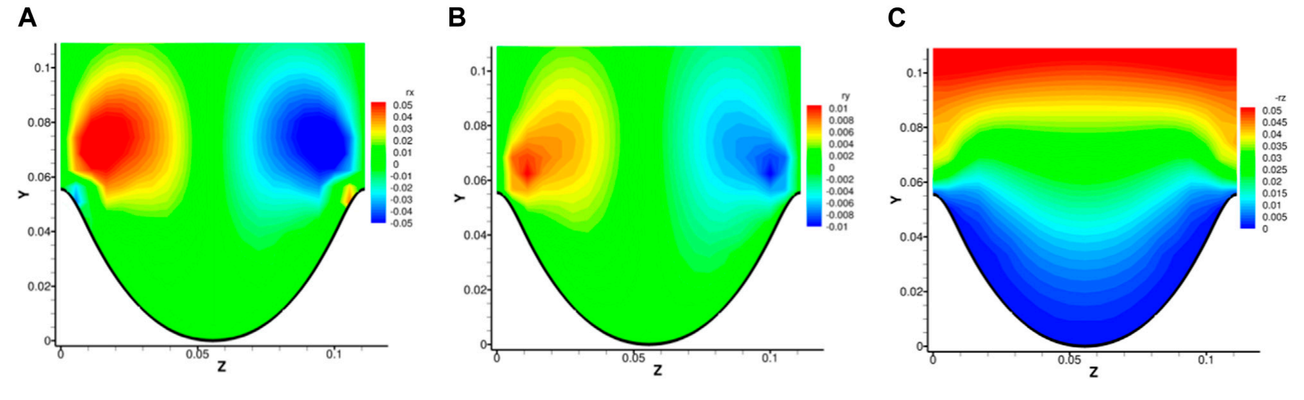

FIGURE 6 | Distribution of mean Liutex near riblet surfaces. **(A)** $\overline{R_x}$, **(B)** $\overline{R_y}$, **(C)** $\overline{R_z}$.

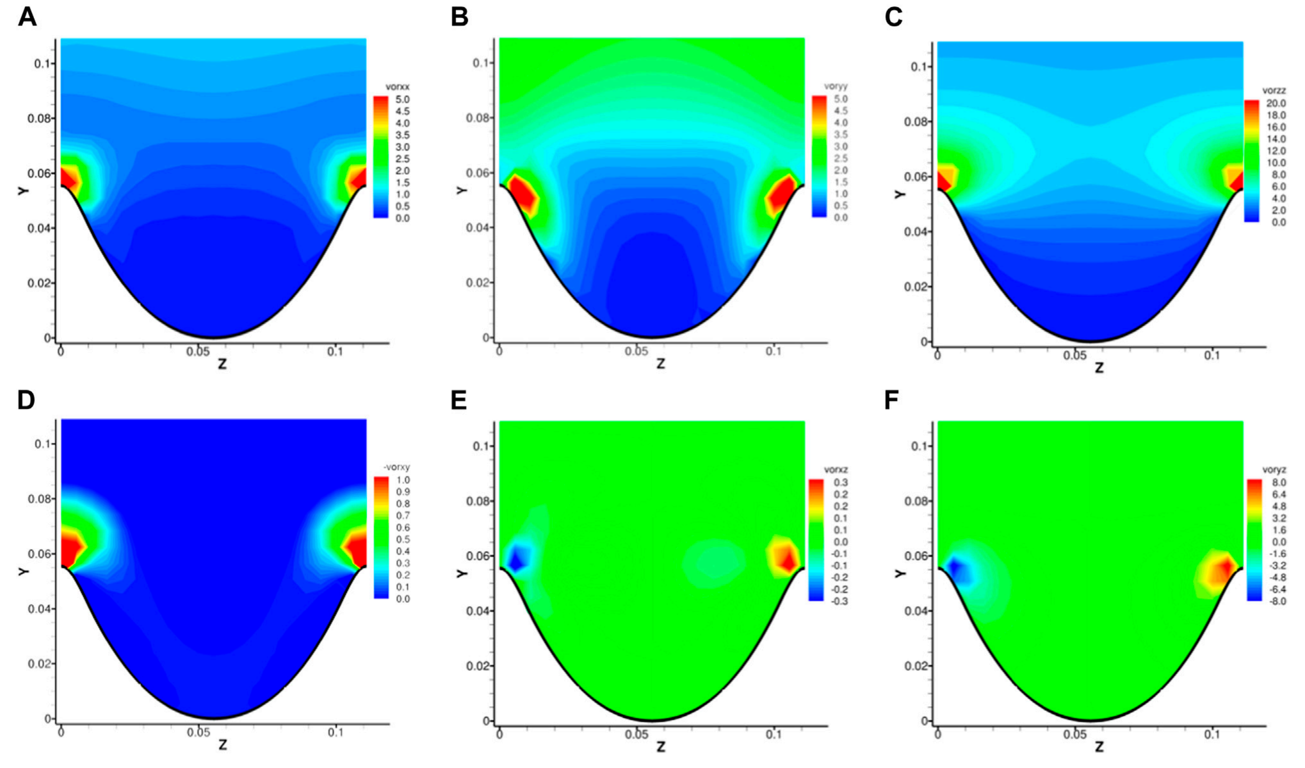

FIGURE 7 | Distributions of second moments of vorticity near riblet surfaces. **(A)** $\overline{\omega_x'\omega_x'}$, **(B)** $\overline{\omega_y'\omega_y'}$, **(C)** $\overline{\omega_z'\omega_z'}$, **(D)** $-\overline{\omega_x'\omega_y'}$, **(E)** $\overline{\omega_x'\omega_z'}$, **(F)** $\overline{\omega_y'\omega_z'}$.

three dimensions, and hence the name "alternating direction." For the riblet case, we selected Lagrange interpolation and two points from each fluid side of the interfaces to do interpolation. Note that the first adjacent fluid nodes near the interfaces were not included for stability reasons.

To calculate wall shear stresses on a riblet surface, velocity gradients need to be calculated on these surfaces, which are not necessarily on mesh nodes. To obtain velocity gradients, we carried out interpolation the same way as described above on one dimensional basis. Then we used a simple finite difference based on the interface point and an interpolated point about the local mesh size away. Once velocity gradients are obtained, the wall shear stress τ_w can be calculated by

$$\tau_w = \mu\left(\frac{\partial V_\parallel}{\partial n}\right)\Big|_w \tag{5}$$

where $V_\parallel$ is the velocity parallel to the wall surface, and n is the normal direction to the wall surface. It is not obvious when calculating wall shear stresses on riblet surfaces than flat surfaces.

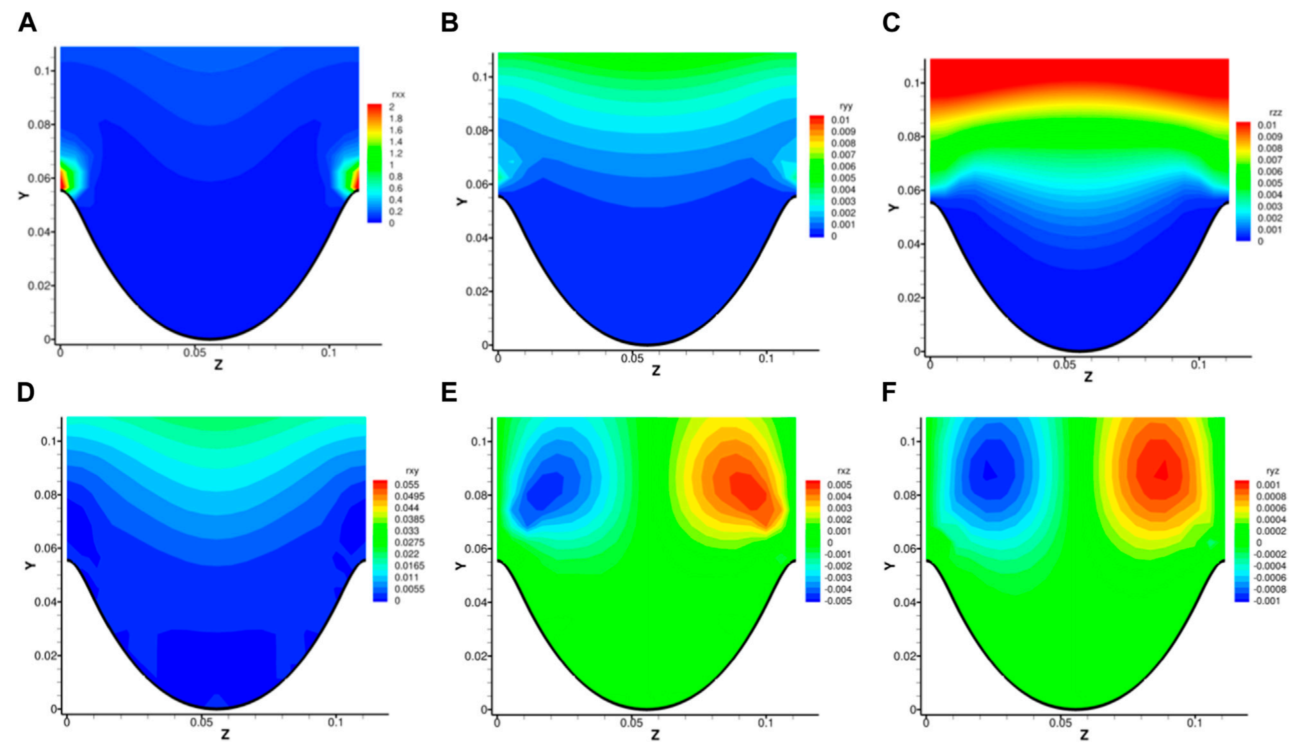

FIGURE 8 | Distributions of second moments of Liutex components near riblet surfaces. **(A)** $\overline{R_xR_x}$, **(B)** $\overline{R_yR_y}$, **(C)** $\overline{R_zR_z}$, **(D)** $-\overline{R_xR_y}$, **(E)** $\overline{R_xR_z}$, **(F)** $\overline{R_yR_z}$.

For riblet surfaces, the normal direction is $[\,0\;\; n_2\;\; n_3\,]^T$, the partial derivative $\partial V_{\parallel}/\partial n$ can be computed by

$$\frac{\partial V_{\parallel}}{\partial n} = \frac{\partial u}{\partial y} n_2 + \frac{\partial u}{\partial z} n_3 \tag{6}$$

Then, the drag can be expressed as a line integral (actually a surface integral, however we can simply take average in streamwise direction because of the homogeneity)

$$D = \int_0^L \mu \frac{\partial V_{\parallel}}{\partial n} ds = \mu\left[\int_0^L \frac{\partial u}{\partial y} n_2 ds + \int_0^L \frac{\partial u}{\partial z} n_3 ds\right] \tag{7}$$

where L is the length of the curved surface in the spanwise direction. Transforming the curve integral into coordinate integral we get

$$D = \mu\left[\int_0^{L_3} \left|\frac{\partial u}{\partial y}\right| dz + \int_0^{L_2} \left|\frac{\partial u}{\partial z}\right| dy\right] \tag{8}$$

where L_2 and L_3 are the normal and spanwise extent of the riblet surfaces. Note before using Eq. **8** to integrate, riblet-wise average should be carried out and the symmetry of the riblet surface used first to make the integrand single-valued in the y direction. Finally, to be comparable to the flat plate case, the skin friction coefficient c_f is defined as

$$c_f = \frac{D/L_3}{\frac{1}{2}\rho u_b^2} = \frac{2D}{\rho u_b^2} \tag{9}$$

where u_b is the bulk velocity.

NUMERICAL RESULTS

Drag Reduction Rate

The initial condition for both cases with and without riblet control is interpolated from a direct numerical simulation of turbulent channel flow at Re_τ= 180 with a coarser grid and a larger computational domain. After the initial transient stage of 300 non-dimensional time units, with bulk velocity, 2/3 of the fluids have flown through the computational domain 50 times, the friction coefficients are recorded for the following 500 time-units and are shown in **Figure 2**. Note that with the definition of skin friction coefficient c_f presented in the last section, comparison of c_f is equivalent to comparison of the total drag exerted on the whole wall surfaces. The cumulative averages of skin friction coefficients are also shown in **Figure 2** with a clear drag reduction observed. The mean skin friction coefficients for flat plate and riblet wall are 8.12×10^{-3} and 7.65×10^{-3}, which means the drag has been reduced by 5.77%. The friction Reynolds number is Re_τ= 178.4, slightly smaller than the nominal Reynolds number Re_τ= 180. Based on this actual Reynolds number, the width of the riblets in wall units is 19.8. We will continue to use wall units based on Re_τ= 180 in the following text. For corresponding triangular riblets with same width in wall units, and same height-width ratio, Walsh [3] reported a 2% drag reduction, while Choi [7] reported a 5% drag reduction. Similar settings for blade riblets in a larger Reynolds number of Re_τ= 550 result in a 4.45% drag reduction [45]. Generally, the current drag reduction rate of the scalloped riblet is higher than

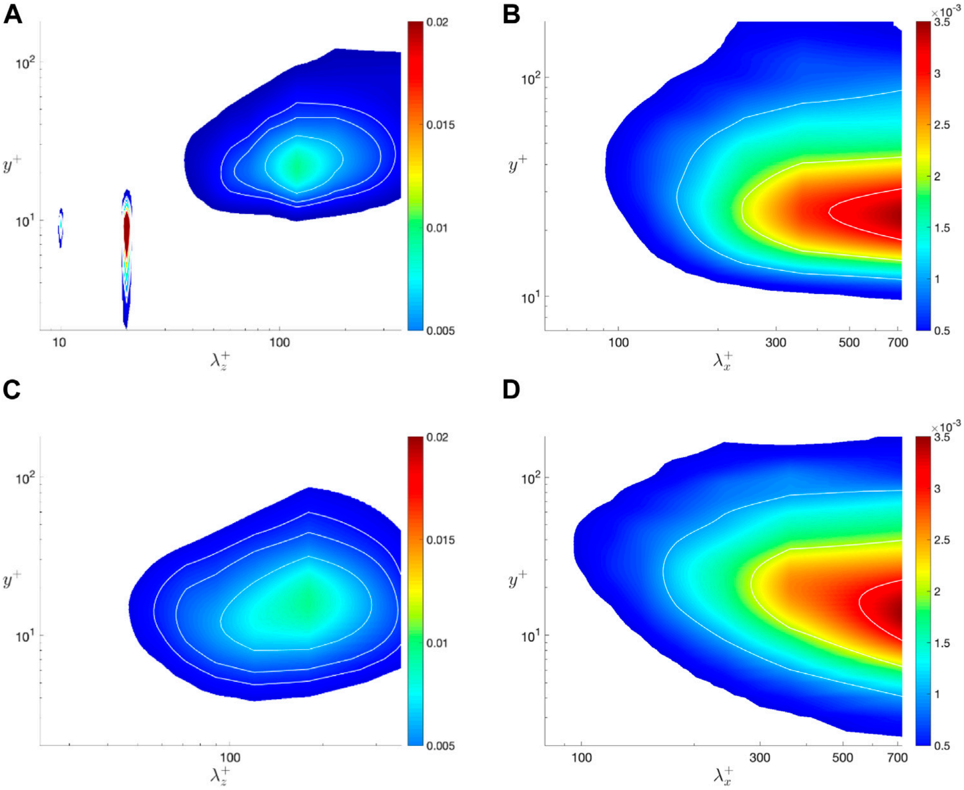

FIGURE 9 | Contours of pre-multiplied energy spectra of channel flow with and without scalloped riblet surface: **(A)** $k_z\Phi_{uu}$ with riblet surface; **(B)** $k_x\Phi_{uu}$ with riblet surface; **(C)** $k_z\Phi_{uu}$ without riblet surface; **(D)** $k_x\Phi_{uu}$ without riblet surface.

the corresponding triangular riblets with sharper tips. In addition, the scalloped tips are beneficial for the manufacturing and maintenance. The stochastic and intermittent behavior of the instantaneous skin friction coefficients come from the limited size of the computation domain and thus a small statistical sample. A simple Fourier analysis reveals that a peak exists for the frequency corresponding to a time period of $T = 125$, which should be understood as a quantity related to the spatial scales in homogeneous directions. However, we will not make further discussions here.

Mean Flow and Second-Order Statistics

The streamwise, time-, and riblet-wise averaged flow field near a riblet is shown in **Figure 3**. First, it is clear that all three velocity components in the valley are quite small, which makes the skin friction on the valley surface of the riblet rather small. On the other hand, the mean streamwise velocity rapidly increases along the y direction, creating high drag regions on the tips of the riblets. In addition, two secondary vortices can be found near the riblet tips, which has been reported by Choi *et al.* [7] and Wang et al. [35]. However, how such mean vortices correspond to instantaneous flow field remains unexplored.

Figure 4 shows the Reynolds stresses near riblet surfaces with primes denoting fluctuations. It can be observed from the normal stresses in **Figures 4A–C** that fluctuations inside the riblet valley are quite small, and above $y \approx 0.11$ ($y^+ \approx 20$ in wall units) the flow becomes almost uniform in the spanwise direction. This uniformity is in accordance with the assumptions of the viscous limit. Note the location of “W” shaped contour of $\overline{v'v'}$ is not the same as the mean secondary vortices. In addition, these fluctuations are superposed to the mean flow, and they cannot be created by these mean vortices. As shown in **Figure 4D**, $\overline{u'v'}$ is always negative near the riblet surface, which means a negative wall-normal fluctuation is accompanied by a positive streamwise fluctuations, and *vice versa*. In terms of quadrant analysis, more events happen in the second and forth quadrant of a $u' - v'$ plane, which are termed ejections and sweeps. Intuitively, a downward fluctuation brings high-speed flow towards the wall, thus creating a positive streamwise fluctuation, and an upward fluctuation brings low-speed flow away from the wall, creating a negative streamwise fluctuation. Different from **Figures 4A–D**, the green color in **Figures 4E, F** means no correlation between fluctuations. For the concentrations around $y = 0.08$ in **Figure 4E**, we can see that for positive streamwise fluctuations, the correlated spanwise velocity would drive them towards the riblet tips, while for negative streamwise fluctuations, the correlated spanwise velocity would drive them to the top of the riblet valleys. This observation is in accordance with the average streamwise velocity in **Figure 3**. A similar situation can be observed for $\overline{v'w'}$ in **Figure 4F**. From the distributions of normal Reynolds stresses, we can see that the streamwise fluctuations are two-orders larger than that of the wall-normal and spanwise fluctuation, thus our

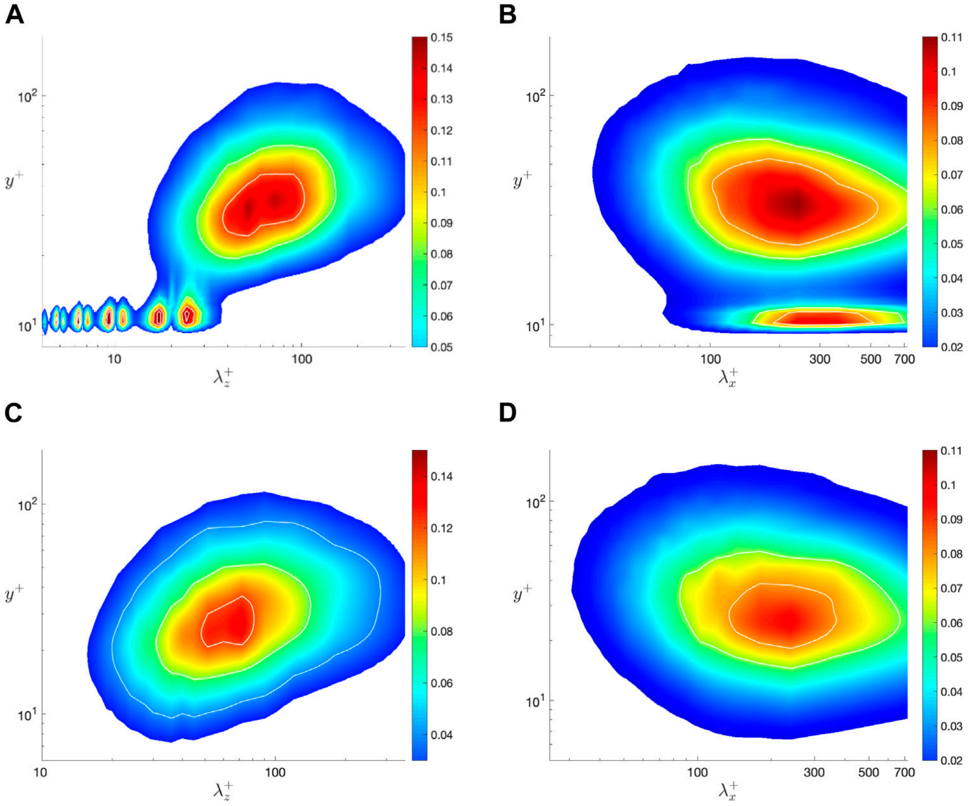

FIGURE 10 | Contours of pre-multiplied energy spectra of channel flow with and without scalloped riblet surface: **(A)** $k_z\Phi_{R_xR_x}$ with riblet surface; **(B)** $k_x\Phi_{R_xR_x}$ with riblet surface; **(C)** $k_z\Phi_{R_xR_x}$ without riblet surface; **(D)** $k_x\Phi_{R_xR_x}$ without riblet surface.

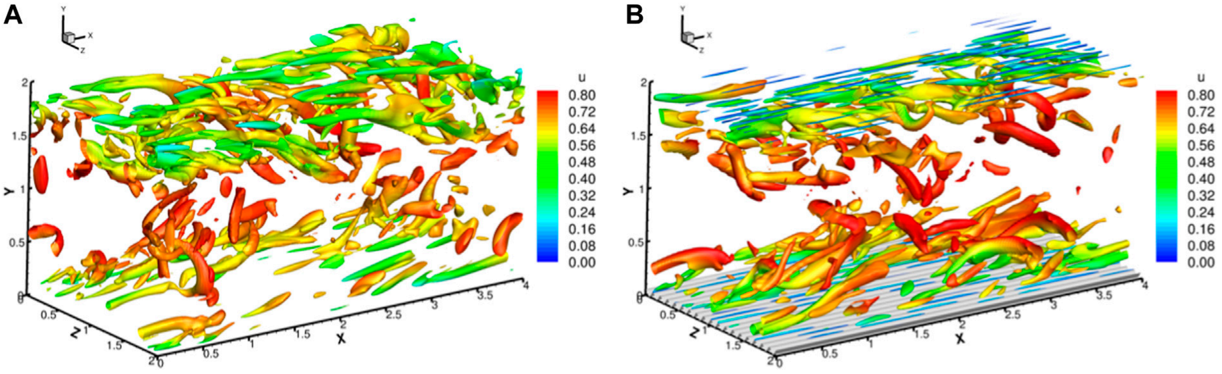

FIGURE 11 | Instantaneous vortical structures visualized by iso-surfaces of Liutex magnitude $R = 0.95$ for **(A)** flat plate channel and **(B)** riblet-controlled channel.

interpretation of transport of streamwise fluctuations by spanwise fluctuations. On the other hand, the wall-normal and spanwise fluctuations are in the same order as shown in **Figures 4B, C**. Therefore, **Figure 4F** can also be interpreted as spanwise fluctuations towards riblet tips would be lifted up while spanwise fluctuations towards the top of the riblet valley tends to be pushed downwards. Another thing worth noting is that the concentrations of $\overline{u'w'}$ are located substantially higher than those of $\overline{v'w'}$. Those correlations cannot be accredited to a single or several vortices, if we view fluctuations as results of instantaneous vortices, but only a statistical average effect of many vortices.

The distribution of mean vorticity and mean Liutex are shown in **Figures 5**, **6**. We can see that for the spanwise and wall-normal components, the magnitude of vorticity components are two-orders larger than that of Liutex components. This is because besides Liutex-represented rotational motion, vorticity also

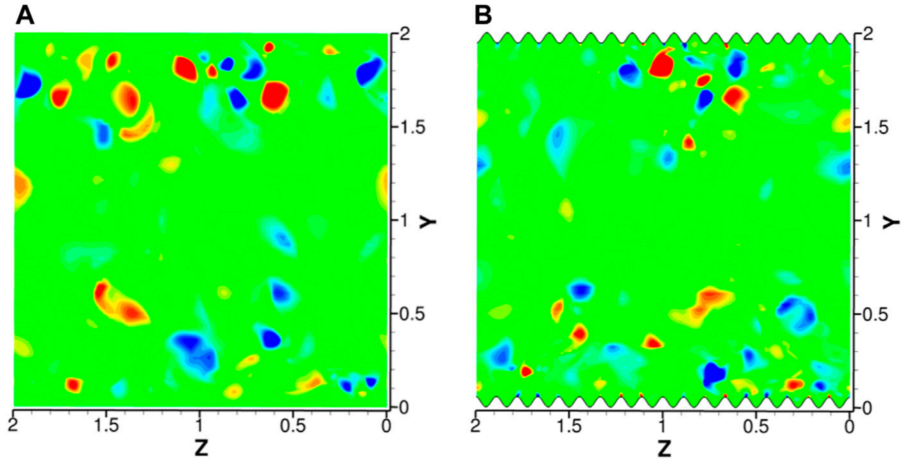

FIGURE 12 | Instantaneous contours of streamwise component of Liutex vector for flat plate case **(A)** and riblet case **(B)**.

contains pure shear, and contributions of high shears from $\partial u/\partial z$ and $\partial u/\partial y$ make the magnitude of vorticity components very large near the wall. A similar situation can be found for the streamwise component but with a smaller difference. This is because no background shear is present in the streamwise direction. Two mean streamwise vortices can be observed in accordance with the mean velocity field shown in **Figure 3**. In the vortex centers, it can be observed that Liutex takes up 50% of the vorticity magnitude, meaning the magnitude of Liutex is in balance with the magnitude of shear. Another observation is that, by no surprise, shears are closer to the wall while Liutex regions are located further away from the wall.

Second-order momentums of vorticity and Liutex components are shown in **Figures 7, 8** respectively. The locations of concentrations of both $\overline{\omega'_x\omega'_x}$ and $\overline{R_xR_x}$ are on top of the tips of riblets but with different magnitude, indicating possible instantaneous streamwise vortices just above riblet tips, which we will verify in the following. As we noted above, shear is very large near the riblet tips in the spanwise and wall-normal direction. Therefore, the magnitude in the concentrations of $\overline{\omega'_y\omega'_y}$ and $\overline{\omega'_z\omega'_z}$ is substantially larger than that of $\overline{R_yR_y}$ and $\overline{R_zR_z}$. Note that we have used fluctuations denoted by prime for vorticity while using the original variable for Liutex, based on the idea that turbulence velocity fluctuations are created with the generations of multiple scale vortices. For example, a pure shear flow like a laminar boundary layer would have substantial spanwise vorticity near the wall, which from the Liutex system will all be classified as shear. Such shear would only affect the mean flow, but not the fluctuations. Thus, the fluctuations are assumed to come from the formation of vortices and the shears near the riblet tips acts as a bank for the rotational motion. The concentrations of both $\overline{\omega'_y\omega'_y}$ and $\overline{\omega'_z\omega'_z}$ disappear in the contours of $\overline{R_yR_y}$ and $\overline{R_zR_z}$ as shown in **Figures 7B, C, 8B, C**. There are no clear spanwise and wall-normal vortex patterns in the vicinity of riblet surfaces. For the cross-correlation terms, the strong correlation in $\overline{\omega'_x\omega'_y}$ in **Figure 7D** is not presented in **Figure 8D**, which means despite a high correlation of shear, the streamwise and wall-normal vortices are statistically decoupled above riblet tips. Similar for $\overline{\omega'_x\omega'_z}$ and $\overline{\omega'_y\omega'_z}$ as shown in **Figures 7E, F**, shear contributes mainly for the concentrations near riblet tips, while the correlation concentrations of $\overline{R_xR_z}$ and $\overline{R_yR_z}$ are well further away from the wall. An interesting observation is the similarities between the distributions of cross-correlations of Liutex components in **Figures 8D–F** and the distributions of shear Reynolds stresses shown in **Figures 4D–F**. Even though the concentration locations are shifted upward or downward a little bit for $x-z$ and $y-z$ correlations, the trend remains the same. As stated, the Liutex correlations are calculated using the original variable rather than fluctuations, which makes it easier to construct turbulence models based on the Liutex vector. Ding et al. [42] introduced a subgrid model for large eddy simulation based upon the eddy viscosity hypothesis. Non-isotropic models can also be easily formulated.

Premultiplied Power Spectrum Density

Contours of pre-multiplied energy spectra of flat plate channel and riblet controlled channel are shown in **Figure 9**. k_x and k_z are the streamwise and spanwise wavenumbers and Φ_{uu} is the energy spectra of streamwise velocity fluctuations. It can be seen from **Figure 9A** that high energy regions can be found around wavenumber $\lambda_z^+ = 20$ and $\lambda_z^+ = 10$ at the height of $y^+ = 10$. Note that $\lambda_z^+ = 20$ corresponds to the width of the riblet while $y^+ = 10$ corresponds to the height of riblets. This is no surprise, as riblets enforce zero velocity inside the solid region and thus create periodic patterns at wavenumber $\lambda_z^+ = 20$. Harmonics includes $\lambda_z^+ = 10$, $\lambda_z^+ = 5$ and so on can be found in the pre-multiplied spectrum, but not shown in **Figure 9A** for wavenumbers less or equal to 5 because of their significance. On the other hand, the concentration of energy power spectra around $y^+ = 20$ represents the low-speed streaks, typical coherent structures found in wall bounded turbulence. These streaks had a typical spacing around 100 in wall units. However, compared to $k_z\Phi_{uu}$ shown in **Figure 9C** for the flat plate channel, the spacing between the

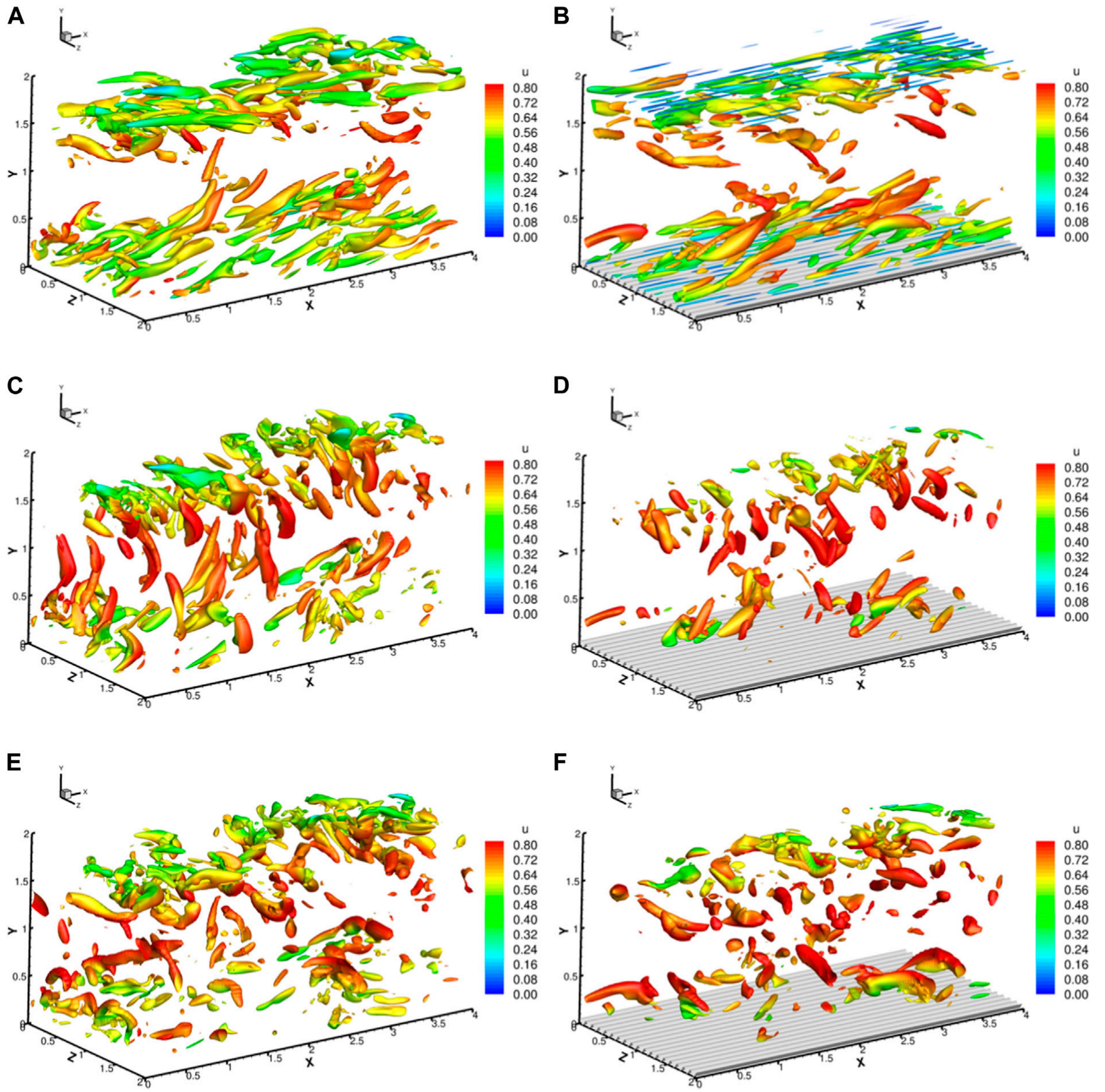

FIGURE 13 | Instantaneous iso-surfaces of absolute values of Liutex components for flat plate channel and riblet controlled channel. **(A)** $|R_x|$ = without riblets, **(B)** $|R_x|$ = with riblets, **(C)** $|R_y|$ = without riblets, **(D)** $|R_y|$ = with riblets, **(E)** $|R_z|$ = without riblets, **(F)** $|R_z|$ = with riblets.

streaks decrease, which means that riblet, viewed as an inner-layer control method, also alters the buffer layer. The magnitude corresponding to the streaks remains basically the same. For the streamwise velocity component, the energy spectrum concentrates at a length scale equal to the length of the computational domain at the height of the buffer layer as shown in **Figures 9B, D**. In addition, the contours have been made more parallel to the streamwise direction by the riblet control, indicating a regulation of the flow field.

Low-speed streaks and streamwise vortices have been viewed as critical in the turbulence generation cycle. Here we adopt the Liutex methodology and use its streamwise component to represent streamwise vortices. The pre-multiplied energy spectra of R_x with and without riblet control is shown in **Figure 10**. The situation is more complex for R_x with riblet control above the height of riblets $y^+ = 10$ with a series of concentrations ranging from $\lambda_z^+ = 3$ to 25 as shown in **Figure 10A**. It seems that those small concentrations appear in pairs, a pair around $\lambda_z^+ = 20$, then a pair around $\lambda_z^+ = 10$ and so on. It has been implied from **Figure 8A** that streamwise vortices exist just above the riblet tips. However, they are not always present for all riblet tips and they can be both negative and positive, which might be the reason for the energy spectrum pattern seen in **Figure 10A**. The larger scale at $y^+ = 40$ with riblet control is stronger than the scale at $y^+ = 30$ without riblet control. Note that, if we measure lengths in y direction from the tip rather than the valley of the riblets, the heights at which the larger scale reside will be the same. In addition, we can see from **Figure 10B** that the streamwise vortices at the top of the riblet tips has a length scale of around $\lambda_x^+ = 200 - 300$, which our computational domain still can capture with $L_x^+ = 720$. The length scale is slightly larger than the length scale at $y^+ = 40$ with riblet control, which is stronger than that without riblet control as shown in **Figure 10D**. Overall, from the pre-multiplied energy spectra of u and R_x, we can see that for the current riblet control, the statistical property changes are not limited to the viscous sublayer. The buffer layer and the bottom of the log layer are also affected by the riblet control. Spectra of R_x more clearly shows the existence and influences of streamwise vortices just above the riblet tips, which we will further investigate in the following.

Instantaneous Flow Field

Instantaneous vortical structures are shown by iso-surfaces of Liutex magnitude $R = 0.95$ for typical snapshots both with and without riblet control in **Figure 11**. Despite the chaotic appearance, streamwise vortices, hairpin and arc vortices, typical structures in a turbulent channel, can be observed in **Figure 11A**. The streamwise vortices just above the riblet tips that are mentioned above can be observed in **Figure 11B**. Note that we have removed the top riblet surface for visualization. Instantaneous contours of streamwise Liutex components at $x = 2$ with and without riblets are shown in **Figure 12**. It can be seen that some riblet tips have those streamwise vortices, and some do not. In addition, the streamwise Liutex can be either positive or negative in a statistically balanced way. Therefore, they cannot be observed from the mean flow field as shown in **Figure 3** and the mean vorticity and Liutex field as shown in **Figures 5A**, **6A**. However, from the discussion above, those streamwise vortices should be very important in influencing the second-order moment statistics, and thus have a significant influence on the generation cycle of wall turbulence.

Figure 13 shows iso-surfaces of absolute values of Liutex components. It can be seen from **Figures 13A, B** that the streamwise vortices are located near the wall surfaces and it is reconfirmed that the vortices on the top of riblet tips are actually streamwise. For the snapshot shown in **Figure 13C**, multiple lengthy vortices in the y direction can be observed, but for the riblet control case in **Figure 13D**, the y-direction vortices are lesser, and lack the directional arrangement. For iso-surfaces of $|R_z|$ in **Figures 13E, F**, we can find fewer structures in the riblet controlled case, and the structures tend to be more statistically isotropic. A visual inspection reveals possible weakening of spanwise and wall-normal vortices by riblet control.

CONCLUSION

We considered the kind of scalloped riblets constructed by smoothly connecting two third-order polynomials, and selected a scalloped riblet with shape parameters $A = 25$ and $B = 1.6$. The turbulent channel flows with and without riblet control were simulated with $W^+ = 20$, and height-width ratio $\gamma = 0.5$. The drag reduction rate was 5.77%, which is generally larger than corresponding triangular riblets with sharper tips. The flow fields were then investigated carefully. Mean flow fields, Reynolds stress, correlations of vorticity and Liutex components, pre-multiplied spectra of streamwise velocity and Liutex component, and instantaneous flow fields were presented. It was found that streamwise vortices just above the riblet tips, which have a length scale of 200–300 in wall units, play a significant role in the controlling the flow field. Further investigations, especially the causal relations between those streamwise vortices and the drag reduction, should be analyzed. Moreover, it is imperative to consider the influence of the Reynolds number in the context of scalloped riblets, particularly in high Reynolds number flows, where the application of riblets for drag reduction is targeted.

DATA AVAILABILITY STATEMENT

The data that support the findings of this study are available from the corresponding author upon reasonable request.

AUTHOR CONTRIBUTIONS

HY: investigation; visualization; writing original draft. YH: review and editing. YW: conceptualization; investigation; methodology; code development; writing, editing of the manuscript. YQ: review and editing. SF: review and editing. All authors contributed to the article and approved the submitted version.

FUNDING

The current study is supported by Jiangsu Shuangchuang Project (JSSCTD202209), the National Science Foundation of China (Grant No. 12302312) and the National Science Foundation of the Jiangsu Higher Education Institutions of China (Grant No. 22KJB130011).

CONFLICT OF INTEREST

The authors declare that the research was conducted in the absence of any commercial or financial relationships that could be construed as a potential conflict of interest.

REFERENCES

1. Abbas A, Bugeda G, Ferrer E, Fu S, Periaux J, Pons-Prats J, et al. Drag Reduction via Turbulent Boundary Layer Flow Control. *Sci China Technol Sci* (2017) 60(9):1281–90. doi:10.1007/s11431-016-9013-6
2. Walsh M. Turbulent Boundary Layer Drag Reduction Using Riblets. In: 20th Aerospace Sciences Meeting; January 11-14, 1982; Orlando, Florida (1982).
3. Walsh MJ. Riblets as a Viscous Drag Reduction Technique. *AIAA J* (1983) 21(4):485–6. doi:10.2514/3.60126
4. Bacher E, Smith C. A Combined Visualization-Anemometry Study of the Turbulent Drag Reducing Mechanisms of Triangular Micro-Groove Surface

Modifications. In: Shear Flow Control Conference; March 12-14, 1985; Boulder, Colorado (1985).

5. Bechert DW, Bruse M, Hage W, Van Der Hoeven JGT, Hoppe G. Experiments on Drag-Reducing Surfaces and Their Optimization with an Adjustable Geometry. *J Fluid Mech* (1997) 338:59–87. doi:10.1017/s0022112096004673
6. Walsh MJ. Effect of Detailed Surface Geometry on Riblet Drag Reduction Performance. *J Aircraft* (1990) 27(6):572–3. doi:10.2514/3.25323
7. Choi H, Moin P, Kim J. Direct Numerical-Simulation of Turbulent-Flow over Riblets. *J Fluid Mech* (1993) 255:503–39. doi:10.1017/s0022112093002575
8. Choi K-S. Near-Wall Structure of a Turbulent Boundary Layer with Riblets. *J Fluid Mech* (2006) 208:417–58. doi:10.1017/s0022112089002892
9. Rastegari A, Akhavan R. The Common Mechanism of Turbulent Skin-Friction Drag Reduction with Superhydrophobic Longitudinal Microgrooves and Riblets. *J Fluid Mech* (2018) 838:68–104. doi:10.1017/jfm.2017.865
10. Bechert DW, Bartenwerfer M. The Viscous-Flow on Surfaces with Longitudinal Ribs. *J Fluid Mech* (1989) 206:105–29. doi:10.1017/s0022112089002247
11. Luchini P, Manzo F, Pozzi A. Resistance of a Grooved Surface to Parallel Flow and Cross-Flow. *J Fluid Mech Digital Archive* (2006) 228:87. doi:10.1017/s0022112091002641
12. Goldstein DB, Tuan TC. Secondary Flow Induced by Riblets. *J Fluid Mech* (1998) 363:115–51. doi:10.1017/s0022112098008921
13. Baron A, Quadrio M. Turbulent Drag Reduction by Spanwise wall Oscillations. *Appl Scientific Res* (1995) 55(4):311–26. doi:10.1007/bf00856638
14. Jung WJ, Mangiavacchi N, Akhavan R. Suppression of Turbulence in Wall-Bounded Flows by High-Frequency Spanwise Oscillations. *Phys Fluids A: Fluid Dyn* (1992) 4(8):1605–7. doi:10.1063/1.858381
15. Suzuki Y, Kasagi N. Turbulent Drag Reduction-Mechanism above a Riblet Surface. *Aiaa J* (1994) 32(9):1781–90. doi:10.2514/3.12174
16. GarcÍA-Mayoral R, JimÉNez J. Hydrodynamic Stability and Breakdown of the Viscous Regime over Riblets. *J Fluid Mech* (2011) 678:317–47. doi:10.1017/jfm.2011.114
17. Szodruch J. Viscous Drag Reduction on Transport Aircraft. In: 29th Aerospace Sciences Meeting; January 11-14, 1988; Reno, Nevada (1988).
18. Garcia-Mayoral R, Jimenez J. Drag Reduction by Riblets. *Philos Trans A Math Phys Eng Sci* (2011) 369:1412–27. doi:10.1098/rsta.2010.0359
19. Stalio E, Nobile E. Direct Numerical Simulation of Heat Transfer over Riblets. *Int J Heat Fluid Flow* (2003) 24(3):356–71. doi:10.1016/s0142-727x(03)00004-3
20. Peet Y, Sagaut P, Charron Y. Towards Large Eddy Simulations of Turbulent Drag Reduction Using Sinusoidal Riblets. In: Proceedings of the 5th IASME/WSEAS International Conference on Fluid Mechanics and Aerodynamics; August 25-27, 2007; Athens, Greece (2007).
21. Sasamori M, Iihama O, Mamor H, Iwamoto K, Murata A. Experimental and Numerical Studies on Optimal Shape of A Sinusoidal Riblet for Drag Reduction in Wall Turbulence. In: Ninth International Symposium on Turbulence and Shear Flow Phenomena; June 30 - July 3 (2015); Australia (2015).
22. Boomsma A, Sotiropoulos F. Direct Numerical Simulation of Sharkskin Denticles in Turbulent Channel Flow. *Phys Fluids* (2016) 28(3). doi:10.1063/1.4942474
23. Launder BE, Li S. On the Prediction of Riblet Performance with Engineering Turbulence Models. *Appl scientific Res* (1993) 50:283–98. doi:10.1007/bf00850562
24. Wang Y, Huang Y, Fu S. On the Tip Sharpness of Riblets for Turbulent Drag Reduction. *Acta Mechanica Sinica* (2022) 38(4):321389. doi:10.1007/s10409-022-09019-x
25. Klumpp S, Meinke M, Schröder W. Numerical Simulation of Riblet Controlled Spatial Transition in a Zero-Pressure-Gradient Boundary Layer. *Flow, Turbulence and Combustion* (2010) 85(1):57–71. doi:10.1007/s10494-010-9251-x
26. Gautier R, Laizet S, Lamballais E. A DNS Study of Jet Control with Microjets Using an Immersed Boundary Method. *Int J Comput Fluid Dyn* (2014) 28(6-10):393–410. doi:10.1080/10618562.2014.950046
27. Saffman P. Vortex Dynamics. In: *Theoretical Approaches to Turbulence*. Berlin, Germany: Springer (1985). p. 263–77.
28. Hunt JCR, Wray AA, Moin P. Eddies, Streams, and Convergence Zones in Turbulent Flows. In: Proceedings of the 1988 Summer Program; June 17-26, 1988; Carnegie Mellon University (1988).
29. Chong MS, Perry AE, Cantwell BJ. A General Classification of Three-Dimensional Flow fields. *Phys Fluids A: Fluid Dyn* (1990) 2(5):765–77. doi:10.1063/1.857730
30. Jeong J, Hussain F. On the Identification of a Vortex. *J Fluid Mech* (1995)(-1) 285.
31. Zhou J, Adrian RJ, Balachandar S, Kendall TM. Mechanisms for Generating Coherent Packets of Hairpin Vortices in Channel Flow. *J Fluid Mech* (1999) 387:353–96. doi:10.1017/s002211209900467x
32. Liu CQ, Wang Y, Yang Y, Duan Z. New omega Vortex Identification Method. *Sci China-Physics Mech Astron* (2016) 59(8):684711. doi:10.1007/s11433-016-0022-6
33. Gao Y, Liu C, Ouyang Z, Xia Z, Wang Z, Liu B, et al. Competing Spin Fluctuations and Trace of Vortex Dynamics in the Two-Dimensional Triangular-Lattice Antiferromagnet AgCrS2. *Phys Fluids* (2018) 30(8): 265802. doi:10.1088/1361-648X/aac622
34. Liu C, Gao Y, Tian S, Dong X. Rortex—A New Vortex Vector Definition and Vorticity Tensor and Vector Decompositions. *Phys Fluids* (2018) 30(3). doi:10.1063/1.5023001
35. Wang Y-q., Gao Y, Liu J, Liu C. Explicit Formula for the Liutex Vector and Physical Meaning of Vorticity Based on the Liutex-Shear Decomposition. *J Hydrodynamics* (2019) 31(3):464–74. doi:10.1007/s42241-019-0032-2
36. Dong X, Gao Y, Liu C. New Normalized Rortex/vortex Identification Method. *Phys Fluids* (2019) 31(1). doi:10.1063/1.5066016
37. Liu J, Liu C. Modified Normalized Rortex/vortex Identification Method. *Phys Fluids* (2019) 31(6). doi:10.1063/1.5109437
38. Gao Y, Liu J, Yu Y, Liu C. A Liutex Based Definition and Identification of Vortex Core center Lines. *J Hydrodynamics* (2019) 31(3):445–54. doi:10.1007/s42241-019-0048-7
39. Xu H, Cai X, Liu C. Liutex (Vortex) Core Definition and Automatic Identification for Turbulence Vortex Structures. *J Hydrodynamics* (2019) 31(5):857–63. doi:10.1007/s42241-019-0066-5
40. Liu J, Gao Y, Wang Y, Liu C. Objective Omega Vortex Identification Method. *J Hydrodynamics* (2019) 31(3):455–63. doi:10.1007/s42241-019-0028-y
41. Kolár V, Sístek J. Consequences of the Close Relation between Rortex and Swirling Strength. *Phys Fluids* (2020) 32(9). doi:10.1063/5.0023732
42. Ding Y, Pang B, Yan B, Wang Y, Chen Y, Qian Y. A Liutex-Based Subgrid Stress Model for Large-Eddy Simulation. *J Hydrodynamics* (2023) 34(6): 1145–50. doi:10.1007/s42241-023-0085-0
43. Laizet S, Lamballais E. High-Order Compact Schemes for Incompressible Flows: A Simple and Efficient Method with Quasi-Spectral Accuracy. *J Comput Phys* (2009) 228(16):5989–6015. doi:10.1016/j.jcp.2009.05.010
44. Laizet S, Li N. Incompact3d: A Powerful Tool to Tackle Turbulence Problems with up to O(105) Computational Cores. *Int J Numer Methods Fluids* (2010) 67(11):1735–57. doi:10.1002/fld.2480
45. García-Mayoral R, Jiménez J. Scaling of Turbulent Structures in Riblet Channels up to Re τ ≈ 550. *Phys Fluids* (2012) 24(10). doi:10.1063/1.4757669

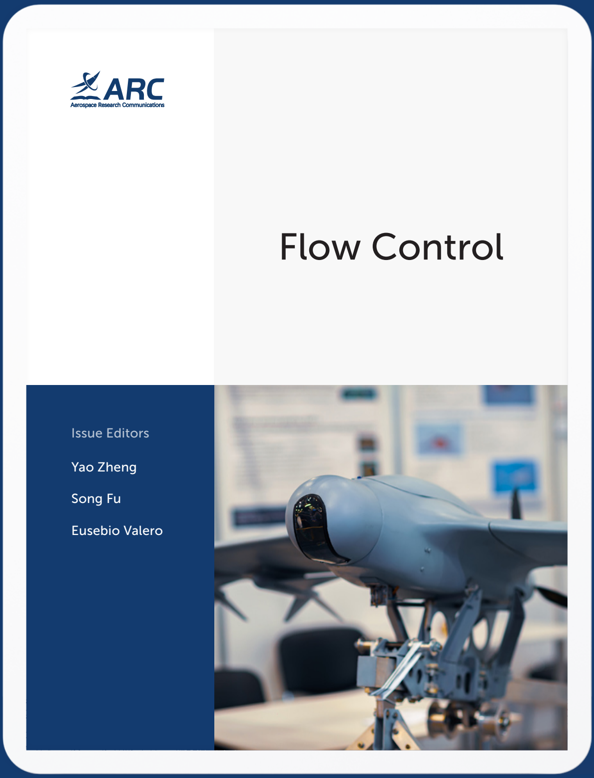

ARC
Aerospace Research Communications

Flow Control

Issue Editors
Yao Zheng
Song Fu
Eusebio Valero